RADIO-PATHOLOGICAL INVESTIGATION OF MYELIN LOSS AND OLIGODENDROCYTE DEGENERATION USING MULTIMODAL FUNCTIONAL MRI IN ALZHEIMER'S DISEASE

WAI-YEUNG CHENG

PhD

2023

The Hong Kong Polytechnic University

Department of Health Technology and Informatics

Radio-pathological investigation of myelin loss and oligodendrocyte degeneration using multimodal functional MRI in Alzheimer's disease

Wai-Yeung CHENG

A thesis submitted in partial fulfilment of the requirements for the degree of Doctor of Philosophy

March 2023

CERTIFICATE OF ORIGINALITY

I hereby declare that this thesis is my own work and that, to the best of my knowledge and belief, it reproduces no material previously published or written, nor material that has been accepted for the award of any other degree or diploma, except where due acknowledgement has been made in the text.

_____ (Signed)

.

Wai-Yeung CHENG (Name of Student)

Contents

Abstract

Alzheimer's disease (AD) is the most common cause of dementia characterized by excessive amyloid-β plaque formations and cognitive impairment. This neurodegenerative disease exists in two forms: familial AD and sporadic AD. Both are suggested to be triggered by protein misfoldings. Familial and sporadic AD are associated with mutations of the amyloid cascade pathway and biological aging, respectively. However, when abnormal protein aggregations become detectable, the cognitive impairments in the patients are already irreversible. Emerging evidence suggested that myelin loss and oligodendrocyte degeneration are some of the earliest events in both types of AD, but the cellular mechanism remains unknown. By delineating the biological process leading to early myelin loss in AD, new direction towards early disease detection and patient management may be achievable. To fill the gap of knowledge, this study characterizes the myelin pathology of AD among different transgenic mouse model using functional magnetic resonance-based neuroimaging (fMRI), followed by a histopathological examination of the cellular changes.

To investigate the robustness of fMRI on demyelination, we first studied the effects of demyelination with cuprizone on amyloid deposition in AD mice models, R1.40 and APP/PS1. mice predisposed for familial AD (R.140 and APP/PS1) between 3 and 4 months old and fed cuprizone for chemically induced demyelination before subjection to multimodal functional MRI. Diffusion kurtosis imaging, magnetic resonance spectroscopy, magnetization transfer and T2 weighted volumetric analysis were performed to study structural and chemical changes of the whole cerebrum. Perpendicular diffusion from white matter tracts was not found between both the treated and untreated wild-types (WT) and R1.40 strain. Histologically, however, mature oligodendrocyte (OL) populations and the myelin protein, MAG, were significantly reduced in the cuprizone mice. No neuronal loss was detected, yet DNA damage stained by 53BP1 was prevalent in both neurons and OLs and more prevalent in cuprizone mice. This unaffected neuron count compared to the decrease in mature OLs indicate the vulnerability of the OLs. Complementary investigation into the more aggressive APP/PS1 strain showed increase diffusivity in the white matter region of the cuprizone treated. Histological analysis showed the selective reduction in mature OLs without effect on the overall OL population. The compromised OL differentiation may contribute to the increased diffusivity through insufficient OL maturation and myelin maintenance. An elevated level of amyloid protein was also observed with cuprizone-mediated demyelination in APP/PS1 strain. Magnetic resonance spectroscopy showed a significant increase of glutamate and glutamine in APP/PS1 mice with or without demyelination. This increase may indicate an excessive activation of glutamate receptors that can result in cell death. Altogether, this study was able to suggest the vulnerability of myelin integrity and OLs to DNA damage and show the potential acceleration of AD progression driven by demyelination.

To investigate the effects of the strongest genetic risk factor of sporadic AD, APOE, on the age-related myelin breakdown, a cross sectional age-dependent study of the humanized APOE (hAPOE) knock-in mice was conducted to understand the cellular mechanism underlying common fMRI findings in early sporadic AD. At 6, 10 and 16 months, transgenic mice for Apoe knockout (KO) and isoforms ε3 and ε4 were put into a battery of behavioural, radiological, and histological evaluations. As APOE acts as a lipid transporter around the body and a provider of cholesterol for myelination, we expect lipid-based alterations in myelin and OLs. Observational study showed significant increase in weight of the 10-month hAPOE4 with no such difference in the 6- and 16-month-old and minimal difference in the spontaneous alternation of working memory using Y-maze. Metabolic analysis of the 10-months for food intake and physical activity showed no difference, however, the respiration quotient denoting basal metabolic rate suggests lipids as the main source of energy solely in the hAPOE4 mice compared to proteins in the WT, KO and hAPOE3. No significant changes were found in the diffusivity of 6 months, yet, in 10 months, the anterior cingulate of the hAPOE4 showed insignificant increase of perpendicular diffusivity. The movement of water perpendicular of the white matter tract suggests compromised myelin structures that can result in leaky axons. By 16 months, this difference has stabilized with each diffusivity modality levelled. Nonetheless, the decrease in mature OLs is still prevalent in the hAPOE4 in comparison. Similarly, to the APP/PS1, hAPOE4 showed an increase in glutamate and glutamine levels compared to other cohorts. This comparison may indicate a similar mechanism to acute demyelination seen in the previous study. Statistics with Pearson correlation coefficient showed altered correlations specific to hAPOE4 in reference to its diffusivity with its cellular pathologies that may demonstrate a compensatory effect of a reduction in mature OLs attempting to myelinate more than each cell may be capable of. This event may stress these cells and induce excessive DNA damage. Together, this study was able to correlate the genetic risk factors of AD with the radio-histological effects, providing a basis for future AD diagnosis.

Acknowledgement

This thesis is not one piece of work contributed by one person, but instead, it is a collaborative effort of everyone that has been part of my life since the first day I stepped back into Hong Kong in 2018.

First and foremost, I offer my wholehearted gratitude to my supervisor, Dr. Franki Kai-Hei TSE, who was the reason I returned to Hong Kong after more than 20 years. His offer to join him as a research assistant in his post-doctoral efforts to investigate Alzheimer's disease became my gateway into one of the most challenging and rewarding scientific endeavour of my life. After one year of a plethora of failures from me as a research assistant, for some reason, he still offered me a PhD position with him. Even now, after almost four years of arguments and failures, he has never given up on me, presenting me chance after chance to correct myself and change my educational perspective. This thesis along with a multitude of opportunities from journal publications to conference attendances to my school housing would not have been possible without Dr. TSE's generosity and patience. His comments and advices towards my educational career have, without a doubt, been the driving force of my PhD. I would also like to show my gratefulness to Prof. Karl HERRUP, who was my first point of contact with Dr. TSE. Even though my time with Prof. HERRUP was short, his insightfulness and comments on my work have been inspiring.

I want to thank all the collaborators for the valuable comprehension of their respective fields. I would want to thank our City University of Hong Kong collaborators, Dr. Kannie CHAN, Dr. Jianpan HUANG, and Ms. Zilin CHEN for their knowledge and efforts in helping us complete such a large MRI cohort. I would like to specifically thank Dr. HUANG for always being available whenever I had issues with coding. I would also like to thank our Hong Kong University collaborator, Dr. Henry MAK, for providing us with clinical data and their understanding. Thank you to our team in the PolyU TSE lab including Sunny YEUNG, Kingston MOK, and Iris MA. Without your knowledge and support, many of my studies would not be complete. Thank you to the friends I've made in our department including Dr. Martin YEUNG, Dr. Alex WONG, and Dr. Brandon CHAN. Your knowledge both in your fields and outside of school have helped me push through. For my fiancé, Ireen, who has been through my worst of times and still continues to love me unconditionally. For my parents half a world away in Atlanta, who have guided me every step of my life even now.

And finally, thank you to everyone who has taken part in my last 4 years. From the previous HERRUP lab to my current TSE lab and church family, from the bottom of my heart, none of this would be possible without you. I hope that this work will make a difference in how we perceive Alzheimer's disease, and that one day, we can fully comprehend its effects and find a cure for this neurodegenerative disease.

Publications

Published and part of this study

1. **Cheng GWY**, Ma IWT, Huang J, Yeung SHS, Ho P, Chen Z, Mak HKF, Herrup K, Chan KWY, Tse KH. Early demyelination divergently exacerbates axonopathy and amyloidopathy in APPSwe and APPSwe/PSEN1dE9 2 transgenic mouse models. Manuscript prepared for Journal of Neuroscience. 2023.
2. **Mok KKS, **Yeung SHS, ****Cheng GWY**, Ma IWT, Lee RH, Herrup K, Tse KH. Apolipoprotein E ε4 disrupts oligodendrocyte differentiation by interfering with astrocyte-derived lipid transport. J Neurochem. 2022 Dec 22. doi: 10.1111/jnc.15748. Epub ahead of print. PMID: 36549843.
3. **Cheng GWY**, Mok KKS, Yeung SHS, Kofler J, Herrup K, Tse KH. Apolipoprotein E ε4 Mediates Myelin Breakdown by Targeting Oligodendrocytes in Sporadic Alzheimer Disease. J Neuropathol Exp Neurol. 2022 Aug 16;81(9):717-730. doi: 10.1093/jnen/nlac054. PMID: 35779013; PMCID: PMC9393713.

Published with collaboration

1. Law LH, Huang J, Xiao P, Liu Y, Chen Z, Lai JHC, Han X, **Cheng GWY**, Tse KH, Chan KWY. Multiple CEST contrast imaging of nose-to-brain drug delivery using iohexol liposomes at 3T MRI. J Control Release. 2023 Jan 10;354:208-220. doi: 10.1016/j.jconrel.2023.01.011. Epub ahead of print. PMID: 36623695.
2. Huang J, Lai JHC, Tse KH, **Cheng GWY**, Liu Y, Chen Z, Han X, Chen L, Xu J, Chan KWY. Deep neural network based CEST and AREX processing: Application in imaging a model of Alzheimer's disease at 3 T. Magn Reson Med. 2022 Mar;87(3):1529-1545. doi: 10.1002/mrm.29044. Epub 2021 Oct 17. PMID: 34657318.
3. Huang J, van Zijl PCM, Han X, Dong CM, **Cheng GWY**, Tse KH, Knutsson L, Chen L, Lai JHC, Wu EX, Xu J, Chan KWY. Altered d-glucose in brain parenchyma and cerebrospinal fluid of early Alzheimer's disease detected by dynamic glucose-enhanced MRI. Sci Adv. 2020 May 13;6(20):eaba3884. doi: 10.1126/sciadv.aba3884. PMID: 32426510; PMCID: PMC7220384.

Abstracts

1. Yeung MHY, **Cheng GWY**, TSE KH. APOE-mediated lipid accumulation in endothelium – A pilot investigation of a common pathology in chronic kidney disease and age-related dementia. ISN World Congress of Nephrology. 2023.
2. **Cheng GWY**, Huang J, Yeung MHY, Chen Z, Mok KKS, Yeung SHS, Herrup K, Mak HKF, Chan KWY, Tse KH. APOE4 directly disrupts lipid profile and myelination in the aging mouse brain. Society for Neuroscience. 2022.
3. Ma IWT, Yeung SHS, **Cheng GWY**, Mok KKS, Herrup K, Tse KH. Bridging integrator 1 (BIN1)-mediated cell cycle regulation– bridging ATM and Myc functions in oligodendrocyte. Society for Neuroscience. 2022.
4. **Cheng GWY**, Huang J, Mok KKS, Yeung SHS, Chen Z, Herrup K, Mak HKF, Chan KWY, Tse KH. APOE4 compromises white matter integrity by harnessing oligodendrocyte differentiation– a radio-pathological investigation –. Society for Neuroscience. 2021.
5. Tse KH, **Cheng GWY**, Huang J, Mok KKS, Yeung SHS, Chen Z, Mak HKF, Chan KWY, Herrup K. Does demyelination accelerate the neuropathology progression of Alzheimer's disease? – a radio-pathological investigation. Society for Neuroscience. 2021.
6. Yeung SHS, Cheng A, **Cheng GWY**, Mok KKS, Herrup K, Tse KH. Divergent effects of ATM mutations on oligodendrocytes- the cellular basis of myelin pathology in Ataxia Telangiectasia. Society for Neuroscience. 2021.
7. Huang H, Lai JHC, TSE KH, **Cheng GWY**, Liu Y, Chen Z, Han X, Chen L, Xu J, Chan KWY. CEST and AREX data analysis based on deep neural network: application to image Alzheimer's disease at 3T ISMRM 2021 D-56 3707.
8. **GWY**, Herrup K, Tse KH. Apolipoprotein ε4 contributes to oligodendrocyte vulnerability and decreased myelination in Alzheimer's disease. Alzheimer's Association International Conference. 2019.

Abbreviations

53BP1	p53-binding protein 1
AD	Alzheimer's disease
APC-CC1	Adenomatous polyposis coli clone 1
APOE	Apolipoprotein
APP	Amyloid precursor protein
ASPA	Aspartoacylase
AxD	Axial diffusivity
CNS	Central nervous system
CPZ	Cuprizone
DKI	Diffusion kurtosis imaging
FA	Fractional anisotropy
fAD	Familial Alzheimer's disease
GLX	Glutamate/glutamine
IHC	Immunohistochemistry
Ki67	Kiel 67
MAG	Myelin associated glycoprotein
MBP	Myelin basic protein
MD	Mean diffusivity
MOG	Myelin-oligodendrocyte glycoprotein
MRI	Magnetic resonance imaging
MRS	Magnetic resonance spectroscopy
NAA	N-acetylaspartate
Nkx2.2	NK2 homeobox 2
Olig2	Oligodendrocyte transcription factor 2
PCR	Polymerase chain reaction
PLP	Proteolipid protein
PS1	Presenilin-1
RD	Radial diffusivity
sAD	Sporadic Alzheimer's disease
WMH	White matter hyperintensity

Figures List

1.0 Introduction

1.1 Myelin in the central nervous system

Myelin is a cholesterol-rich layer that forms around axons of a neuron. Disconnected bundles of myelin of up to 100 layers wrap sections of axons while leaving "naked" sections, called the nodes of Ranvier discovered by Louis-Antoine Ranvier in 1872, between these bundles. As a result of this lipid-based structure's insulating properties, action potentials can "jump" along the nodes of Ranvier, allowing for faster propagations. This transduction of electrical signals is called saltatory conduction, accelerating axon conduction from 10m/s to up to 150m/s (3). Basic motor, sensory, and cognitive functions are all indirectly regulated by the propagation, and as such, loss of myelin in the central nervous system (CNS) has been associated with degenerative events such as neuroinflammation in multiple sclerosis (MS), motor impairments in Huntington's disease (HD), and cognitive decline in Alzheimer's disease (4, 5, 6, 7). Cognitive impairments are the first noticeable symptoms of Alzheimer's as these directly influence the patient's daily interactions. Indeed, according to Braak's staging, the first signs of amyloid aggregation indicative of Alzheimer's begin in the brain stem. However, the affected functions such as the sleep cycle and moods regulated by this region are largely unnoticeable as they are pushed off as regular occurrences (8). Common cognitive impairments seen in early Alzheimer's includes losing items, poor judgment, anxiety, and repeating questions (NIH, 2022). These symptoms are in-line with the progression of plaque deposition according to Braak as deposition move from the brainstem to the hippocampus to the sensory and motor areas of the neocortex (8). As such, the temporal order of Alzheimer's symptoms starts with mild changes confused with carelessness followed by perceivable memory complications and finally to severe impairments of motor and sensory functions. Indeed, there are regional differences in the amount of myelin present. Due to its lipid-heavy content, myelin is presented as a white, cream colour, giving regions with dense myelin content the name, white matter, and regions of higher neuron content, grey matter.

1.1.1 Myelin composition

The composition of myelin contributes to its responsibilities in the CNS. The dry mass of myelin has a high proportion of lipids, ranging from 70 to 85%. Because of myelin's high lipid content, the overall

structure's water composition can equal to around 40%. As a result, water-based imaging techniques such as magnetic resonance imaging could help visualize myelin content *in vivo*. Comparatively, its protein content ranges only from 15 to 30%, much lower than most other biological membranes such as the mitochondrial membranes (around 75%) and phospholipids (around 50%). However, it was found that these proteins, while few, are some of the longest living proteins within the body, surviving for 7 to 8 months, making myelin one of the most stable structures in the body (9). As the function of myelin is to attach to axons and wrap around them, the associated proteins help initiate, maintain, and solidify this connection.

One such protein is the myelin associated glycoprotein (MAG) localized in the periaxonal zones (10, 11). Because of its proximity to the inner myelin tongue and axon, it is crucial in the initial adhesion steps of myelin onto the axon (12, 13). However, MAG knockouts have shown that its absence could be compensated by other molecules (14, 15). Other proteins such as myelin basic protein (MBP) and proteolipid protein (PLP) are found in between compact layers of myelin, acting as glue to preserve the integrity of the multi-layered wrapping. Lower amounts of these two proteins draw a correlation to increase myelin breakdown in both demyelinating diseases such as multiple sclerosis (MS) and neuromyelitis optica (NMO) (16, 17). While lower MBP and PLP values may indicate the lowered myelin levels, increases of these proteins may also point to fragmented myelin accumulations caused by demyelination seen in increased axonal diffusion (18, 19, 20). On the surface of the myelin, myelin oligodendrocyte proteins (MOG) are observed with a role of maintenance. The protein is a linking point between the sheath and oligodendrocyte to continually supply the structure with lipids to prevent its breakdown (21). These proteins are considered the backbone of myelin composition with much research using them as markers of myelin status. Changes in myelin protein levels help further divide the effect and mechanism of each result, generating a variety of theories on each protein's individual effect.

Myelin is composed of a variation of lipids not limited to cholesterol. Additionally, there are no lipid fractions that are exclusive to myelin asides from mitochondria-specific lipid, diphosphatidylglycerol. The most abundant type of lipid in myelin is cerebroside, also called galactosylceramide, as its concentration is directly proportional to the amount of myelin present (22). While this may be true,

knockout of this lipid does not hinder myelin formation, however, aging animals developed consistent limb paralysis, indicating the effect of cerebroside on myelin maintenance instead of myelination (23). Other lipid fractions found in myelin include sulfatides, lecithin, and sphingomyelin. Regionally, fractions of myelin lipids do not seem differ in their compositions as the tight-knitted ratios of lipids are imperative for efficient myelin.

Asides the cerebral spinal fluid-filled ventricles, there are no regions of the brain that lack myelin. However, there are regions that are less myelinated. The hypomyelinated regions are called the grey matter while the heavily myelinated regions are called the white matter. While their compositions are distinct, grey and white matter are distributed among all regions of the brain. Grey matter consists of mostly neuronal cell bodies with axons that are not heavily myelinated. These cell bodies are responsible for containing the genetic material of the cell, maintaining the electrical potentials of the neuron, and receiving neurotransmitters from neighbouring cells for processing. While demyelination may not directly affect these cell bodies, deterioration of the myelin may accompany Wallerian degeneration, or axonal degeneration, resulting in the death of the cell.

1.1.2 Oligodendrocytes, the producers of myelin

To understand the process of demyelination and myelin loss, the mechanism at which axons myelin must be known. Myelin, specifically in the CNS, is produced and maintained solely by the oligodendrocytes (OL). OLs are grouped into a group of non-neuronal cells called glia, Latin for "glue." Within this group are also ependymal cells, Schwann cells, astrocytes, and microglia. These cells are responsible for maintaining cerebrospinal fluid homeostasis, myelinating the peripheral nervous system (PNS), maintaining biochemical control over the cerebral environment, and responding to immunological factors, respectively. Even though these cells do not contribute directly to the production of myelin, they provide components to support OLs such as lipids and clearance of extracellular molecules to sustain healthy myelination. Thus, one OL can myelinate as many as 20 to 60 axons (24).

Before OLs can myelinate surrounding axons, they must differentiate and mature. OPCs originate from the subventricular zone and ventricular zone of the medial ganglionic eminence (25, 26, 27). Early formations of OPCs come from the medial ganglionic eminence while later OPCs come from the ventricular and subventricular zones (28, 29, 30). While the cell is destined to become a glial cell, different expression ratios of proteins can promote differentiation into either OLs or astrocytes (31, 32). OPCs distinctly express NG2-proteoglycan and platelet-derived growth factor α (PDGRFα) on their cell surfaces. Migration of the OPCs towards the cortex initiates the differentiation into pre-myelinating OLs through expressions of Olig2, SOX10, and Nkx2.2 (33, 34, 35). OPCs are responsible for repopulating regions of the CNS that have depleted OLs and astrocytes. Its divergent differentiation pathways have been proposed to be due to the changing microenvironments as OPCs transplanted into P7 mouse telencephalon differentiated into MBP-expressing OLs yet in 6 month old cortex differentiated into GFAP-expressing astrocytes (36). Further information on OPC migration and development can be on p.31. Regarding aging, OPC populations have been shown to decline with age with less OPC recruitment to OL-lacking regions and slower rate of differentiation (37). Whether this is due to extrinsic factors such as demyelination or changes in microenvironment or intrinsic factors such as DNA damage or gene expression is still being studied. However, one study has shown that OPC cross-transplant of aged (10 months) with young (2 months) rats retain their age characteristics with slower differentiation of the aged OPC compared to the young OPC (38). Interestingly, introduction of c-Myc, a gene-regulating protein, has impacted OPC proliferation and differentiation. Increased expression of c-Myc is associated with an increase in OPC proliferation (39, 40) while suppression decreases proliferation but increases differentiation (40, 41). This shows that extrinsic factors such as myelin changes may not directly affect OPC development. Throughout their lifetime, OLs will mature into myelinating OLs through the expressions of myelin regulatory factor (MyRF) and previously mentioned myelin proteins. Once OLs have entered this post-mitotic stage, they will extend their processes towards axons and begin myelination.

Lipids used for myelination are produced from OLs and astrocytes. While OLs have the capacity to produce lipids, the main source comes from astrocytes. Studies have shown that deletion of sterol

regulatory element-binding protein (SREBP), a necessary catalyst of neural lipid biosynthesis, within OLs did not affect myelination, yet deletion of the same protein in astrocytes caused a consistent hypomyelination (42, 43). Transfer of these lipids from astrocytes to oligodendrocytes is monitored by apolipoprotein ε (APOE), a lipoprotein produced by the activation of two transcription factors, liver and retinoid x receptors, found in astrocytes (44). Recently, research was done on an isoform of APOE, APOE4, that shows decreased localization of cholesterol along axons and increased accumulations of intracellular lipids (45). This suggests that myelin lipids are dependent on the APOE carrier and that an isoform difference may hinder proper myelination.

1.1.3 Process of myelination

Myelinogenesis involves meticulous interactions between an OL and the axon. Research has shown that OLs select axons for myelination based on size with unknown biochemical cues. (46, 47, 48). In culture, axons with diameters of less than 400nm were seldom myelinated, but diameters above 200nm were the minimum length for proper myelination (49, 50). Neuronal electrical activity has been proposed as it had been shown that optic nerves of mice living in the dark, naturally blind, or having blocked sodium-dependent action potentials are hypomyelinated.

Sensory impairments such as hearing and sight have been implicated as risks for both dementia and AD with patients with visual impairment and sight loss (51, 52, 53). However, there are contrasting views on the risk of Alzheimer's due to visual impairments. Studies have shown that visual impairments are associated with optic atrophy that could be caused by underlying mitochondrial dysfunction, a common theory of Alzheimer's pathogenesis (54). Additionally, visual loss may be complemented by deficient social interaction, which has been shown to increase the risk of Alzheimer's (55, 56).

Poor myelination of the optic nerve is associated with poor vision (57) as seen in Beauvieux syndrome, a disease due to delayed myelination of the optic nerve (58), and Wolfram syndrome, an autosomal-recessive disorder associated with juvenile optic nerve atrophy and neurodegeneration. While hypomyelination of the optic nerves negatively impacts vision, extensive myelination of the

surrounding retinal nerve fibers is associated with myopia and strabismus due to the physical hindrance of the thickened fibers from enwrapped myelin (59). According to studies, poor vision does increase the risk of dementia (51, 60), but whether this is due to influence from the nervous system or social interaction has not been studied. Environmental light intensities can also affect myelination similarly to activity-dependent myelination of the CNS (61). Artificial opening of rabbit eyes at the fifth postnatal day was shown to accelerate myelination with significant increases of myelin basic protein, proteolipid protein, and cerebrosides as compared to control (62). However, rats dark-reared rats of up to 30 days old have shown no differences in myelination of optic nerve fibers in comparison to normal 12-hour dark-light cycle (63).

While the effects of hypomyelination have not shown to directly affect the circadian rhythm, knockdown of *Bmal1*, a gene regulating the circadian rhythm, within postnatal 30 days showed significant reductions in OPC populations in the corpus callosum, which resulted in downstream reductions in CC1+ mature OLs and myelin basic protein expression, resulting in sleep deprivation (64). Due to this relationship, this may explain the higher prevalence of multiple sclerosis in night shift workers (64).

Once engaged to the axon, the cytoplasmic process of the OL extends onto the axon where MAG is expressed (Figure 1). The OL extension flattens into a layer, and the myelin twists around the axon in a corkscrew motion (65). The innermost layers become the shortest lateral layer as the myelin wraps around the axon, increasing its thickness and elongating it while producing an uneven spread of myelination (66, 67). Nawaz et al (68) had shown that the moving edge of the myelin is non-adhesive to the axon and that the actin filament is coordinated with this moving edge and not with the rest of the myelin membrane. Continuous assembly and disassembly of these filaments aid in the movement of the myelin tongue, elongating it. MBP and PLP, representing 30 to 40% of all myelin proteins, is then released between layers to act as both an adhesive and tightener to preserve the integrity of the myelin (69, 70, 71). Once established, each single sheath can be maintained for around seven to eight months.

The upkeep of myelin is crucial in a healthy brain as its fibre density is regional. Within the brain, there are numerous myelin-axon bundles known as the white matter tract to provide long distance connections. Bundles of dense myelinated axons within the deep cortical regions such as the corpus callosum and anterior commissure connect the hemispheres, allowing the brain to communicate with itself. Furthermore, neuron rich grey matter also exemplifies this increased myelin density in the inner layers of the cerebral cortex. This segregation of myelin densities may be due to the importance of the region in survival. Interestingly, the order in which regions become myelinated in the brain goes from central to peripheral, caudal to rostral, dorsal to ventral, and sensory to motor (72). One of the first regions of myelination happens within the first days of life at the dorsal brainstem, a region responsible for involuntary functions such as cardiovascular and respiratory control. Within a year, this is followed by regions of the white matter tract such as the splenium and regions adjacent to it such as the corona radiata. Finally, by 24 months, the anterior temporal and frontal cortex are myelinated (73). In reference to the central and peripheral of the brain, many deeper regions of the grey matter are myelinated by the first 8 months while the subcortical regions by 16 months (74). This suggests the body's preference of myelinating the vital regions first while putting cognitive abilities last. Conversely, the first regions of myelin loss are these last to myelinate regions (75, 76, 77). As a result, neurodegenerative diseases usually affect cognitive abilities such as memory and personalities.

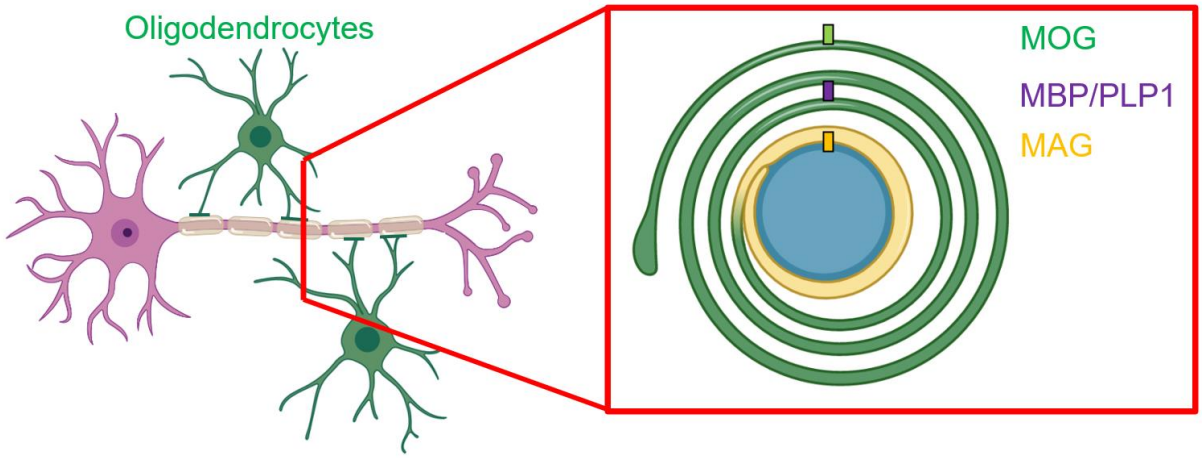

Figure 1: Myelination is initiated by the reach of cytoplasmic membrane of neighbouring oligodendrocytes. Once attached to the axon, oligodendrocytes secrete varying proteins to maintain the myelin sheath. Within the innermost sheath, MAG is expressed for attachment to the axon. MBP and PLP are expressed in between layers to keep the sheath compact, and MOG is expressed in the outer lip to maintain a connection to the oligodendrocytes to continually supply lipids to the sheath.

1.1.4 Myelin's effect on cerebral health

The contribution of myelin pathology to neurodegenerative diseases is emerging, with many of the diseases showing detectable myelin loss. MS is the most prevalent demyelinating disease, with white matter lesions in both CNS and PNS. Patients of the disease exhibit many common neuropathic symptoms such as depression, anxiety, and cognitive impairments. MS aetiology is relatively unknown, but many researchers propose that it is a result of a combination of genetic and environmental factors. This disease targets OLs in an undefined process. Reports have shown the reduction of OPCs tagged with BCAN and SOX6 in white matter lesions and normal appearing white matter (78, 79, 80, 81, 82). As a result, the insufficiency of OLs to maintain pre-existing myelin structures cause demyelination in affected areas. Because of the body's ability to remyelinate, albeit slowly, MS patients can have these periodic acute "attacks" that cause temporary symptoms before a period of recovery. Other types of demyelinating diseases include NMO, demyelination-based inflammation of the optic nerve causing visual impairments and loss of colour vision, and inflammatory demyelinating diseases, a wide range of diseases stemming from MS. Consequently, the demyelination of regional nerves has been suggested to inhibit their regional functions. The vulnerability of the frontal cortex responsible for higher thinking in addition to demyelinating effects indicate cognitive impairment of neurodegenerative disorders may be caused by its prioritized degeneration (83).

Despite myelin and OL's indisputable relation, their effect on the surrounding environment is crucial in sustaining a healthy brain. Astrocyte is one of the major cells that plays a central role in myelin upkeep. As stated previously, astrocytes provide lipids to OLs for myelination, but astrocytes also promote OL differentiation and myelination. Astrocytic secretions of leukaemia inhibitory factor-like protein (LIF), neuregulin-1, γ-secretase, and neurotrophin-3 from astrocytes have been shown to promote OL differentiation (84, 85, 86, 87). One of which has been postulated to promote AD pathology. Asides from biochemical effects, myelin plasticity due to increase of activity-dependent electrical impulses of axons have also been shown to promote myelination through LIF produced from astrocytes (88, 89). In addition, astrocytes activate in the presence of myelin debris. During myelin loss, myelin fragments broken down from sheaths are taken up by astrocytes and induce an immune response.

Additional microglia and activated-astrocytes are recruited to the site to remove the fragments, and an upregulation of NF-κB and other inflammatory cytokines were found in these myelin-positive activated astrocytes (90). Additionally, myelin fragment removal is mediated by macrophages and microglia of the brain immune system. After Wallerian degeneration, myelin fragments are opsonized before undergoing phagocytosis (91, 92, 93). Complement proteins bind onto myelin fragments onto complement receptor 3 for microglia and macrophage recognition. Another type of macrophage phagocytosis mechanism is through the macrophage receptor with a collagenous structure (MARCO). Cysteine-rich domains allow them to bind to myelin lipids more effectively which enhance myelin removal. This theory is supported by previous studies should the upregulation of MARCO response in the inflammatory stimuli of the white matter tract myelin debris in the spinal cord (94, 95). The blood-brain barrier (BBB) is also a target of variating myelin status. Cognitive impairments due to disrupted brain vasculature encompasses common neurodegenerative events such as ischaemic and haemorrhagic strokes. The proximity of the myelin-OL connection and BBB indicates alterations of one structure could affect the other. Degradation of myelin, resulting in the release of proteins such as MBP and PLP, have been implicated in increased BBB permeability in MS progression (96, 97, 98). Thus, while white matter events are localized, their effects may be more widespread pass the site of lesion.

1.1.5 Models of demyelination

To study the effects of myelin loss, researchers induce demyelination through several methods. One approach is through the treatment of cuprizone. Cuprizone is a copper chelator that demyelinates the brain by targeting OL apoptosis (99, 100). While its mechanism is unknown, treatment with cuprizone has shown to be deleterious to OLs in addition to be demyelinating in the corpus callosum (101, 102, 103). Unlike demyelinating toxins such as lysolecithin and ethidium bromide that activate an immune response, demyelination by cuprizone is a non-immune response (99). However, the effects of cuprizone are not continuous with treatment. Acute demyelination is seen within four weeks of cuprizone treatment followed by intrinsic remyelination. It was proposed that chelation of copper leads to ferroptosis-mediated oligodendrocyte reduction as early as 2 week. During the first two days of cuprizone treatment, there was significant reduction of ferritin and increase in ferroptosis markers such

as NCOA4 and TfR1, preceding oligodendrocyte loss. By 1 week, there was a significant oligodendrocyte loss of 65%. However, treatment with Fer-1, an inhibitor of ferroptosis, prevented significant oligodendrocyte loss in the first 2 weeks.

We used 0.2% cuprizone due to the high toxicity and early deaths of 0.3-0.5% and insignificant demyelination of 0.1% cuprizone treatment (104). However, another study had shown similar degrees of demyelination using 0.1% and 0.2% (105). Furthermore, numerous studies have used 0.2% cuprizone to induce demyelination due to the greater demyelination without inducing apparent health risks (99, 106, 107). Thus, we have chosen 0.2% cuprizone. Asides from oligodendrocytes, cuprizone has been shown to affect astrocytic and microglial activation. Astrogliosis stained by GFAP and Ki-67 was found in cuprizone treated mice at three weeks of treatment. Additionally, a significant increase of Iba-1 microglia populations was found in the cuprizone model (103).

Since the demyelinating effects of cuprizone is not instant, mice were given four weeks of 0.2% cuprizone treatment before further processing (102, 108). Peak demyelination and oligodendrocyte reduction happens between four to five weeks of 0.2% cuprizone treatment. The expression of myelin proteins such as PLP, MOG, MBP, and CNPase and oligodendrocyte numbers all show lowest levels between four and five weeks of 0.2% cuprizone with steady decrease from induction (102, 103, 109). Chronic cuprizone treatment past five weeks has shown intrinsic remyelination at six and twelve weeks (107). Thus, we performed radiological imaging immediately after the four-week treatment to ensure minimal remyelination.

1.2 Alzheimer's disease

In 1906, Dr. Alois Alzheimer noticed severe cognitive impairments in Auguste Deter, a 51-years-old patient from the Frankfurt asylum. Deter exhibited chronic symptoms of dementia, delusions, and insomnia, common symptoms in neurodegenerative disorders. These symptoms were seldom seen at this early age (110). She died shortly after at the age of 55, and her brain was extracted and transported to Dr. Alzheimer for analysis using the Bielschowsky stain. Dr. Alzheimer observed remarkable dark

aggregations resembling plaques of unknown origins. Four years later, Alzheimer admitted a second patient, Johann F., who showed similar symptoms as Deter (111). At 56 years old, Johann could not answer questions properly, had frequent epileptic episodes, and showed incontinence. One year later, he passed away, and his brain dissection showed the same cerebral plaques as Deter. Both patients showed early symptoms and classic pathological signs of Alzheimer's disease (AD) as people know it today. However, this was only the diagnosis for one type of AD.

For the next 100 years, AD is widely regarded as an age-related disorder with symptoms of gradual memory loss, delusion, and depression. Making up 60-70% of all dementia cases (World Health Organization, 2020), AD is a complex disease with no known aetiology, and yet, its hallmark, amyloid-β plaque, continues to be a persistent root of this neurodegenerative disorder. In 1992, Sir Prof. John Hardy coined this theory as the amyloid cascade hypothesis, a cause-and-effect speculation relating the amyloid-beta protein deposition to AD diagnosis. He proposed that these plaques induce neuronal apoptosis, which led to a slow deterioration in cognition (112). This soon became the central dogma for AD research with therapy and diagnosis focusing on this misfolded protein. However, it was recently shown that these treatments did not rid nor cure the neurological symptoms nor the gradual neurodegeneration (113). Historically, there have been several anti-amyloid drugs aimed at treating Alzheimer's. Gantenerumab is a monoclonal antibody that binds onto the N-terminal and mid-region epitope of the folded amyloid-β monomer, recruiting glial cells for phagocytosis (114). While it was shown with PET that there were indeed significant reductions in cerebral amyloid, during phase 3, the drug failed to generate statistical significance in Clinical Dementia Rating-Sum of Boxes compared to the placebo group. Similarly, other monoclonal antibodies used for amyloid clearance by binding onto amyloid-β to induce phagocytosis such as bapineuzumab (115) and solanezumab (116) have been either insignificant in phase 3 or did not show sufficient cognitive improvements. However, recently, a new amyloid-binding drug called aducanumab that targets both soluble and insoluble amyloid-β aggregates in contrast to monomers has shown improvements in two of its trials, ENGAGE and EMERGE, which have shown 22% decreased rate of cognitive decline. Hence, a new hypothesis is imperative as the aging population grows.

Aging is the greatest risk factor for AD, but AD can be separated into two types based on its pathology: familial AD (fAD) and sporadic AD (sAD). fAD is a genetic disease leading to AD signs and symptoms from as early as 60 years old. Mutations of the amyloid precursor protein (APP), presenilin-1 (PS1), or presenilin-2 (PS2) directly cause the build-up of insoluble amyloid fragments, resulting in aggregations of plaques that damage neurons. Prevalence of this form of AD, however, only encompasses 5% of all AD. The other 95% is from sAD, a disease with no concrete cause but with similar amyloid depositions (117). Unfortunately, many efforts towards AD research has been put forth based on fAD findings even though it represents the minority of cases. Multiple hypotheses have stemmed trying to target specific symptoms such as the reduction of the neurotransmitter acetylcholine and the hyperphosphorylation of the tau protein. All of which target specific pathological pathways of AD, but none have shown to be consistent nor distinct in all AD patients. Consistently, though, females do show a significantly higher chance of developing AD with 1 in 5 females developing the disease at age 65, and almost two-thirds of all American AD cases are females (Alzheimer's Association, 2021).

1.2.1 Amyloid precursor protein, the pathological hallmark of Alzheimer's

As stated previously, one of the accepted causes of AD is through amyloid deposition. In fAD, mutation of APP causing overproduction of this protein or PS1/PS2 causing production of an insoluble APP fragment is the cause of neurodegenerative events. This processing of APP, specifically the APP659 isoform, within the brain follows two divergent paths: non-amyloidogenic and amyloidogenic (Figure 2). The non-amyloidogenic process involves an initial cleavage of the protein at Lys16 and Leu17 by the α-secretase, controlled by a disintegrin and metalloproteinase domain-containing protein-10 (ADAM10), followed by a second cleavage by the γ-secretase, resulting in a soluble APPα, C-terminal fragment α (CTF-α), and the amyloid intracellular domain (AICD) (118). While its function is still unknown, CTF-α levels could be used as an early detection for AD as its increase indicates APP's preference for the non-amyloidogenic pathway (119). Additional fragments of P3 peptide and AICD are also produced from a second cleavage by γ-secretase. Neither product has shown to have significant effects on AD progression. However, in the amyloidogenic process, the initial cleavage is made by the β-secretase, controlled by the beta-site APP

cleaving enzyme 1 (BACE1) at Asp1 and Glu11, creating the APPβ section ranging in size from 37 to 49 residues, with 40 (Aβ40) and 42 (Aβ42) as the most common fragments seen in AD. It has been shown that competition between α- and β-secretase can drive the cleavage of APP as the 81% decrease in α-secretase in fAD patients correlated with a 185% increase in β-secretase (120). More than 50 mutations of APP such as mutations K670N with M671L and E693G, which accelerate protofibril formation, may initiate and increase the likelihood of the harmful variant (121, 122). The γ-secretase then makes its original cut to create the C-terminal fragment β (CTF-β) and AICD.

APP and its cleaving enzymes, PS1 and PS2, are the strongest genetic risk factors for fAD, an early-onset version of AD. It is known that their overexpression and mutations could promote APP processing towards the pathological amyloidogenic pathway. As the *APP* gene is located on chromosome 21, 30% of people with Down's syndrome in their 50s have AD, rising to 50% by their 60s (123). The APP exists as a membrane-spanning protein in both different isoforms and fragments to carry out specific functions ranging from platelet aggregation to neural plasticity. Among its isoforms, APP695, 751, and 770 (numbered from the number of amino acids present) are the most common with inclusion of two other proteins from the APP family, amyloid-like protein 1 and 2 (APLP1 and APLP2) (Figure 3). Shared domains among APP isoforms include the Kunitz protease inhibitor (KPI) and OX2 homology sequence, each suggested to affect the pathology of AD. APP-KPI mRNA has been shown to be relatively preserved in comparison to APP695 mRNA, which lacks the KPI domain, in AD brain (124, 125, 126). Its function is unknown, yet correlation studies have seen an increased expression of KPI in focal ischemia, inhibition of serine within the cerebral coagulation cascade, and amyloid deposition in the AD brain (127, 128, 129). Additionally, KPI has been implicated to bind to low-density lipoprotein receptor-related proteins (LRP), a known risk-factor of AD, which decreases in AD patients (130, 131, 132). The effects of lipids on AD progression may point to an amyloid-independent pathway, which will be addressed later. However, OX2 has a more unknown role as its presence does not seem to indicate a function, but its likeliness to Thy-1, a neuronal marker used by some to drive APP expression, suggests a neural correlation (133). However, APP695, lacking both KPI and OX2, is the most prominent isoform that makes up the core of amyloid plaques as it is highly expressed within neurons

(134, 135). Despite residing within the same family as APP, APLP1 and APLP2 do not contain the Aβ domain, and, therefore, has not been shown to affect the aggregations.

The role of APP is ubiquitous throughout the body with different ratios of its isoforms in different tissue types (126, 136). Interestingly, compensatory effects of the body were capable of supporting mice with APP knocked out, possibly due to homologous sequences with APLP1 and APLP2 (137). However, double or triple knockouts of these genes were fatal at birth (138, 139, 140). Cellularly, APP localizes in the different membrane structures of the cell such as the plasma membrane and endoplasmic reticulum with some appearing in the post-synaptic regions of axons and dendrites (141, 142). After protein synthesis, APP is subjected to N- and O-glycosylation and potential tyrosine sulfation along the secretory pathway of the Golgi and becomes abundant in intracellular membrane compartments (143, 144). Processing of the APP results in its transport from vesicles to the active zones of synapses where it is either cleaved by α-secretase, favouring the non-amyloidogenic pathway, or reabsorbed back into the endosome. However, retention of APP within the endosome promotes the amyloidogenic pathway. Moreover, as secretases also proceed with the secretory pathway and contained within individual vesicles, β-secretase are spatially separated from the APP, limiting their interactions (145). The convergence of these vesicles is known to be triggered via a clathrin-dependent neuronal response (146, 147).

Amyloid-beta is an extracellular fragment created by the cleavage of the amyloid precursor protein by the beta- and gamma-secretase. Oligomerization of amyloid-beta creates amyloid fibrils and plaques associated with synaptic loss. Extracellular amyloid-beta oligomers block long-term potentiation (148), dysregulate calcium ion movements of axons (149, 150), and regulate glutamate release (151, 152). Grading of Alzheimer's disease can be done with Braak staging, a multi-level system grading the progression of neurofibrillary tangles in the Alzheimer's brain. However, the progression of these tangles is comparably different with the beginning of plaque deposition. Previous research has shown that plaque deposition may begin in the temporobasal and frontomedial areas of the cortex, before progressing towards the medial temporal lobe, and finally into the striatum (153, 154).

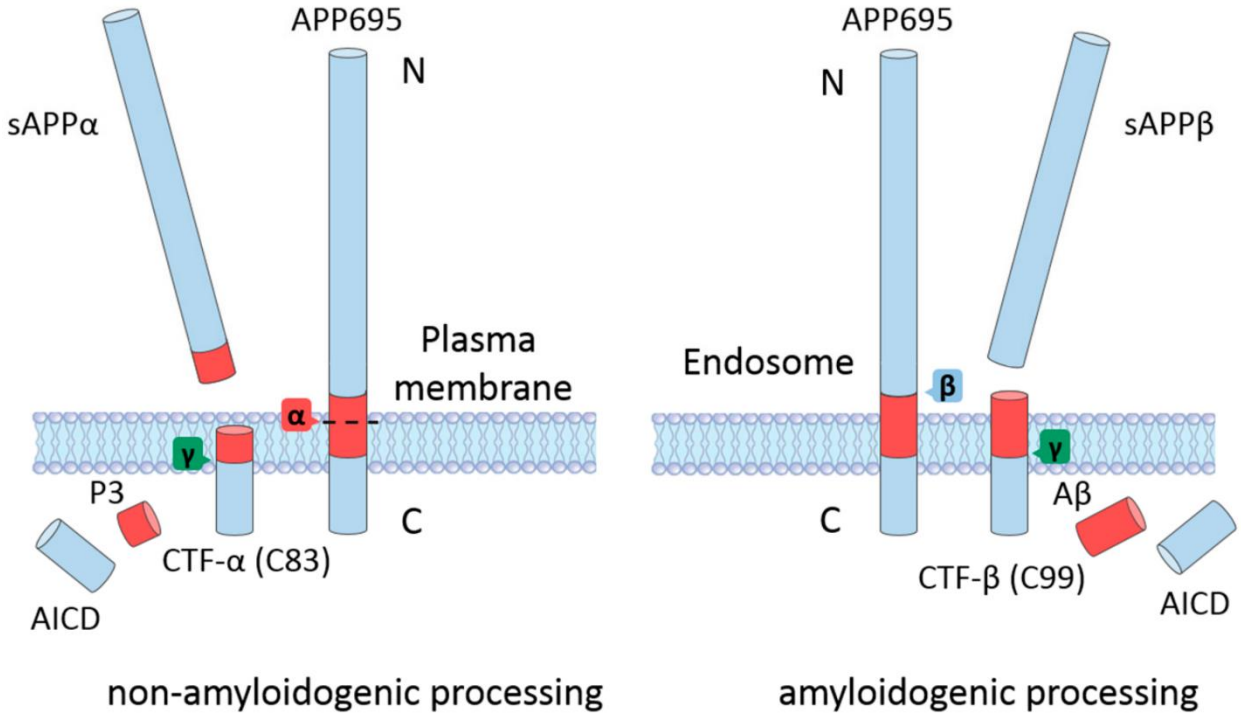

Figure 2: The cleavage of APP may follow 2 pathways. The non-amyloidogenic pathway processes the APP with α- and γ- secretase to create soluble fragments. However, the amyloidogenic pathway produces Aβ with an initial cleavage by β-secretase.

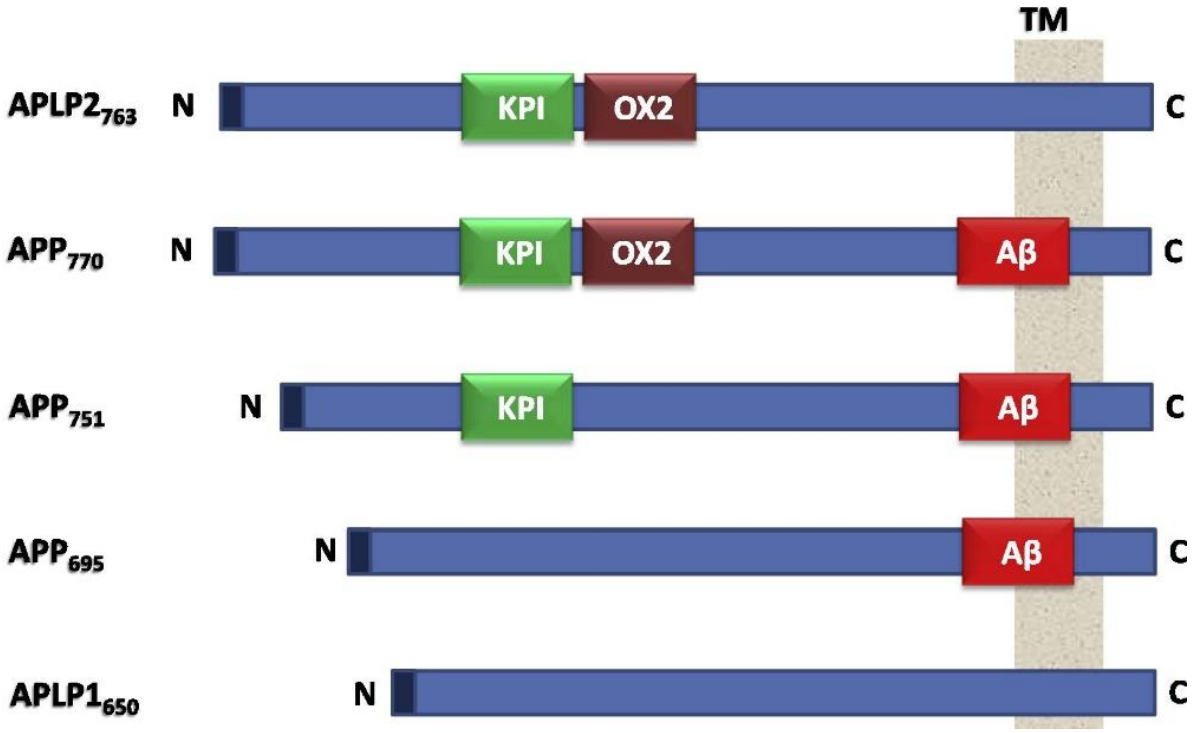

Figure 3: Within the APP family, APLP2763, APP770, APP751, APP695, and APLP650 are the most common isoforms of APP. KPI domains are only present in APLP2763, APP770, and APP751 while OX2 is only present in APLP2763 and APP770. However, the plaque creating Aβ, resting directly on the cell transmembrane (TM), only exists within APP. Adapted from Nalivaeva, N.N. and Turner, A.J., 2013.

1.2.2 Impact of amyloid plaques

Interestingly, there are many paths in which amyloid plaques take to result in neurodegeneration. Whether intracellular or extracellular Aβ accumulations initiate neurodegeneration continues to be of debate, but it is agreed that differences in accumulations may be of importance when analysing the mechanism in which each proceed (155, 156, 157). Umeda et al showed that Aβ42 accumulations within neuronal endoplasmic reticulum, endosomes, and mitochondria had caused up-regulation of Grp78, a chaperone protein responsible for correcting misfolded proteins, leakage of cathepsin D, and cytochrome c release, respectively, induce neuronal death (158, 159). Intraneuronal (in soma and neurites) build-up of Aβ in both AD patients and five fAD mutation mice (5xFAD) has correlated with a consistent elevated level of cyclin-dependent kinase 5 (P25), a protein responsible for the extension of dendrites and synapse, in the roles of apoptosis as this increase corresponds with significant decreases in pyramidal neuron numbers (160, 161, 162).

To understand and to simplify AD progression, Professor Heiko Braak characterized AD into different pathological stages by the metastatic nature of neurofibrillary tangles (NFT), or accumulations of the tau protein, among brain regions (163, 164). Stages I and II localizes NFT lesions to the lateral trans-entorhinal and entorhinal cortex with amyloid plaques appearing within the CA1 of the hippocampus. These regions are responsible for the perception of position and directions, which explains what patients consider as simple forgetfuless when trying to reach from place to place (165). Stages III and IV sees lesions spreading into the neocortex with plaques becoming a prominent feature. Within the final stages V and VI, NFT and plaques dominate the cortex, even occupying the occipital lobe and producing hallucinations. Unfortunately, these kinds of cellular modifications can only be verified at post-mortem stage. Thus, family medical history may show genetic risk-factors that may specifically target changes or mutations within these regions.

Genetic risk factors such as lipid carrier apolipoprotein (APOE) and secretase proteins such as ADAM10 and BACE1 can affect cognitive impairments leading to AD. Pre-existing conditions and environmental factors are also strong candidates for increasing the risks of AD. Diabetes, one of the

most common diseases affecting more than 400 million people worldwide, has been linked to AD onset with patients with Type 1 diabetes being 93% more likely to develop dementia (alz.org). There is a strong correlation between high blood sugar and AD with patients having Type 2 diabetes exhibiting severe increases in Aβ by disrupting its clearance (166). Down syndrome is also a risk factor as the APP gene is located on chromosome 21, and overexpression of the gene dramatically increases Aβ formation. Additionally, conditions and disorders of the cardiovascular system can promote AD. Discussed within myelin, the connection between vasculature and neural structures is closely related with the degeneration of one leading to damages of the other. As a result, conditions such as obesity, high blood pressure, and high cholesterol can increase the risk of AD, and disorders such as atherosclerosis and strokes can even trigger cognitive decline. Environmental factors such as an increase of nitrogen dioxide intake, silicon amounts, and vitamin D deficiencies have all strongly correlated with an increased risk for AD (167). Altogether, numerous factors can affect AD progression in both the young and the old, with no distinct factors that directly cause AD. This "shotgun" method has consistently put AD as one of the world's most enigmatic diseases even when such a large percentage of the population will one day be diagnosed for it.

1.2.3 Diagnosis of Alzheimer's

Diagnosis for AD is difficult with much of the diagnostics being confirmed only after life-affecting symptoms appear. Genetic analysis for fAD could be done for screening for genetically predisposed mutations such as APP, PS1, and PS2. Familial AD is a genetic disease with mutations of the amyloid precursor, presenilin-1, or presenilin-2 genes causing early amyloid plaque build-up, which leads to Alzheimer's. Early symptoms at an age between 35 and 50 associated with fAD such as consistent confusion and difficulties in completing familiar tasks may prompt the patient to receiving screening for mutations of these three proteins. Since these three proteins and their mutations are known to predispose the patient to Alzheimer's, they can be used to screen for fAD. In contrast, sAD is not diagnosed in this manner as there is no direct linkage to genetics. For this form of Alzheimer's, cognitive tests such as mini-mental state examination (MMSE) are done at an older age followed by amyloid-based PET scans to confirm of sAD. However, sAD is more difficult to diagnose for as prodromal

symptoms are variable and its pathogenesis is still unknown. Genetic risk factors such as APOE4 and ADAM10 could be filtered for. Memory tests such as the MMSE and the Alzheimer's Disease Assessment Scale-Cognitive (ADAS-Cog) have become common tools for memory diagnosis (168, 169, 170, 171). Neuroimaging using a combination of positron emission topography (PET) and Pittsburgh compound B (PiB) enable the characterization of amyloid plaques in vivo. Although PET-PiB screening has been the staple for AD diagnosis since inception, its sensitivity as a diagnostic test remains doubtful as not all patients with amyloid aggregations develops AD. Because of such difficulties in assessing for AD, the number of treatments has become just as few and just as vague. Most treatments have aimed at the removal of amyloid plaques. Treatments from Merck & Co, AstraZeneca, and Eli Lilly and Company (verubecestat and lanabecestat) targeting the inhibition of BACE1 have been postulated to promote APP cleavage towards the non-amyloidogenic pathway. However, both treatments have been cancelled post-phase III due to ineffectiveness and liver toxicity, respectively. In 2022, a drug named aducanumab from Biogen and Eisai was approved for public use. Its mechanism involved the binding of an amyloid antibody at amino acids 3 to 7, inhibiting its aggregation capabilities (172). Nonetheless, these drugs are not a cure. Lifestyle therapies such as Dr. Dale Bredesen's ReCODE have also had limited success at treating cognitive symptoms through replenishing nutrients, lowering excess inflammation factors, and keeping an active lifestyle (173).

The lack of neither a cause nor treatment warrants a thorough investigation into these factors. Because of symptoms of cognitive impairments and amyloid-independent neurodegeneration, it is hypothesized that myelin loss resulting in neuronal loss may be factors in AD progression.

1.3 Apolipoprotein ε, the strongest genetic risk factor for sporadic Alzheimer's

Apolipoproteins are a class of proteins responsible for binding to lipids and facilitating lipoprotein uptake and clearance. One type of apolipoprotein is apolipoprotein ε (APOE), a lipid transporter mainly produced in the liver and in astrocytes (174). Activation through dimerization of transcription factors, liver and retinoid x receptors, initiates APOE production. APOE's role in the body is mainly as a lipid transporter whether systemically in the blood stream or between astrocytes and OLs. APOE mainly

binds to very low-density lipids (VLDL) and low density lipids (LDL). As APOE has been shown to be unable to cross the BBB, it is inferred that the liver produces the systemic APOE while the astrocytes produce brain APOE (175). Because of its role as a lipid transporter, APOE is known to affect many vascular diseases, which will be described later.

1.3.1 APOE isoforms and structure

In humans, this APOE exists in three isoforms caused by two single nucleotide polymorphisms that change the amino acid content in positions 112 and 158: APOE2, APOE3, and APOE4. APOE2 consists of cysteines in both positions, and this isoform's allelic frequency in the human population is 8.40%. Comparatively, APOE2 is considered a neuroprotective version of the *APOE* gene. Studies have associated the presence of APOE2 with reduced Aβ deposition in both non-demented and AD brains (176, 177, 178). In addition, APOE2 has been shown to protect cognition in individuals over 90 years old and patients who already exhibit AD pathology (179, 180, 181). This isoform has even been associated with longevity (182, 183, 184). However, APOE2 has also been associated with an increased risk for cerebral amyloid angiopathy, post-traumatic stress disorder, and macular degeneration (185, 186, 187). The mechanism of this rare allele is still unknown. APOE3 is considered the neutral allele and consists of a cysteine and arginine in residue 112 and 158, respectively. Unlike APOE2, APOE3 makes up the majority of the human population, accounting for 77.90% of APOE genotype. The third isoform, APOE4, is the strongest genetic risk factor for sAD. Both residue positions become arginine, and this isoform comprises of 13.70% of the population. Interestingly, APOE4 is the ancestral isoform of APOE, with the other isoforms having mutated to its current state. It has been shown that the presence of APOE4 increases the amyloid burden, exacerbating AD pathology (188, 189). In addition, APOE4 also increases the risk of atherosclerosis (190). The overtake of APOE3 prevalence is most likely due to its non-malign characteristic compared to APOE2 and APOE4 as APOE3 has no predisposed risk factors. In reference to AD, pairings of these alleles produce different risks. Homozygous APOE2 reduces the risk of AD by 40% while homozygous APOE4 increases the risk to more than 14.9 times. Interestingly, having only one APOE4 allele with either APOE2 or APOE3 increases the risk of AD by 2.6 and 3.2 times, respectively. While the direct mechanisms are unknown, it is most likely due to lipid

metabolism as APOE's role is as a lipid transporter. APOE are lipoproteins responsible for the transport of VLDL and LDL systemically around the body. In the brain, we hypothesized here that it transports lipids from astrocytes to oligodendrocytes for myelin production. While the mechanism of lipid transport has not been directly tested, the effects of altering APOE and lipid levels have affected myelin protein expressions. In addition, the effect of each isoform of APOE has also been tested. Through employing lovastatin, a cholesterol synthesis inhibitor, onto *Apoe*$^{-/-}$ oligodendrocyte culture, the myelin basic protein expression was reduced compared to the rescue with lipidated recombinant hAPOE3 and hAPOE4 (191). This experiment shows the importance of APOE in providing lipids for myelin production. Biochemically, It contains two domains: the NH_2-terminal (or N-terminal) from residue 1-165 and the COOH-terminal (or C-terminal) from residue 225-299. While the N-terminal does not participate in lipid binding nor aggregations, the residue difference between APOE3 and APOE4 introduces a salt bridge between arginine 112 and glutamate 109, displacing the arginine 61 side chain and increasing the APOE4 preference towards VLDLs (192).

As a result of its isoform-dependent effect on various pathologies, the physical structure of the protein is of interest. APOE is a 34kDa, 299 amino acid protein that is encoded on chromosome 19. It contains two domains: the NH_2-terminal (or N-terminal) from residue 1-165 and the COOH-terminal (or C-terminal) from residue 225-299. While the N-terminal does not participate in lipid binding nor aggregations, the residue difference between APOE3 and APOE4 introduces a salt bridge between arginine 112 and glutamate 109, displacing the arginine 61 side chain and increasing the APOE4 preference towards VLDLs (192). In contrast, the C-terminal is responsible for adhesion and binding to lipids. At concentrations under 10 μM and in the absence of lipids, APOE forms tetramers with itself and larger aggregates at higher concentrations (193, 194). Unexpectedly, in the presence of phospholipids, APOE dissociates into monomers when bound onto lipoproteins, suggesting the monomeric form as the active form of APOE.

1.3.2 APOE's relevance to Alzheimer's

Even though APOE is systemic, its relevance in pathology resides within the brain. As a lipid transporter produced in astrocytes, APOE's main role is to provide lipids to OLs for myelination. However, it was proposed that the level of myelination is inversely proportional to the levels of APOE. A comparison of grey and white matter cholesterol and APOE levels found that although the cholesterol levels of white matter were higher than grey matter, APOE levels were higher in grey matter than white matter (195). This suggests regional effects of regional APOE that is independent from levels of cholesterol. As the strongest genetic risk factor for sAD, APOE4 has been associated with its hallmark, amyloid plaques. A previous study had shown using Cre-mediated induced APOE4 expression in APP/PS1 mice, mice model for amyloid deposition, the significantly elevated levels of Aβ40 and Aβ42 during the first 9 months of the mice compared to APOE3 (189). Additionally, the Aβ burden was significantly increased in APOE4 carriers (196, 197, 198). Moreover, hyperphosphorylated tau neurofibrillary tangles, a biomarker of many neurodegenerative disease, were found more in APOE4 carriers and greater in APOE4 homozygotes (197, 199, 200). Another prevalent detection in AD patients carrying APOE4 is white matter hyperintensities (WMH), intense white signals in the periventricular regions detected through magnetic resonance imaging (MRI) T2-weighted fluid attenuated inversion recovery (FLAIR). White signals indicate the presence of water, suggesting WMHs as water build-up. However, it is unclear whether the pooling is due to compromised vascular integrity or "leaking" axons due to myelin loss as both events produce intense white signals. Carriers of the APOE4 allele have been shown to have a higher risk of WMH (201).

1.3.3 Oligodendrocytes utilises APOE for myelination

OLs are the main receivers of lipidated APOE for myelination. They are vulnerable and sensitive to their environment, affected by microglia activation and myelin debris. Thus, the relationship between OL and myelin is tightly connected with each affecting each other. One of the main resources for OLs are lipids, which are necessary for myelination. The BBB prevents most molecules from transferring between blood vessels and the brain including lipids, and therefore all lipid components for myelin must be synthesized within the brain, namely astrocytes. Even during early development while the BBB is

still not completely formed, the brain has already taken up the responsibility in being the main producer or brain lipids (42, 202). Because of this limitation and the importance of lipids, changes in lipid levels strongly affect OL survival.

It has been shown that mutations in Niemann-Pick disease type C protein, which is responsible for moving cholesterol out of an endo-lysosomal system, that prevent successful utilizations of cholesterol reduce the number of mOLs (203, 204, 205). This shows that there is an inhibitory effect on OL maturation from the inability to process cholesterol. Additionally, we have previously shown in both homozygous APOE4 humans and mice that while the overall OL population (including OPCs and mOLs) is not significantly affected, mOLs specifically show a decrease in both grey and WM. However, the lack of APOE does not eliminate the whole myelination process as APOE and squalene synthase knockouts have shown consistent myelination indicating a compensatory effect. One study from Lombardi et al. suggests that activated microglia have the potential to horizontally transfer lipids to OLs (206). Even neurons have the ability to synthesize cholesterol, but its use has not been verified to affect myelination (207).

Effects from other steroids may also affect OLs survival and differentiation. Oxysterol, a precursor of cholesterol, has been shown to negatively regulate myelin genes within the peripheral nervous system, yet it has also been shown to promote myelin genes within the CNS (208, 209). Liver X receptor (LXR) α and β are oxysterols that have been shown to activate APOE production. Because of its polar effects depending on the nervous system, it is possible that there is a separate factor controlling myelination. The dimerization of LXR activates APOE production, and thereby, initiates lipid transport from astrocytes to OLs and promotes myelination. Meanwhile, an accumulation of monomer LXR inhibits myelination through OL toxicity from peroxisome production and disrupting calcium and potassium homeostasis (210). These feedback loops from oxysterols and myelin may hold the key to the enigmatic process of myelination, promotion of myelination through processed sterols followed by negative feedback from build-up of the unprocessed sterols.

1.4 Radiological diagnosis of neurodegeneration

Diagnosis of neurodegenerative diseases is difficult due to many diseases having no physical symptoms, and specimen collection requires invasive methods into the nervous system. Immunological responses manifested as fevers, coughs, and enteric irritations are not prominent in neurological disorders as these are diseases of bodily degeneration instead of pathogen induced. Sampling of the brain is further complicated, requiring the sample to be sacrificed and involving tedious preparation steps. Thus, radiological diagnosis using MRI and positron emission tomography (PET) have become a vital tool as an in vivo diagnostic method for many neurological diseases.

MRI utilises the magnetic properties of the hydrogen nuclei to visualise its presence within the body. The nuclei's inclusion in all water molecules means the MRI is able to use water as a way of detecting and differentiating structures within a living organism. A magnetic field is generated around the imaging area before a radio frequency pulse is emanated at various phases, resulting in dissonance of atomic spins. The amount of time necessary for the excited atom to return to an equilibrium state is calculated and realised as an image. Within the MRI are multiple modalities that can manipulate these properties to not only give locations of water but also the movement of water, compounds with differing hydrogen stereochemistry, and compounds with differing hydrogen content. One way is for volumetric analysis of the scanned region. Volumetric brain analysis has become one of the hallmarks for Alzheimer's diagnosis as volume loss has been correlated to atrophy (211, 212, 213). According to previous studies, region-based volume loss could help differentiate Alzheimer's from other forms of cognitive impairment disorders with greater reductions in hippocampal volume indicating severity of cognitive impairment and cortical reductions as indicative of Alzheimer's (214). In Alzheimer's patients, the whole brain atrophy rate could be as fast as 1.9 to 2.5% per year (215, 216) while in regular patients only by 0.22% (217). Among these modalities are two that visualises movement and presence of macromolecules: diffusion kurtosis imaging (DKI) and magnetic resonance spectroscopy (MRS).

1.4.1 Diffusivity properties of the brain

DKI estimates the skewed distribution of water diffusion based on a non-gaussian distribution, helping to indicate extremities within the distribution. Indications of higher water diffusion parallel to known tracts suggests healthy water movement while higher diffusion perpendicular to tracts may suggest compromised tract integrity (218). By utilising anisotropic and directional diffusivity values of DKI, the statuses of water-based structures could be calculated.

One of such values is fractional anisotropy (FA), a zero to one index indicating the diffusivity restrictions with zero expressing unrestricted isotropic diffusion and one expressing mono-directional diffusion. Through an age study, it was shown that FA values reached a peak between 23 and 39 years old (219) corresponding to another study's proposal of peaked grey matter volume at a similar age (83). In a neurologically diseased brain, FA has shown regional decreases corresponding to the disease severity (220, 221). Confirmation of reliability of FA in MS patients show similarly reduced FA in a demyelinated brain (222, 223). However, studies have shown that grey matter lesions may have higher FA values than normal-appearing grey matter (224). This research show that FA is a good indicator of myelin integrity, a vital part of cognitive abilities.

Perpendicular diffusivity is calculated with radial diffusivity (RD), parallel diffusivity with axial diffusivity (AxD), and average diffusivities of RD and AxD with mean diffusivity (MD). RD has exemplified higher sensitivity towards myelin structures, especially within white matter regions. Shiverer mutant mice exhibiting a deletion of part of the *MBP* gene causing dysmyelination showed significantly increased RD signals while AxD values remained unchanged (225). Likewise, cuprizone-induced demyelination showed similar increase of RD values in the corpus callosum with insignificant changes in AxD (107, 226, 227, 228). AxD has been more variable as it has not been specifically associated with a neurological pathology. Studies have shown that while parallel diffusivity indicates normal water diffusion in white matter tracts, an increase in AxD levels may show white matter atrophy (229), yet others have denied of such claims when it was seen that AxD values diminished in the beginning of cuprizone-induced demyelination but bot sustained throughout the process (230). Taking

the mean of these directional diffusivities gives MD. White matter regions such as the corpus callosum are directional, with myelin fibres going in an axial direction, which is why RD is a good indicator of myelin integrity within these regions. However, grey matter myelin is a multidirectional fibre, branching out in all directions. As a result, MD may be more sensitive in grey matter due to its inclusion of both RD and AxD. Indeed, a previous study has shown that lower MD correlates to a greater density in cellular structures such as vasculature and axons and changes in the directionality of tissue organisation (231, 232, 233).

Asides from diffusivity, specific macromolecules could be detected using MRS. In a magnetic field, the hydrogen nuclei absorb the electromagnetic radiation depending on the stereochemistry and functional groups of the molecule. Differently bonded hydrogens of organic molecules would return to resting states at different rates, allowing for the differentiations of molecules. Among a variety of metabolites identifiable with MRS, several could bring insight into the mechanism of neurodegeneration. One such molecule is n-acetylaspartate (NAA), producing one of the largest peaks in an MRS scan. NAA is concentrated in neurons but also present in OLs and myelin. The deacylation of it by aspartoacylase (ASPA) provides acetate necessary for lipid production (234). Another metabolite is choline, a component of myelin and phosphatidylcholine. Increased levels of choline have been shown to correlate with increased OPC and myelin levels (235, 236, 237, 238). Representations of metabolites within the brain could help support the pathogenesis of neurodegenerative diseases.

1.4.2 Utilisation of MRI in neurological diseases

The use of MRI has been a key diagnostic tool for MS. As MS is a demyelinating disease, MRI detection of WM lesions based on water content and diffusivity has been the gold standard in identifying affected regions. Activated brain regions require an increase in blood circulation to bring more oxygen for energy consumption. Ratios between blood flow and oxygen consumption using T2-weighted imaging, thus, have revealed lesion sites based on activation of neuronal activity in both CNS and PNS (239, 240, 241). Asides from demyelination, recent study has shown a regional lesion specific to MS seen in T2-FLAIR imaging. The central vein, a lesion involving the frontal periventricular WM, is consistently

seen in MS patients and can be used to differentiate MS from other diseases (242, 243, 244). Likewise, the manipulation of gadolinium contrasting agent in BBB breakdown seen in many other inflammatory autoimmune disorders also aids in diagnosing both the stage and type of MS. Preserved integrity of BBB normally prevents gadolinium from crossing, but in diseased systems such as MS and AD, the leakage of gadolinium out of the BBB further confirms disease diagnostics.

Similarly, MRI has been previously utilized to help diagnose for AD pathology. Volumetric T1-weighted scans are commonly paired with cognitive tests to estimate regional atrophy of GM, ventricles, and hippocampus (245, 246, 247). Reductions in these areas have strongly correlated with cognitive impairments. Alternatively, structural properties based on glucose uptake detected by dynamic glucose-enhanced MRI have shown that transgenic AD mice for amyloid plaques have a higher uptake compared to WT mice of the same age (248). Further studies have shown that normal appearing white and grey matter surrounding affected magnetic resonance images may already display cellular and structural changes (249, 250, 251). The utilisation of radiological diagnosis could help complement what is already known about neurodegeneration and support white matter-based hypotheses to elucidate the questions in these diseases.

2.0 Methods

2.1 Animal ethics

All experiments were done with compliance to The Government of the Hong Kong Special Administrative Region Department of Health's Animals (Control of Experiments) Ordinance Chapter 340. All animal experiments were performed under valid licenses provided by the Hong Kong Department of Health: (19-178) in DH/SHS/8/2/4/ Pt.8, (19-181) in HD/SHS/8/2/4/ Pt.8, (21-343) in HD/HT&A/8/2/4 Pt.8, and (22-45) in DH/HT&A/8/2/4 Pt.9. All mice were kept and cared for at The Animal and Plant Care Facility (APCF) at The Hong Kong University of Science and Technology (HKUST) and/or Centralized Animal Facilities (CAF) at The Hong Kong Polytechnic University (PolyU) in compliance with the Ordinance and The Code of Practice for Care and Use of Animals for Experimental Purposes of Hong Kong. All animal experiments and analysis were approved by the Animal Subjects Ethics Sub-Committee at The Hong Kong Polytechnic University.

2.2 Human Samples

All human tissue samples were provided by Alzheimer's Disease Research Center Neuropathology Core at the University of Pittsburgh with the approval of the Committee for Oversight of Research and Clinical Training Involving Decedents at the University of Pittsburgh. Additionally, the study was approved by the Institutional Review Board at the Hong Kong Polytechnic University – IRB (HSEARS20190809001). All postmortem tissues were formalin-fixed paraffin-embedded from sporadic Alzheimer's (mean age=83.0 years, n=18), familial Alzheimer's (mean age=50.3 years, n=7), and age-matched healthy controls (NC, mean age=78.0 years, n=9) were classified by Braak staging (163) and Institute on Aging and Reagan Institute diagnosis criteria (252). Genotyping was confirmed by conventional immunohistochemistry with Leica BOND RX of human brain stem with human APOE4 (Clone 4E4, MABN43).

2.3 Animal Subjects

Animals were first housed in The Animal and Plant Care Facility (HKUST) before being relocated to The Centralized Animal Facility (PolyU) in June 2019. This was due to the retirement of Professor Karl Herrup and the relocation to PolyU. The movement was conducted by Dr. Kai-Hei TSE utilising Ferndale and Friends from HKUST to PolyU. All animals were moved from individually ventilated cages to filter top transport cages with minimal agitations of the cage. Post-arrival, all mice were housed in the quarantine zone of the CAF for one month under close inspection before being transferred into the individually ventilated cages in room Y1428 in the Y-core of PolyU. All mice are housed in room Y1428 under the care of Hong Kong Polytechnic University's Centralised Animal Facility (CAF). Mice husbandry was done by Mr. Gerald Wai-Yeung CHENG and Mr. Sunny Hoi-Sang YEUNG. Mice are housed in individually ventilated cages (IVC) and grouped accordingly as breeding or maintenance cages. The purpose of breeding cages, which allows cohabitation of males and females, is to maintain a stable population by controlling the reproduction rates. Breeding cages are grouped from one to two males with three to four females. The purpose of maintenance cages, which allows for cohabitation of only one sex, is to maintain the growth of the mice without reproduction. Maintenance cages are grouped from four to seven mice of the same gender. Regarding groups of males, only males from the

same litter were housed together to prevent territorial offenses. However, females from different litters could be housed together. Each IVC is padded with wood shavings and provided with water and diet ad libitum. Centralised diet from CAF (5053, Purina PicoLab® Rodent Diet 20 5053) is topped up and refilled every Wednesday at 11:00am. Light cycles within room 1428 are separated into two 12-hour cycles: 7:00 to 18:59 at 8 lux and 19:00 to 6:59 at 0 lux. Light intensities are raised to 80lux during weekly cage changes by the CAF staff. Humidity within room Y1428 is maintained between 58% and 71%, and the temperature is maintained between 20°C and 23°C. New-born mice are weaned at 4 weeks old. During weaning, each mouse is provided an identification number by ear punching. Routine checks of each cage were done every Monday and Friday.

Mice that were part of the cuprizone treatment cohort were housed in filter cages in room Y1431. As cuprizone has neurotoxic effects, mice under this treatment were placed in filter cages to prevent contamination of the central air vent system in the IVCs. Mice of the same treatment were placed in the same cage without preference for genotype. The cuprizone treatment (0.2% w/w, TD.140803, irradiated, Envigo, Indianapolis, IN, US) and control treatment (0.0% w/w, TD.00588, irradiated, Envigo, Indianapolis, IN, US) were provided at 150g per cage with ad libitum water for 4 weeks. The treatments were topped up to 150g every Monday and Thursday, and the weights and activity of each mouse were observed and recorded to record any changes in their health status every Monday and Thursday. Routine checks of each cage were done every Monday and Friday. No abnormalities such as acute weight loss, abnormal gaits, nor aggressive/passive interactions were observed.

Longitudinal study is the continuous data acquisition of an individual over a period. In age-dependent diseases such as Alzheimer's disease, it is important to monitor minute changes in cognitive abilities, motor skills, or mental health in patients to diagnosis for disease progression. While a longitudinal study would provide more accurate data regarding radiological age-dependent changes, our hypothesis our hypothesis focuses on cellular changes which cannot be continuously monitored by any in vivo technique over 16 months period. We acknowledge the benefits of longitudinal studies where individual mice's white or grey matter volumetric or diffusivity parameters could be followed with age as these

procedures do not require the sacrifice of the mice. However, quantitative analysis of cellular properties such as immunohistochemistry, western blot, or qPCR would not be possible in vivo. Since our hypothesis proposes the detection of both myelin loss and oligodendrocyte degeneration, mice must be sacrificed for cell analysis. Additionally, further dissection of brain regions was necessary for region-based effects from aging. As such, a cross-sectional study was done. A cross-sectional study is the data acquisition at set time points. Our experiments acquired radiological data (in vivo) and histological data (post-mortem) at specific ages to correlate myelin densities to cellular alterations. Since we are focusing on how age-dependent myelin and oligodendrocyte changes can affect each other at different ages instead of how age affects myelin and oligodendrocytes, we do not require a longitudinal study.

Sex differences was a considered factor in the construction of the proposal. Indications of sex are made within the captions of all figures shown as male/female. Myelination has been shown to differ between rodent sexes. In wild-type males, the density of oligodendrocytes and expression of myelin proteins and genes such as MBP and PLP are greater than females (253, 254). The delineation is further supported by female's up-regulation of androgen receptors responsible for remyelination in demyelinated lesions compared to undetectable changes in the male (255). These results indicate a diverging path of myelination and remyelination between males and females. Further review of Alzheimer's disease mouse model, APP/PS1, showed myelin vulnerability of female APP/PS1 mice with significantly lower total white matter volume and myelinated fibers (256). Previous studies of the inclusion of cuprizone have also produced sex differences. It is agreed that cuprizone induces similar degrees of demyelination between male and females (257, 258). However, in females, cuprizone had deregulated the estrous cycle (258) and increased anxiety and reduced motor coordination in males (257). To remove factors that could produce variation, only one sex was used for our experiments. The choice of males is due to the female's estrous cycle, which cycle every four to five days (259). During the estrous cycle, higher levels of progesterone are produced in the metestrus phase (AA). Progesterone is known for oligodendrogenesis (260) and up-regulation of MBP (261). Additionally, increases of progesterone levels have shown protective effects against cuprizone (262). As a result, males were chosen due to minimal external factors that could influence demyelination.

2.3.1 R1.40

The R1.40 mice (B6.129-Tg(APPSw)40Btla/Mmjax) for human amyloid beta (A4) precursor protein (APPSwe) were created by the manipulation of a yeast artificial chromosome (YAC) containing the entire human APP gene with substitution mutations of asparagine for lysine and leucine for methionine ($APP_{K670N/M671L}$), isoleucine for valine (APP_{V717I}), or both (263) (Figure 4). The production of the APP YAC was through, first, its digestion by SacI and ligation into SacI-digested λ phage ZAPII. Exons 16 and 17 were isolated with the 1.8 kbp HindIII fragment with exon 16 and 3kbp EcoRI fragment with exon 17 subcloned into Bluescript. The substitution mutations were introduced in the appropriate exons through PCR mutagenesis. Products were linearized with StuI and inserted into the wild-type APP gene by a two-step yeast gene replacement outlined by Ketner et al (264). R1.40 mice exhibit amyloid plaque deposition by 14 months of age (263) (Figure 5). Transgenic mice were acquired from Jackson Laboratory (034831-JAX, Bar Harbor, USA) and allowed to inbreed among wild-types and hemizygotes. Mice were provided *ad libitum* water and diet for 12-weeks before administered with either 18% protein control diet (ENVIGO, TD.00588) or 0.02% cuprizone diet (ENVIGO, TD.140803) for 4 weeks. The R1.40 mice were employed to model mild amyloid deposition and the effects of acute demyelination by cuprizone.

2.3.2 APP/PS1

The APP/PS1 mice (B6.Cg-Tg(APPswe,PSEN1dE9)85Dbo/Mmjax) for two inserted cDNA transgene were created with the Swedish mutation for the amyloid beta (A4) precursor protein (APPSwe) and human presenilin-1 "DeltaE9" mutation ($PS1_{L166P}$) inserted into the pTSC21 vector (265) (Figure 4). The vector was inserted into the XhoI cloning site and NotI/PvuI digested and injected into the C57BL/6 male pronuclei oocytes. APP/PS1 mice exhibit amyloid plaque deposition by 6 months of age (Figure 6). Clinically, amyloid plaques appear first due to accumulating aggregations of the amyloid oligomers. This abnormal aggregation induces an immune response that triggers the activation and proliferation of microglia and astrocytes, known as gliosis. Finally, it is due to the inflammation recruited by the immune response and the overproduction of these plaques do synapses begin to suffer as axons degenerate. Transgenic mice were acquired from Jackson Laboratory (034832-JAX, Bar Harbor, USA)

and allowed to inbreed among wild-types and hemizygotes. APP/PS1 mice were provided *ad libitum* water and normal diet for 8 weeks before administered with either 18% protein control diet (ENVIGO, TD.00588) or 0.2% cuprizone diet for 4 weeks. The APP/PS1 mice were employed to model aggressive amyloid deposition. The addition of cuprizone questioned if the aggression of deposition would prepone amyloid deposition and affect neuron and OL survivability.

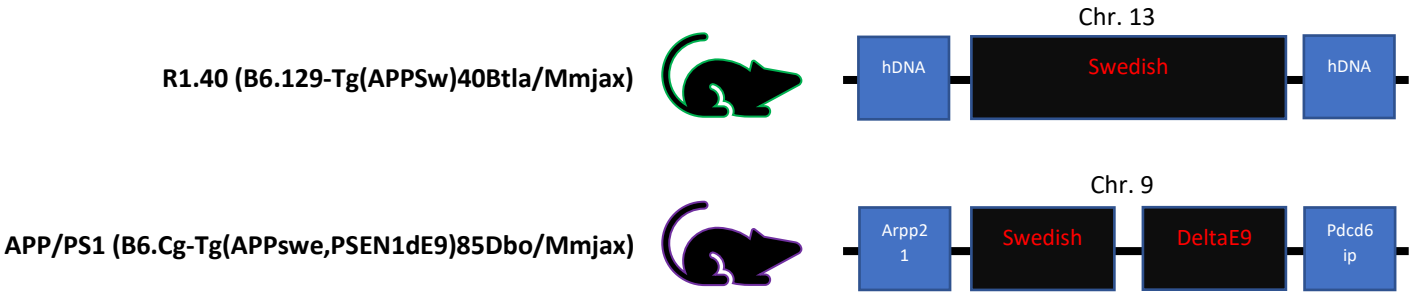

Figure 4: Mutations of the R1.40 (Top) and APP/PS1 (Bottom) mice models.

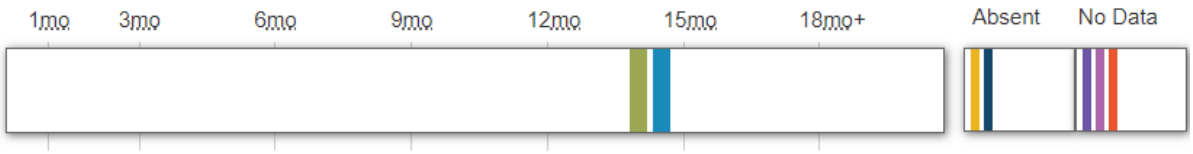

Plaques	By 13.5 months homozygous mice develop both parenchymal and vascular amyloid deposits which first appear in the frontal cortex. No Aβ deposition at 5 months (Lehman et al., 2003).
Tangles	No mature tangles, but some changes in phosphorylated tau.
Neuronal Loss	Unknown.
Gliosis	Reactive astrocytes and microglia in 14-16 month old animals (Kulnane et al., 2001).
Synaptic Loss	Unknown.
Changes in LTP/LTD	Absent.
Cognitive Impairment	Unknown.

Figure 5: Age of onset of neurological events of R1.40 mice.

Plaques	Aβ deposition begins at 6 weeks of age in the cortex and 3-4 months of age in the hippocampus (Radde et al., 2006).
Tangles	Phosphorylated tau-positive neuritic processes around plaques have been observed, but no mature tangles (Radde et al., 2006).
Neuronal Loss	Global neuron loss is not observed, but modest neuron loss was found in the granule cell layer of the dentate gyrus and other subregions with high neuronal density in 17-month old animals (Rupp et al., 2011).
Gliosis	Activated microglia around Aβ deposits at 6 weeks as well as increased astrogliosis (Radde et al., 2006). Levels of CCL2 and TNFα increase at later ages (Lee et al., 2010).
Synaptic Loss	Dendritic spine loss around plaques reported to begin approximately 4 weeks after plaque formation and continue for several months (Bittner et al., 2012).
Changes in LTP/LTD	Hippocampal CA1 LTP normal at 4.5 months of age, but impaired at 8 and 15 months of age (Gengler et al., 2010).
Cognitive Impairment	Cognitive deficits in spatial learning and memory in the Morris water maze reported at 7 months (Serneels et al., 2009). Impaired reversal learning of a food-rewarded four-arm spatial maze task observed at 8 months (Radde et al., 2006).

Figure 6: Age of onset of neurological events of APP/PS1 mice.

2.3.3 *Apoe*$^{-/-}$

The *Apoe*$^{-/-}$ mice (*Apoe*^{tm1Unc}) for the complete knock-out of the endogenous mice Apoe were created by Piedrahita et al (266) (Figure 7). The *Apoe* gene was knocked-out using gene targeting of the mice embryonic stem cell where two plasmids, pJPB63 and pNMC109, containing neomycin-resistant genes were introduced and replaced *Apoe* using electroporation. Homozygotes for *Apoe*$^{-/-}$ disrupted gene were utilized to inbreed with no wild-types as this strain could survive and remain fertile as homozygotes in complete absence of *Apoe*. Mice were obtained from Jackson Laboratory (IMSR_JAX:002052, Bar Harbor, USA) and were allowed to mature up to 6-, 12-, and 16-months and provided *ad libitum* water and normal diet. The purpose of utilizing *Apoe*$^{-/-}$ is to understand the influence of the lack of a lipid transporter within the body. Concurrently, it is to provide a negative control for the further implementation of the humanized APOE3 and APOE4 knock-ins.

2.3.4 APOE3 and APOE4

Humanized APOE3 (RBRC03390, B6;129-Apoe$^{<tm>/3SfuRbrc}$) and APOE4 (RBRC03418, B6;129-Apoe$^{<tm(HAPOE4)Sfu>/SfuRbrc}$) knock-in mice were obtained through RIKEN BIoResource Researchi Center, Japan. Mice were developed by Hamanaka Hiroki of Mitsubishi Kasei Institute of Life Sciences by introduction of the knock-in section into E14TG2aIV embryonic stem cells by electroporation. Part of exon 2, entire exon 3, and most of exon 4 of the mouse *Apoe* sequence were deleted, and hAPOE3 or hAPOE4 cDNA was inserted (267) (Figure 7). Transgenic mice were allowed to inbreed with wild-types, heterozygotes, and homozygotes for either the APOE3 or APOE4 gene within its own strain. Heterozygotes of the humanized APOE gene were only employed for breeding while wild-types and homozygotes were utilized for experimentation. Mice were allowed to mature up to 6-, 12-, and 16-months. The implementation of transgenic humanized APOE3 and APOE4 mice may help to understand the effect of isoform difference on its correlation with AD. As only the APOE4 isoform significantly increases the risk of AD, through which cells or structure does this influence is of importance towards the progress of AD understanding and treatment.

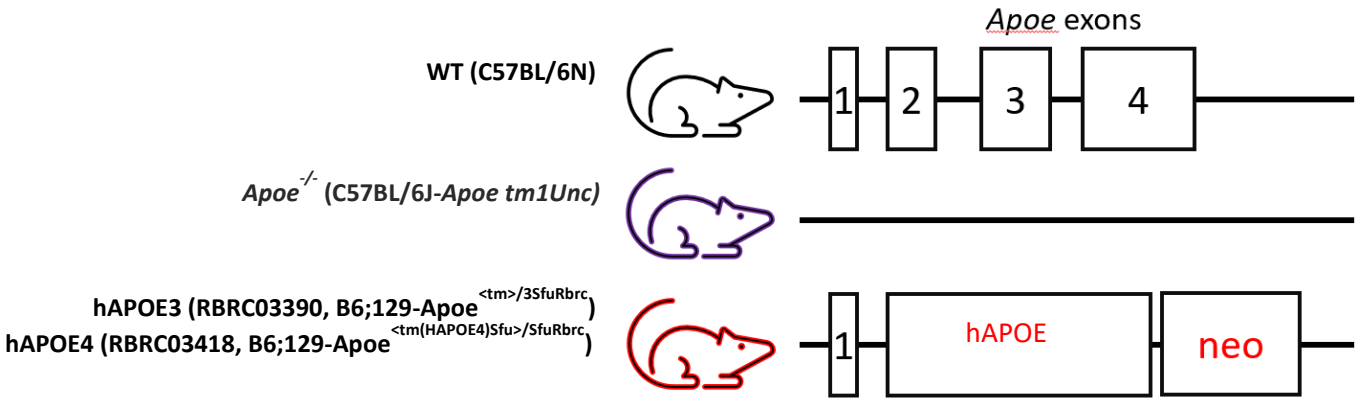

Figure 7: Transgenic mice for APOE. The exons of the endogenous Apoe gene are presented in the C57BL/6 mice (Top). In the Apoe$^{-/-}$, the full Apoe gene is removed (Middle). In the hAPOE3 and hAPOE4 mice, all of exons 2 and 3 and part of 4 of the Apoe gene are removed and replaced with the hAPOE gene and neomycin.

2.4 Genotyping of animal samples

Genetic identification of each mouse was performed at weaning and post-mortem. Ear punch was carried out using stainless steel ear punch (KN-292-2-1, Natsume Seisakusho Co., Ltd, Tokyo, Japan) by making an ear hole of diameter 1.5 mm. Punched tissues were stored in a 1.5 mL Eppendorf tube in 4°C for genotyping.

2.4.1 Genotyping of R1.40, hAPOE3, and hAPOE4

The Extract-N-Amp™ Tissue PCR Kit (XNAT2, Sigma-Aldrich, St. Louis, USA) was used for DNA extraction and amplification of R1.40 and humanized APOE transgenic mice. Ear tissues were first submerged into a mixture containing 100 µL of extraction solution (E7526, Sigma-Aldrich, St. Louis, USA) and 25 µL of tissue preparation solution (T3073, Sigma-Aldrich, St. Louis, USA) for 10 min in a 55°C water bath following 3 min on a 95°C heat block. Once extracted, 100 µL of neutralization solution B (N3910, Sigma-Aldrich, St. Louis, USA) was added to cease the denaturation and complete DNA extraction. A solution (per sample) of 10 µL of Extract-N-Amp™ PCR Reaction Mix (E3004, Sigma-Aldrich, St. Louis, USA), 3 µL of distilled water, 1 µL of each appropriate 10x primer solution, and 4 µL of sample DNA extract was combined with vortex mixer and centrifuged to aggregate all solution into the bottom of the 500 µL PCR tubes. Tubes were then processed within a Veriti™ 96-Well Fast Thermal Cycler (4375305, Thermo Scientific, Waltham, USA) using primer-specific protocol.

2.4.2 Genotyping *Apoe*$^{-/-}$ and APP/PS1

Genotyping of APOEKO and APP/PS1 mice were performed as indicated in the following. For DNA extraction, ear tissues were immersed in 100 µL of 0.01 M NaOH and heated at 95°C on a heat block for 45 min. Afterwards, 75 µL of Tris-TAE neutralization buffer was added to halt the denaturation process. The polymerase chain reaction (PCR) solution (per sample) was made with 2.5 µL of ThermoPol® Reaction Buffer (B9004S, New England BioLabs, Ipswich, USA), 0.5 µL of ddNTP, 0.5 µL of each appropriate 10x primer solution, 15.5 µL of distilled water, and 0.125 µL of *Taq* DNA polymerase (M0273S, New England BioLabs, Ipswich, USA), and 5 µL of sample DNA extract. The solution was then combined with vortex mixer and centrifuged to aggregate all solution into the bottom

of the 500 μL PCR tubes. Tubes were then processed within a Veriti™ 96-Well Fast Thermal Cycler (4375305, Thermo Scientific, Waltham, USA) using primer-specific protocol.

2.5 Cuprizone mediated demyelination

Diet incorporated with 0.2% cuprizone (CPZ) diets were purchased through ENVIGO (Madison, USA). R1.40 mice and APP/PS1 mice at 12 and 8 weeks of age, respectively, were removed from IVCs in room Y1428 and relocated into open top filter cages in room Y1431 for 4 weeks of treatment. Each cage held a maximum of three mice and were changed and cleaned weekly. Both control and cuprizone diets were topped up to 150 g biweekly and water changed weekly while their consumption was *ad libitum*. Biweekly inspection of amount of chow eaten, mice weights, and status of each mouse was performed to ensure adherence to proper ethical protocol. If mice were shown to have significant deterioration in health such as gait impairment or appearance of seizures, the mice were humanely euthanized with CO_2 asphyxiation. At the end of the procedure, cuprizone and provided control diets were properly disposed of in the hazardous waste bags in accordance with the Waste Disposal Ordinance (Cap.354) under the Environmental Protection Department of Hong Kong. No deterioration was found in CPZ mice during the 4-week treatment period, and no mice were sacrificed due to complications from the diet.

2.6 Behaviour test for reference memory- Y-maze

The plastic 3-pronged y-maze was measured by Dr. Kai-Hei TSE and produced at Hoi Fat Plastic Decoration Advertising Limited in Mong Kok, Hong Kong. The set-up of the room for the memory test is shown in Figure 8. Mice were relocated from room Y1428, Y1429, or Y1431 into room Y1441 for at least 1 hr to acclimate to the new environment to prevent stress factors that may affect its cognitive or physiological functions. After the acclimation period, each animal was placed on the underside of filter tops to prevent its visuals of the surroundings and placed into the gated 3-pronged y-maze. The dimensions of our grey opaque acrylic Y-maze with 3 prongs are as follows: length is 35cm, width is 7cm, and height is 9cm (268). While there are different single arm lengths of the y-maze ranging from 15cm to 95cm, we had chosen 35cm due to previous reports of cognitive testing of mice using similar

lengths of 39.5cm (269) and 30cm (270). The maze was placed on top of a cart that was locked into place to prevent unnecessary movement during the behaviour test. A tripod was used to hover a camera 85cm above the Y-maze to allow it to visualize the whole maze. To provide additional lighting for the camera, a lamp was placed in the corner of the room with the light aimed at the adjacent wall. The camera was then connected into the laptop where the ANY-MAZE (version 7.2, Stoelting Co. IL, USA) was installed for animal tracking.

After the set-up, mice cages were transferred from room Y1428 or Y1431 to Y1441 by cart to prevent excessive movement of the cages. The temperature of Y1441 was maintained between 18°C and 21°C; the humidity was maintained between 45% and 65%. Once inside room Y1441, mice were acclimatized on an adjacent table to the cart for 1 hr prior to behaviour test. For each trial, mice were transferred from the table to the Y-maze using the cage lid to prevent fear or stress responses from handling the mice. Additionally, black boards were used as a barrier surrounding the Y-maze to prevent outside factors from influencing mice behaviour.

Y-maze is a two-tier behaviour test working and reference spatial memory. Reference memory test was done with no food reward since spontaneous alternation, or the measurement of willingness for mice to explore new environments, requires that the mice have no direct influence from a reward. Additionally, reward-based reference memory tests have been shown to not exhibit significant differences in animal spontaneous alternation nor choice in correct arm entry in Y- and T-maze but only in higher activity (271, 272). Spontaneous alternation manipulates an animal's natural tendency to explore the new. In the working reference memory tests, the mouse is permitted to freely roam the ungated maze for 8 min (273, 274, 275, 276, 277, 278) before homing. The reference spatial memory test requires two phases: a training phase and experimental phase. During the training phase, the mouse is allowed to explore the maze with one gate closed for 4 min. Afterwards, an 1 hr inter-trial resting period is provided before the subject is placed back into the ungated maze for 4 min (279). Tests were done with the following parameters measured: time spent in each arm, time spent in the correct arm, time spent in the incorrect arm, total entries, spontaneous alternation (percentage of alternation equals to the number of

alternations divided by the number of entries and multiplied by 100), average speed of the mouse, and average unmoving time (14).

Reference memory test was done with no food reward since spontaneous alternation, or the measurement of willingness for mice to explore new environments, requires that the mice have no direct influence from a reward. Spontaneous alternation manipulates an animal's natural tendency to explore the new. In the working reference memory tests, the mouse is permitted to freely roam the ungated maze for 8 min (273, 274, 275, 276, 277, 278) before homing. The reference spatial memory test requires two phases: a training phase and experimental phase. During the training phase, the mouse is allowed to explore the maze with one gate closed for 4 min. Afterwards, an 1 hr inter-trial resting period is provided before the subject is placed back into the ungated maze for 4 min (279).

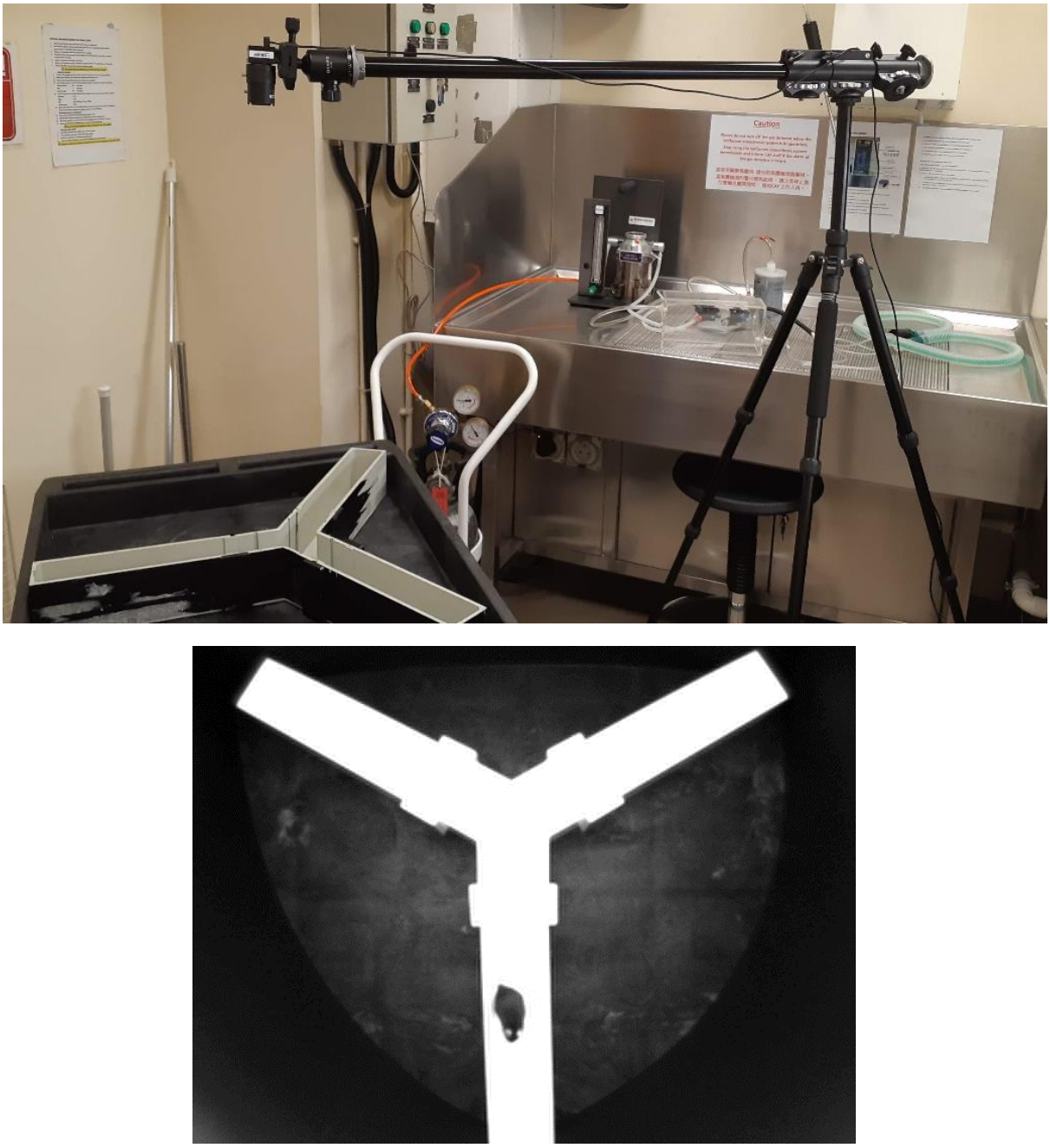

Figure 8: Presented is the set-up of the y-maze behaviour test in room Y1441 of the PolyU CAF (Top). The camera set up using Any-Maze is as shown (Bottom).

2.7 Functional Magnetic Resonance Imaging (MRI)

Magnetic resonance imaging was conducted with the help from Dr. Kannie Wai-Yan CHAN, Dr. Jianpan HUANG, and Ms. Zilin CHEN of City University of Hong Kong (CityU) in room Y7612 in the Yeung Kin Man Academic Building of the City University of Hong Kong. A horizontal bore Bruker 3T BioSpec fMRI system (Figure 9A) was used to acquire five radiological modalities: T1-weighted (T1w), T2-weighted (T2w), diffusion kurtosis (DKI), magnetization transfer (MT), and magnetic resonance spectroscopy (MRS).

All MRI experiments were performed on a horizontal bore 3T Bruker BioSpec system (Bruker, Ettlingen, Germany) equipped with an 82 mm quadrature volume resonator as a transmitter and a single surface coil as a receiver, at City University of Hong Kong (Figure 8). For MRI scan, animal subjects were initially anesthetized using a chamber pervaded with 2% isoflurane in oxygen. Mice without reflex were considered unconscious and placed into the MRI. Subsequently, the mice were placed on the mouse cradle in the scanner with a gas inhalation mask and kept under anaesthesia with 1–1.5% isoflurane in oxygen. Oxygen at a concentration of 93% was generated by an oxygen concentrator (DeVilbiss Healthcare, Somerset, USA). The flow of oxygen was set to 2L/min throughout MRI acquisition. Isoflurane is shown to affect the level of γ-aminobutyric acid (GABA), an inhibitory neurotransmitter regulating chloride ion diffusion. Application of increasing isoflurane concentration has been shown to increase GABA-activated currents in the hippocampal circuitry (280, 281). Increase of GABA hyperpolarizes neurons, inhibits action potentials, and reduces the release of neurotransmitters. These effects have been shown to reduce motor stimulation and decrease cortical activity (282, 283). Even though isoflurane affects neural circuitry, it has not been shown to affect MRI signals (284). To ensure comparable slice orientations, the mice were placed in a prone position with the head fixed to a teeth holder. Mouse body temperature was maintained at 37°C using a warming pad connecting to a water heating system (Thermo Scientific, Waltham, USA). Respiration was continuously monitored using an MRI-compatible monitor system (SA Instruments, Stony Brook, USA) with a signal derived from a pressure transducer placed under the chest of mouse. After localized acquisition, the B_0 field over the mouse brain was shimmed using field mapping and second order

shimming. The image slices were positioned based on a collected sagittal image of the mouse brain with the position of the coronal image slice set to -1.5 mm with respect to the anterior commissure (AC). For each mouse, MRI data of T1/T2 weighted (T1w/T2w) imaging, diffusion tensor imaging (DTI) and magnetization transfer ratio (MTR) imaging and magnetic resonance spectroscopy (MRS) were acquired. For imaging acquisitions, 11 slices of image with a matrix size of 128 ´ 128, a field of view (FOV) of 20 ´ 20 mm and a thickness of 1 mm were acquired (Figure 9B and 9C). T1 and T2 acquisition took 2min 24s. Diffusion kurtosis imaging took 13min. Magnetic resonance spectroscopy acquisition took 9min 49s. Magnetization transfer took 9min 26s. The total acquisition time took 34min 39s with additional average of 15min of acquisition set up. Recovery was done with a heat lamp to prevent heat loss of the mouse until consciousness. Other acquisition parameters for each methodology were specified as the following:

2.7.1 T1/T2 weighted imaging

Both T1w and T2w images were acquired using a rapid acquisition with refocused echoes (RARE) sequence. T1w parameters were set as: repetition time (TR) = 500 ms, echo time (TE) = 14 ms, number of average (NA) = 8, RARE factor = 4 (linear encoding), scan time = 2 min 8 sec. T2w parameters were set as: TR = 3000 ms, TE = 54 ms, NA = 8, RARE factor = 16, scan time = 2 min 24 sec.

2.7.2 DKI imaging

Diffusion kurtosis images (DKI) were acquired using a spin echo-echo planar imaging (SE-EPI) sequence. Imaging parameters were set to: TR = 3000 ms, TE = 36 ms, NA = 4, diffusion encoding δ = 3 ms and diffusion separation Δ = 16 ms, 30 diffusion directions with b = 1000 s/mm2 and 5 unweighted b = 0 s/mm2 images, 2 experiments per direction, resulting in a scan time of 13 min. The diffusion tensor eigenvalues (λ1, λ2, λ3) computed by the ParaVision 6 were used to calculate parameter maps on a pixel-by-pixel basis for the axial diffusivity (AxD) with AxD = λ1, the radial diffusivity (RD) with RD = (λ2 + λ3) / 2, the mean diffusivity (MD) with MD = (λ1 + λ2 + λ3) / 3 and the fractional anisotropy (FA) with:

$$FA = \sqrt{\frac{(\lambda_1 - \lambda_2)^2 + (\lambda_2 - \lambda_3)^2 + (\lambda_1 - \lambda_3)^2}{2(\lambda_1^2 + \lambda_2^2 + \lambda_3^2)}}$$

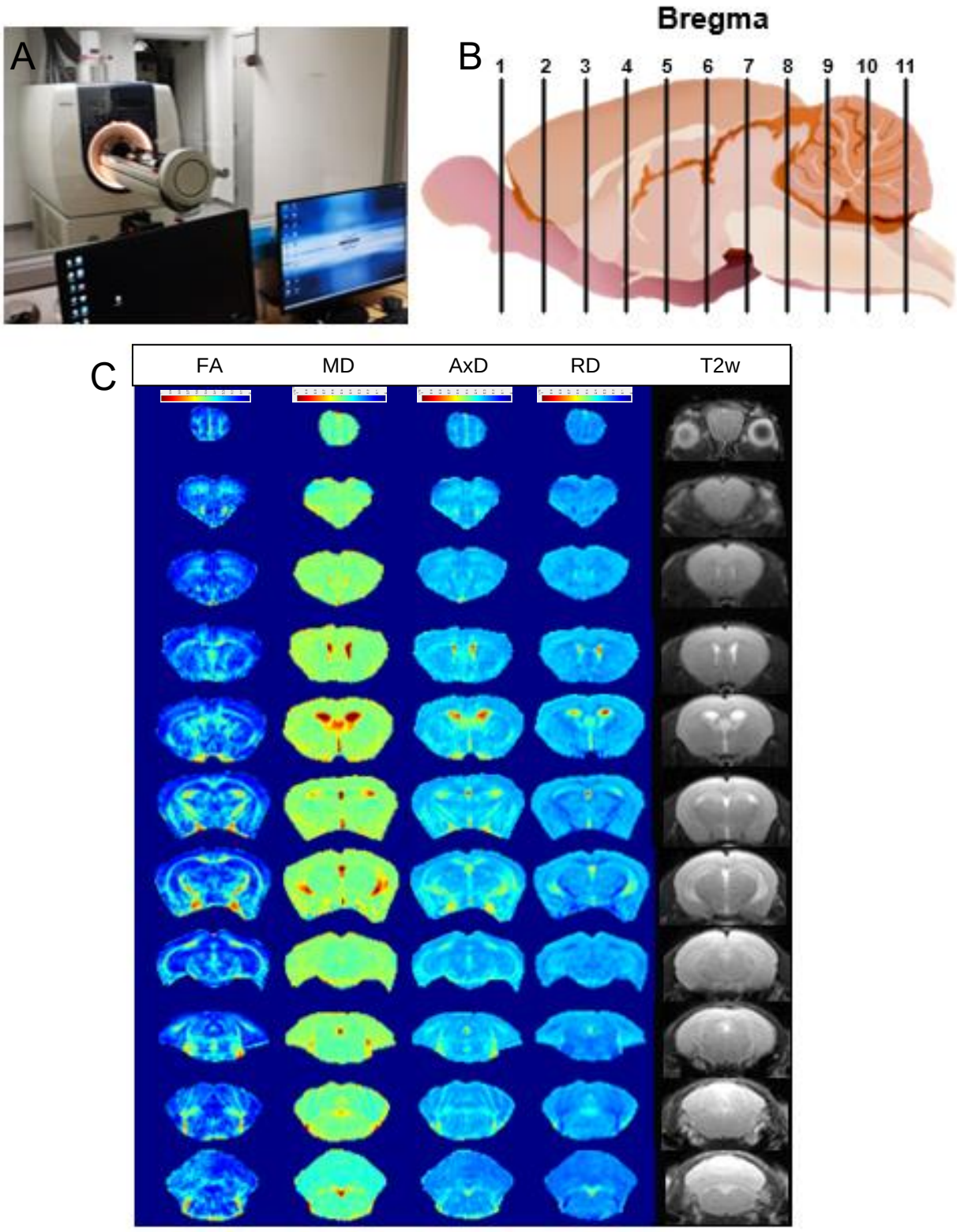

Figure 9: Presented is the CityU room for the 3T Bruker functional MRI (A). The number of slices that was imaged are separated into the respective Bregmas (B). Representative DKI and T2w images are shown (C). Bregma is the location at which the coronal suture, a connective tissue joint that separates the two parietal bones from the frontal bone, and the sagittal suture, the connective tissue joint that separates the two parietal bones, perpendicularly intersects. This region is regarded as the origin for the coordinates of the coronal brain. Bregma values, presented as the distance in millimetres from this origin, are in reference to this point using positive, or more anterior, and negative, or more posterior,

to this position. Each coronal MRI image is approximately 1mm thick, separating our Bregmas by a factor of approximately 1 between each image. Radiological acquisition permitted for 11 images to be taken starting from approximately Bregma 3.6 encompassing only the tip of the frontal cortex with mostly the olfactory bulb to approximately Bregma 7.5 encompassing the posterior cerebellum. All images were with reference to the Allen Brain Atlas. Image heatmap used jet color differentiation to indicate degree of diffusivity using diffusion kurtosis imaging. The range for fractional anisotropy (FA) is a scalar unit between 0 and 1. Values closer to 0 represent an isotropic diffusion while values closer to 1 represent an anisotropic diffusion. Radial (RD), axial (AxD), and mean (MD) diffusivity range between 0 and 1E10-3, 0 and 1E10-3, and 0 and 1E10-3, respectively, with a unit of mm^2/s.

2.7.3 Magnetic Resonance Spectroscopy

The voxel of interest (VOI) for MRS acquisition was localized in cortex region of each mouse with reference to the acquired T2 weighted image. Localized shimming up to second order was performed using voxel-based field mapping before each MRS acquisition. MRS data were acquired using the stimulated echo acquisition mode (STEAM) sequence with outer volume suppression. The acquisition parameters were voxel size = 3 × 3 × 3 mm, FID = 2048 points, averages = 256, TE = 3ms, mixing time (TM) = 10 ms, TR = 2300 ms, scan time = 9 min 49 s. The location of the volume encompasses the cortex, corpus callosum, hippocampus, and thalamus (Figure 4). Water suppression was achieved using the variable pulse power and optimized relaxation (VAPOR) method. MRS data processing and analysis were performed in MATLAB (MathWorks, USA). MRS spectra were aligned by setting the creatine peak at 1.3 parts per million (ppm) against lipids, NAA, and glutamine/glutamate levels. Creatine has been shown to directly affect the survival of oligodendrocytes by increasing production of mitochondrial ATP specifically in oligodendrocytes (285). Additionally, the deletion of creatine-synthesizing enzyme, guanidinoacetate methyltransferase, significantly reduced creatine expression and mature oligodendrocyte populations, delayed myelination, and impaired axonal integrity by increased expression of non-phosphorylated neurofilaments (286). Hence, creatine levels may represent oligodendrocyte population statuses. However, these studies were done in cell culture and cerebellum using single cell analysis. Previous reports have shown that creatine levels remain consistent among normal control and Alzheimer's patients (287, 288, 289, 290). Furthermore, levels of MRS detected metabolite changes against creatine were established in Alzheimer's evaluations. Our MRS was done over a volume encompassing the cortex, corpus callosum, and hippocampus. The region is significantly larger than the single cell analysis. This form of analysis would decrease the effects of the level of creatine.

2.8 Isolation of brain and organs

Post-MRI, animals were returned to PolyU room Y1104 for sacrifice and extraction in a class II biosafety cabinet. Mice were irreversibly anesthetized by intraperitoneal injection with avertin (1.25%, 2,2,2-tribromoethanol) and checked for consciousness by hind feet pinching to assess for nociceptive

reflex before transcardial perfusion. Ice-cold phosphate buffer solution (PBS) was perfused through a peristaltic pump at 4.5 mL/min. The choice of avertin had been approved due to the single survival procedure nature of the euthanasia. Ear punches were removed for post-mortem genotype confirmation.

Once the mouse has been checked and confirmed as unconscious, the mouse was transferred onto the operating stage where its appendages were pinned down with sanitized needles. The skin on the chest of the mouse was first picked up with forceps, and a cut was made to expose the sternum. An incision was made under the sternum, and the diaphragm was similarly opened to expose the heart. A hypodermic needle fitted into the tubing of the peristaltic pump was then inserted into the ventricle of the heart, and ice-cold PBS was used at 4.5 mL/min to perfuse the mouse for 3 to 4 min. As an adult mouse has an average of 2.5 mL of circulating blood, an excess of PBS was used to ensure complete removal of blood. After perfusion, a vertical incision of the skin from the nape to the nose was made in addition to a horizontal cut between the eyes within the scalp. Subsequently, a similar cut along the median line from the eyes to the spine to expose the brain was executed. The brain was carefully removed by nicking the optic nerves and placing it onto a petri dish. The extracted brain was bisected into the left and right hemispheres. The left hemisphere was snap frozen in dry ice for storage, and the right hemisphere was fixed in 8 mL of 4% paraformaldehyde for 24 hrs at 4°C. The difference between the left and right hemispheres were not studied. Instead, choosing one hemisphere of the brain is for consistency as our previous works have used the left hemisphere for protein expression and right for immunohistochemistry. Fixed brain tissues were then dehydrated with 30% w/v sucrose/PBS for a minimum of 48 h, segregated into 2 mm blocks using brain matrix, embedded into cassettes with optimal cutting temperature (OCT) in dry ice, and cryosectioned using Cryostar NX70 Cryostat at 10 mm sections on charged slides. Embedded tissues and unused sectioned slides were stored in -80°C while unused brain tissues were cryopreserved with 20% glycine/sucrose in -20°C.

2.9 Tissue re-dehydration

Tissues kept in cryoprotectant are required to be re-dehydrated before embedding. Tissues were first removed from the cryoprotectant and washed with 30% sucrose/PBS three times to remove excess

glycine. After wash, each tissue was submerged in 3 mL of 30% sucrose/PBS for 10 days with daily replacement of the solution to maintain higher concentration in the solution. Each tissue was then submerged in 40% sucrose/PBS for 4 additional days with daily solution replacement to further dehydrate the tissue. Finally, the tissue was submerged in 2 mL of OCT in addition to 2 mL of the 40% sucrose/PBS solution for 3 days before embedded in OCT.

2.10 Chromogenic Immunohistochemistry and Imaging

Mounted brain sections stored in -80°C were washed 3 times with PBS to remove excess OCT before converters were placed on each slide. Leica Bond Polymer Refine Detection (Wetzlar, Germany) was used for immunohistochemistry (IHC) in addition to pre-made primary antibody solutions. Staining protocols for Leica Bond Rx were optimized for heat induced epitope retrieval (HIER) pH of pH 6 (ER1) or pH 9 (ER2), time necessary for antigen retrieval, antibody dilutions, and incubation period. All antibodies used include the following: Olig2 (MABN50, 1:500 Millipore, CA, USA, heat induced epitope retrieval (HIER) with ER1 solution for 20 min), ASPA (ABN1698, 1:500 Millipore, CA, USA, HIER with ER1 solution for 20min), Nkx 2.2 (ab191077, 1:1000 Abcam, Cambridge, HIER with ER2 solution for 20 min), APC-CC1 (Clone CC1, MABC200, 1:500 Millipore, CA, USA, HIER with ER1 solution for 20 min), PLP1 (Clone E9V1N, CST 28702S, 1:500, HIER with ER1 solution for 20 min); amyloid marker, anti-β-Amyloid 1-16 (Clone 6E10, 803014, 1:5000, BioLegend, CA, USA, HIER with ER1 solution for 20 min). All sections were counter-stained with haematoxylin. After staining, tissues were immediately removed and placed into distilled water for transfer into dehydration. Slides were placed into a slide staining rack and washed for 30 sec with agitation in order from 70% ethanol, 90% ethanol, 100% ethanol twice, and xylene twice. Tissues were then mounted using DPX high grade xylene mountant (06522-100mL, Sigma-Aldrich, St. Louis, USA). Imaging was done with Leica Aperio CSO Scanner in 20x double magnification (Leica BioSystems, Wetzlar, Germany) or NanoZoomer S210 Digital slide scanner (C13239-01, Hamamatsu Photonics, Shizuoka, Japan).

Human samples of the frontal cortex, cerebella cortex, brainstem, and hippocampus were used for further conventional immunohistochemistry. Paraffin tissue slides were first heated at 60°C for 1 hr to

melt the paraffin before deparaffinization with xylene for 10 min. Rehydration was then done through 30 sec washes in a decreasing ethanol concentration. Antigen retrieval was then performed using pH 9.0 Tris-EDTA buffer (10 mM Tris Base, 1 mM EDTA solution, 0.05% Tween 20) at 100°C water bath for 30 min. Quenching residual peroxidase was performed with 3% hydrogen peroxide before blocked with normal donkey serum for 30 min. Primary antibody incubation was performed for myelin basic protein (SMI-99P, 1:3000, Covance/BioLegend, CA, USA), Olig2 (MABN50, 1:500 Millipore, CA, USA), APC-CC1 (Clone CC1, MABC200, 1:500 Millipore, CA, USA), and myelin regulatory factor (ABN45, 1:300, Millipore, CA, USA) at 4°C overnight. Secondary antibody incubation was then performed with DAB-based detection kits (VectaStain Elite ABC HRP Kit; DAB Peroxidase HRP Substrate Kit, Vector Laboratories, Burlingame, CA) and counter-stained with hematoxylin. All human tissues were imaged with an upright microscope (BX53 with DP80 camera, Olympus, Tokyo, Japan), and scanned with a Leica Aperio CS2 digital pathology slide scanner (Leica Microsystems, Hong Kong SAR).

2.11 Whole brain immunofluorescence and imaging

Mounted brain sections stored in -80°C were washed 3 times with PBS before blocked with 5 % normal donkey serum in PBS containing 0.3% Triton X-100 for 30 min in 20°C. Tissues were then incubated with primary antibodies for either 2 hrs in 20°C or a minimum of 12 hrs in 4°C, washed 3 times with PBS, and applied with corresponding secondary antibodies for 1 hr in 20°C. All antibodies used include the following: Olig2 (MABN50, 1:500 Millipore, CA, USA), ASPA (ABN1698, 1:500 Millipore, CA, USA), APC-CC1 (Clone CC1, MABC200, 1:500 Millipore, CA, USA), 53BP1 (ab36823, 1:5000 Abcam, Cambridge, UK), MBP (SMI-99P, 1:3000, Covance/BioLegend, CA, USA). All nuclei were counterstained with 4’,6-diamidino-2phenylindole (DAPI, 1:1000) for 10 min in 20°C and mounted by Hydromount (National Diagnostics, Atlanta, USA) with 22 x 50 cm coverslips. Slides were then visualized by an upright microscope equipped with Excelitas Tech X-Cite® 120Q fluorescence illuminator (BX53 with DP80 camera, Olympus, HKUST) or Nikon Eclipse Ti2-E Fluorescence Imaging System (University Research Facility in Life Sciences, PolyU).

Images were taken using two parameters: stitched whole brain and 20x magnified regions. Whole brain imaging was done with 20x magnification (2424 pixels x 2424 pixels) and 1% blending as optimized by Nikon Eclipse Ti2-E Fluorescence Imaging System with a LED light source. Wavelengths of channels used were 365 nm for DAPI at 5% intensity and 20 ms exposure, 457.5 nm for FITC at 50% intensity and 200ms exposure, 610 nm for mCherry at 50% intensity and 200ms exposure, and 710 nm for Cy5 at 50% intensity and 200ms exposure. Regions of interests (frontal cortex, parietal cortex, occipital cortex, genu, isthmus, splenium, and hippocampus) were then manually focused to initiate automatic imaging and stitching of the whole brain with an average of 60 stitched images equating to an average cortical length of 7 mm with CFI Plan Apo 20×/0.75 Dry objective. Single region images (850 μm x 850 μm) were taken with the same 20x magnification. Regions of interest are duplicated with the seven regions used to focus.

2.12 Quantitative Analysis

Cellular quantifications of fluorescent immunohistochemistry were performed by manual counting while chromogenic immunohistochemistry by automated analysis using QuPath (291). Each region of interest (anterior cingulate, motor cortex, somatosensory cortex, genu, cinglum, external capsule, thalamus, anterior commissure, and septohippocampal nuclei) was manually drawn out using the polygon function. Analysed cerebral regions were chosen to correlate with human findings in APOE4 isoform patients by Dr. Henry Mak (292). Since APOE4 is the greatest genetic risk factor for sporadic Alzheimer's, we proposed that the anterior cingulate (293), motor cortex (294), somatosensory cortex (295, 296), corpus callosum (297, 298), and hippocampus (299, 300, 301) seen in humans would be translated with the most affected regions in the Alzheimer's transgenic mice. Cell detection of haematoxylin optical density was done with a pixel size of 0.5 μm. Nuclear parameters were set as the following: background radius of 8 μm, median filter radius of 0 μm, sigma of 0 μm, minimum area of 10 μm^2, and maximum area of 400 μm^2. The threshold of the DAB intensity was set at 0.1 with a max background intensity of 2 and cell expansion of 5 μm.

2.13 Western Blotting

Snap frozen brain tissue (left hemispheres) were defrosted on ice and dissected with a stereo microscope into cortex, hippocampus, WM, and cerebellum. Each portion was then pulverized in a dounce homogenizer with PBS and separated into two solutions: one for protein analysis and one for RNA extraction. For protein analysis, appropriate amounts of RIPA lysis buffer with PhosphoSTOP and Protease Inhibitor were added and shaken at 4°C for 1 h. Protein solutions were then stored in -80°C until usage.

After preparation, protein samples were analysed for protein concentrations per each sample. Samples were centrifuged at 4°C at 10,000G for 20 m. The supernatant was extracted as the cytoplasmic fraction while keeping the remaining precipitate as nucleic fraction stored in -80°C. Each cytoplasmic fraction was then diluted 1:40 or 1:50 against Bio-Rad protein assay (5000002, Hercules, US) to standardize protein concentration to 25 to 30 µg per sample using Milli-Q water and 6x loading dye with 5% beta-mercaptoethanol.

Electrophoresis of protein samples (20 µL) were done using 1.5 mm thick sodium dodecyl sulfate–polyacrylamide gel electrophoresis (SDS-PAGE) gels with Precision Plus Protein Dual Color Standards (1610374, Hercules, US). Resolving gel percentages were determined by the size of desired protein while stacking gel percentages were kept at 5%. All gels were run on Mini-PROTEAN Tetra Vertical Electrophoresis Cell with PowerPac Basic Power Supply (Bio-Rad) at 100 V for 30 min before increasing voltage to 120 V for 60 min. Gels were then removed and placed on methanol-exposed polyvinylidene fluoride (PVDF) membrane to be transferred in Trans-Blot Turbo Transfer System (Bio-Rad) at 25 V and 1.0 A for 1 hr. After transfer of protein from gel to membrane, each membrane was blocked with 4 mL of 5% non-fat milk for 30 min on a lab tube roller and incubated with appropriate primary antibodies overnight in 20°C. All antibodies include the following: β-Amyloid, 1-16 Antibody (1:000, Clone 6E10, N-terminal, a.a. 1-16, human specific only, 803014 BioLegend, CA, USA), MOG (1:1000, MAB5680, Millipore, CA, USA), MAG (MAB1567, 1:3000, Millipore, CA, USA), MBP (SMI-99P, 1:3000, Covance/BioLegend, CA, USA), GAPDH (ab8245, 1:10000, Abcam, Cambridge,

UK). Horseradish peroxidase conjugated secondary antibodies were then incubated for 1 h in 20°C before visualized with Forte (Millipore, Immobilon Forte Western HRP Substrate, WBLUF0500) or Dura (SuperSignal™ West Dura Extended Duration Substrate, 34075, Thermo Scientific) enhanced chemiluminescence for 5 m and imaged in ChemiDoc™ MP Imaging System (Bio-Rad). Analysis of western blots were done using ImageJ (302). Intensities of each band were measured for area under curve of the associated peaks. All intensity levels were normalized with housekeeping gene, GAPDH.

2.14 Statistical Analysis

All statistical analysis were done on GraphPad Prism 9 (version 9.5.0., San Diego, US). Two-way analysis of variance (ANOVA) was performed on all comparisons due to each investigation having two independent variables (303). The Tukey post-hoc multiple comparison test was performed to minimalize Type I error due to differing sample size (304, 305, 306, 307, 308). All data in graphs are expressed as mean ± standard error of mean (SEM) with statistical significance set at $p \leq 0.05$. Global changes in ANOVA refers to the effect of the proposed variable on the results, exclusive of trend. Outlier test was done on all cohorts to exclude outlying values. For the outlier test, quartiles 1 and 3 were found individually per genotype and age group. The lower and upper limits for indicating the outlier is calculated by subtraction from quartile 1 and addition of quartile 3, respectively, with 1.5 times the interquartile range.

Stratified randomisation was done for the choice of mouse for treatment groups. Since genotype is a covariate that must be maintained, we randomised the choice of mice once their respective genotypes were confirmed. Confounders were minimized by maintaining consistence in the location of treatment. However, 12 of the wildtypes and R1.40 mice were treated in HKUST and 22 of the wildtypes and APP/PS1 mice were treated in room Y1431 in PolyU. Regarding blinding, after radiological and histological acquisition, sections were annotated for the regions of interest. Annotations for brain regions were blindly done with no knowledge of genotype nor treatment groups.

3.0 Demyelination accelerate amyloid pathology in transgenic mouse models

3.1 Experimental Design

Our central hypothesis proposes that myelin loss triggered by the APOE4 isoform could initiated or accelerate Alzheimer's disease. This proposal is separated into two sections to answer this question. Our first proposal is that myelin loss accelerates AD pathology. The first aim we had was to show that demyelination or the reduction in myelin would affect amyloid plaque deposition, the hallmark of Alzheimer's. By employing young mice between 3 and 4 months old that were predisposed for amyloid plaques and treating them with cuprizone, a demyelinating treatment, we radiologically and histologically observed for changes in oligodendrocytes, myelin, and amyloid plaques to understand if the genetics or treatment would affect these bodies. As we observed increased expression of the amyloid protein in the brain with cuprizone, we then aimed to see if APOE4, the greatest genetic risk factor of sporadic Alzheimer's, would create similar effects. Our second hypothesis is APOE4 accelerates myelin/OL loss. As APOE is a lipid carrier within the brain, we proposed that its normal functions are impaired, leading to the inability of oligodendrocytes to maintain or create myelin and leading to the previous result of increased amyloid. Altogether, the reduced myelin would increase amyloid aggregations and initiate the symptoms of Alzheimer's.

One of the neuropathological hallmarks of AD is the appearance of amyloid plaques in the brain. While the aging population intrinsically develop these plaques, AD brains show a heavier burden of the protein aggregations when compared to a healthy patient of the same age. As multiple sclerosis patients undergo demyelination in conjunction with cognitive impairment similarly to AD, we hypothesize that a significant loss of myelin may accelerate plaque deposition, and, ultimately, initiate the cascade of pathological events of AD. As the sole producer of myelin, OLs are hypothesized to be affected by the toxicity of cuprizone and reduce in numbers due to an accumulation of DNA double strand breaks (309). To investigate this hypothesis, transgenic mice predisposed for amyloid plaque deposition were employed: (a) the R1.40 mice with the overexpression of APPSwe mutation of six to eight copies and (b) the APP/PS1 mice with both the overexpression of APPSwe mutation and the presenilin-1 mutated

gene responsible for amyloid cleavage. The choice of using both R1.40 and APP/PS1 mice is to study the effects of demyelination during different levels of amyloidosis. While R1.40 exhibit diffuse amyloid plaques at 14 months due to its mutation only in the APP gene (263), APP/PS1 exhibit plaques as early as 6 months as it contains both mutations of the APP and PS1 genes (265). By employing both genotypes at approximately the same age, we may study the effects of demyelination dependent of proximity to detectable amyloidosis. The mutation in R1.40 promotes the increase in amyloid burden without influencing the amyloid pathways (310). In contrast the extra PS1 mutation in APP/PS1 promotes the amyloidogenic pathway as it results in a partial loss of function in the gamma secretase, an enzyme making the cleavage to produce amyloid-beta, resulting in an accumulation of the amyloid-beta 42 peptide (311, 312, 313). Additionally, cognitive impairments correlating to amyloid deposition are seen by 21 months in R1.40 and 9 months in APP/PS1 (314). Both mice cohorts were subjected to 4 weeks of cuprizone treatment, an acute demyelinating diet before subjection to memory test (Y-maze), radiological assessment with MRI, and cellular and protein analysis. Results were collected to analyse the cognitive function, axonal and myelin integrity, and cellular changes, respectively.

Amyloid plaque deposition is the hallmark of Alzheimer's disease. The cause of such accumulations is still unknown, but its appearance is correlated with neurodegeneration such as neuronal loss, myelin loss, and cognitive decline. However, one of the first signs of neurodegeneration is myelin loss seen as early as 35 years old (83). Indeed, the loss of myelin is random among the population similarly to the onset of Alzheimer's. Recent research supported this theory by showing the increase of amyloid in a demyelinating mice model (315). As such, we propose that more severe myelin loss could contribute to the onset of Alzheimer's by affecting amyloid deposition and that we can utilise non-invasive MRI for early detection of myelin change to analyse the risk of Alzheimer's.

3.2 Effect of APP on weight

The mass of all mice was weighed before sacrifice to investigate physical manifestations of either genotypic or dietary differences (Figure 10). First, strains with the control diet are compared. The WT weighs a mean of 28.1g. In comparison to WT, the R1.40, a transgenic model for the overexpression of

the APP gene, weighs 32.8g, a 15.4% increase (p=0.1819). However, the APP/PS1, a transgenic model for both the overexpression of the APP gene and mutation of the PS1 gene, weighs a mean of 24.9g, a 12.5% decrease compared to WT (p=0.1296). While neither comparison with WT yields significance, the comparison of R1.40 and APP/PS1 exhibits a 24.2% decrease in weight of the APP/PS1 (p=0.0025).

Investigation into a diet change to CPZ shows little developments of all three genotypes. While the WT maintains a mean weight of 29.6g, a minimal 4.2% increase (p=0.9437), R1.40 shows slight 8.7% decrease to 30.0g (p=0.8589), and APP/PS1 shows 9.8% increase to 28.0g (p=0.5606). Among the genotypes with CPZ, there is no significant differences in weight. Physically, the three genotypes of mice show minimal change in weights. Comparison of 3- and 4-month WT shows no significant difference between their ages, suggesting minimal weight changes within this month. As such, weight differences among genotypes represent a genotype-dependent change instead of age-dependent. According to weight and observed motor skills, the one-month difference between 3 and 4 months show no physiological difference. A rotary rod could provide a more detailed observation of the motor skills of the transgenic mice. While the R1.40 mice has not been tested with the rotary rod, the APP/PS1 strain has shown no motor skill deficits at all ages but significant cognitive deficits with age (316, 317).

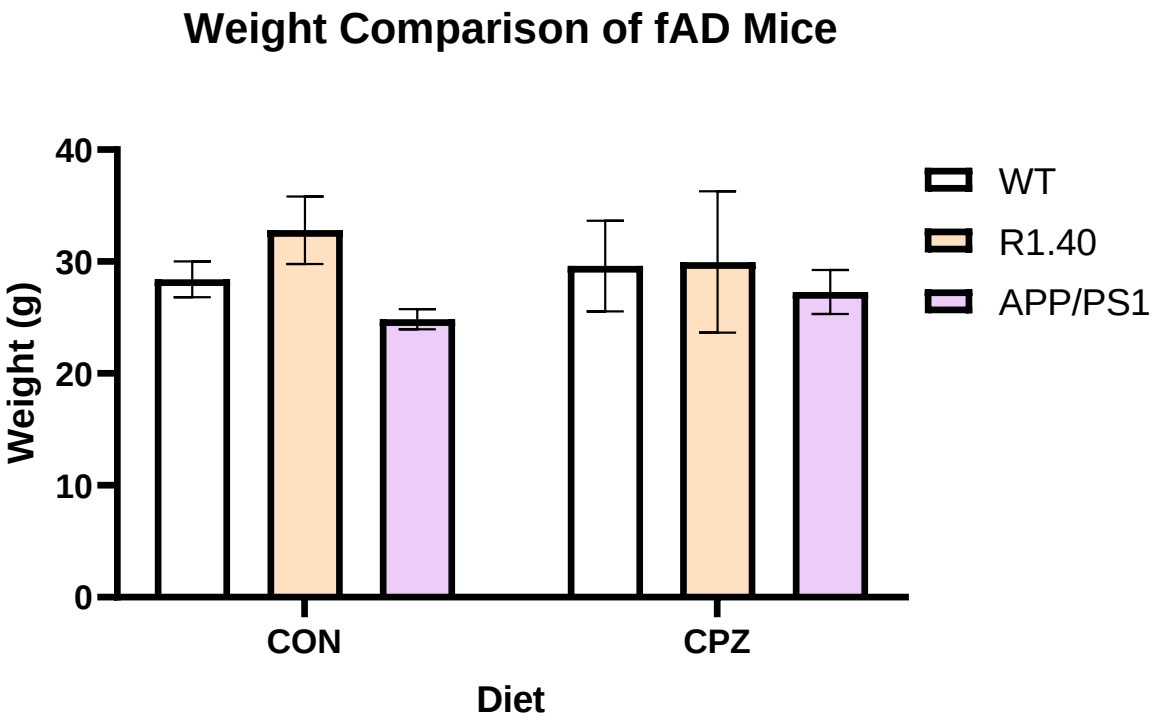

*Figure 10: Male mice treated with control or CPZ diets between the ages of 3 and 4 months were weighed before sacrifice. Significant differences of two-way ANOVA in weight among genotype and diet are indicated by asterisks: **p < 0.01. All values are of two-way ANOVA mean ± SEM. (WT-CON, n=8; WT-CPZ, n=8; R1.40-CON, n=3; R1.40-CPZ, n=3; APP/PS1-CON, n=7; APP/PS1-CPZ, n=7).*

3.3 DKI of fAD predisposed mice model

3.3.1 DKI comparisons of control diet mice

The fAD cohort of mice (R1.40 and APP/PS1) were treated with CPZ diet for 4 weeks before sacrificed. The intrinsic neurological diffusivity effects of each genotype were first observed under control diet to see the effects of amyloid-based mutations on white matter diffusivity. Genotypes undergoing control diets were first analysed among three grey matter regions (neocortex, anterior cingulate, and hippocampus) and three white matter regions (genu, external capsule, and cingulum) (Figure 11). Neocortical FA show gradual increase from the posterior to anterior brain. In addition, FA shows significant increases, especially in the anterior Bregma 2.70, in APP/PS1 compared to WT (+24.8%, p=0.0062) and R1.40 (+26.2%, p=0.0402) (Figure 12). Correspondingly, APP/PS1 continues to show anisotropic diffusivity throughout the neocortex with decreased RD against WT and with significance compared to R1.40 (Figure 18). However, AxD trends show decreased WT diffusivities compared to both fAD genotypes. Between R1.40 and APP/PS1, though, APP/PS1 exhibits continuous lowered AxD (Figure 24). This less diffusive status is further exemplified in MD with APP/PS1 showing significantly decreased values against R1.40 at Bregma -0.21 (-11.3%, p=0.0053) and Bregma 2.00 (-9.6%, p=0.025) (Figure 30). Further isolation of the neocortex into anterior cingulate shows no statistical significance. Observation of its Bregma-based graph shows abrupt drop in FA at Bregma -0.21 (Figure 13). Overall directional diffusivity against WT shows increased diffusivity of R1.40 but decreased diffusivity of APP/PS1. Similarly, to the neocortex, APP/PS1 shows lesser RD among genotypes with significance against R1.40 at Bregma -0.21 (-9.7%, p=0.024) and 2.00 (-10.9%, p=0.0126) (Figure 19). AxD continues to show decreased diffusivity of APP/PS1 comparatively to WT and R1.40 (Figure 25). This pattern is further emphasized in MD where global APP/PS1 values are consistently significantly elevated against R1.40. Investigation of the hippocampus, though, show no such changes (Figure 14, 20, 26, and 32). Grey matter analysis suggests the diffusive toll of the R1.40 APP mutation as more drastic than WT and APP/PS1. Surprisingly, the addition of the PS1 mutation seems to prevent more severe white matter diffusion as APP/PS1 consistently shows higher FA and lower directional diffusion. At this young age, white matter alterations, while undetectable in the hippocampus, has already surfaced in the fAD mice.

With such differences in the grey matter, the white matter was then analysed to find similar changes. First, WT anterior genu at Bregma 2.70 exhibited drastic FA reductions compared to R1.40 (-28.3%, p=0.0543) and significantly to APP/PS1 (-40.0%, p=0.0035) (Figure 15). The posterior genu showed no such difference with much of the FA values overlapping. In contrast, RD and AxD shows severe R1.40 reductions in Bregma -0.21 against WT (-23.8%, p<0.0001 and -28.8%, p<0.0001, respectively) and APP/PS1 (-22.6%, p<0.0001 and -24.2%, p<0.0001, respectively) (Figure 21 and 27). Altogether, in Bregma -0.21, effects of R1.40 mutations exhibited severe significant increases of MD while APP/PS1 mutations exhibited significant decreases, yet other Bregmas showed no such change (Figure 33). Continued analysis of the white matter tract showed no FA changes in the external capsule among genotypes. However, directional diffusivity analysis shows significant elevations of R1.40 diffusivities and significant reductions of APP/PS1 diffusivities in Bregma -1.35 and -0.21 (Figure 23). Likewise, this pattern is observed in the cingulum. Taken together, the intrinsic influences of fAD mutations suggest the adverse effects of the APP mutation. Interestingly, the Aβ-producing PS1 mutation shows protective influences on white matter diffusivity.

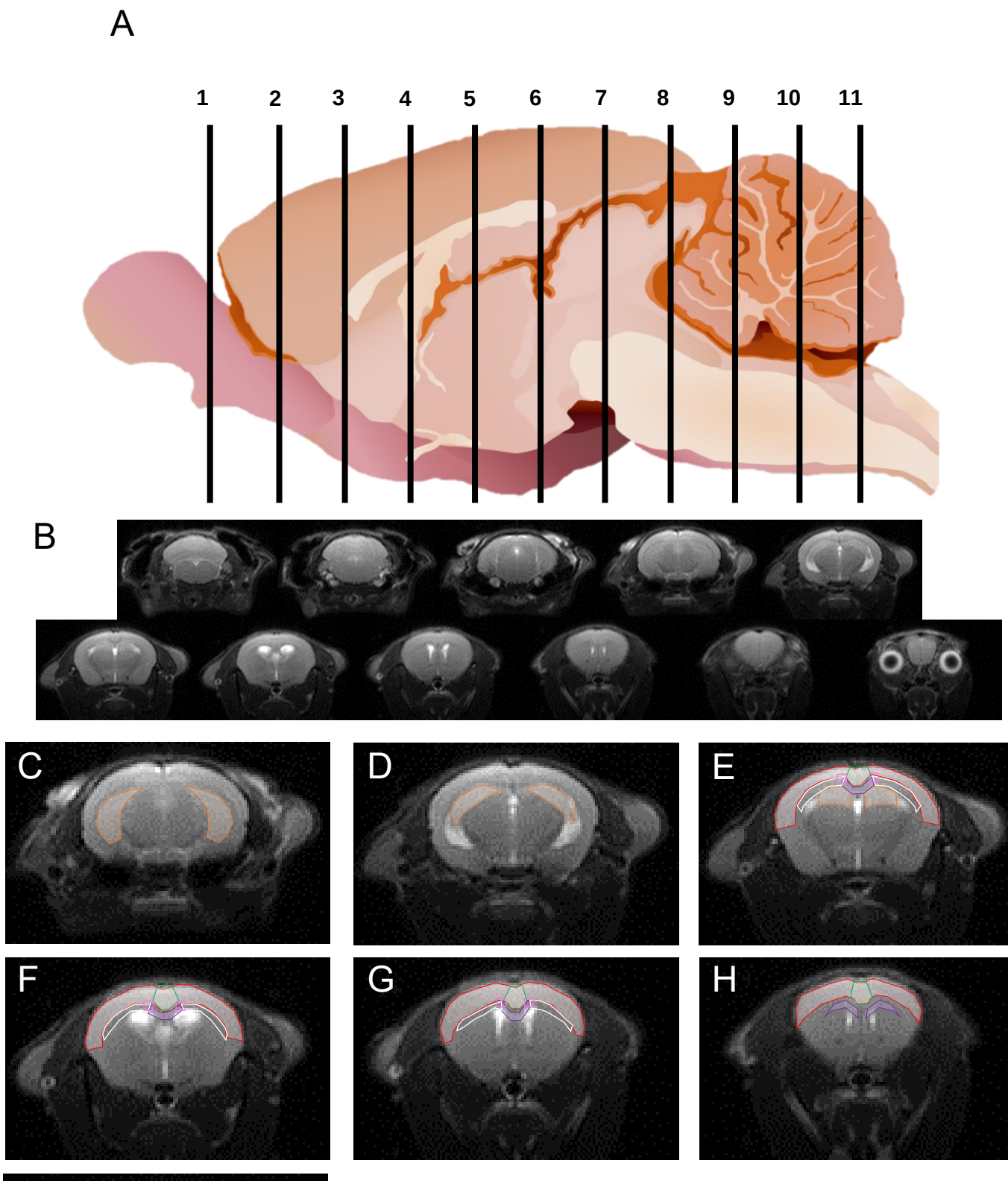

Figure 11: All mice brains were imaged coronally accordingly to their Bregmas, or coronal cross sections (A). Representatives of each Bregma is presented as T2-weighted images starting from the posterior (B). Regional analysis is segregated according to seven associated Bregmas (C-I) indicating ROIs: cortex (red), anterior cingulate (green), hippocampus (orange), genu (violet), external capsule (white), and cingulum (pink). Lines segregating the brain coronally were done in reference to the Allen mice brain atlas. Each line is an approximate 1mm apart with figures 11C-I showing MRI-acquired T2-weight images representing lines 8 to 1, respectively.

3.3.2 DKI comparisons of cuprizone diet mice

Mice were then treated with the acute demyelinating diet, CPZ, to see if genetic mutations would accentuate or minimize the effects of demyelination. Here, only the CPZ treated mice will be compared. FA comparisons of the neocortex show consistent increases from posterior to anterior brain with significant increase in Bregma 2.70 of APP/PS1 compared to WT (+27.7%, p=0.0189) (Figure 12). This difference is also found in RD (-11.3%, p=0.0022) (Figure 18). In the anterior cingulate, the drop in FA Bregma -0.21 is consistent with the control diet with minimal changes among modalities (Figure 13). In contrast, the hippocampus exhibits significant increases of R1.40 directional diffusivity in Bregma -1.35 and decreases of APP/PS1 (Figure 14). The effects of CPZ does not seem to drastically alter grey matter diffusivities in the young mice brain, but the more diffusive effects in the R1.40 is apparent.

Analysis of white matter tract shows similar effects of fAD mutations. In the genu, the posterior Bregmas -1.35 and -0.21 show increased APP/PS1 FA compared to R1.40 (+33.9%, p=0.0157) with minimal effects with WT. With R1.40, even though it does not yield significance, R1.40 shows substantial decrease of FA compared to WT in the posterior brain (-20.8%, p=0.0805) (Figure 15). Conversely, directional diffusivity values for APP/PS1, while comparable to WT, exhibits elevations against R1.40 especially in Bregma 0.80. Regarding the external capsule, the WT and R1.40 curves of RD, AxD, and MD are similar from Bregma -1.35 to -0.21 with the APP/PS1 maintaining lowered diffusivity (Figure 23, 29, and 33). In Bregma 0.80, R1.40 makes a sudden drop lower than both WT and APP/PS1, though yielding no significance (Figure 27). Further analysis of the cingulum shows insignificant diffusivity modalities. However, while directional diffusivities show positional increase from Bregma -1.35 to 0.80 in WT and APP/PS1 brains, R1.40 consistently exhibits an inverse “V,” having peaked values at -0.21 (Figure 28). White matter tract changes are not as apparent as ones found in the grey matter, but in both regions, APP/PS1 consistently shows anisotropic diffusivity with increased FAs and decreased RD, AxD, and MDs.

Independent investigations of diet suggest discernible changes of diet in intrinsic genetic alterations to brain diffusivity. Under both control and CPZ diets, the two fAD model mice exhibit polarized

influences. The R1.40 model, containing only the overexpressed APP mutation, consistently shows lower FA and increased RD, AxD, and MD when compared to both WT and APP/PS1. Nevertheless, the APP/PS1 model, containing both an overexpressed APP and PS1 mutation, show the opposite, increased FA and decreased RD, AxD, and MD when compared to WT and R1.40. In the control diet, these effects are more apparent in the grey matter, suggesting genotype-dependent changes could induce a considerable toll on the brain. The addition of CPZ, though, reduced the number of changes among genotypes even though in some regions this polarizing influence is still present. Next, independent genotypes will be analysed for differences based on diet to understand if individual genotypes would produce different diffusivities with different demyelination status.

3.3.3 DKI comparisons of WT mice

By evaluating the differences in diffusivity between control and CPZ diet in WT, the normal effects of CPZ on control mice would be realized to set the baseline of demyelination in transgenic mice. At first glance, there is a clear elevation of neocortical FA in CPZ treated WT among all Bregmas, specifically -0.21 (+33.3%, p=0.0661) and 0.80 (+24.1%, p=0.2194) (Figure 12). RD diet-based analysis shows 10.95% decrease in control diet compared to only 6.76% decrease in CPZ from Bregma -1.35 to 2.70 with no significance per Bregma (Figure 18). Similarly, AxD and MD show higher values in CPZ with no significance (Figure 24 and 30). Anterior cingulate values also show insignificant increases of both FA and directional diffusivities (Figure 13). Interestingly, in the hippocampus, there is widespread increase of FA across Bregmas with significance at -2.50 (+29.6%, p=0.04) (Figure 14). However, minimal differences are found in the other modalities. Grey matter shows an overall increase in FA and all diffusivities.

In the genu, there is a decrease in FA of both control and CPZ diet with overlapping values (Figure 15). At Bregma 0.80, directional diffusivities all show peak values of CPZ diet surpassing other Bregmas with RD showing significance (+11.6%, p=0.0456) (Figure 21). The external capsule in both control and CPZ diet shows a similar consistent FA increase from Bregma -1.35 to 0.80 (Figure 17). While insignificant, at Bregma -0.21, both treatments exhibited a peak across RD, AxD, and MD. Further

investigation into the white matter tract shows unchanged FA with overall elevated diffusivities in CPZ mice. Correspondingly, the white matter tract displays increased diffusivities across all regions comparable to grey matter.

3.3.4 DKI comparisons of R1.40 mice

R1.40 mice exhibited overall higher diffusivities when compared with WT and APP/PS1 in both control and CPZ diet. Interestingly, the influence of CPZ is unlike that of WT. Regarding grey matter, the neocortical FA of both treatments sees similar increases from posterior and anterior brain with a similar level as WT. However, R1.40 RD levels are noticeably higher compared to WT. Moreover, the effects of CPZ seems to reduce directional diffusivities in the R1.40 model. All neocortical diffusivity modalities show lower levels of diffusion in the CPZ mice, contrasting that of the WT (Figure 12, 18, 30). At the anterior cingulate, CPZ mice show both FA linear decrease from Bregma -1.35 to 2.00, contrasting that of the levelled WT FA, and overall decreased levels with significance at Bregma -0.21 (-27.2%, p=0.0169) (Figure 13). Likewise, RD, AxD, and MD values suggest lower diffusivities in CPZ mice (Figure 19, 25, and 31). In contrast, hippocampal FA, while unchanged, shows an increase in directional diffusivities (Figure 14). It seems the diffusivity of grey matter in R1.40 exhibits an inverse relationship to WT, having lower diffusivities across the neocortex and anterior cingulate while having increased diffusivities in the hippocampus, suggesting distinct mechanisms between these two grey matter regions.

However, regions of the white matter tract seem to react differently to CPZ. In the genu, while FA generally shows lowered values in CPZ, RD, AxD, and MD show decreased levels (Figure 15, 21, 27). Previously in WT, peaks in RD and AxD could be seen in Bregma 0.80. However, R1.40 mice of both diets exhibit these peaks at -0.21, instead. Specifically in AxD, Bregma -0.21 and 0.80 shows significant decreases of CPZ mice (-15.8%, p=0.0311; -17.4%, p=0.0257, respectively) (Figure 27). As such, MD shows a corresponding decrease at Bregma -0.21 (-14.4%, p=0.0456) (Figure 33).

3.3.5 DKI comparisons of APP/PS1 mice

APP/PS1 mice were previously shown to have higher FAs and lower RDs, AxDs, and MDs. Here, the effects of diet are analysed to understand of the APP and PS1 mutations would produce similar consequences as WT or R1.40. Neocortical FA follows identical increasing trend as WT and R1.40 with minimal differences between diet (Figure 12). Directional diffusivities all show overall elevated values in CPZ treated mice with significance in Bregma 0.80 (+8.2%, p=0.0455) (Figure 30). The anterior cingulate exhibits similar values in all modalities, but at Bregma -0.21, FA shows the same consistent sharp decrease as WT and R1.40 (Figure 13). Interestingly, the influence of CPZ in the hippocampus increased its diffusivities while keeping FA unchanged (Figure 14). This result is similar to R1.40 yet detracts from WT's unaltered diffusivity. APP/PS1 grey matter suggests increased diffusivity in the analysed cortical regions comparable to CPZ's effect on WT. However, the increase in hippocampus is comparable to R1.40. This difference continues to suggest hippocampus's separated mechanism from other grey matter regions.

Genu FA shows sharp significant decrease of CPZ mice at Bregma -0.21 (-23.9%, p=0.0021) (Figure 15). RD levels show similar peak of both control and CPZ diet with CPZ showing significant increase similar to WT at Bregma 0.80 (+13.9%, p=0.0067) (Figure 21). This peak is continuously expressed in AxD (+11.8%, p=0.0147) and MD (+12.9%, p=0.0021) (Figure 27 and 33). Regarding the external capsule and cingulum, neither FAs show significant differences between control and CPZ diet (Figure 16 and 17). Both regions exhibit significantly increased RD at Bregma 0.80 with external capsule showing an increase of 11.7% (p=0.0096) and cingulum of 12.1% (p=0.0214) (Figure 23). However, the cingulum is the only one showing increased AxD, also at Bregma 0.80 (+13.6%, p=0.0019) (Figure 28). MD, though, show elevated levels of both external capsule (+10.1%, p=0.0238) and cingulum (+12.8%, p=0.0011) (Figure 35 and 33). Interestingly, this pattern in the white matter tract regions parallel that of WT and differ from R1.40's elevated diffusivities at Bregma -0.21, suggesting the effects of CPZ may be region based depending on the genotype of the model.

The influence of CPZ, and ultimately, demyelination, seems to differ depending on amyloid-based gene mutation statuses. Investigation into WT and APP/PS1 shows that CPZ significantly elevates diffusivity in grey and white matter regions. Some regions, such as the neocortex and genu, are more susceptible to the diet change as seen with more significantly altered diffusivities while other regions, such as the anterior cingulate and external capsule, exhibit less changes. Even though CPZ does produce similar changes within genotypes, cross-type analyse does show overall higher FA and lower RD, AxD, and MD in APP/PS1, suggesting protective effects of the two mutations. However, the R1.40, harbouring only the overexpressed APP mutation, exhibits opposite trends compared to WT and APP/PS1. The R1.40 model treated with CPZ exhibits decreased diffusivities among all modalities. In addition, consistent sharp increases in diffusivities at Bregma -0.21 and 0.80 suggest possible vulnerabilities in these regions. Altogether, this analysis shows that the demyelinating effects of CPZ varies depending on genotype. As represented, it is possible that even though mutations of APP and PS1 may cause fAD, having both mutations at the same time may have a cancelling effect as this study shows the lesser diffusive APP/PS1 brain.

3.3.6 DKI comparisons of APP overexpression and PS1 control treatment mice

To further show the differing effects of the presence of the PS1 mutation, R1.40 and APP/PS1 mice with control diet will first be compared. FA and AxD show no significant changes within the three grey matter regions. As suggested previously, APP/PS1 exhibits significantly lower diffusivities in multiple Bregmas of the grey matter. In the white matter, while FA remains unchanged in all regions, directional diffusivity modalities show similar significant decreases of APP/PS1. In some regions, such as the genu, the MD decrease is as low as 58.1% ($p>0.0001$) at Bregma -0.21 (Figure 33). These alterations implicate that the overexpression of APP alone could drastically create a more diffusive white matter. The addition of the PS1 mutation may be beneficial towards preventing diffusive structures in the brain.

3.3.7 DKI comparisons of APP overexpression and PS1 cuprizone treatment mice

By changing the diet to CPZ, the diffusivity changes between R1.40 and APP/PS1 become less. Interestingly, the significant changes are no longer in both grey and white matter. The cortical regions

remain unchanged while in the hippocampus, RD and MD values at Bregma -1.35 show decreases of 16.6% (p=0.0088) and 17.4% (p=0.0059), respectively (Figure 20). In the white matter, both genotypes exhibit contrasting changes depending on the previously mentioned Bregmas, -0.21 and 0.80. The genu and cingulum exhibit significant changes while the external capsule remains consistent between genotypes (Figure 15). The CPZ diet does not seem to affect the diffusivities of R1.40 and APP/PS1 severely. Conversely, it is possible CPZ converges the diffusivity changes between APP and PS1 mutated mice.

The influence of the APP mutation alone seems to induce higher diffusivities without the need of the PS1 mutation nor demyelinating CPZ. Interestingly, the addition of PS1 seems to decrease diffusivity in the brain. In addition, Bregma -0.21 and 0.80 seems to be more vulnerable to both genotypic and diet-based changes, even against WT. While there are Bregma-based differences, this does not indicate different forms of myelin as they still represent the same cerebral region.

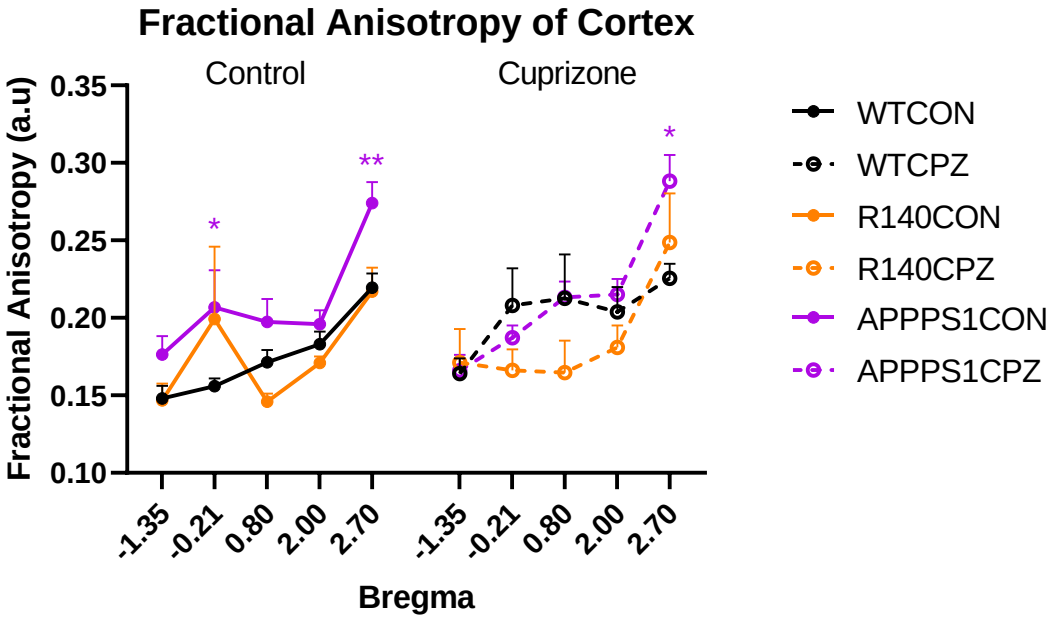

*Figure 12: The cortical FA of genotypic and diet groups were analysed for changes in anisotropic diffusion of water of white matter in the mice brain. Genotypes are individually grouped to observe the effect of diet. All values are of two-way ANOVA mean ± SEM. Statistically significant stars are color-coded according to transgenic genotype against WT. *p<0.05; **p<0.01. (WT-CON, n=8; WT-CPZ, n=8; R1.40-CON, n=3; R1.40-CPZ, n=3; APP/PS1-CON, n=7; APP/PS1-CPZ, n=7).*

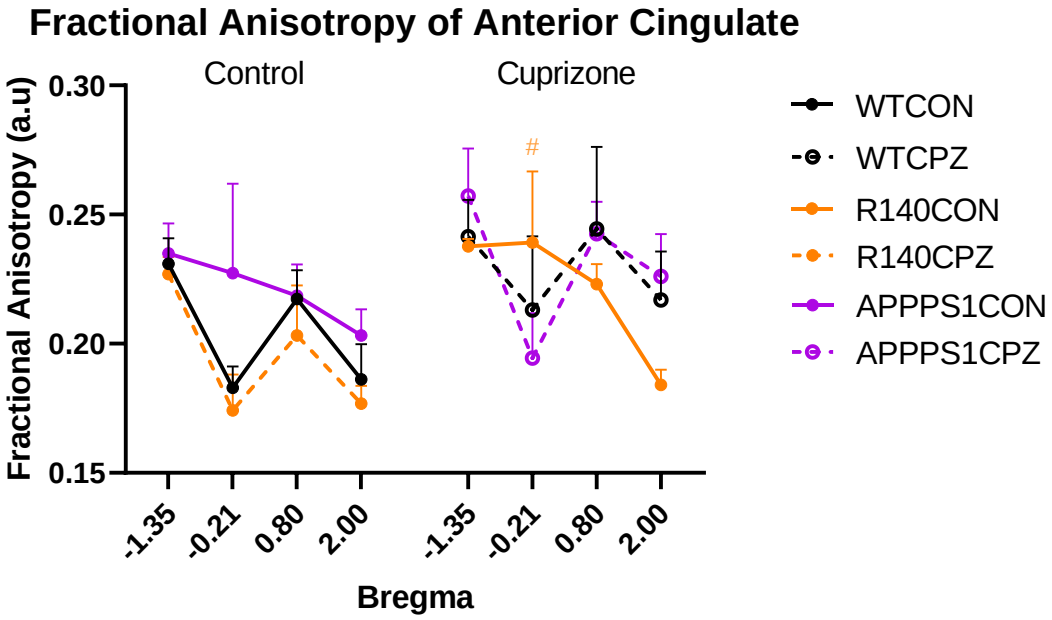

Figure 13: The anterior cingulate FA of genotypic and diet groups were analysed for changes in anisotropic diffusion of water of white matter in the mice brain. Genotypes are individually grouped to observe the effect of diet. All values are of two-way ANOVA mean ± SEM. Statistically significant hashes are color-coded according to CPZ change against CON. #p<0.05. (WT-CON, n=8; WT-CPZ, n=8; R1.40-CON, n=3; R1.40-CPZ, n=3; APP/PS1-CON, n=7; APP/PS1-CPZ, n=7).

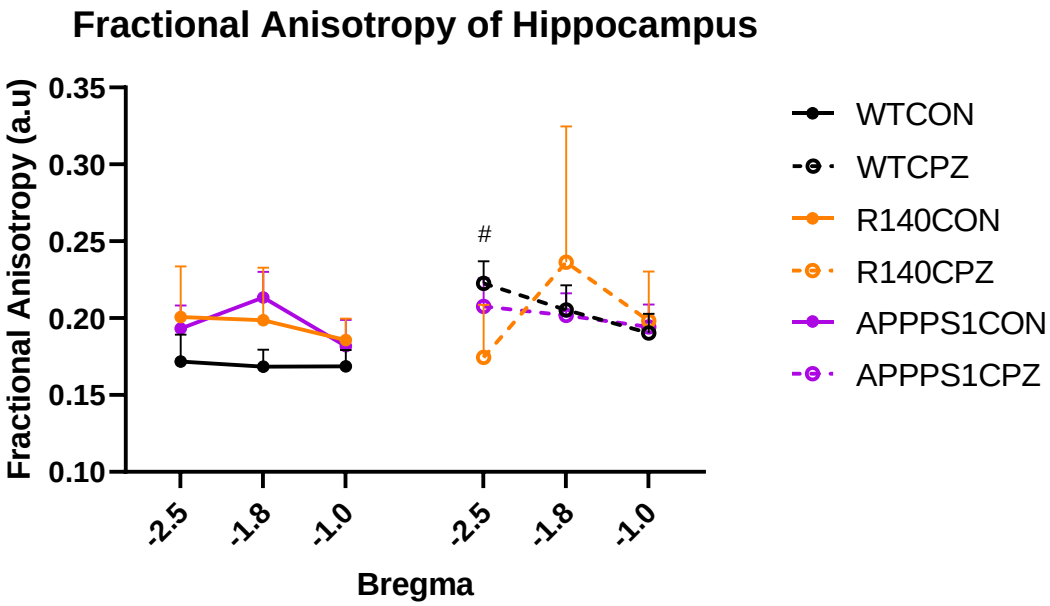

Figure 14: The hippocampal FA of genotypic and diet groups were analysed for changes in anisotropic diffusion of water of white matter in the mice brain. Genotypes are individually grouped to observe the effect of diet. All values are of two-way ANOVA mean ± SEM. Statistically significant hashes are color-coded according to CPZ change against CON. #p<0.05. (WT-CON, n=8; WT-CPZ, n=8; R1.40-CON, n=3; R1.40-CPZ, n=3; APP/PS1-CON, n=7; APP/PS1-CPZ, n=7).

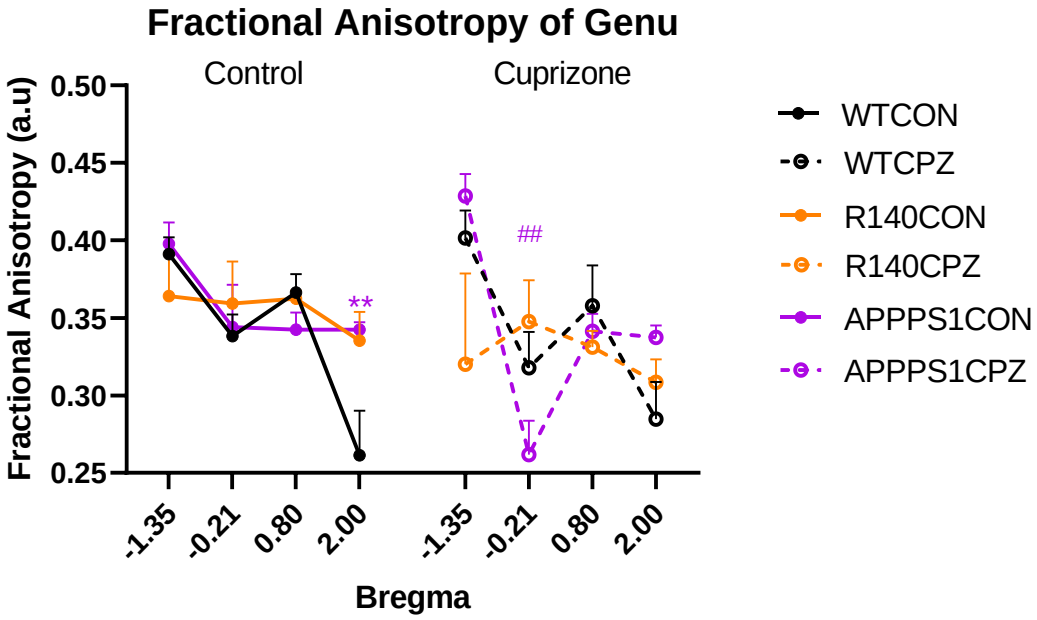

*Figure 15: The genu FA of genotypic and diet groups were analysed for changes in anisotropic diffusion of water of white matter in the mice brain. Genotypes are individually grouped to observe the effect of diet. All values are of two-way ANOVA mean ± SEM. Statistically significant stars are color-coded according to transgenic genotype against WT. **p<0.01. Statistically significant hashes are color-coded according to CPZ change against CON. ##p<0.01. (WT-CON, n=8; WT-CPZ, n=8; R1.40-CON, n=3; R1.40-CPZ, n=3; APP/PS1-CON, n=7; APP/PS1-CPZ, n=7).*

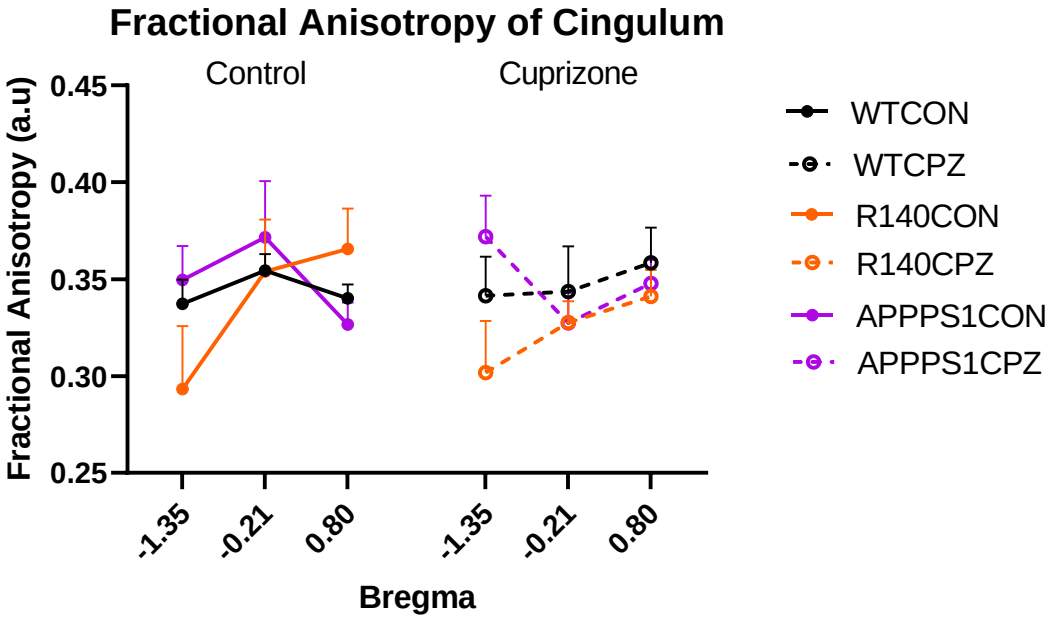

Figure 16: The cingulum FA of genotypic and diet groups were analysed for changes in anisotropic diffusion of water of white matter in the mice brain. Genotypes are individually grouped to observe the effect of diet. All values are of two-way ANOVA mean ± SEM. (WT-CON, n=8; WT-CPZ, n=8; R1.40-CON, n=3; R1.40-CPZ, n=3; APP/PS1-CON, n=7; APP/PS1-CPZ, n=7).

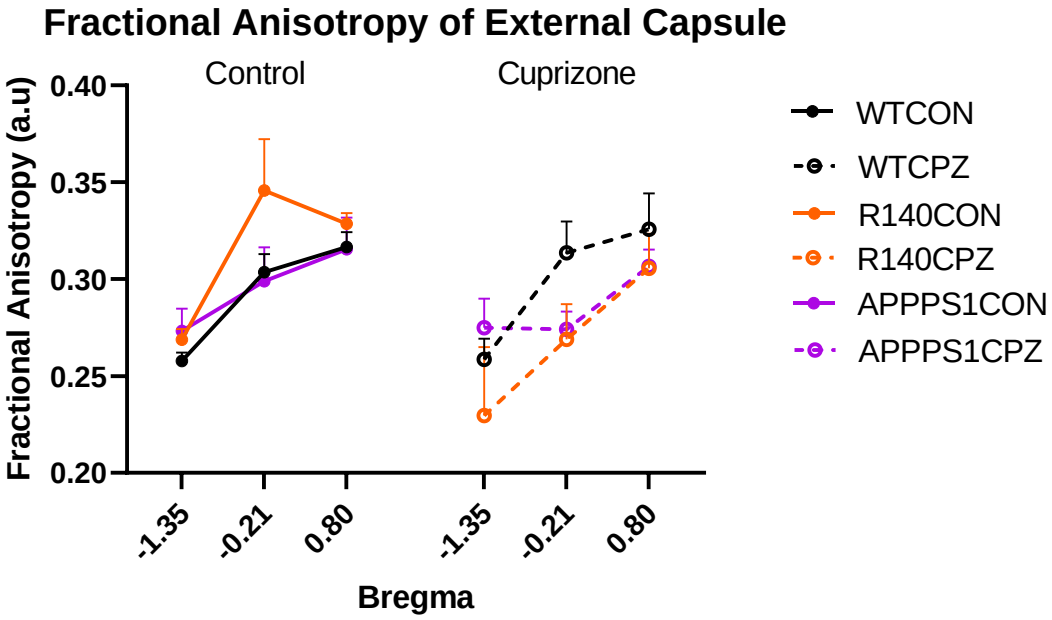

Figure 17: The external capsule FA of genotypic and diet groups were analysed for changes in anisotropic diffusion of water of white matter in the mice brain. Genotypes are individually grouped to observe the effect of diet. All values are of two-way ANOVA mean ± SEM. (WT-CON, n=8; WT-CPZ, n=8; R1.40-CON, n=3; R1.40-CPZ, n=3; APP/PS1-CON, n=7; APP/PS1-CPZ, n=7).

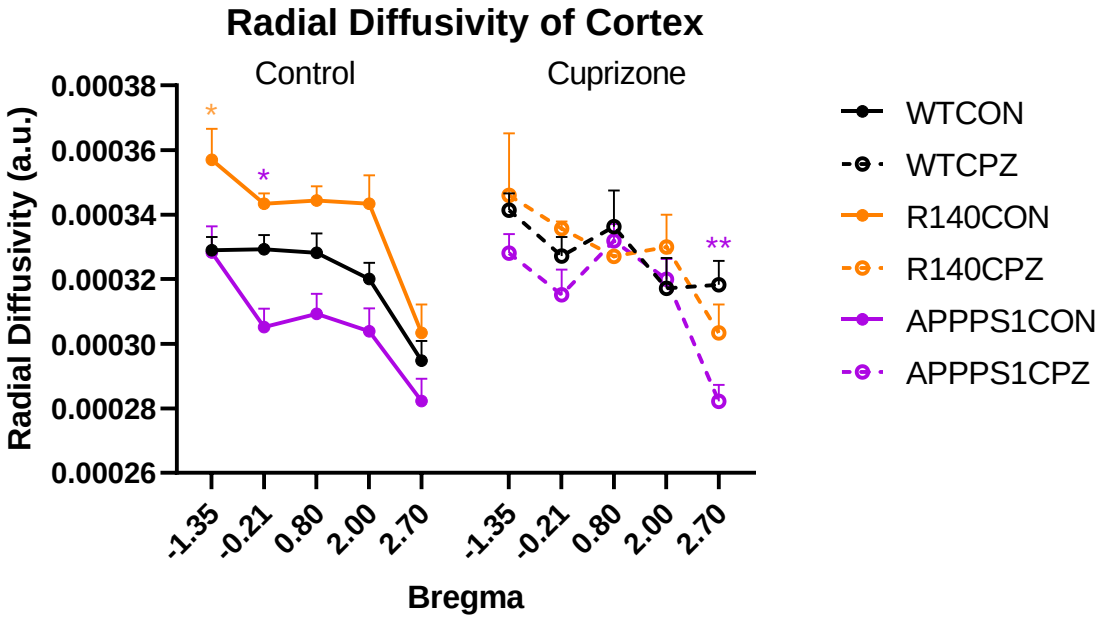

*Figure 18: The cortical RD of genotypic and diet groups were analysed for changes in perpendicular diffusion of water of white matter in the mice brain. Genotypes are individually grouped to observe the effect of diet. All values are of two-way ANOVA mean ± SEM. Statistically significant stars are color-coded according to transgenic genotype against WT. *p<0.05; **p<0.01. (WT-CON, n=8; WT-CPZ, n=8; R1.40-CON, n=3; R1.40-CPZ, n=3; APP/PS1-CON, n=7; APP/PS1-CPZ, n=7).*

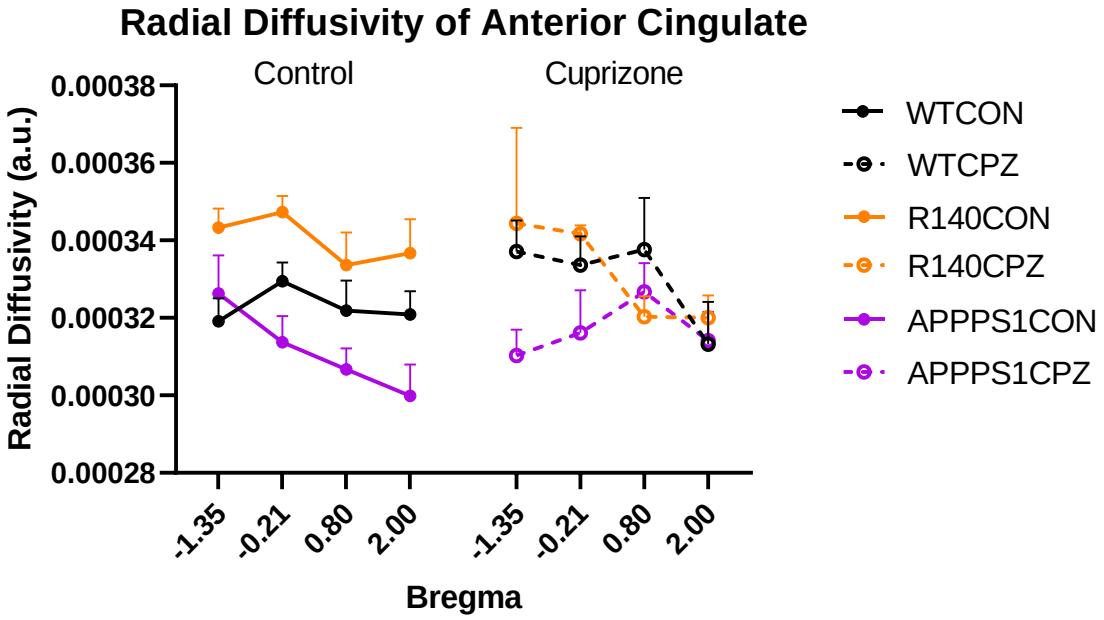

Figure 19: The anterior cingulate RD of genotypic and diet groups were analysed for changes in perpendicular diffusion of water of white matter in the mice brain. Genotypes are individually grouped to observe the effect of diet. All values are of two-way ANOVA mean ± SEM. (WT-CON, n=8; WT-CPZ, n=8; R1.40-CON, n=3; R1.40-CPZ, n=3; APP/PS1-CON, n=7; APP/PS1-CPZ, n=7).

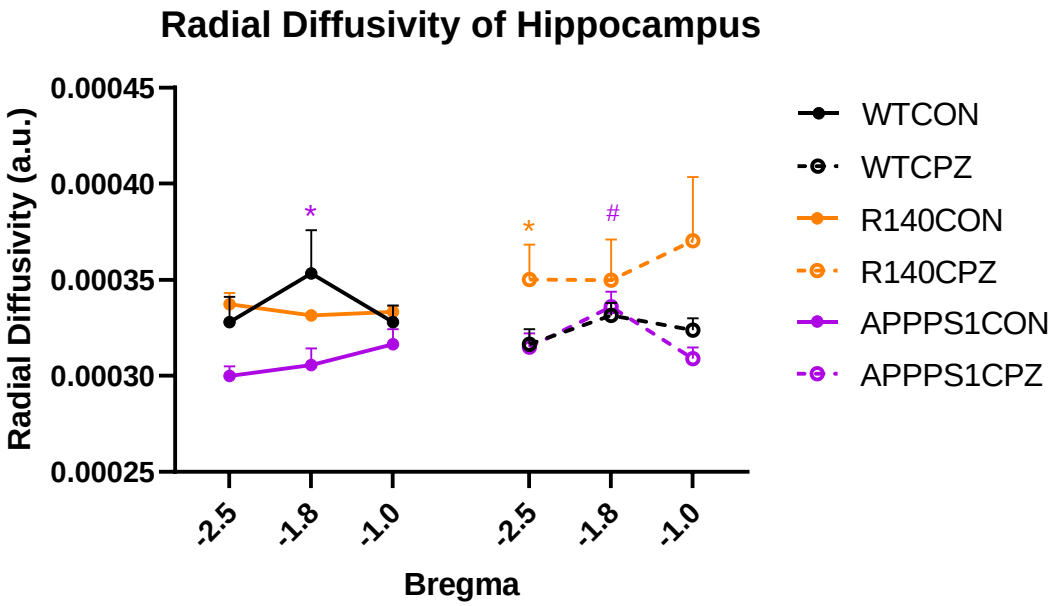

*Figure 20: The hippocampal AxD of genotypic and diet groups were analysed for changes in axial diffusion of water of white matter in the mice brain. Genotypes are individually grouped to observe the effect of diet. All values are of two-way ANOVA mean ± SEM. Statistically significant stars are color-coded according to transgenic genotype against WT. *p<0.05. Statistically significant hashes are color-coded according to CPZ change against CON. #p<0.05. (WT-CON, n=8; WT-CPZ, n=8; R1.40-CON, n=3; R1.40-CPZ, n=3; APP/PS1-CON, n=7; APP/PS1-CPZ, n=7).*

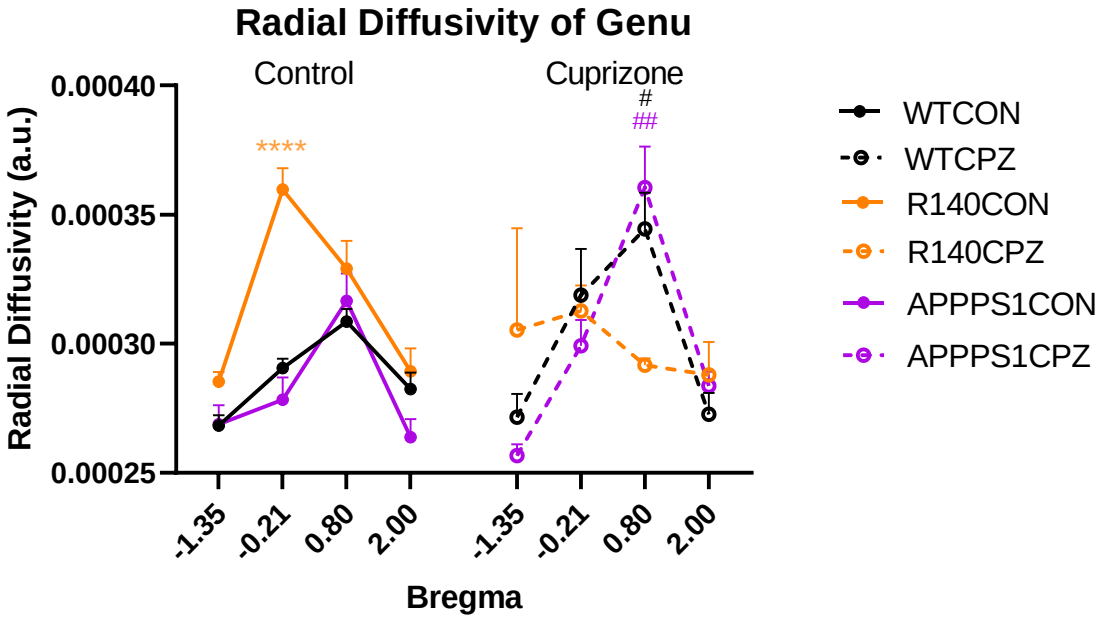

*Figure 21: The genu RD of genotypic and diet groups were analysed for changes in perpendicular diffusion of water of white matter in the mice brain. Genotypes are individually grouped to observe the effect of diet. All values are of two-way ANOVA mean ± SEM. Statistically significant stars are color-coded according to transgenic genotype against WT. ****p<0.0001. Statistically significant hashes are color-coded according to CPZ change against CON. #p<0.05; ##p<0.01. (WT-CON, n=8; WT-CPZ, n=8; R1.40-CON, n=3; R1.40-CPZ, n=3; APP/PS1-CON, n=7; APP/PS1-CPZ, n=7).*

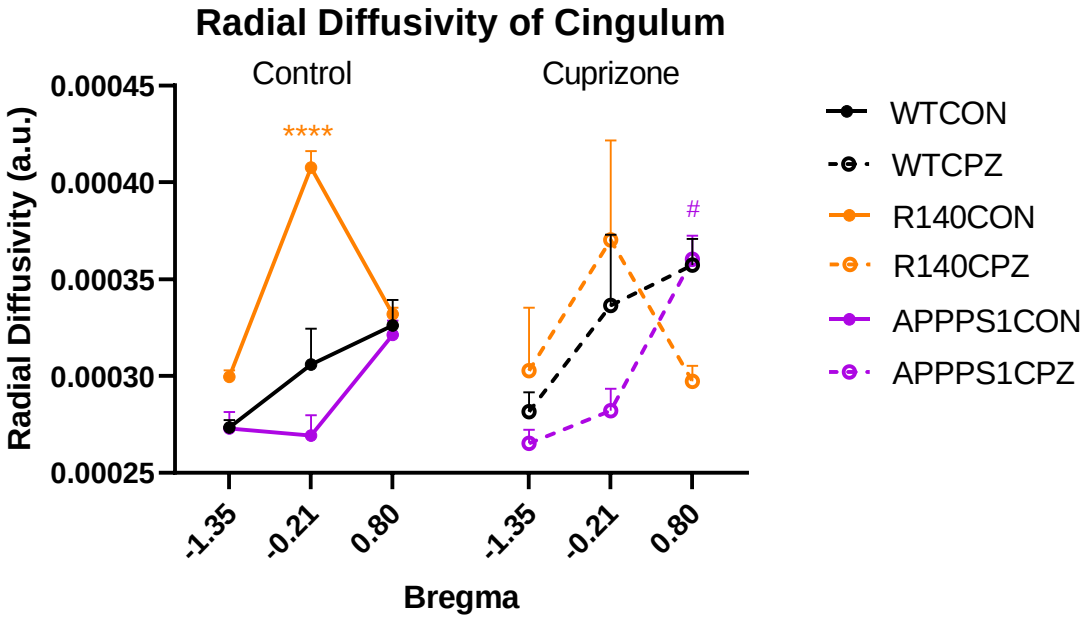

*Figure 22: The cingulum RD of genotypic and diet groups were analysed for changes in perpendicular diffusion of water of white matter in the mice brain. Genotypes are individually grouped to observe the effect of diet. All values are of two-way ANOVA mean ± SEM. Statistically significant stars are color-coded according to transgenic genotype against WT. ****p<0.0001. Statistically significant hashes are color-coded according to CPZ change against CON. #p<0.05. (WT-CON, n=8; WT-CPZ, n=8; R1.40-CON, n=3; R1.40-CPZ, n=3; APP/PS1-CON, n=7; APP/PS1-CPZ, n=7).*

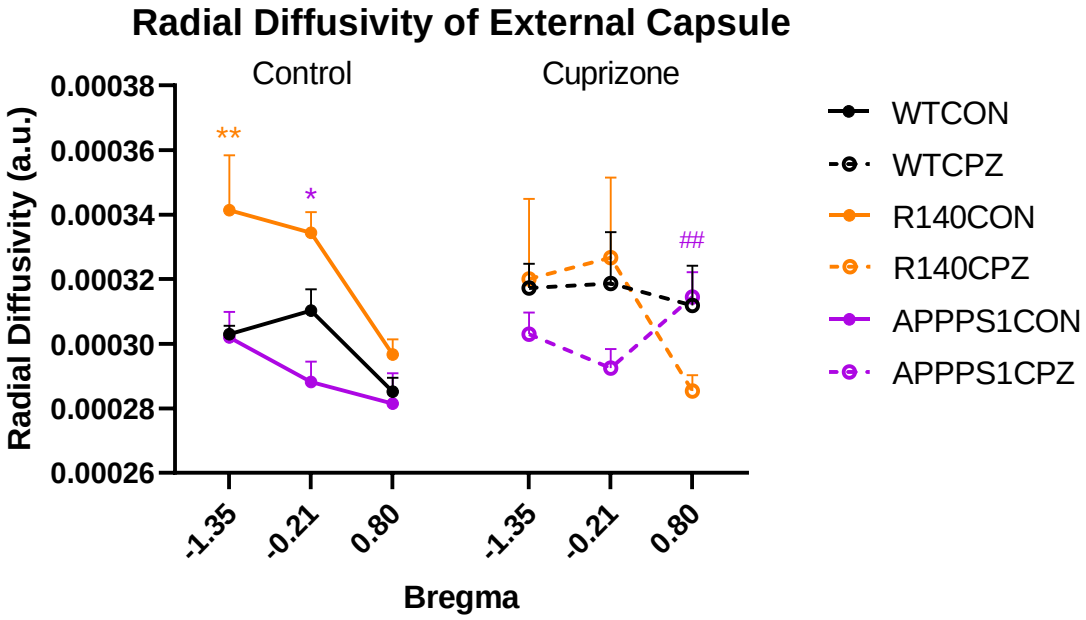

*Figure 23: The external capsule RD of genotypic and diet groups were analysed for changes in perpendicular diffusion of water of white matter in the mice brain. Genotypes are individually grouped to observe the effect of diet. All values are of two-way ANOVA mean ± SEM. Statistically significant stars are color-coded according to transgenic genotype against WT. *p<0.05; **p<0.01. Statistically significant hashes are color-coded according to CPZ change against CON. ##p<0.01. (WT-CON, n=8; WT-CPZ, n=8; R1.40-CON, n=3; R1.40-CPZ, n=3; APP/PS1-CON, n=7; APP/PS1-CPZ, n=7).*

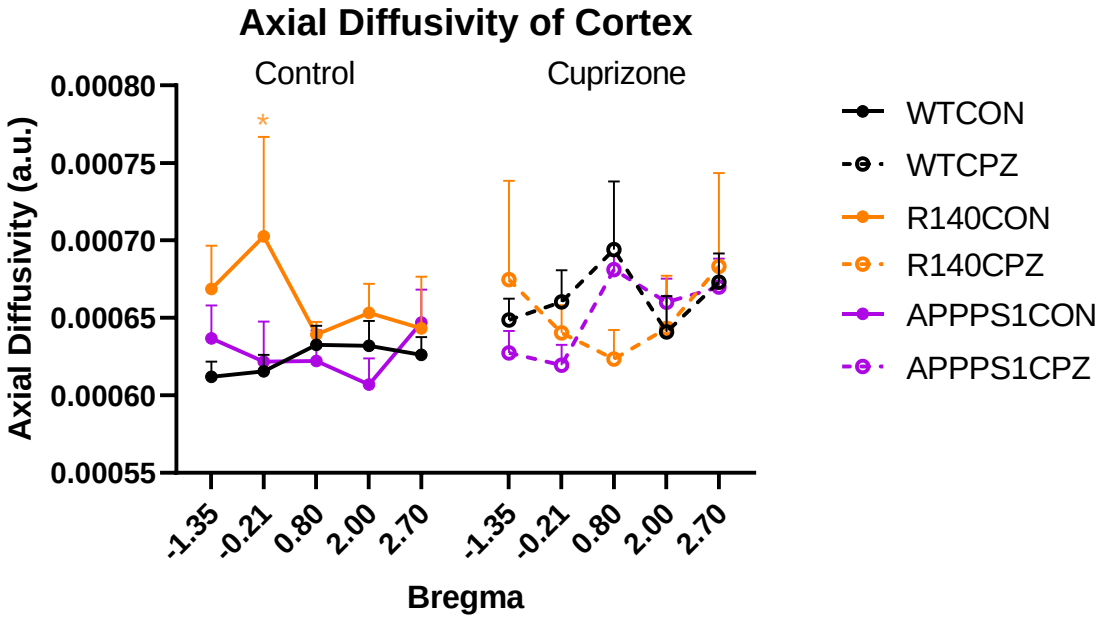

*Figure 24: The cortical AxD of genotypic and diet groups were analysed for changes in axial diffusion of water of white matter in the mice brain. Genotypes are individually grouped to observe the effect of diet. All values are of two-way ANOVA mean ± SEM. Statistically significant stars are color-coded according to transgenic genotype against WT. *p<0.05. (WT-CON, n=8; WT-CPZ, n=8; R1.40-CON, n=3; R1.40-CPZ, n=3; APP/PS1-CON, n=7; APP/PS1-CPZ, n=7).*

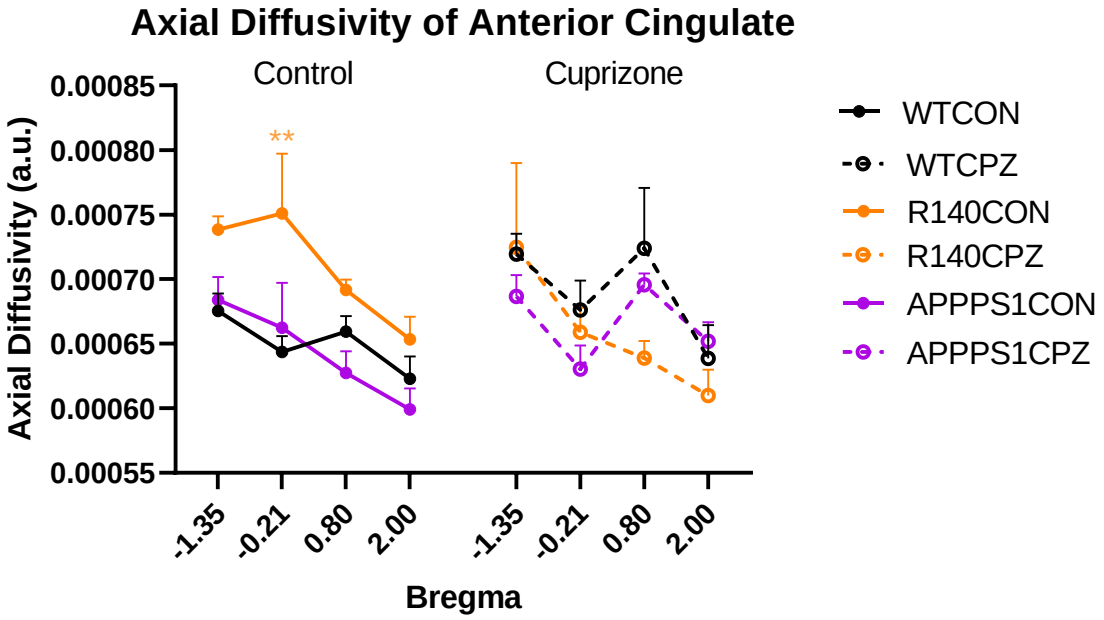

*Figure 25: The anterior cingulate AxD of genotypic and diet groups were analysed for changes in axial diffusion of water of white matter in the mice brain. Genotypes are individually grouped to observe the effect of diet. All values are of two-way ANOVA mean ± SEM. Statistically significant stars are color-coded according to transgenic genotype against WT. **p<0.01. (WT-CON, n=8; WT-CPZ, n=8; R1.40-CON, n=3; R1.40-CPZ, n=3; APP/PS1-CON, n=7; APP/PS1-CPZ, n=7).*

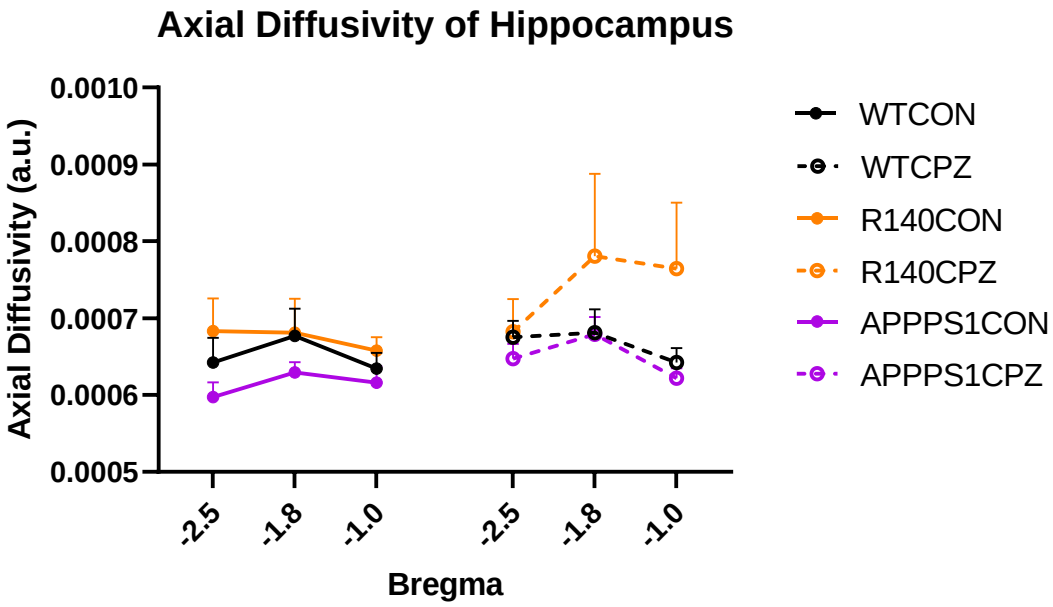

Figure 26: The hippocampal RD of genotypic and diet groups were analysed for changes in perpendicular diffusion of water of white matter in the mice brain. Genotypes are individually grouped to observe the effect of diet. All values are of two-way ANOVA mean ± SEM. (WT-CON, n=8; WT-CPZ, n=8; R1.40-CON, n=3; R1.40-CPZ, n=3; APP/PS1-CON, n=7; APP/PS1-CPZ, n=7).

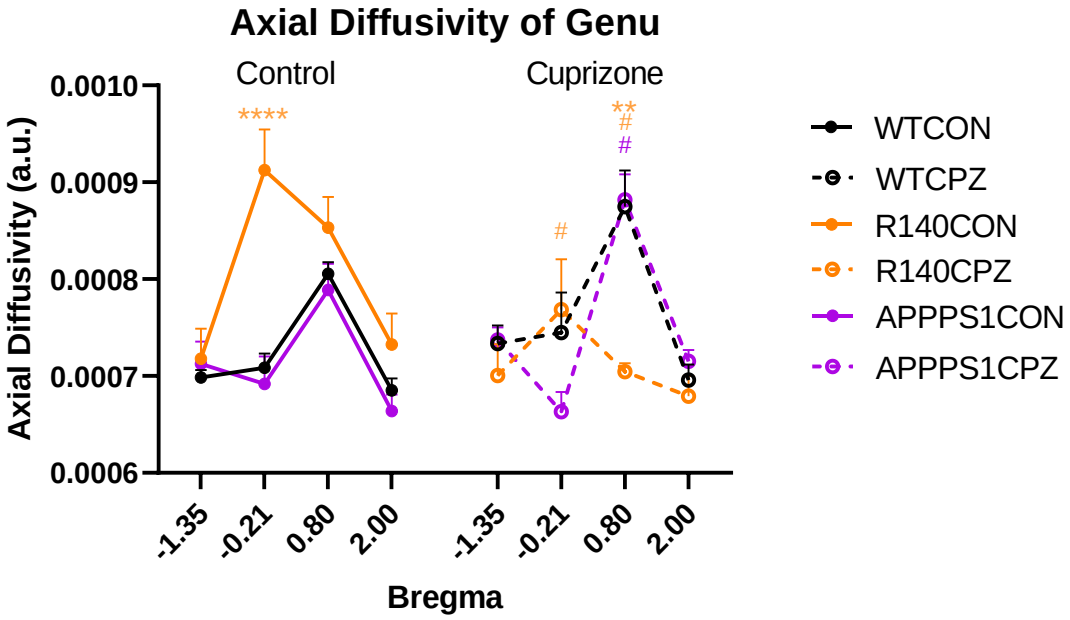

*Figure 27: The genu AxD of genotypic and diet groups were analysed for changes in axial diffusion of water of white matter in the mice brain. Genotypes are individually grouped to observe the effect of diet. All values are of two-way ANOVA mean ± SEM. Statistically significant stars are color-coded according to transgenic genotype against WT. **p<0.01; ****p<0.0001. Statistically significant hashes are color-coded according to CPZ change against CON. #p<0.05. (WT-CON, n=8; WT-CPZ, n=8; R1.40-CON, n=3; R1.40-CPZ, n=3; APP/PS1-CON, n=7; APP/PS1-CPZ, n=7).*

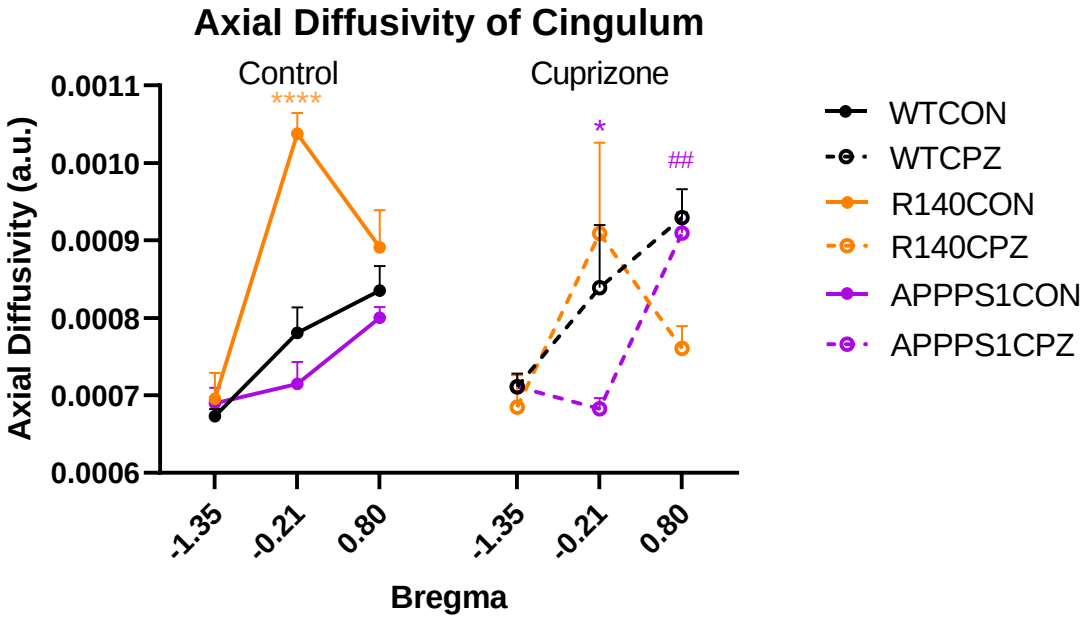

*Figure 28: The cingulum AxD of genotypic and diet groups were analysed for changes in axial diffusion of water of white matter in the mice brain. Genotypes are individually grouped to observe the effect of diet. All values are of two-way ANOVA mean ± SEM. Statistically significant stars are color-coded according to transgenic genotype against WT. *p<0.05; ****p<0.0001. Statistically significant hashes are color-coded according to CPZ change against CON. ##p<0.01. (WT-CON, n=8; WT-CPZ, n=8; R1.40-CON, n=3; R1.40-CPZ, n=3; APP/PS1-CON, n=7; APP/PS1-CPZ, n=7).*

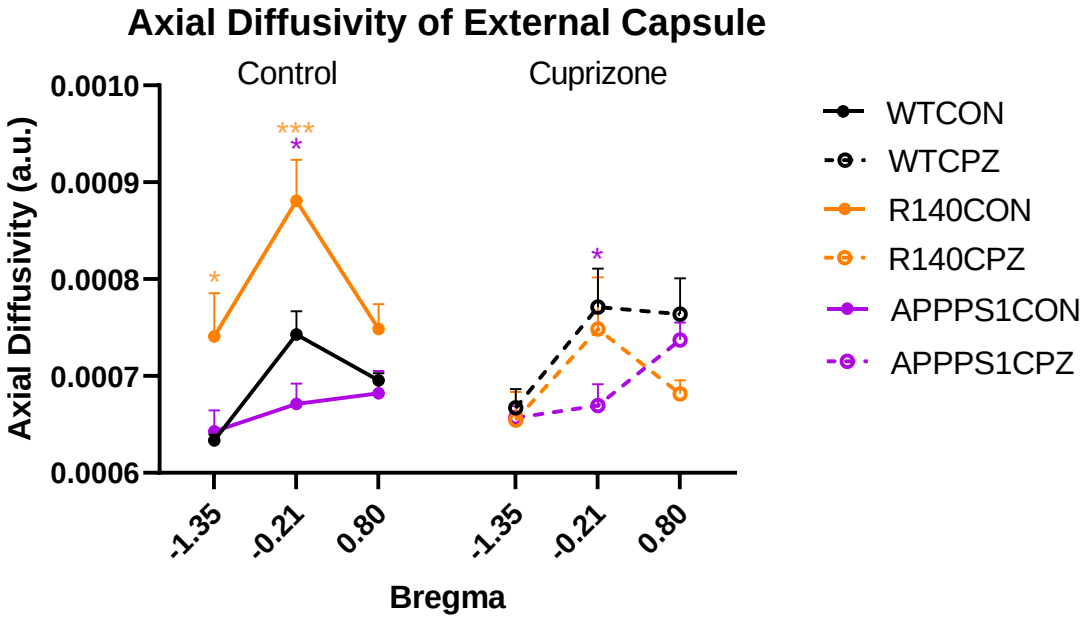

*Figure 29: The external capsule AxD of genotypic and diet groups were analysed for changes in axial diffusion of water of white matter in the mice brain. Genotypes are individually grouped to observe the effect of diet. All values are of two-way ANOVA mean ± SEM. Statistically significant stars are color-coded according to transgenic genotype against WT. *p<0.05; ***p<0.001. (WT-CON, n=8; WT-CPZ, n=8; R1.40-CON, n=3; R1.40-CPZ, n=3; APP/PS1-CON, n=7; APP/PS1-CPZ, n=7).*

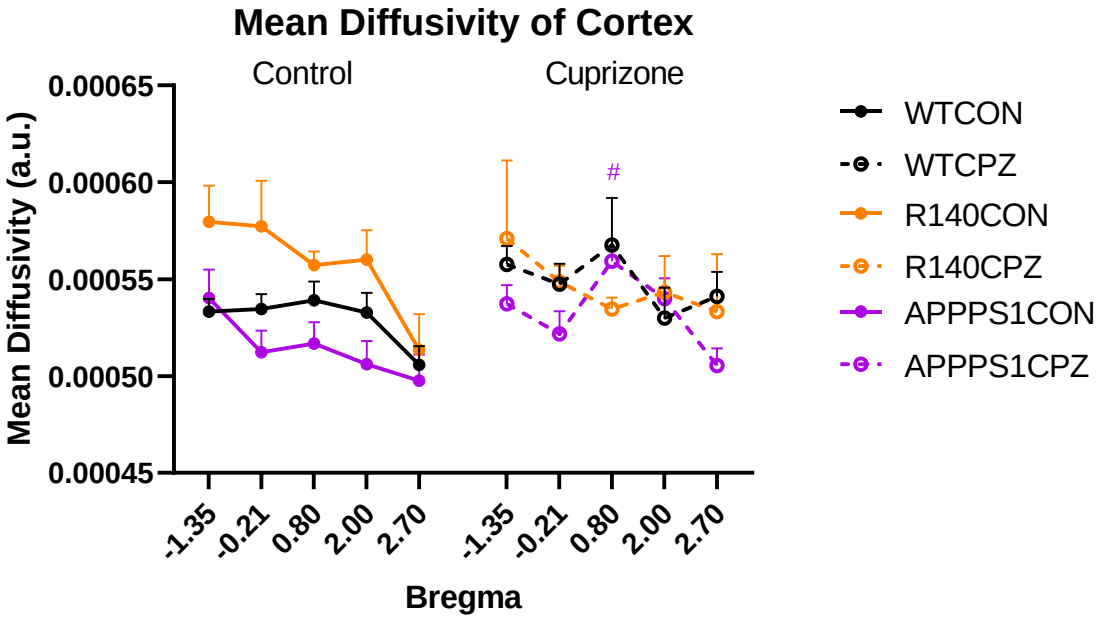

Figure 30: The cortical MD of genotypic and diet groups were analysed for changes in mean diffusion of water of white matter in the mice brain. Genotypes are individually grouped to observe the effect of diet. All values are of two-way ANOVA mean ± SEM. Statistically significant hashes are color-coded according to CPZ change against CON. #p<0.05. (WT-CON, n=8; WT-CPZ, n=8; R1.40-CON, n=3; R1.40-CPZ, n=3; APP/PS1-CON, n=7; APP/PS1-CPZ, n=7).

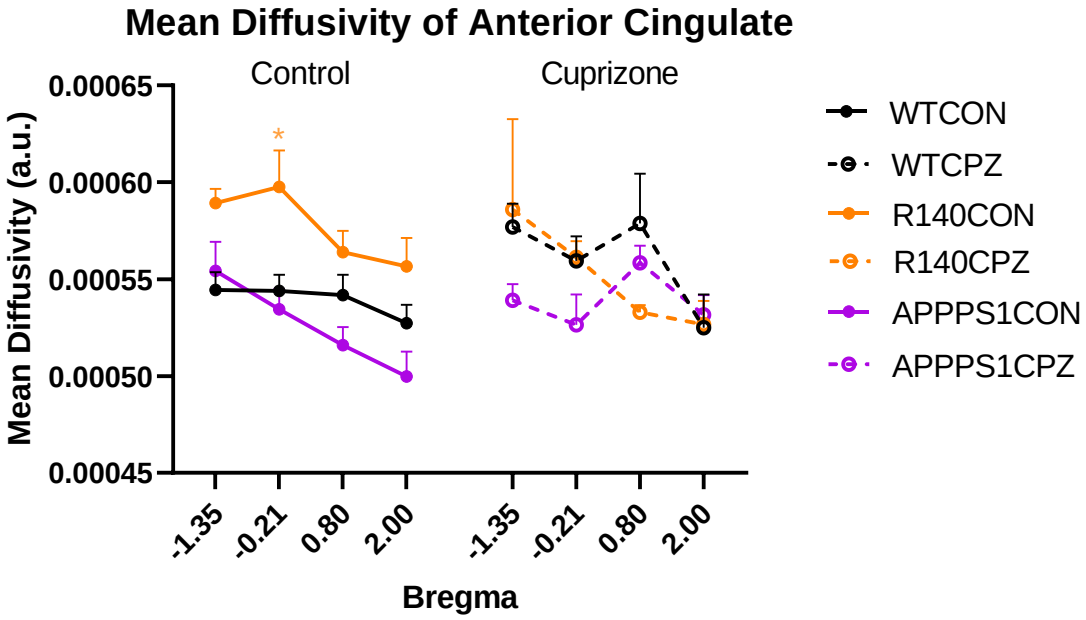

*Figure 31: The anterior cingulate MD of genotypic and diet groups were analysed for changes in mean diffusion of water of white matter in the mice brain. Genotypes are individually grouped to observe the effect of diet. All values are of two-way ANOVA mean ± SEM. Statistically significant stars are color-coded according to transgenic genotype against WT. *p<0.05. (WT-CON, n=8; WT-CPZ, n=8; R1.40-CON, n=3; R1.40-CPZ, n=3; APP/PS1-CON, n=7; APP/PS1-CPZ, n=7).*

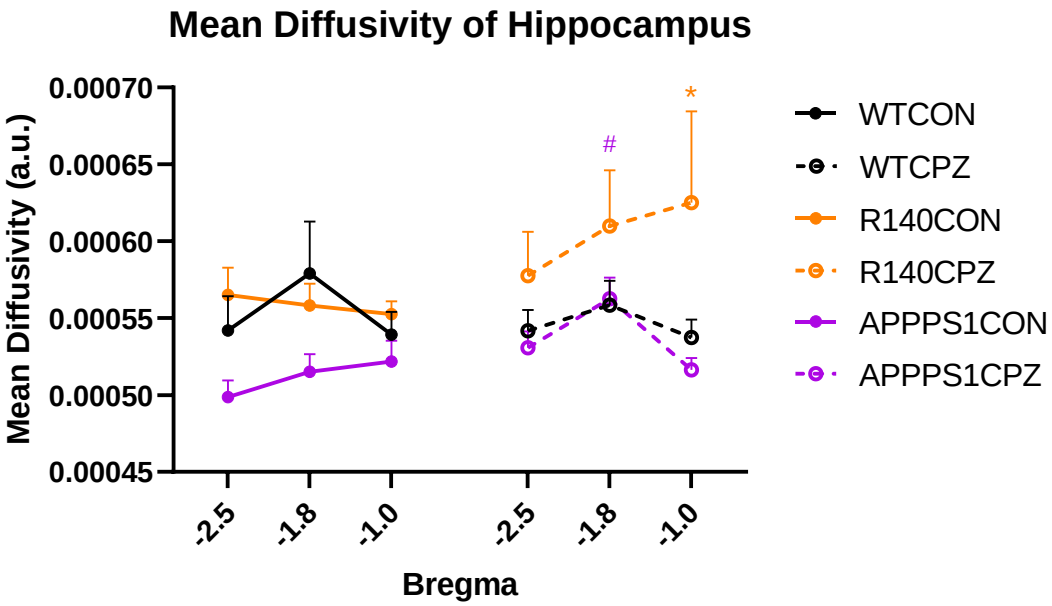

*Figure 32: The hippocampal MD of genotypic and diet groups were analysed for changes in mean diffusion of water of white matter in the mice brain. Genotypes are individually grouped to observe the effect of diet. All values are of two-way ANOVA mean ± SEM. Statistically significant stars are color-coded according to transgenic genotype against WT. *p<0.05. Statistically significant hashes are color-coded according to CPZ change against CON. #p<0.05. (WT-CON, n=8; WT-CPZ, n=8; R1.40-CON, n=3; R1.40-CPZ, n=3; APP/PS1-CON, n=7; APP/PS1-CPZ, n=7).*

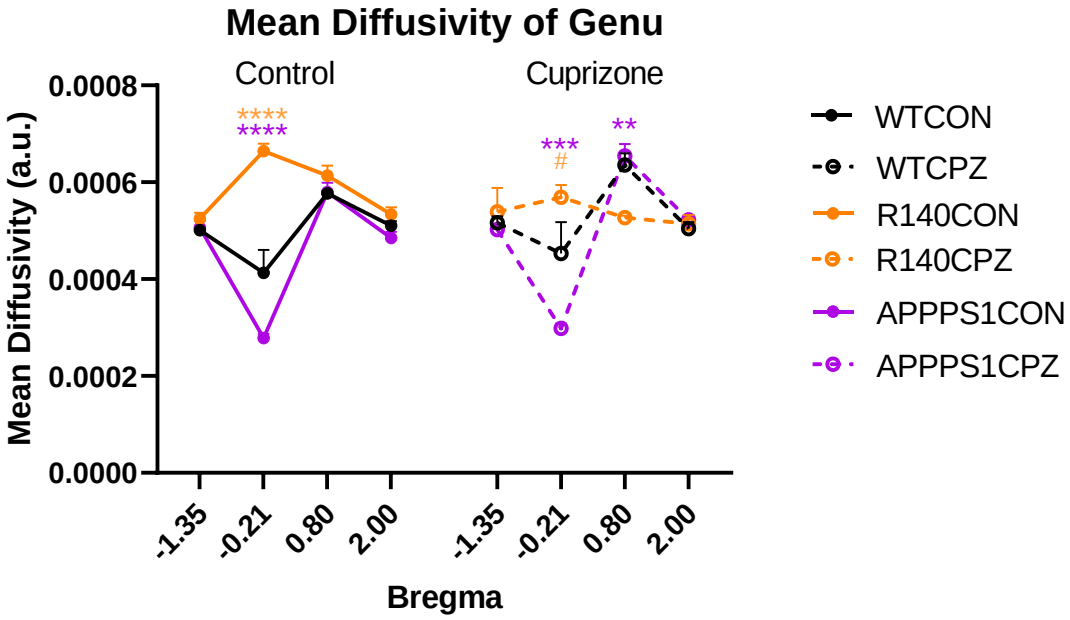

*Figure 33: The genu MD of genotypic and diet groups were analysed for changes in mean diffusion of water of white matter in the mice brain. Genotypes are individually grouped to observe the effect of diet. All values are of two-way ANOVA mean ± SEM. Statistically significant stars are color-coded according to transgenic genotype against WT. **p<0.01; ***p<0.001; ****p<0.0001. Statistically significant hashes are color-coded according to CPZ change against CON. #p<0.05. (WT-CON, n=8; WT-CPZ, n=8; R1.40-CON, n=3; R1.40-CPZ, n=3; APP/PS1-CON, n=7; APP/PS1-CPZ, n=7).*

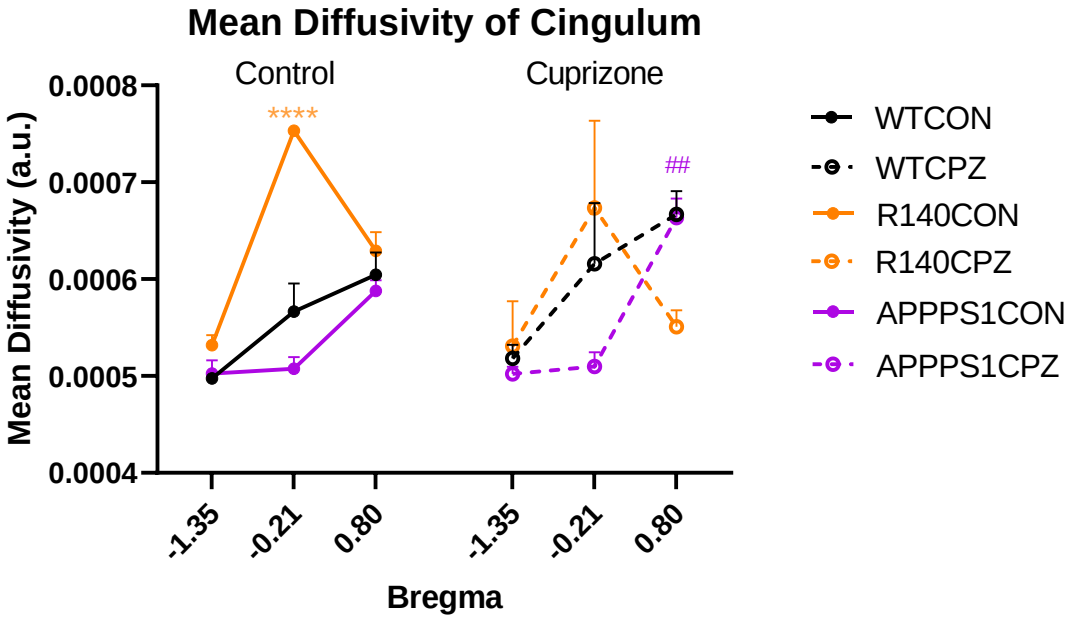

*Figure 34: The cingulum MD of genotypic and diet groups were analysed for changes in mean diffusion of water of white matter in the mice brain. Genotypes are individually grouped to observe the effect of diet. All values are of two-way ANOVA mean ± SEM. Statistically significant stars are color-coded according to transgenic genotype against WT. ****p<0.0001. Statistically significant hashes are color-coded according to CPZ change against CON. ##p<0.01. (WT-CON, n=8; WT-CPZ, n=8; R1.40-CON, n=3; R1.40-CPZ, n=3; APP/PS1-CON, n=7; APP/PS1-CPZ, n=7).*

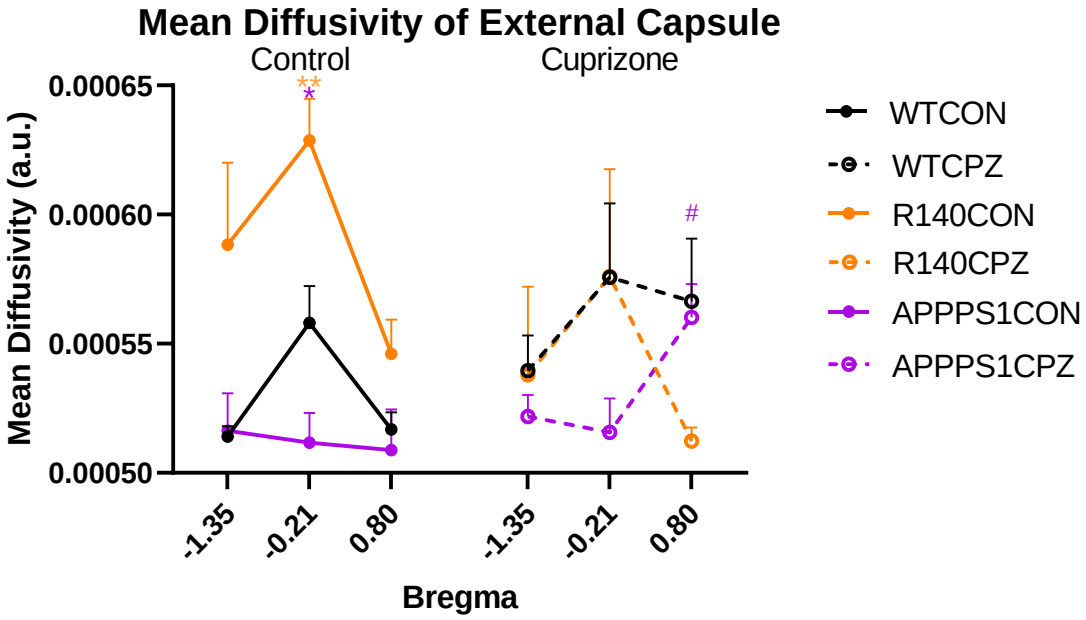

*Figure 35: The external capsule MD of genotypic and diet groups were analysed for changes in mean diffusion of water of white matter in the mice brain. Genotypes are individually grouped to observe the effect of diet. All values are of two-way ANOVA mean ± SEM. Statistically significant stars are color-coded according to transgenic genotype against WT. *p<0.05; **p<0.01. Statistically significant hashes are color-coded according to CPZ change against CON. #p<0.05. (WT-CON, n=8; WT-CPZ, n=8; R1.40-CON, n=3; R1.40-CPZ, n=3; APP/PS1-CON, n=7; APP/PS1-CPZ, n=7).*

3.4 Analysis of myelin and OL populations

3.4.1 Immunohistochemistry and western blot of R1.40

The study of MRI-detected diffusivity solidly suggests R1.40 having higher diffusivity among regions of both grey and white matter in Bregma 0.8. As a result, immunohistochemistry (IHC) of the afflicted regions was done to understand the cellular influences the genotype and the diet has on OLs and myelin. Two main regions, anterior cingulate and genu, were selected for analysis of two OL lineage markers, Olig2 for gross OL population and ASPA for mature OL (mOL) due to their sensitivity in the DKI analysis.

First, the marker for amyloid plaques (6E10) was used for western blot to show R1.40's intrinsic amyloid deposition not present in C57BL/6 mice (Figure 36A, 36B, 36C, 36D, 36E, and 36F). While R1.40 mice show apparent presence 6E10 compared to WT, the difference in diet did not show changes in protein levels. To correlate with the DKI analysis, proteins representations for myelin, MBP and MAG, are analysed. Unexpectedly, MBP levels did not show changes between genotype and diet (Figure 36G). In contrast, MAG levels show significant reductions in WT with CPZ compared to control diet (-50.4%, p=0.0274) but no change in R1.40 (Figure 36H). These results indicate a detailed mechanism of myelination that is broken down into independent roles of different myelin proteins. The tightening of the myelin sheath enforced by MBP suggests lesser influence by CPZ while the attachment of the mOL with the axon coordinated by MAG may be more significantly impacted.

One hypothesis for the reductions of OLs is the accumulation of DNA damage, causing cell death. While the mechanism of the reduction is not part of the study, the quantifications of the DNA damage marker, 53BP1, may lay the base work for future study (Figure 37). First, neuronal quantification was done with neuron marker, NeuN, to look for fluctuations of neuron numbers due to genotype or demyelination (Figure 37A). Cortical neuron numbers show no change in NeuN+ neurons (Figure 37E). Co-staining of 53BP1 with NeuN also shows no alteration of DNA damage puncta in NeuN cells (Figure 37F). Interestingly, a high percentage of NeuN+ cells exhibit 53BP1 (between 70% to 80%) (Figure 37G). The difference seen in Figure 37G is statistically significant as the mean of WT-CON is

approximately 95% of all neurons have DNA damage while for the other genotype and treatment are close to 100%. This high percentage seen in neurons is caused by high levels of oxidative stress due to their higher levels of oxidative phosphorylation and using 20% of the body's oxygen for respiration (318). While this kind of stress is toxic to many cells in the nervous system (319), neurons require DNA damage to accommodate for neural plasticity, aiding in neuronal maturation and maintenance (320, 321). However, the biological difference between 95% and 100% is insignificance as the 5% difference could be accounted for by analytical errors. Thus, it is believed that neuron survivability may not by acutely affected by the demyelination event nor accumulation of DNA damage.

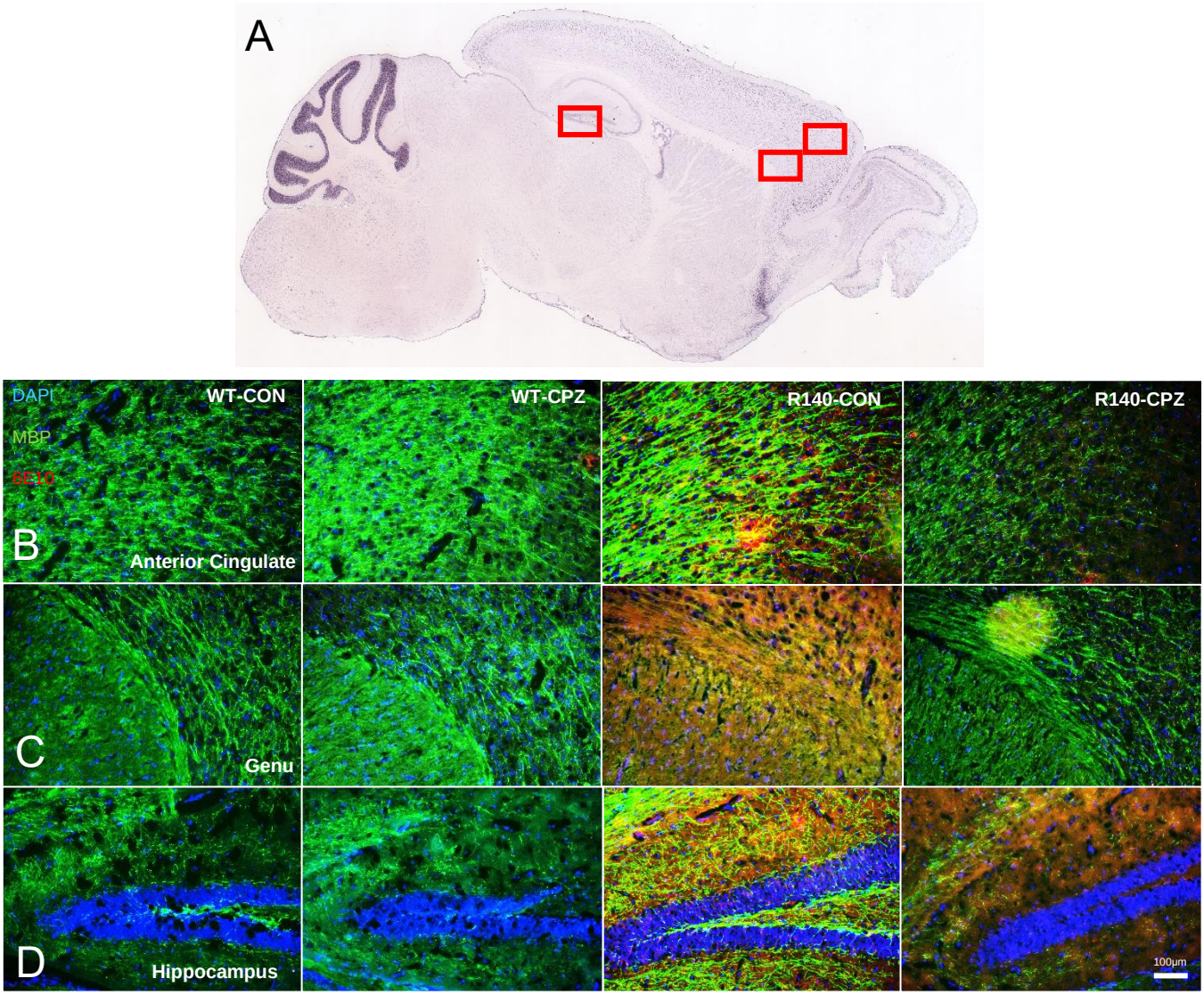

Figure 36: Regions representing myelin densities are highlighted in red boxes (A): anterior cingulate (B), genu (C), and the hippocampus (D). Western blot images for amyloid 6E10 and myelin proteins, MAG and MBP, were studied. Representative analysis of the 6E10, MAG, and MBP are shown (F-H, respectively).

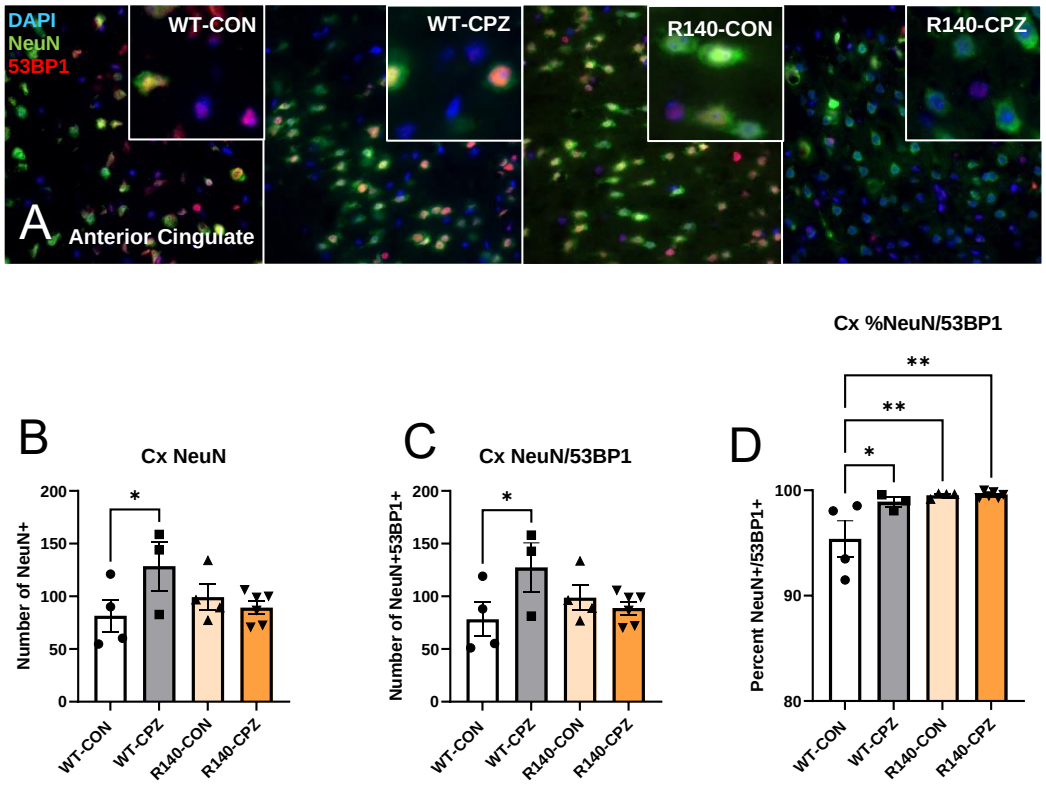

Figure 37: The first column shows the colocalization of neurons stained with NeuN and DNA damage marker 53BP1 in the anterior cingulate (A). Graphical representation is shown (B-D) where neuronal number positive for 53BP1 is relatively unchanged.

3.4.2 Immunohistochemistry for OLs and myelin in APP/PS1

To understand the distribution of effects within the brain, three grey matter (anterior cingulate, motor cortex, and somatosensory cortex) and three white matter (genu, cingulum, and external capsule). In addition, one myelin marker (PLP), four OL lineage markers (Olig2, Nkx2.2., APC-CC1, and ASPA), and one DNA damage marker (53BP1) will be used to find correlations of these three factors in the amyloid-depositing and demyelinating brain. In the APP/PS1 mice cohort, PLP is first used to stain myelin fibres. Myelin densities were calculated with IHC of PLP. Myelin fibre density refers to the area of DAB-stained myelin with PLP divided by the total annotated area. The density is the percentage of area with PLP+ myelin over the total annotated area. Even though no statistical significance with one-way ANOVA was found between control and cuprizone treatment of PLP densities to indicate demyelination, acquired images show fewer PLP+ myelin fibres for the cuprizone treatments. Grey matter myelin fibres of the control diet show no significant change among the regions (Figure 38-40). With CPZ diet, APP/PS1 show a decrease in myelin content in all three regions. However, this trend is not present in the white matter regions of either genotype or diets (Figure 41-43). Interestingly, this is inconsistent with the lower diffusivities found in DKI as there is apparent demyelination in the APP/PS1 brain.

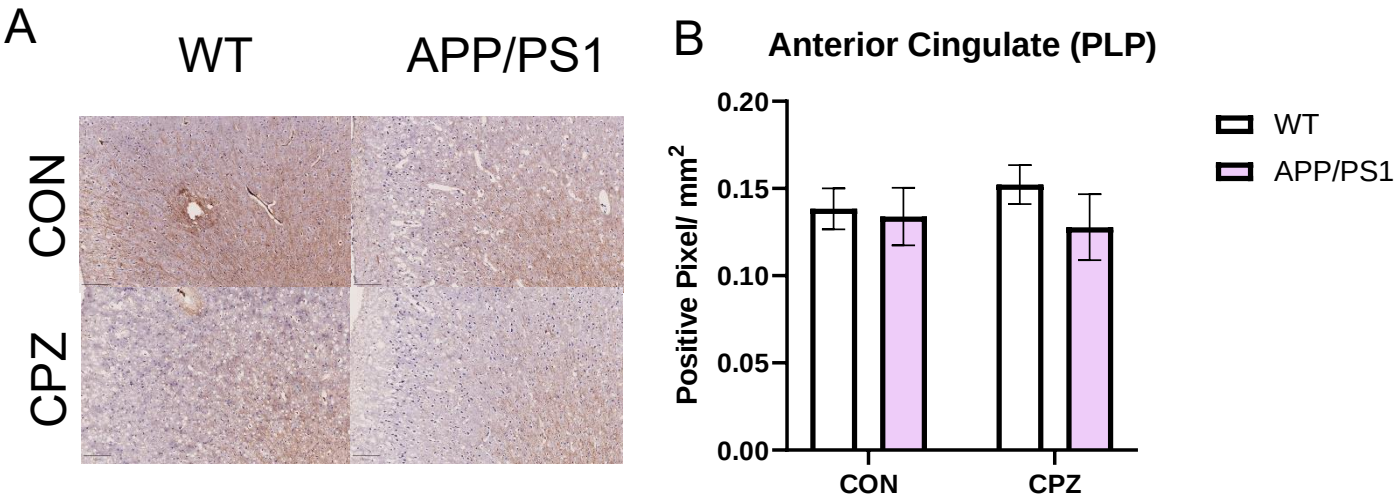

Figure 38: Chromogenic immunohistochemistry using the myelin marker, PLP, reveals the myelin fibre densities within the anterior cingulate. Images of the region of interest based on genotype and diet show representative densities of the myelin fibres (A). Quantifications based on the positive pixels of PLP per mm2 are shown between same diets (B). All values are of two-way ANOVA mean ± SEM. (WT-CON, n=4; WT-CPZ, n=4; APP/PS1-CON, n=7; APP/PS1-CPZ, n=7).

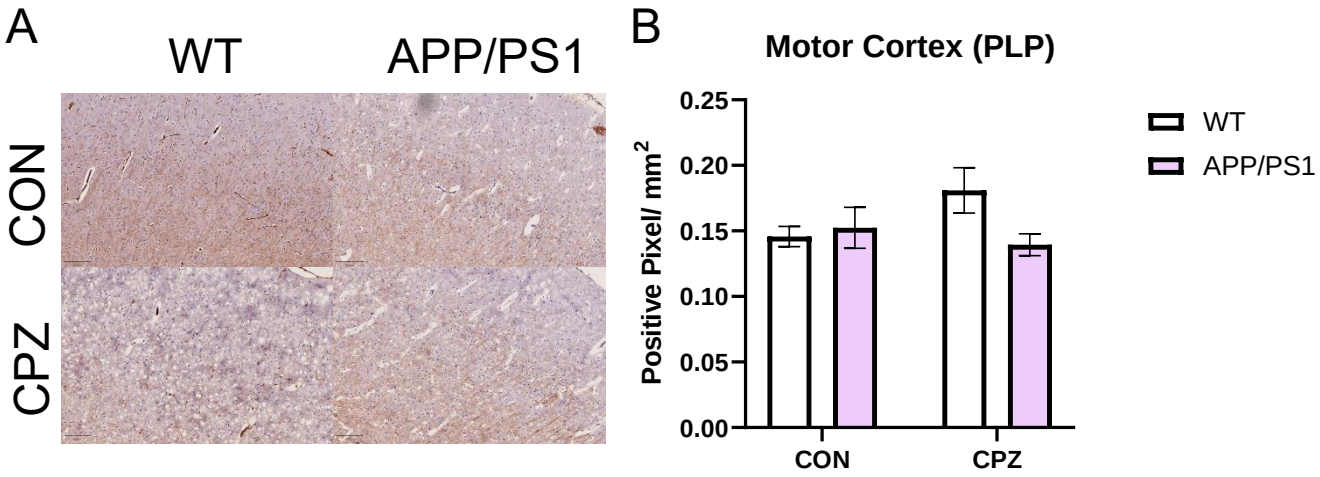

Figure 39: Chromogenic immunohistochemistry using the myelin marker, PLP, reveals the myelin fibre densities within the motor cortex. Images of the region of interest based on genotype and diet show representative densities of the myelin fibres (A). Quantifications based on the positive pixels of PLP per mm2 are shown between same diets (B). All values are of two-way ANOVA mean ± SEM. (WT-CON, n=4; WT-CPZ, n=4; APP/PS1-CON, n=7; APP/PS1-CPZ, n=7).

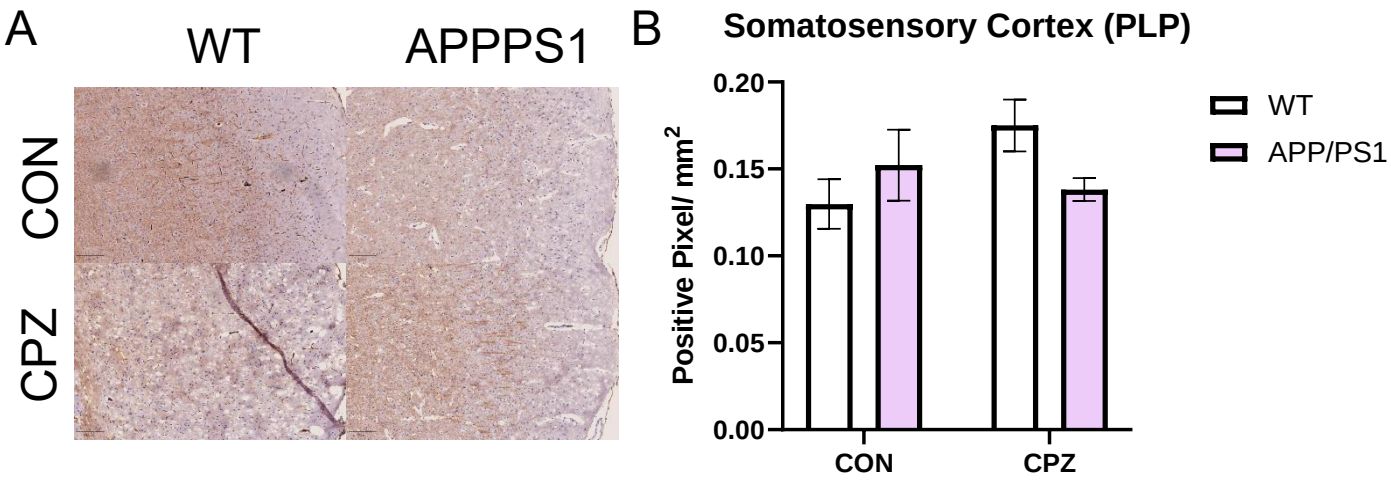

Figure 40: Chromogenic immunohistochemistry using the myelin marker, PLP, reveals the myelin fibre densities within the somatosensory cortex. Images of the region of interest based on genotype and diet show representative densities of the myelin fibres (A). Quantifications based on the positive pixels of PLP per mm2 are shown between same diets (B). All values are of two-way ANOVA mean ± SEM. (WT-CON, n=4; WT-CPZ, n=4; APP/PS1-CON, n=7; APP/PS1-CPZ, n=7).

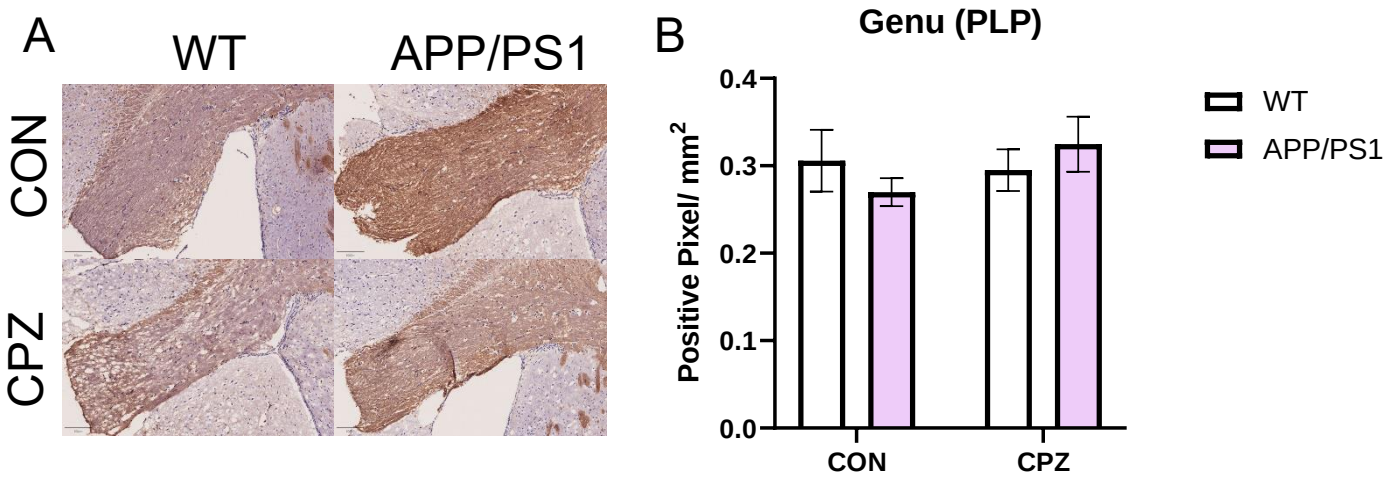

Figure 41: Chromogenic immunohistochemistry using the myelin marker, PLP, reveals the myelin fibre densities within the genu. Images of the region of interest based on genotype and diet show representative densities of the myelin fibres (A). Quantifications based on the positive pixels of PLP per mm2 are shown between same diets (B). All values are of two-way ANOVA mean ± SEM. (WT-CON, n=4; WT-CPZ, n=4; APP/PS1-CON, n=7; APP/PS1-CPZ, n=7).

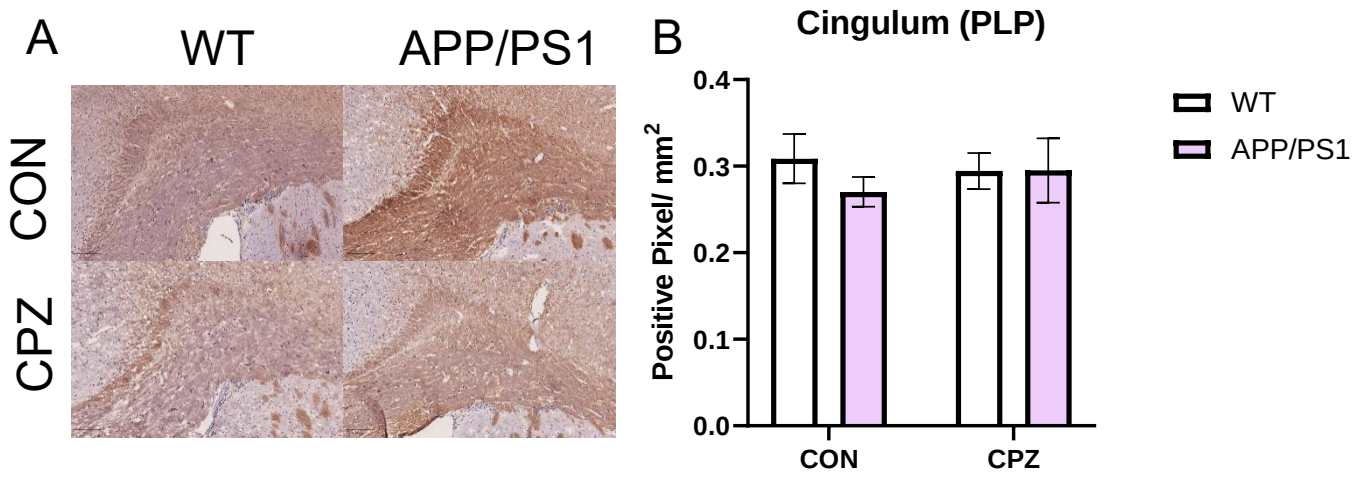

Figure 42: Chromogenic immunohistochemistry using the myelin marker, PLP, reveals the myelin fibre densities within the cingulum. Images of the region of interest based on genotype and diet show representative densities of the myelin fibres (A). Quantifications based on the positive pixels of PLP per mm^2 are shown between same diets (B). All values are of two-way ANOVA mean ± SEM. (WT-CON, n=4; WT-CPZ, n=4; APP/PS1-CON, n=7; APP/PS1-CPZ, n=7).

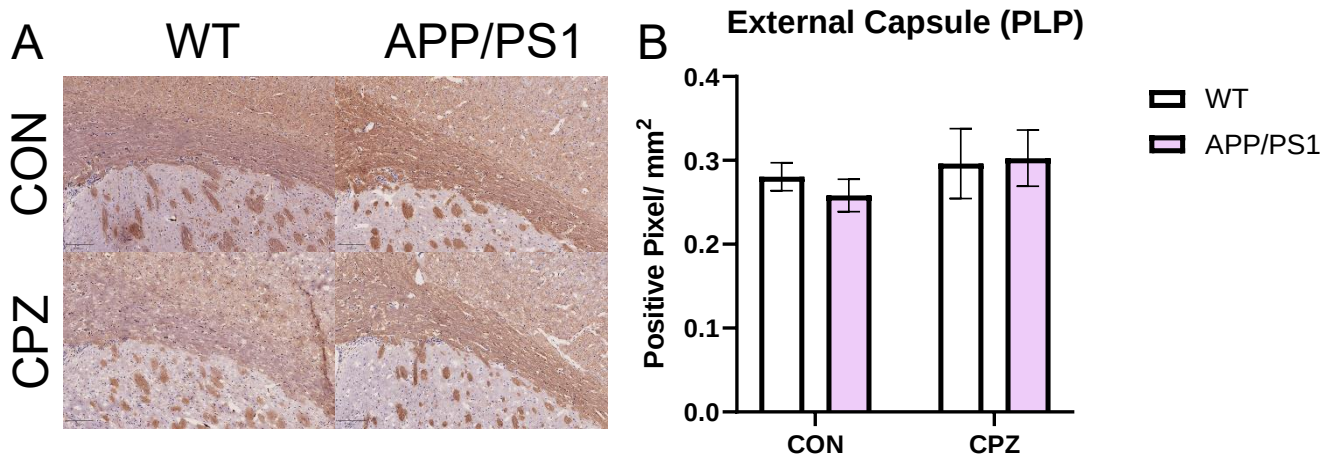

Figure 43: Chromogenic immunohistochemistry using the myelin marker, PLP, reveals the myelin fibre densities within the external capsule. Images of the region of interest based on genotype and diet show representative densities of the myelin fibres (A). Quantifications based on the positive pixels of PLP per mm2 are shown between same diets (B). All values are of two-way ANOVA mean ± SEM. (WT-CON, n=4; WT-CPZ, n=4; APP/PS1-CON, n=7; APP/PS1-CPZ, n=7).

Quantification of OLs was then done to see if the effects of genotype and demyelination influenced the cells or the myelin directly. Gross OL population stained with Olig2 show APP/PS1 mutation as intrinsically harmful to OLs as grey matter regions of control diet show decrease in Olig2+ OLs compared to WT (Figure 44-46). This decrease is similar in CPZ, except at a lower level. In the white matter tract regions, mice with control and CPZ diet independently show no change. However, a comparison of the control diet and CPZ diet levels show decrease in Olig2+ cells of the demyelinated genotypes (Figure 47-49). Demyelination from CPZ has shown influence on OL numbers. Whether this reduction is caused by an agonistic or maturation factor will be investigated with other OL lineage markers.

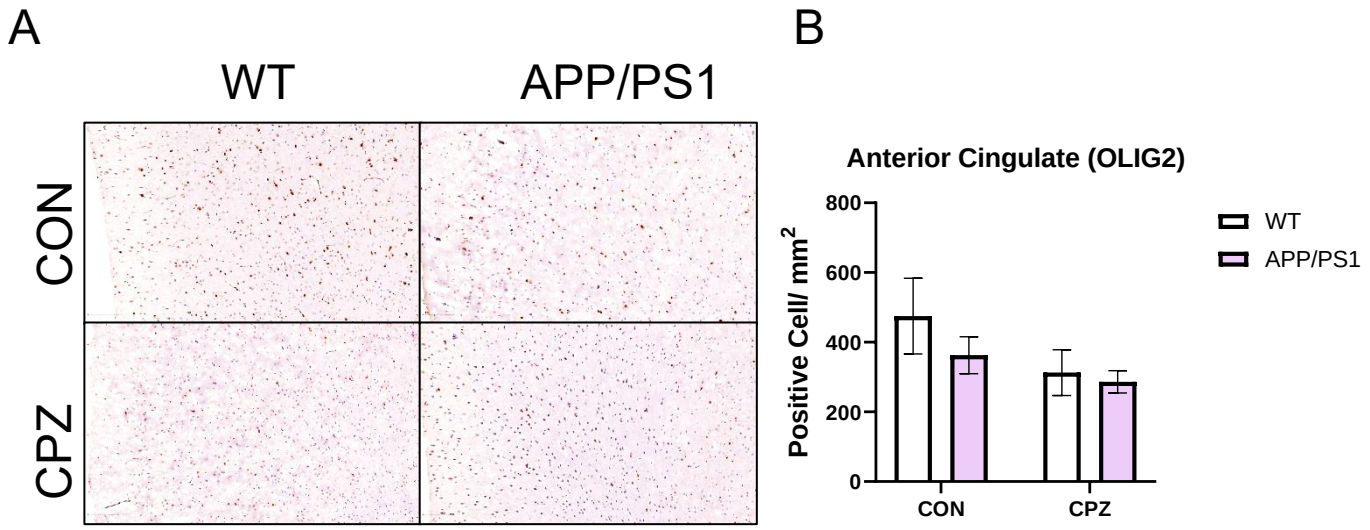

Figure 44: Chromogenic immunohistochemistry using the gross OL marker, Olig2, reveals the OL population within the anterior cingulate. Images of the region of interest based on genotype and diet show representative densities of the OL population (A). Quantifications based on the number of positive cells per mm2 are shown between same diets (B). All values are of two-way ANOVA mean ± SEM. (WT-CON, n=4; WT-CPZ, n=4; APP/PS1-CON, n=7; APP/PS1-CPZ, n=7).

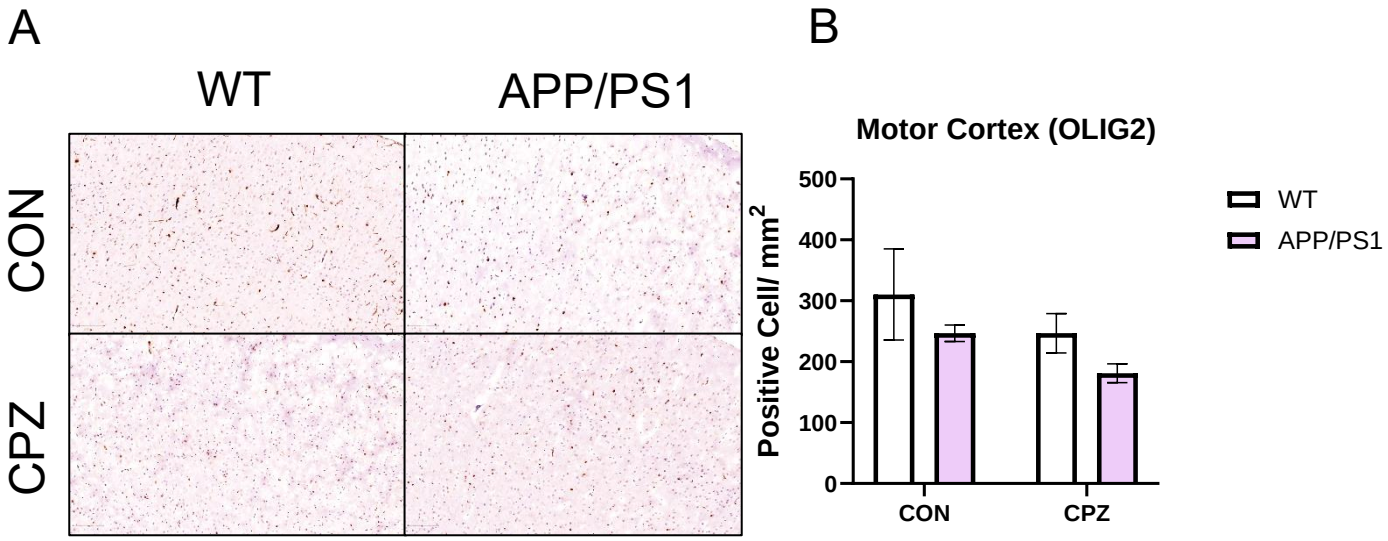

Figure 45: Chromogenic immunohistochemistry using the gross OL marker, Olig2, reveals the OL population within the motor cortex. Images of the region of interest based on genotype and diet show representative densities of the OL population (A). Quantifications based on the number of positive cells per mm2 are shown between same diets (B). All values are of two-way ANOVA mean ± SEM. (WT-CON, n=4; WT-CPZ, n=4; APP/PS1-CON, n=7; APP/PS1-CPZ, n=7).

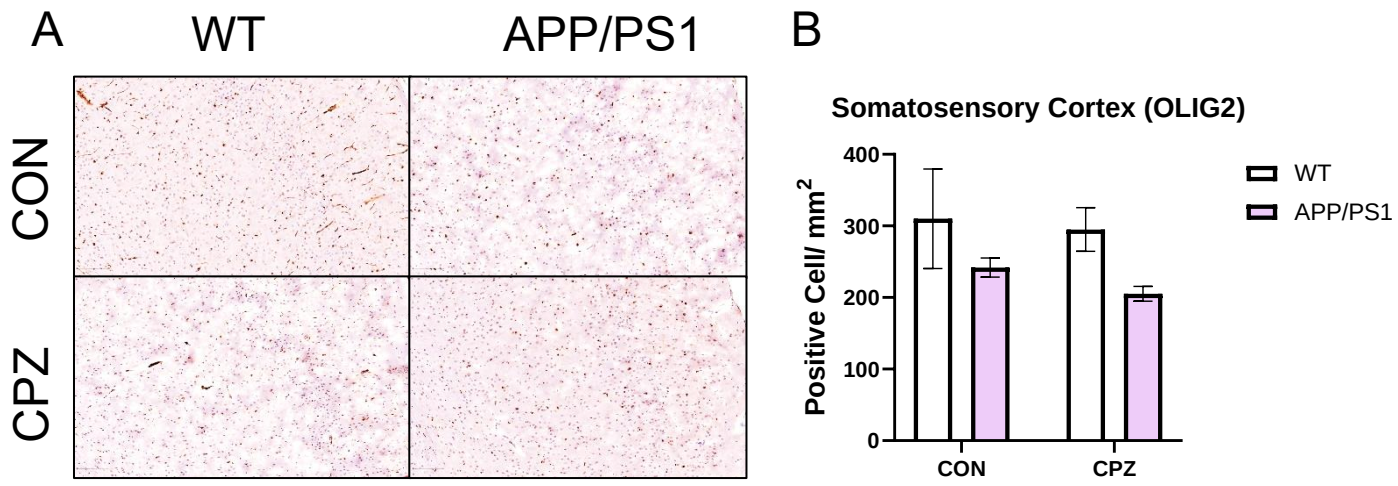

Figure 46: Chromogenic immunohistochemistry using the gross OL marker, Olig2, reveals the OL population within the somatosensory cortex. Images of the region of interest based on genotype and diet show representative densities of the OL population (A). Quantifications based on the number of positive cells per mm2 are shown between same diets (B). All values are of two-way ANOVA mean ± SEM. (WT-CON, n=4; WT-CPZ, n=4; APP/PS1-CON, n=7; APP/PS1-CPZ, n=7).

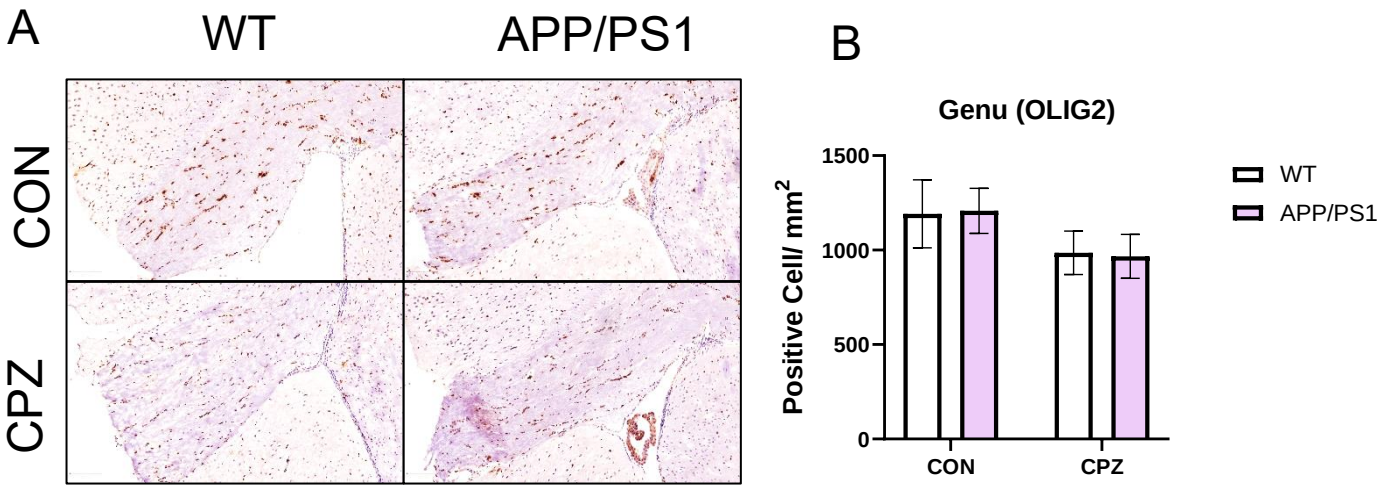

Figure 47: Chromogenic immunohistochemistry using the gross OL marker, Olig2, reveals the OL population within the genu. Images of the region of interest based on genotype and diet show representative densities of the OL population (A). Quantifications based on the number of positive cells per mm2 are shown between same diets (B). All values are of two-way ANOVA mean ± SEM. (WT-CON, n=4; WT-CPZ, n=4; APP/PS1-CON, n=7; APP/PS1-CPZ, n=7).

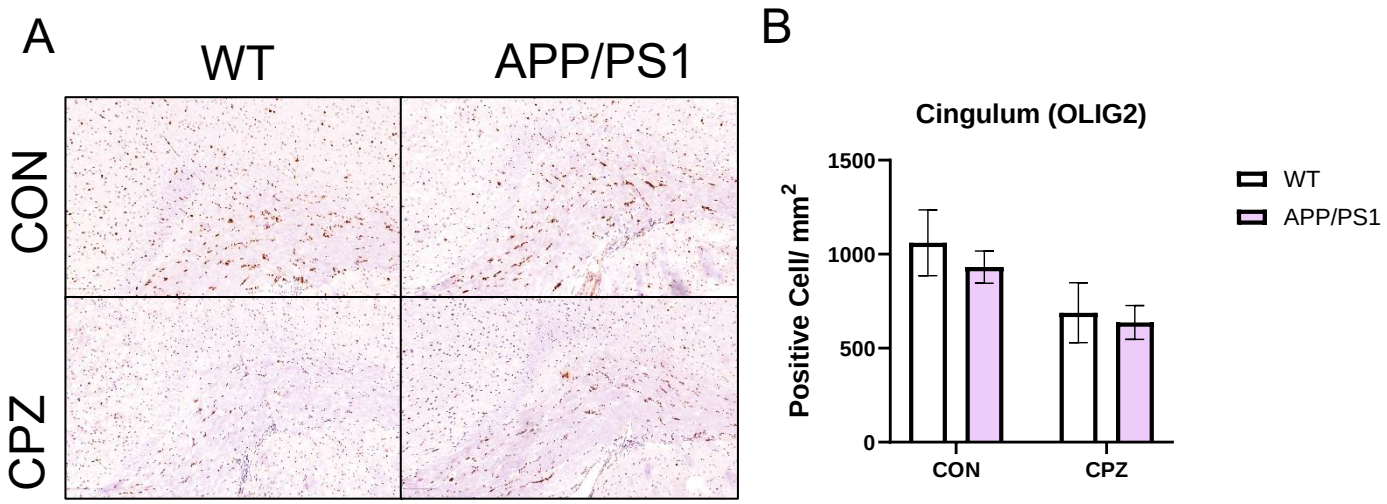

Figure 48: Chromogenic immunohistochemistry using the gross OL marker, Olig2, reveals the OL population within the cingulum. Images of the region of interest based on genotype and diet show representative densities of the OL population (A). Quantifications based on the number of positive cells per mm2 are shown between same diets (B). All values are of two-way ANOVA mean ± SEM. (WT-CON, n=4; WT-CPZ, n=4; APP/PS1-CON, n=7; APP/PS1-CPZ, n=7)..

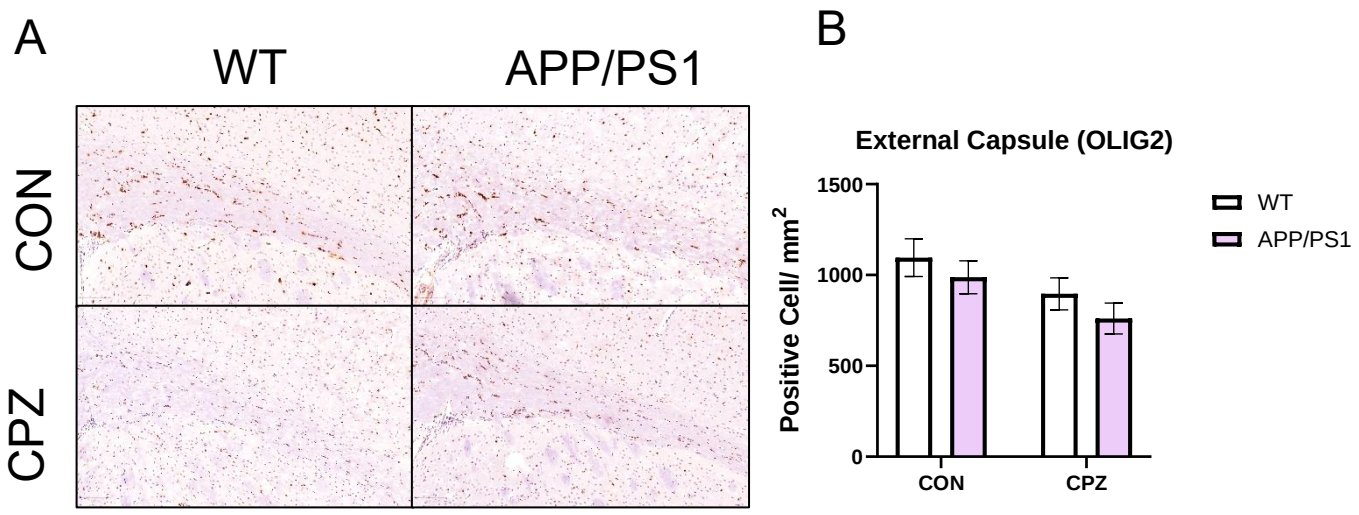

Figure 49: Chromogenic immunohistochemistry using the gross OL marker, Olig2, reveals the OL population within the external capsule. Images of the region of interest based on genotype and diet show representative densities of the OL population (A). Quantifications based on the number of positive cells per mm2 are shown between same diets (B). All values are of two-way ANOVA mean ± SEM. (WT-CON, n=4; WT-CPZ, n=4; APP/PS1-CON, n=7; APP/PS1-CPZ, n=7).

OL precursor cells (OPCs) were then stained with Nkx2.2 to see if the cellular changes were a result of maturation complications. Within the grey matter, the motor cortex shows the most change in Nkx2.2+ cells in the APP/PS1 CPZ mice, exhibiting lowered numbers (Figure 50-52). In contrast, the white matter tract shows more changes in Nkx2.2+ cell numbers (Figure 53-55). While the genu show minimal differences, the cingulum shows significant reductions in Nkx2.2+ cells in WT CPZ mice compared to WT control diet (-52.4%, p=0.0187) (Figure 54B). Concurrently, APP/PS1 mice show similar decreases without yielding significance. In the external capsule, WT with CPZ exhibits decreased Nkx2.2+ cells while other genotypes and diet remains levelled. It seems OPCs are more vulnerable in the white matter tract compared to grey matter as more changes are observed.

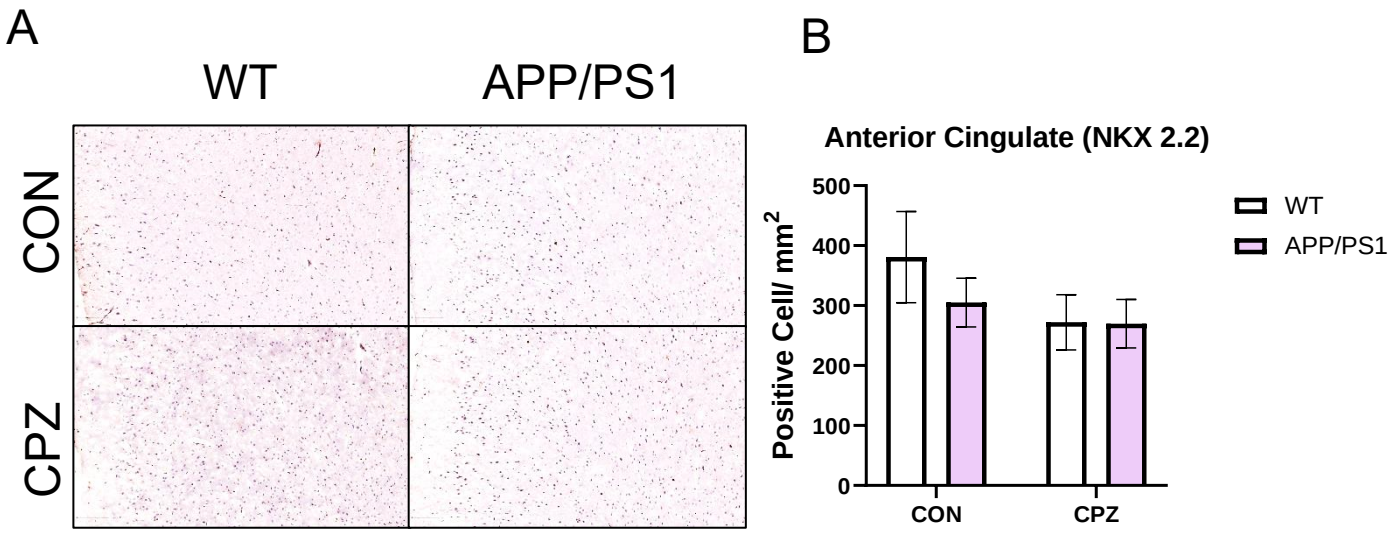

Figure 50: Chromogenic immunohistochemistry using the immature OL marker, Nkx2.2, reveals the OL population within the anterior cingulate. Images of the region of interest based on genotype and diet show representative densities of the OL population (A). Quantifications based on the number of positive cells per mm2 are shown between same diets (B). All values are of two-way ANOVA mean ± SEM. (WT-CON, n=4; WT-CPZ, n=4; APP/PS1-CON, n=7; APP/PS1-CPZ, n=7).

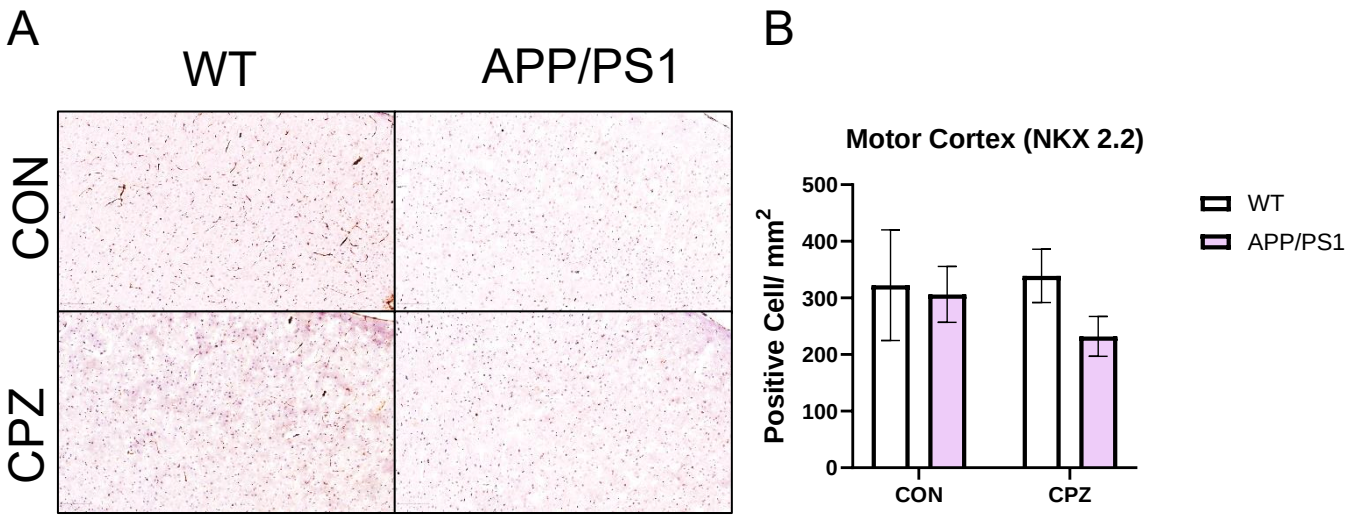

Figure 51: Chromogenic immunohistochemistry using the immature OL marker, Nkx2.2, reveals the OL population within the motor cortex. Images of the region of interest based on genotype and diet show representative densities of the OL population (A). Quantifications based on the number of positive cells per mm2 are shown between same diets (B). All values are of two-way ANOVA mean ± SEM. (WT-CON, n=4; WT-CPZ, n=4; APP/PS1-CON, n=7; APP/PS1-CPZ, n=7).

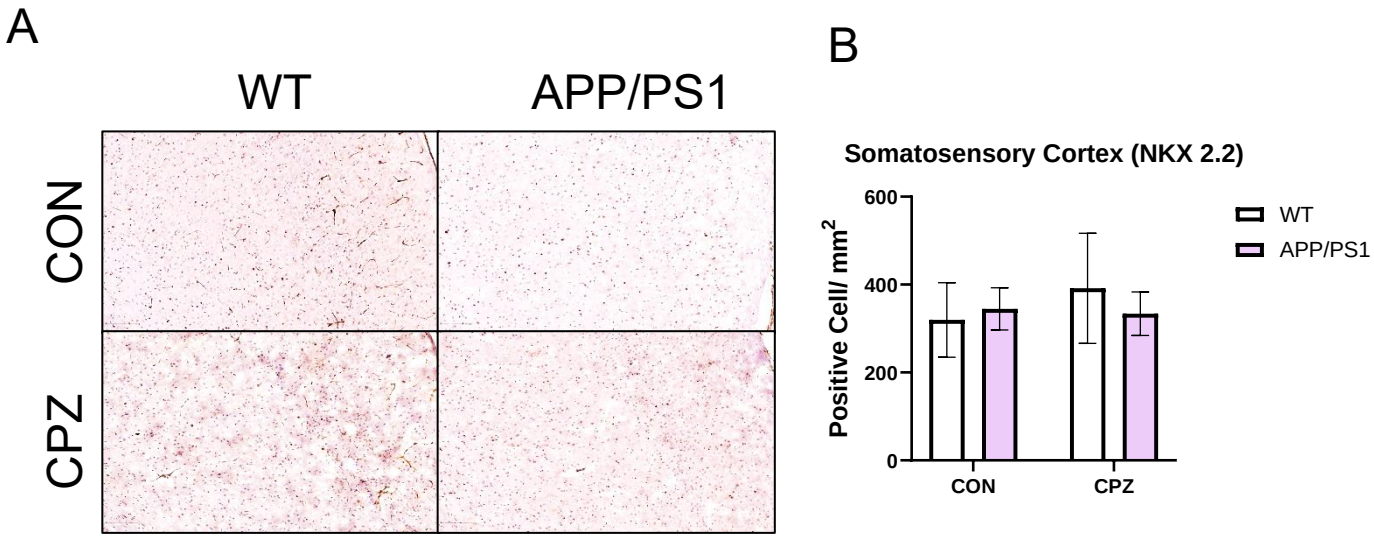

Figure 52: Chromogenic immunohistochemistry using the immature OL marker, Nkx2.2, reveals the OL population within the somatosensory cortex. Images of the region of interest based on genotype and diet show representative densities of the OL population (A). Quantifications based on the number of positive cells per mm2 are shown between same diets (B). All values are of two-way ANOVA mean ± SEM. (WT-CON, n=4; WT-CPZ, n=4; APP/PS1-CON, n=7; APP/PS1-CPZ, n=7).

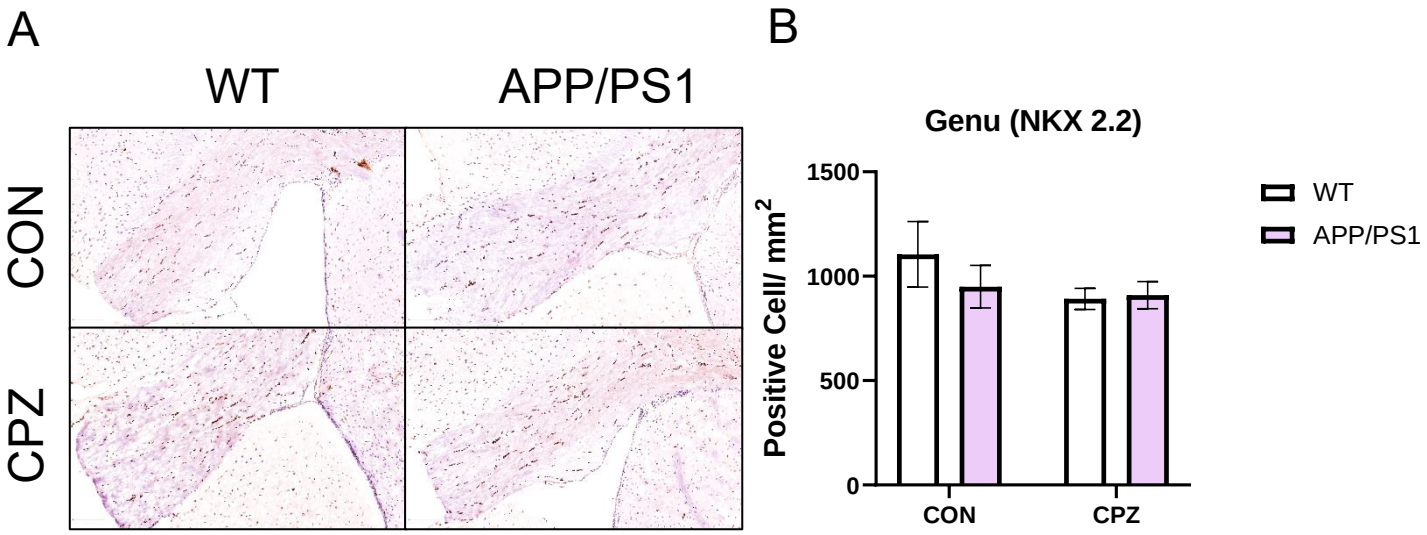

Figure 53: Chromogenic immunohistochemistry using the immature OL marker, Nkx2.2, reveals the OL population within the genu. Images of the region of interest based on genotype and diet show representative densities of the OL population (A). Quantifications based on the number of positive cells per mm2 are shown between same diets (B). All values are of two-way ANOVA mean ± SEM. (WT-CON, n=4; WT-CPZ, n=4; APP/PS1-CON, n=7; APP/PS1-CPZ, n=7).

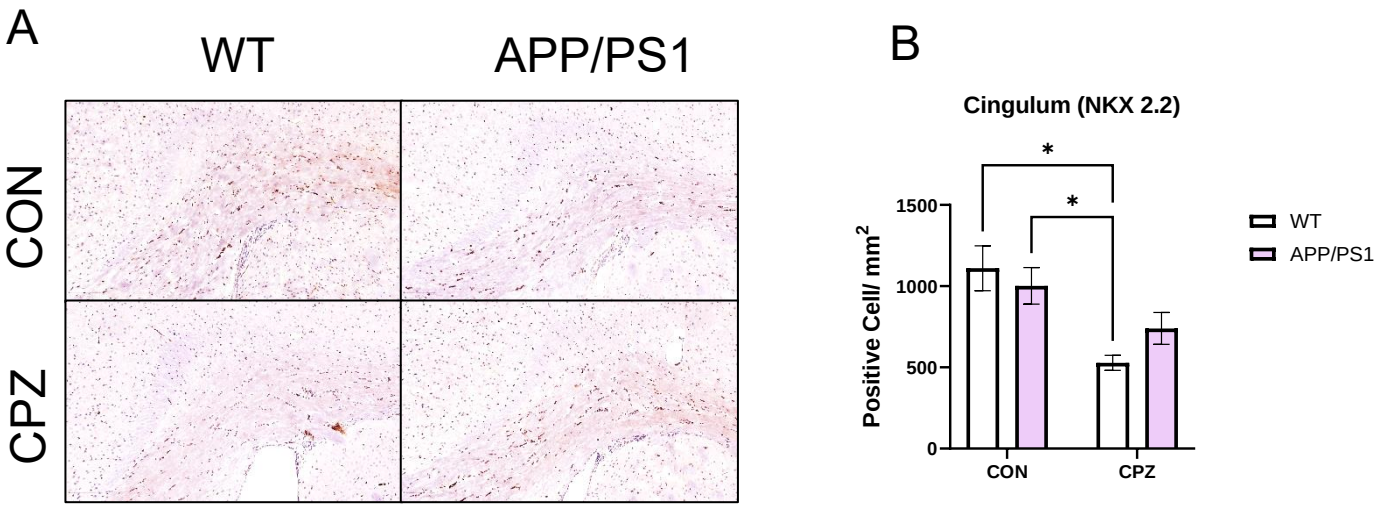

*Figure 54: Chromogenic immunohistochemistry using the immature OL marker, Nkx2.2, reveals the OL population within the cingulum. Images of the region of interest based on genotype and diet show representative densities of the OL population (A). Quantifications based on the number of positive cells per mm^2 are shown between same diets (B). *p < 0.05. All values are of two-way ANOVA mean ± SEM. (WT-CON, n=4; WT-CPZ, n=4; APP/PS1-CON, n=7; APP/PS1-CPZ, n=7).*

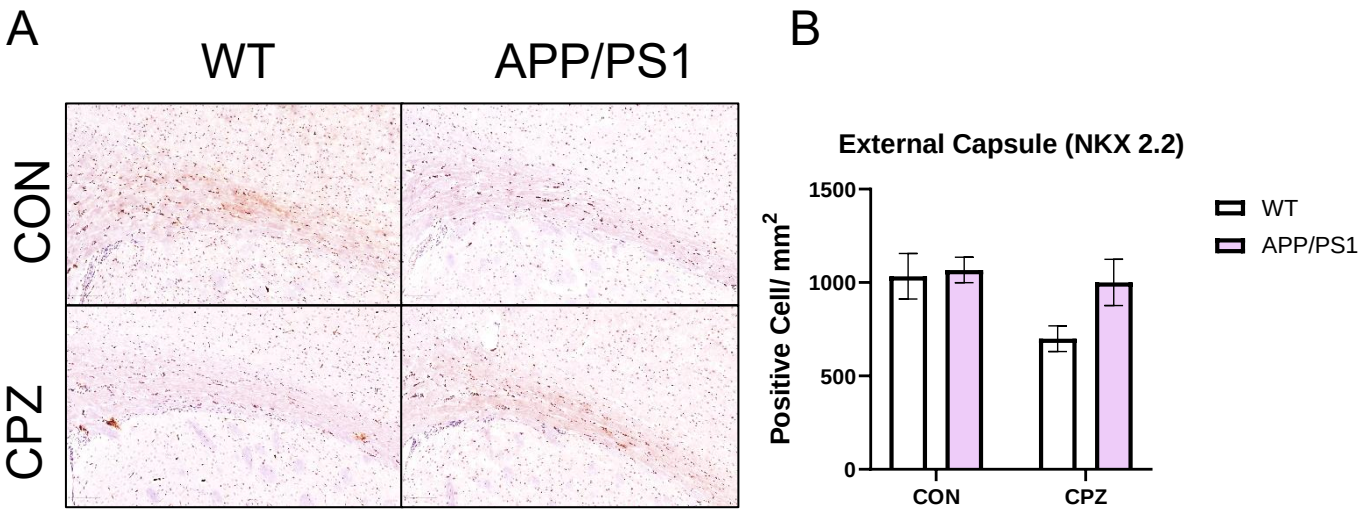

Figure 55: Chromogenic immunohistochemistry using the immature OL marker, Nkx2.2, reveals the OL population within the external capsule. Images of the region of interest based on genotype and diet show representative densities of the OL population (A). Quantifications based on the number of positive cells per mm2 are shown between same diets (B). All values are of two-way ANOVA mean ± SEM. (WT-CON, n=4; WT-CPZ, n=4; APP/PS1-CON, n=7; APP/PS1-CPZ, n=7).

Next, mature OLs (mOLs) were quantified using ASPA and APC-CC1 as markers. Using ASPA, it is shown that control diet mice show no difference in ASPA+ cell numbers while CPZ diet compared to control shows more decrease in APP/PS1 compared to WT (Figure 56-58). Similarly, the white matter tract regions show an overall decrease of ASPA+ cells in CPZ mice of both genotypes (Figure 59-61). With APC-CC1, the grey matter, similarly, shows an overall decrease in APC-CC1+ mOLs in CPZ diet with no significance among factors. However, there is a significant decrease of APP/PS1 between control and CPZ diet in the white matter cingulum (-48.3%, $p=0.0163$) and external capsule (-52.5%, $p=0.004$). This reduction in mOLs is comparable to the reduction from the R1.40s, but instead of affecting cortical APC-CC1, it seems APP/PS1 mice exhibit this decrease in mostly the white matter tract.

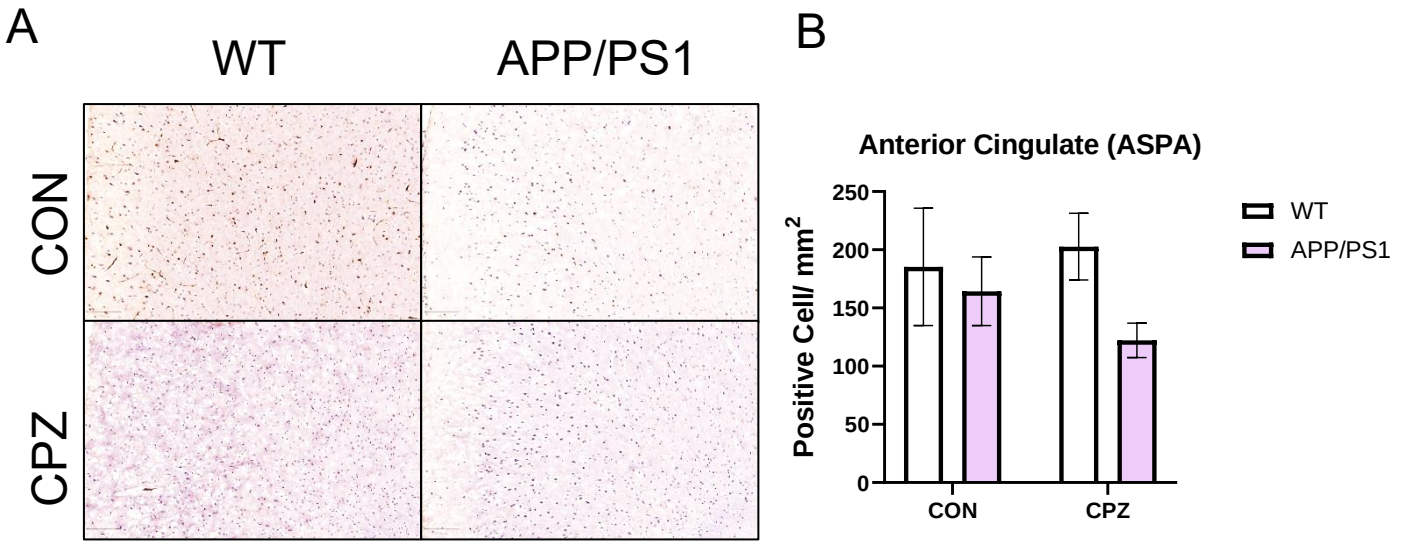

Figure 56: Chromogenic immunohistochemistry using the mature OL marker, ASPA, reveals the OL population within the anterior cingulate. Images of the region of interest based on genotype and diet show representative densities of the OL population (A). Quantifications based on the number of positive cells per mm2 are shown between same diets (B). All values are of two-way ANOVA mean ± SEM. (WT-CON, n=4; WT-CPZ, n=4; APP/PS1-CON, n=7; APP/PS1-CPZ, n=7).

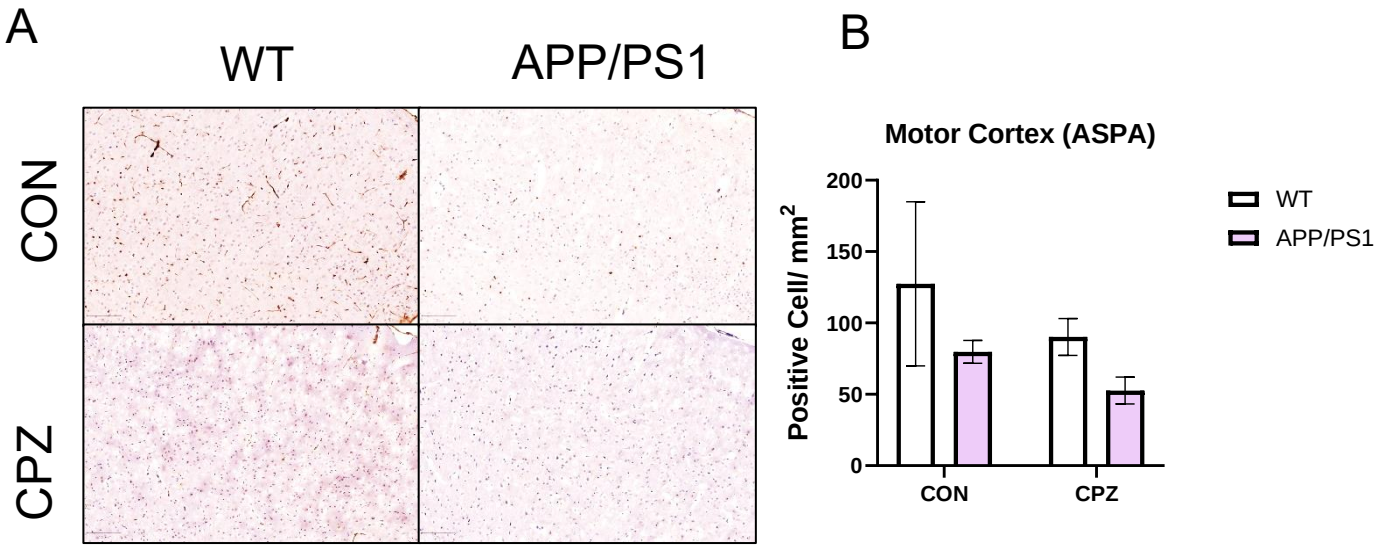

Figure 57: Chromogenic immunohistochemistry using the mature OL marker, ASPA, reveals the OL population within the motor cortex. Images of the region of interest based on genotype and diet show representative densities of the OL population (A). Quantifications based on the number of positive cells per mm2 are shown between same diets (B). All values are of two-way ANOVA mean ± SEM. (WT-CON, n=4; WT-CPZ, n=4; APP/PS1-CON, n=7; APP/PS1-CPZ, n=7).

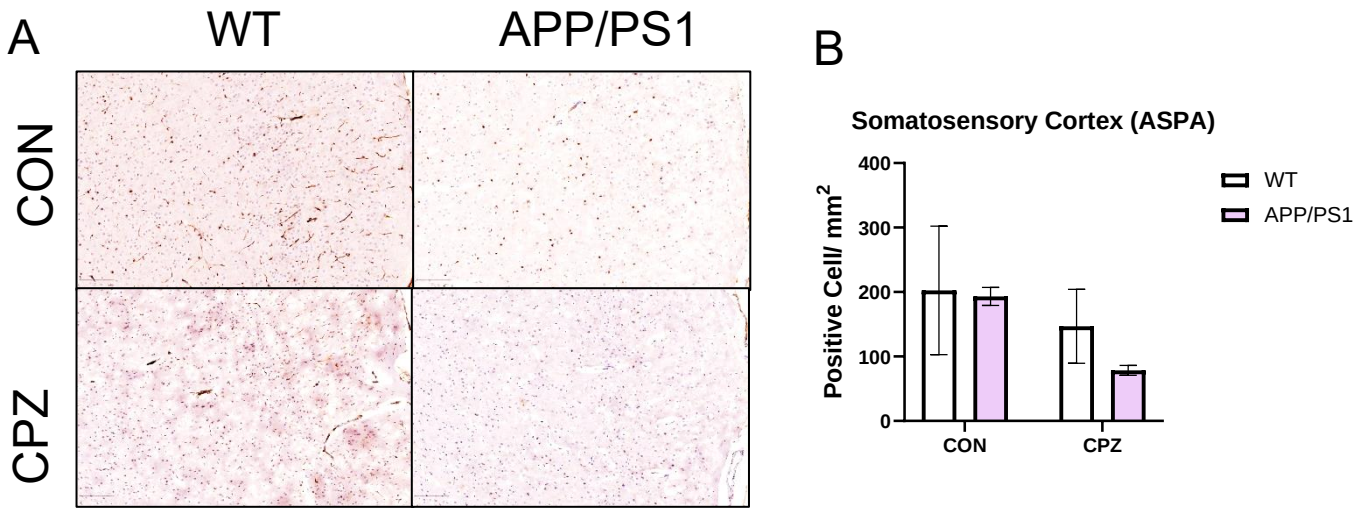

Figure 58: Chromogenic immunohistochemistry using the mature OL marker, ASPA, reveals the OL population within the somatosensory cortex. Images of the region of interest based on genotype and diet show representative densities of the OL population (A). Quantifications based on the number of positive cells per mm2 are shown between same diets (B). All values are of two-way ANOVA mean ± SEM. (WT-CON, n=4; WT-CPZ, n=4; APP/PS1-CON, n=7; APP/PS1-CPZ, n=7).

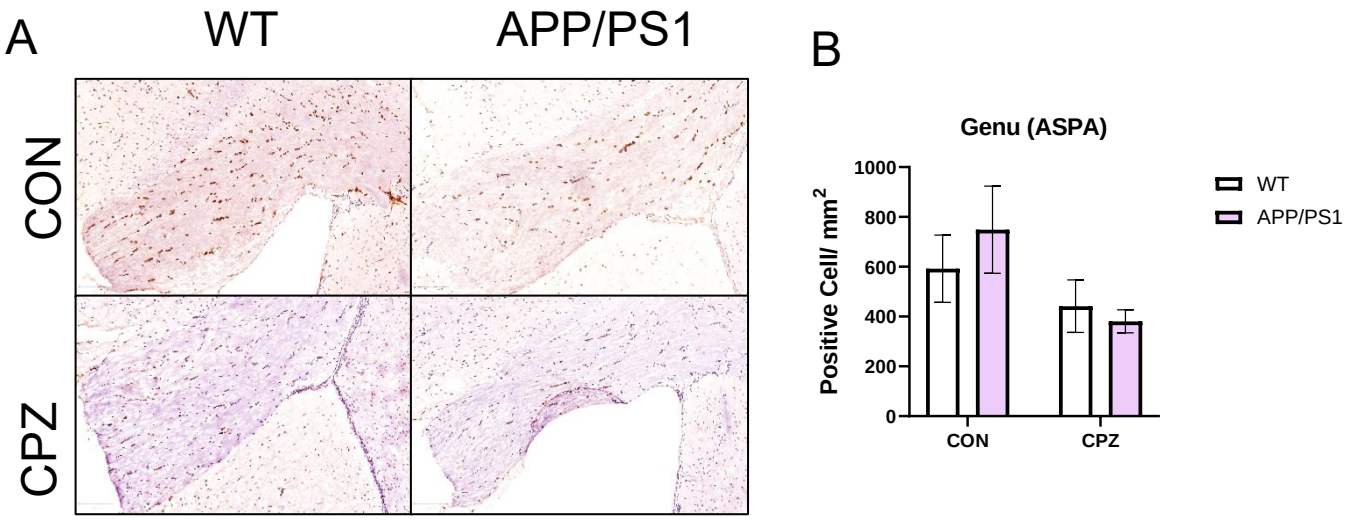

Figure 59: Chromogenic immunohistochemistry using the mature OL marker, ASPA, reveals the OL population within the genu. Images of the region of interest based on genotype and diet show representative densities of the OL population (A). Quantifications based on the number of positive cells per mm2 are shown between same diets (B). All values are of two-way ANOVA mean ± SEM. (WT-CON, n=4; WT-CPZ, n=4; APP/PS1-CON, n=7; APP/PS1-CPZ, n=7).

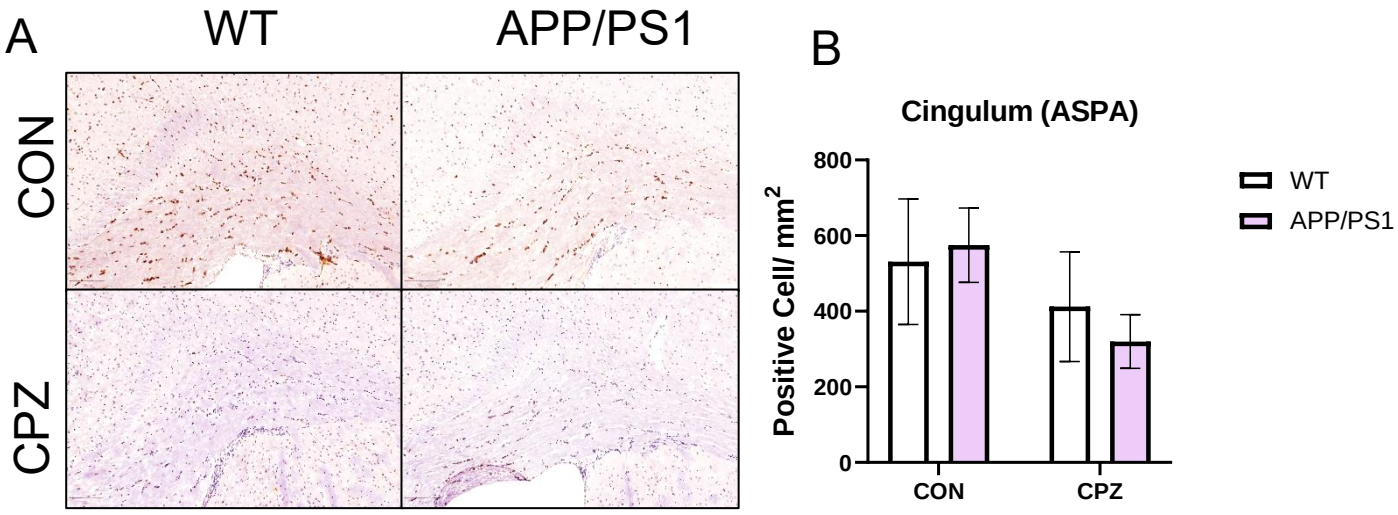

Figure 60: Chromogenic immunohistochemistry using the mature OL marker, ASPA, reveals the OL population within the cingulum. Images of the region of interest based on genotype and diet show representative densities of the OL population (A). Quantifications based on the number of positive cells per mm2 are shown between same diets (B). All values are of two-way ANOVA mean ± SEM. (WT-CON, n=4; WT-CPZ, n=4; APP/PS1-CON, n=7; APP/PS1-CPZ, n=7).

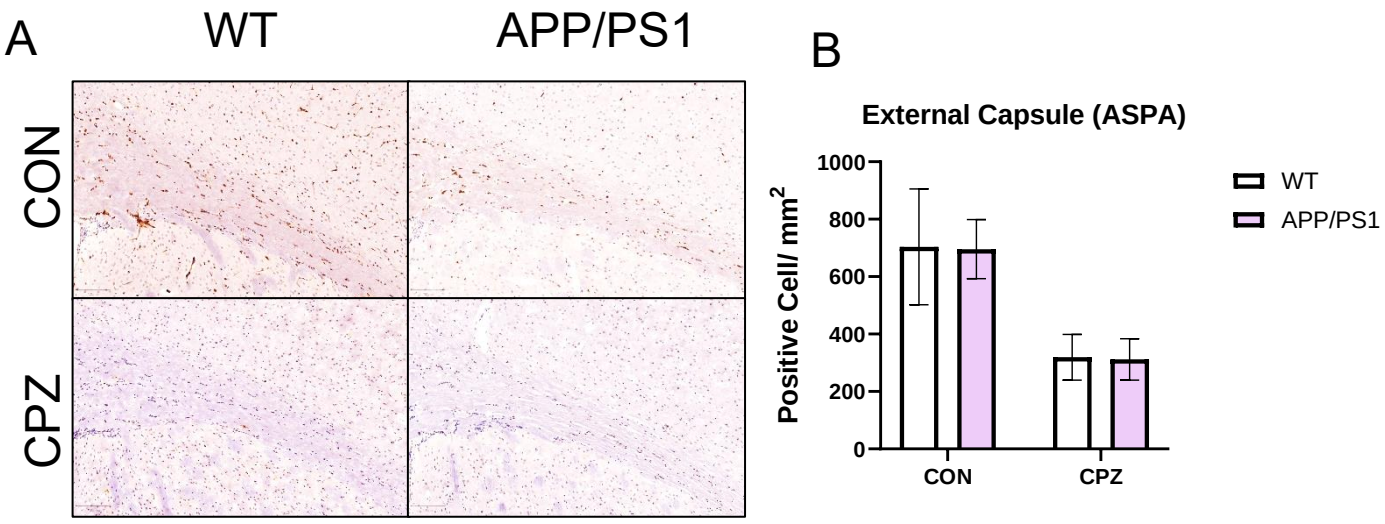

Figure 61: Chromogenic immunohistochemistry using the mature OL marker, ASPA, reveals the OL population within the external capsule. Images of the region of interest based on genotype and diet show representative densities of the OL population (A). Quantifications based on the number of positive cells per mm2 are shown between same diets (B). All values are of two-way ANOVA mean ± SEM. (WT-CON, n=4; WT-CPZ, n=4; APP/PS1-CON, n=7; APP/PS1-CPZ, n=7).

Finally, the relative amount of DNA damage is quantified with reference to the 53BP1 marker. Previously, it was shown that mutation of the APP gene in R1.40 exhibited a more severe increase in cortical DNA damage correlating to its decreased APC-CC1 mOL numbers. Grey matter 53BP1 level show different fluctuations in all three regions. Anterior cingulate show no change in 53BP1+ cell numbers. In the motor and somatosensory cortex, though, there are reductions of APP/PS1 CPZ 53BP1+ cells compared to control diet with the motor cortex yielding significance (-51.1%, p=0.0472). Regarding the white matter tract, the WT with control diet in the genu and external capsule shows the lowest 53BP1+ cell numbers compared to similar elevations of the WT with CPZ diet and APP/PS1 with control and CPZ diets. Within the cingulum, the APP/PS1 of both diets show an increase in 53BP1+ cells. These results suggest increased DNA damage in the APP and PS1 mutation animal both intrinsically and under demyelinating diet.

IHC analysis is able to show the effects of fAD mutations and CPZ diet on the cell status in the brain. It is seen that the molecular status of myelin contrasts the radiological status of DKI. While DKI provides consistent affirmation of APP/PS1's better health due to its lower diffusivities, IHC showed the demyelinated toll of the myelin structure with both APP/PS1 and CPZ independently reducing the PLP levels. In addition, this decrease in PLP level is effectively correlated to the parallel reduction in both gross and mOLs. Similarly to R1.40, the reduction of OLs is most apparent in the grey matter, with mOLs showing the most significant change. However, the amount of DNA damage is most pronounced in the white matter tract even though it does not yield significance. Altogether, this investigation suggests that OLs are vulnerable to DNA damage and that the OLs' decrease, especially of the mOLs, may be reflected in the lower myelin densities of the grey matter.

3.5 Metabolite levels detected with magnetic resonance spectroscopy

Magnetic resonance spectroscopy (MRS) detects biochemical changes in the brain. All MRI-acquired quantification analysis were done with no preference towards left or right hemispheres. All mirror structures (cingulum, external capsule, and hippocampus) were analysed and averaged for each figure by the MATLAB code. The investigation here will look at six distinct chemical peaks associated with AD and lipid changes: glutamate/glutamine, N-acetylaspartate (NAA), choline, myo-inositol, lipid, and lactate (Figure 62A). The neurotransmitters, glutamate/glutamine and NAA, show unaffected levels between genotypes and diet (Figure 63B and 63D). Choline, the precursor to acetylcholine, has a vital role that impacts acetylcholine and dopamine levels, both of which is associated with neurodegeneration. The influence of APP and PS1 mutations exhibits an increased choline level in the control diet of WT (+10.7%, $p=0.0092$) and R1.40 (+17.1%, $p=0.0026$) (Figure 62C). Myo-inositol, a metabolite located mainly in glial cells, and lactate, a metabolite associated with axonal upkeep and lipid metabolism, both show unchanged levels among all mice (Figure 62F and 62G). However, lipid levels show many changes. In the R1.40, there is a significant drop of control diet lipid levels with CPZ diet (-67.1%, $p=0.0047$) (Figure 62E). Within CPZ diet, R1.40 shows severe reduction when compared to WT (-71.3%, $p<0.0001$) and APP/PS1 (-71.1%, $p<0.0001$). Diffusion kurtosis imaging (DKI) of the identical 3x3x3 mm area show no differences in diffusivity modalities (Figure 63-66).

Major changes in the lipid metabolite suggests the effects of genotype and diet. Comparison of control diet, while non-significant, shows APP/PS1 having a higher lipid content than WT and R1.40. Inclusion of CPZ shows drastic reduction of lipid levels in R1.40 while WT and APP/PS1 remains levelled. Furthermore, R1.40 exhibits a stronger reaction towards the diet change. Concurrently, other neurodegenerative metabolites display no change. These results suggest not only R1.40's intrinsic lipid vulnerability but also demyelination's varying effects on different genotypes.

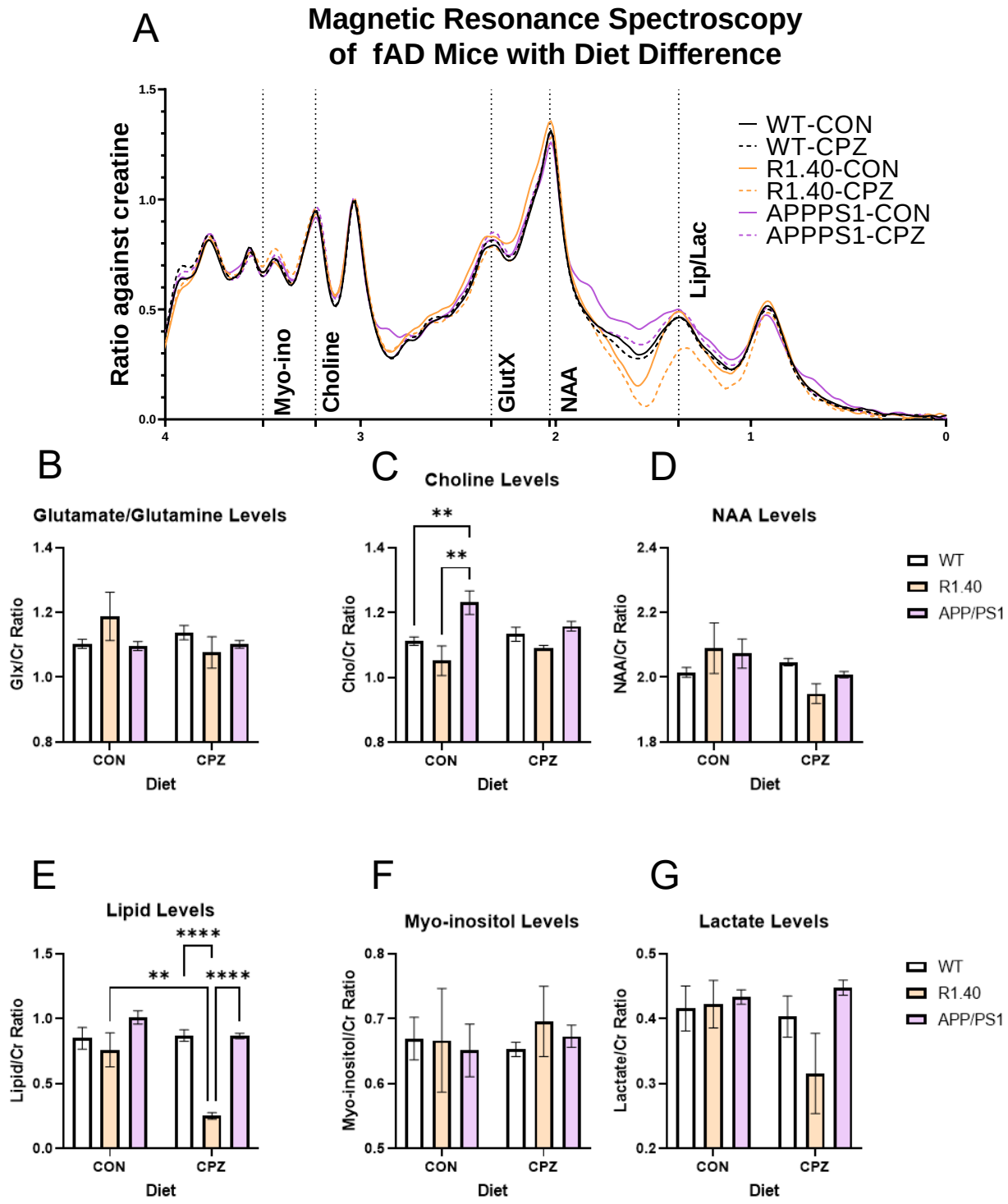

*Figure 62: The mean curve of MRS value is presented as an overall comparison of peak values (A). The location of the volume encompasses the cortex, corpus callosum, hippocampus, and thalamus of the left hemisphere within a 3 × 3 × 3 mm cube between Bregmas -4.7 to -1.8. Area under curve for metabolites of interest are independently compared at their respective peaks and standardized with creatine (B-G). Analysis suggests no significant changes of glutamate/glutamine (B), NAA (D), myo-inositol (F), and lactate (G) levels between genotypes nor diet. However, choline levels of the APP/PS1 with control diet are significantly elevated compared to all groups (C). Additionally, lipid levels of the R1.40, in either diet, are markedly reduced (D). Significant differences of two-way ANOVA between genotype and diet are indicated by asterisks: *p < 0.05, **p < 0.01, ***p < 0.001, ****p < 0.00001. All values are of two-way ANOVA mean ± SEM. (WT-CON, n=8; WT-CPZ, n=8; R1.40-CON, n=3; R1.40-CPZ, n=2; APP/PS1-CON, n=7; APP/PS1-CPZ, n=7).*

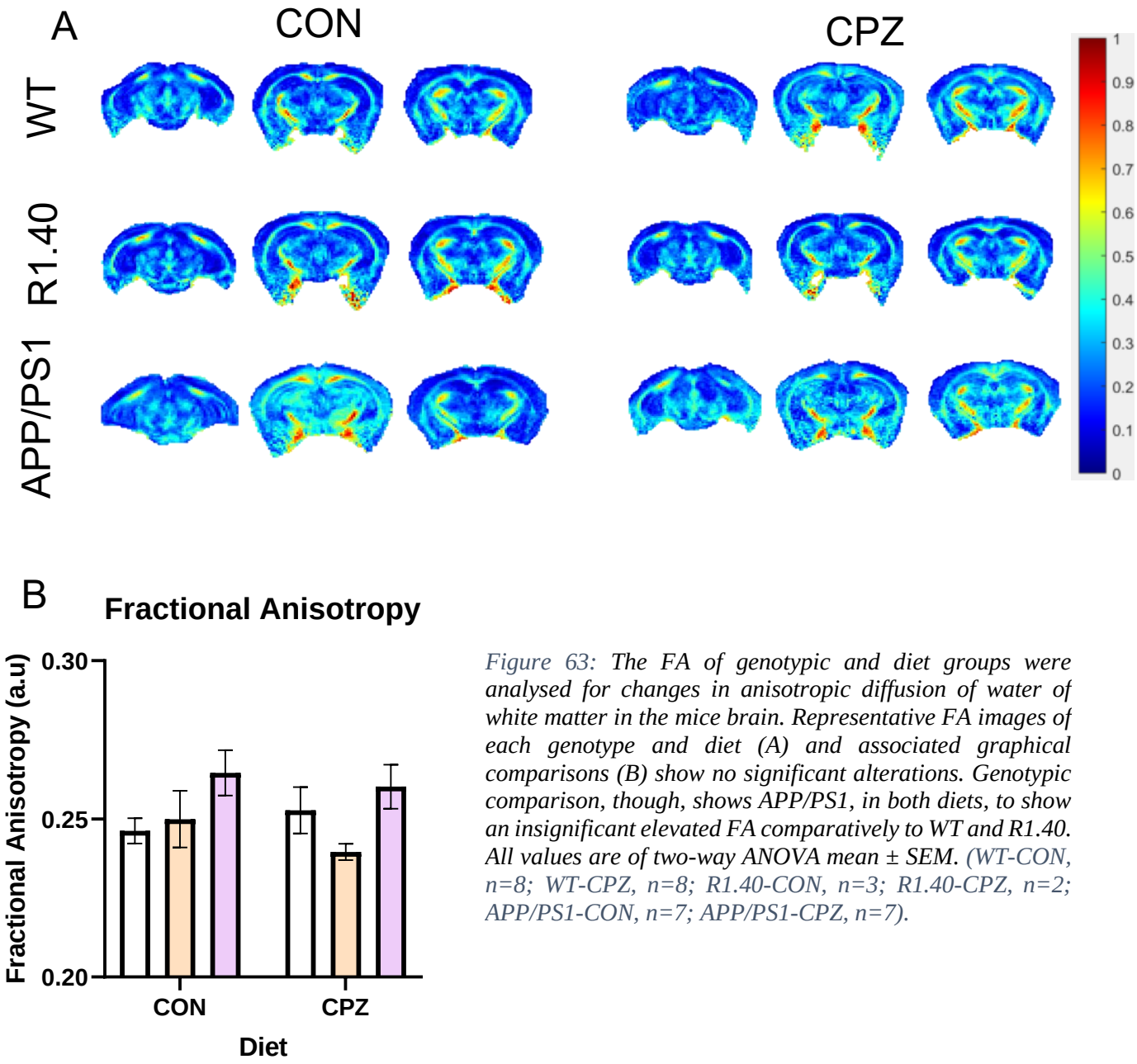

Figure 63: The FA of genotypic and diet groups were analysed for changes in anisotropic diffusion of water of white matter in the mice brain. Representative FA images of each genotype and diet (A) and associated graphical comparisons (B) show no significant alterations. Genotypic comparison, though, shows APP/PS1, in both diets, to show an insignificant elevated FA comparatively to WT and R1.40. All values are of two-way ANOVA mean ± SEM. (WT-CON, n=8; WT-CPZ, n=8; R1.40-CON, n=3; R1.40-CPZ, n=2; APP/PS1-CON, n=7; APP/PS1-CPZ, n=7).

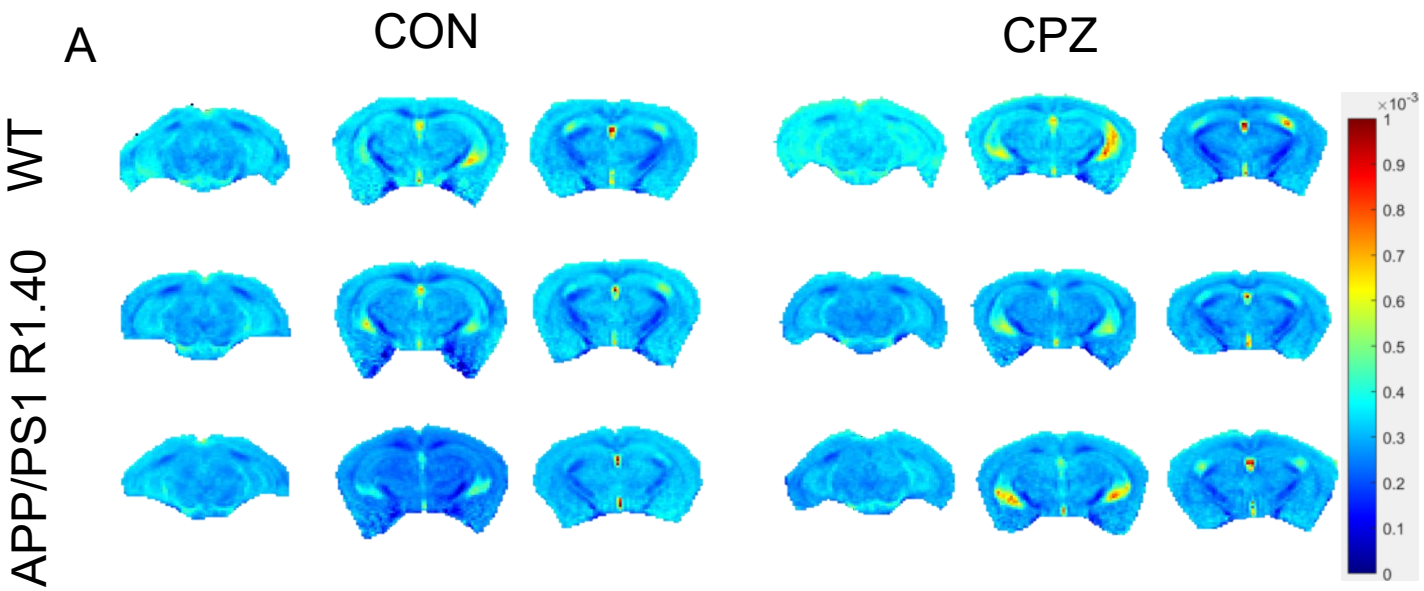

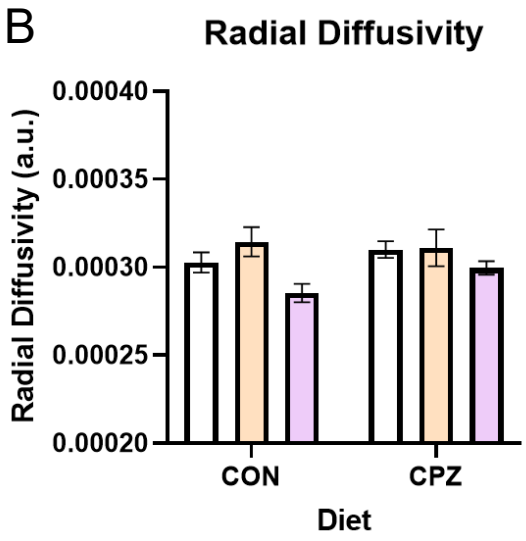

*Figure 64: The RD of genotypic and diet groups were analysed for changes in perpendicular diffusion of water of white matter in the mice brain. Representative RD images of each genotype and diet (A) and associated graphical comparisons (B) show no comparable significant alterations. *p < 0.05. All values are of two-way ANOVA mean ± SEM. (WT-CON, n=8; WT-CPZ, n=8; R1.40-CON, n=3; R1.40-CPZ, n=2; APP/PS1-CON, n=7; APP/PS1-CPZ, n=7).*

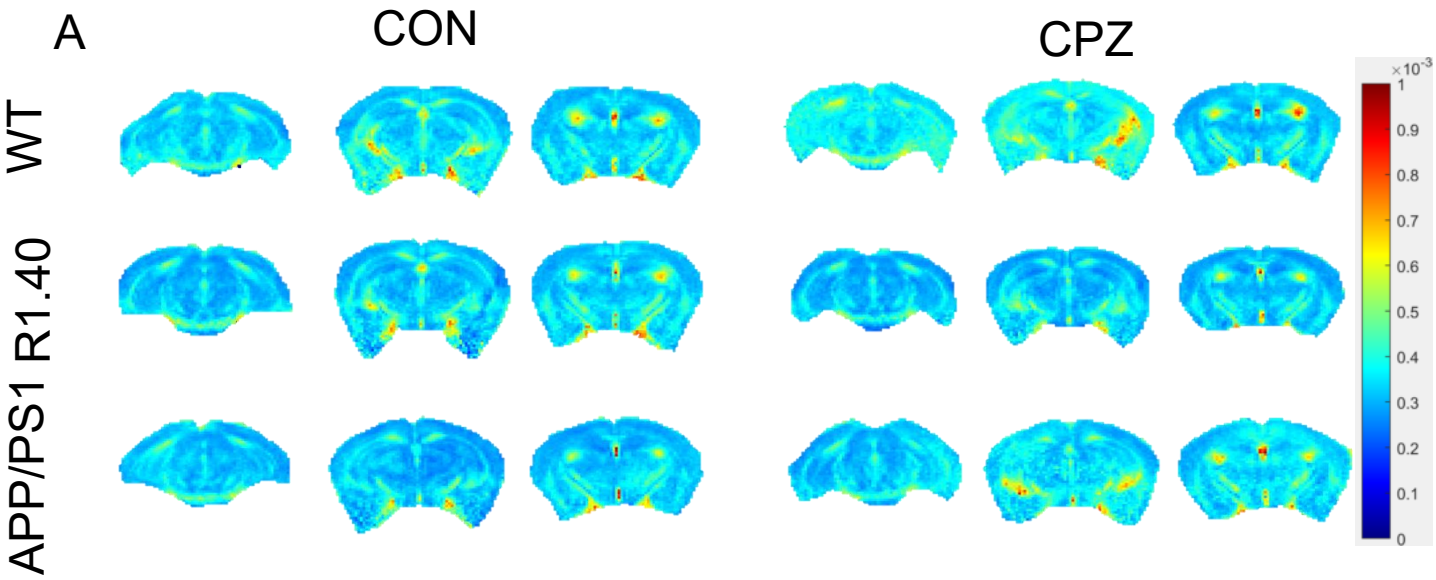

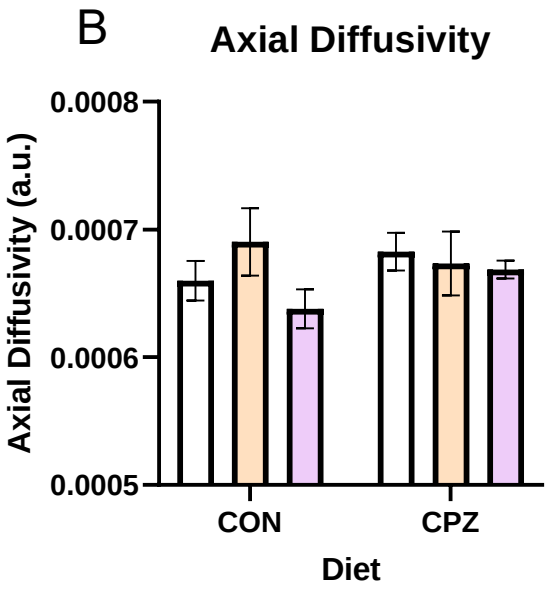

Figure 65: The AxD of genotypic and diet groups were analysed for changes in axial diffusion of water of white matter in the mice brain. Representative AxD images of each genotype and diet (A) and associated graphical comparisons (B) show no comparable significant alterations. All values are of two-way ANOVA mean ± SEM. (WT-CON, n=8; WT-CPZ, n=8; R1.40-CON, n=3; R1.40-CPZ, n=2; APP/PS1-CON, n=7; APP/PS1-CPZ, n=7).

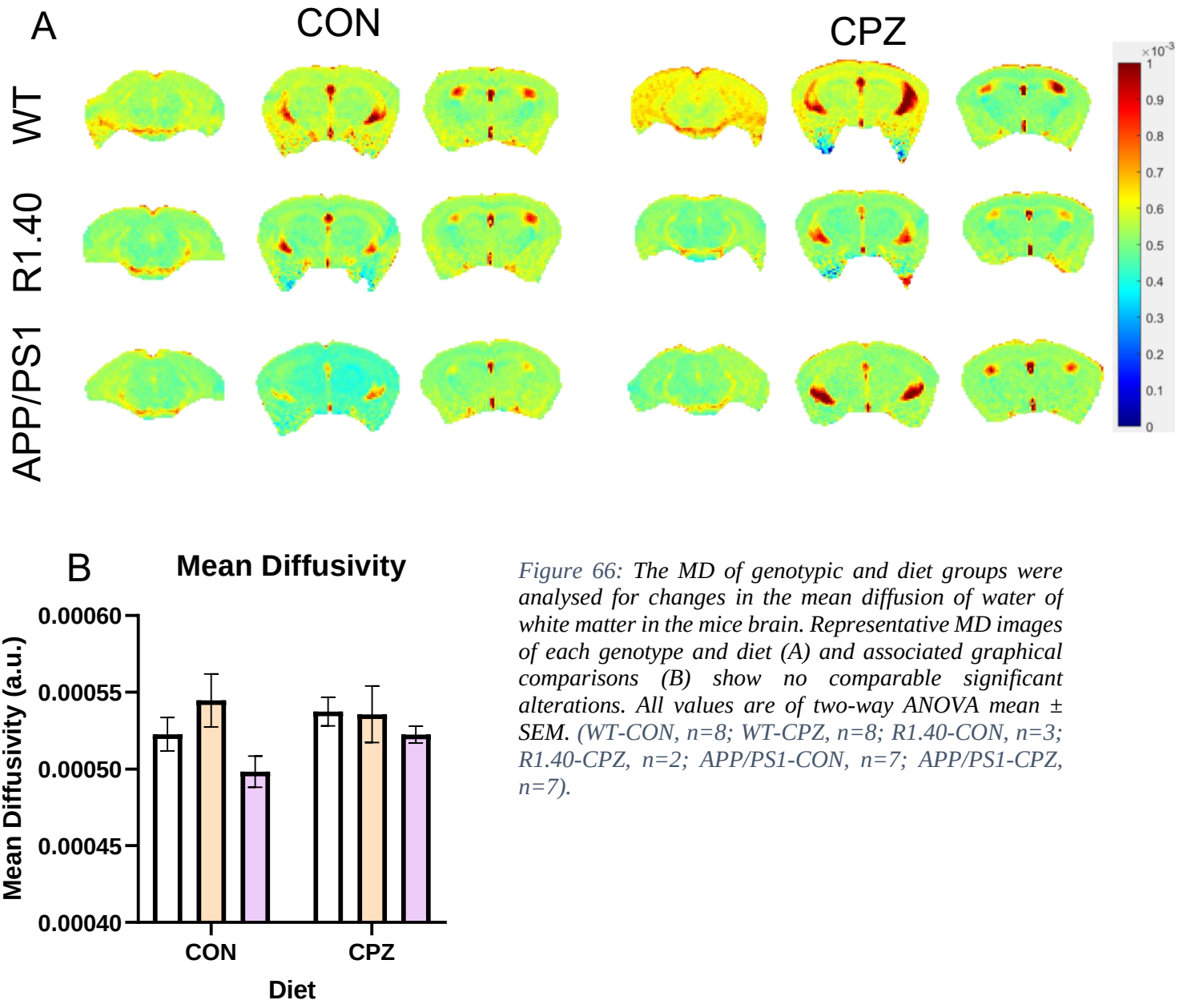

Figure 66: The MD of genotypic and diet groups were analysed for changes in the mean diffusion of water of white matter in the mice brain. Representative MD images of each genotype and diet (A) and associated graphical comparisons (B) show no comparable significant alterations. All values are of two-way ANOVA mean ± SEM. (WT-CON, n=8; WT-CPZ, n=8; R1.40-CON, n=3; R1.40-CPZ, n=2; APP/PS1-CON, n=7; APP/PS1-CPZ, n=7).

3.6 Behavioural analysis of APP expressing mice with Y-maze

Working memory was then studied using a three-pronged y-maze to reveal APP/PS1 underlying cognitive alterations from the effects of amyloid deposition and acute demyelination. R1.40 mice did not undergo behaviour tests due to the limitations of mice movement from HKUST and PolyU. The behaviour test is separated into the analysis of reference memory and episodic memory. The spontaneous alternation, distance travelled, movement speed, time of immobility, and total entries were measured for reference memory as all three arms of the maze were opened during this eight-minute trial (Figure 67A). Comparatively, the total entries, total correct entries, and percentage of time in the correct entry were measured for episodic memory as this trial is separated into a four-minute trial period where one arm was closed and a consecutive four-minute trial after one hour where all arms were opened (Figure 68A).

During the reference memory trial, the spontaneous alternation between WT and APP/PS1 did not exhibit much difference. The CPZ treated cohort, though, show slight increases compared to control diet (Figure 68B). Movements of the CPZ mice also show increases with APP/PS1 mice displaying significance against WT in distance travelled (+49.9%, p=0.0088) (Figure 67C) and movement speed (+50.4%, p=0.0076) (Figure 67D). APP/PS1 mice of both diets also show overall increased movements. Correlatingly, the time immobile decreased is less in the APP/PS1 mice (Figure 67E). Consequently, the total amount of entries into different arms is greater in the APP/PS1 mice (Figure 67F). Through this first trial, it is shown that while neither mouse exhibited observable cognitive changes, APP/PS1's activity is greater than WT's.

For episodic memory, mice's preference for novelty was tested after a training period where one arm was closed and re-opened after a one-hour rest. After the one-hour rest, the mice were placed back into the maze to see if their movement patterns towards the previous opened and closed arms would change. Similarly, to the reference test, APP/PS1 mice of both diets show increases in their total entries (Figure 68B). The percentage of entries into the correct (previously closed) arm shows no change (Figure 68C). However, the time spent in this correct arm shows an unsignificant elevation in the WT treated with

CPZ (Figure 68D). Episodic memory results suggest no cognitive alterations between both genotypes and diets as all four conditions show minimal changes.

Observable cognitive changes are not apparent after two working memory trials. Even though there are differences in the movement of the APP/PS1, neither its spontaneous alternation nor preference for novelty is altered between genotypes and diets. These results suggest that at only 3MO, the APP/PS1 mutations and acute demyelination through CPZ have not influenced the memory of mice. However, the mutations seemingly increase movement activity. Both R1.40 and APP/PS1 mice have previously been observed to have cognitive deficits by 21 and 9 months, respectively (314). This is consistent with our y-maze results where spontaneous alternation was unaffected in the control treatment WT and APP/PS1 mice. While many studies have shown cognitive deficits using y-maze (322, 323), other studies have shown no differences in y-maze (324, 325). It was proposed that complete demyelination happens between 5 and 6 weeks of treatment (326, 327) as lesser time has shown no change in myelin content especially in the hippocampus (325).

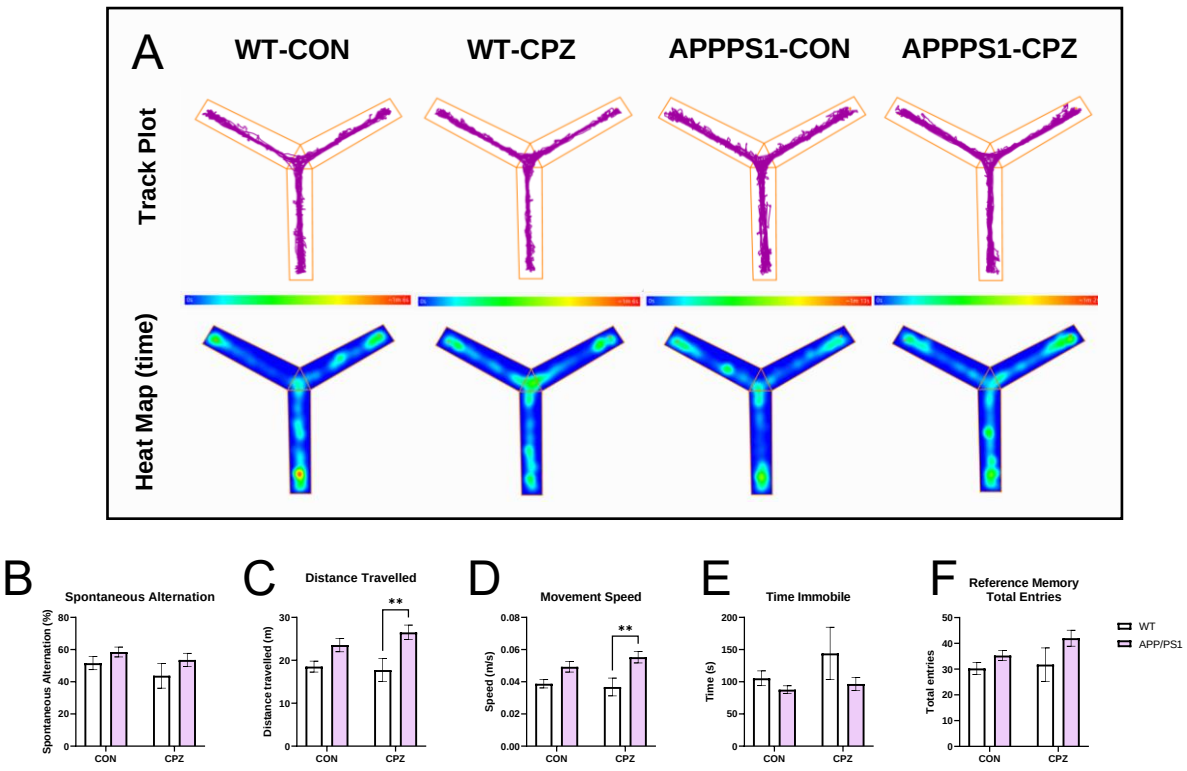

*Figure 67: Working memory was investigated with Y-maze behaviour test and separated into reference memory (A-F) and episodic memory (Next fig). Movement (top A) and heat (bottom A) maps of mice in reference memory shows no particular preference for each arm. Analysis of the spontaneous alternation (B), distance travelled (C), movement speed (D), time immobile (E), and total arm entries (F) from this trial suggest APP/PS1's increased activity with minimal influence from diet. Significant differences of two-way ANOVA in behaviour between genotype and diet are indicated by asterisks: **p < 0.01. All values are of two-way ANOVA mean ± SEM. Heat maps are of scalars with no set values. (WT-CON, n=4; WT-CPZ, n=4; APP/PS1-CON, n=7; APP/PS1-CPZ, n=7).*

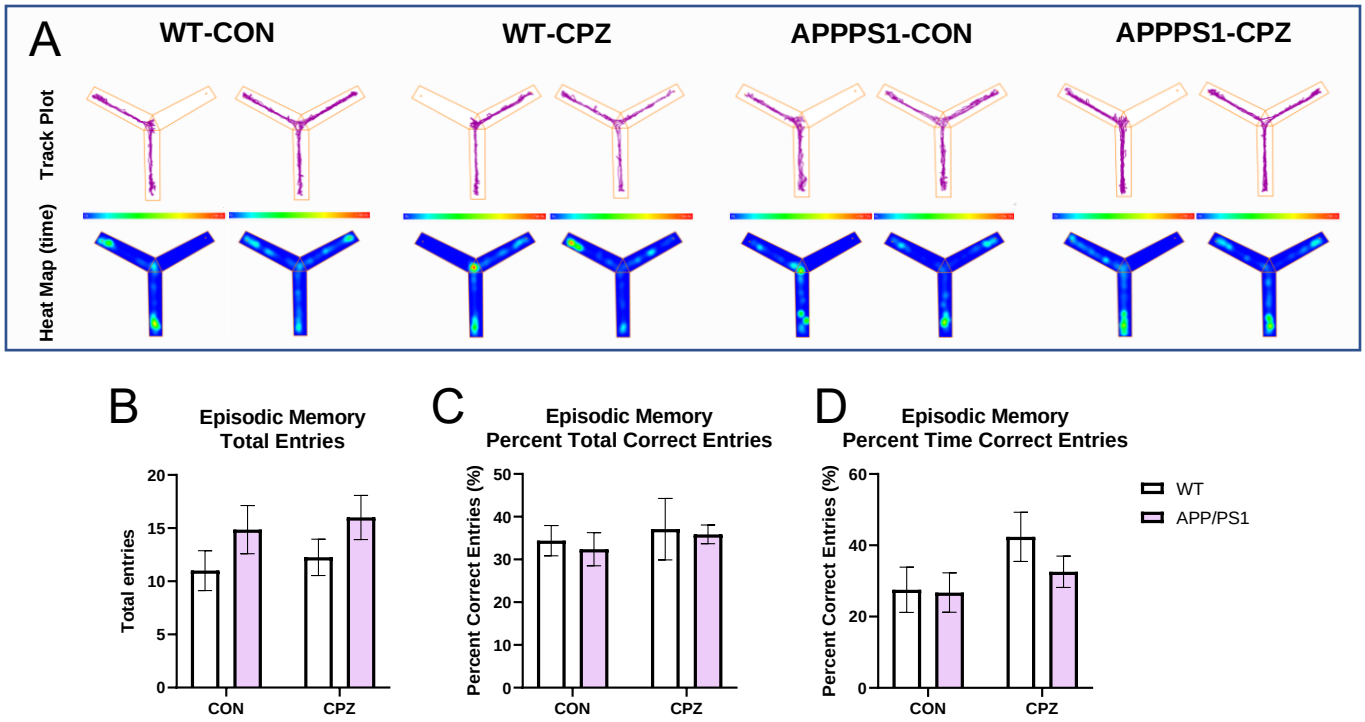

Figure 68: Examination of episodic memory was further divided into a training phase where an arm was blocked (left A) and acquisition phase where all arms were open (right A). Mice were allowed 1hr of resting time away from the maze between phases. No significant impairments of episodic memory were found regarding the mice's preference for arms. All values are of two-way ANOVA mean ± SEM. Heat maps are of scalars with no set values. (WT-CON, n=4; WT-CPZ, n=4; APP/PS1-CON, n=7; APP/PS1-CPZ, n=7).

3.7 Discussion: Demyelination accelerate amyloid pathology in transgenic mouse models

The presence of amyloid plaques is the hallmark of AD. While many symptoms of AD such as dementia and cognitive impairments have become synonymous with the neurodegenerative disease, other disorders such as Parkinson's and multiple sclerosis exhibit similar symptoms. As such, it is possible that a broad spectrum of neurodegenerative events may contribute to the symptoms of AD. Here, we employed two amyloid plaque mice models in addition to a demyelination diet, cuprizone, to assess the extent in which demyelination could affect AD progression.

Radiological analysis by genotype shows contrasting effects from R1.40 and APP/PS1 mice. With the control treatment, R1.40 shows intrinsic higher diffusivities with lower FA values compared to WT and APP/PS1. Based on the amyloid cascade hypothesis, the R1.40 should not exhibit amyloid depositions until 16 months, and it is proposed that these depositions would cause the change in brain diffusivity. Hence, we hypothesised that APP/PS1, an early amyloid deposition model, would generate a more severe increase of diffusivity. Instead, we found that the *PS1* gene seems to rescue the effects of APP overexpression. Previous studies have shown the axonopathy effects overexpression of APP without PS1 mutations (328, 329). While the combination of both mutations did drastically increase the overall amyloid deposition, varicosities from axonal swelling were significantly higher in the APP mice compared to double transgenic for APP and PS1. This is consistent with our findings where only overexpression of APP (R1.40) resulted in a more diffusive brain. FA measurements show no difference among genotypes and treatment groups as previous studies have also not found DTI-acquired FA differences with or without cuprizone (330). This unchanged result may be caused by the sensitivity in detecting micro-changes in the anisotropy of the white matter tract as the white matter change using cuprizone may not be as large. In contrast, AxD shows significantly higher diffusivity especially in white matter regions compared to grey matter regions. This may be because of the parallel nature of the white matter tract, in parallel to the AxD modality, resulting in higher AxD figures. This is seen less in grey matter due to the multi-directional fibers with fewer one-directional fibers to utilise the parallel acquisition of AxD.

The addition of cuprizone, though, resulted in divergent trends in the models. It is proposed that because cuprizone is a demyelinating treatment, the reduction in myelin would expose naked axons and promote axonal leakage. Indeed, previous studies have shown that myelin proteins promote axonal transport. PLP/DM20-deficiency causes early impairments of axonal transport verified by axonal diameters. Additionally, *shiverer* mice lacking MBP also show accumulations and swelling in axons (331, 332). While this is consistent in the WT and APP/PS1 mice where directional diffusivities are increased among grey and white matter tract regions, R1.40 diffusivity shows opposing trends with the addition of cuprizone correlating to a decrease in directional diffusivities. The reasoning for this is unknown and warrants for further investigation.

Further analysis of metabolites shows significant elevation of APP/PS1 choline compared to other genotypes. As stated previously, choline has a vital role in producing acetylcholine and maintaining cell membrane integrity (333). High levels of choline may indicate an accumulation of unprocessed metabolites, leading to lowered levels of acetylcholine. As the reduced levels of acetylcholine of AD patients have been widely studied and the neurotransmitter's supplementation has rescued AD symptoms, its precursor may provide clues to one of many aspects of the disease. Previous study has shown that APP/PS1 mice show reduced cholinergic neurons and hippocampal and cortical acetylcholine levels (334). Our findings of an increased choline level may suggest an inhibition of the production of acetylcholine through the APP and PS1 mutations. Regarding the correlation between the observed increase in choline levels against the theoretical reduction in acetylcholine, a previous study has coined this the choline-leakage hypothesis (335, 336). According to this theory, an increase in amyloid-beta caused by the increase in APP could cause choline leakage out of a cell. This leakage reduces acetylcholine production, leading to symptoms of Alzheimer's. Because MRS does not differentiate between intracellular or extracellular choline signals, it is assumed that it is the overall choline amount. With more extracellular choline due to cell deaths, it is possible that surrounding cells may compensate the decrease in choline levels. However, cuprizone treatment does not affect such levels. Lipid levels, though, show severe reductions only in R1.40 mice.

4.0 APOE4 is detrimental to myelination and oligodendrocyte in the aging brain

4.1 Experimental Design

While age is the greatest risk factor for AD, APOE4 stands as the greatest genetic risk factor for sporadic AD. Apolipoprotein ε's role as a lipid transporter in the brain, therefore, may affect the production of the myelin sheath, an insulating layering of lipids on axons that aid in action potential propagation. OLs are hypothesized to be negatively affected by the change in APOE isoform, hindering their abilities to effectively myelinate. To investigate the influence of both age and APOE status, transgenic mice for *Apoe*$^{-/-}$, hAPOE3$^{+/+}$, and hAPOE4$^{+/+}$ were compared with wild-type C57BL/6 at the ages of 6-, 12-, and 16-months old. Mice are then analysed for cognitive function (Y-maze), axonal diffusivity (MRI), and OL lineage survivability. Results were collected to draw correlations between the influence of age and APOE status on weight, OL, DNA damage, and myelin.

4.2 Effects of Braak staging and APOE status on human myelin content

To relate myelin structure with AD, sAD patients in various Braak stages and fAD patients in Braak VI were first analysed for myelin densities using MBP. Human cortical post-mortem tissues for APOE4 status and Braak staging were analysed at grey and white matter regions (Figure 69A). Analysis of cortical thickness showed no effect by Braak staging nor APOE4 status (Figure 69B). However, at higher Braak stages (V-VI), MBP^{+} intracortical myelin fibres are significantly less dense in both sAD and fAD patients with no influence from APOE4 allelic status (Figure 69C). Observational analysis of myelination in the grey matter, separated into different layers (M1-6), shows distorted myelin fibres with increasing Braak stages of sAD and fAD (Figure 69D). Patches without myelin seen in higher Braak stages may indicate the presence of amyloid plaques. Enlarged views of layers M4-5 show similar myelin densities among groups and clear circular zones of no myelin in the fAD sample (Figure 69G). In addition, while grey matter myelination shows no difference among Braak and APOE4 status (Figure 70E), overall white matter MBP^{+} intensities in V-VI are lower than Braak 0-IV showing a negative correlation between Braak stage and myelin quantities (Figure 69F). However, differentiation of samples for *APOE4* isoform in sAD shows lack of changes in myelin densities. These results may

indicate that while APOE4 status may not affect myelin densities in AD patients, the severity of Braak staging does.

Further analysis of the OL lineage within the frontal cortex shows contradicting results to myelin. Gross OL populations in GM and WM using Olig2 show no changes in OL numbers based on Braak staging (Figure 70A). Yet, sAD carriers of *APOE4* exhibit significant reductions of $Olig2^+$ cells in both GM and WM of the frontal cortex (Figure 70B). Corresponding significant reductions are shown using mOL marker, APC-CC1, in the GM and WM of the frontal cortex (Figure 70C). Likewise, APC-$CC1^+$ cells show greatest significance between *APOE4* status and minimally regarding Braak stages (Figure 70D). However, myelin-regulatory factor (MyRF), a key transcription factor for the myelinating OL, shows no significant changes in *APOE4* groups and only significant difference between NC with Braak VI fAD (Figure 70E and 70F). These results combined human results suggest that OL populations may be affected by APOE4 while myelin densities be affected by Braak staging.

Investigation using aging mice transgenic for human APOE were employed to see if the cellular changes were consistent with human samples. The neocortex and corpus callosum were chosen as representative regions for grey and white matter, respectively. Fluorescence staining of the right hemisphere with MBP shows no changes in MBP intensities among WT, hAPOE3, and hAPOE4 mice in both regions (Figure 71A and 71C). This is confirmed with western blots of MBP, MAG, and MOG at 6 months where no significant differences are found in all three protein expressions (Figure 71B and 71D). Staining with Olig2 shows a maintained lower number of $Olig2^+$ OLs in the neocortex of the hAPOE4 mice with significant reductions at 6 months in the corpus callosum (Figure 71E, 71F, and 71G). Moreover, mOLs stained with APC-CC1 show reductions of hAPOE4 by 6 months with significance in the neocortex but no significant difference in the corpus callosum (Figure 71J). This study paralleled that of human samples with OLs being affected by APOE status. Interestingly, the neuronal population is unchanged among the genotypes at 6 months. This study proposed that OL changes appear from 6 months. Further age-dependent pathological changes including white matter integrity, brain diffusivity, and behaviour will be analysed in the coming sections.

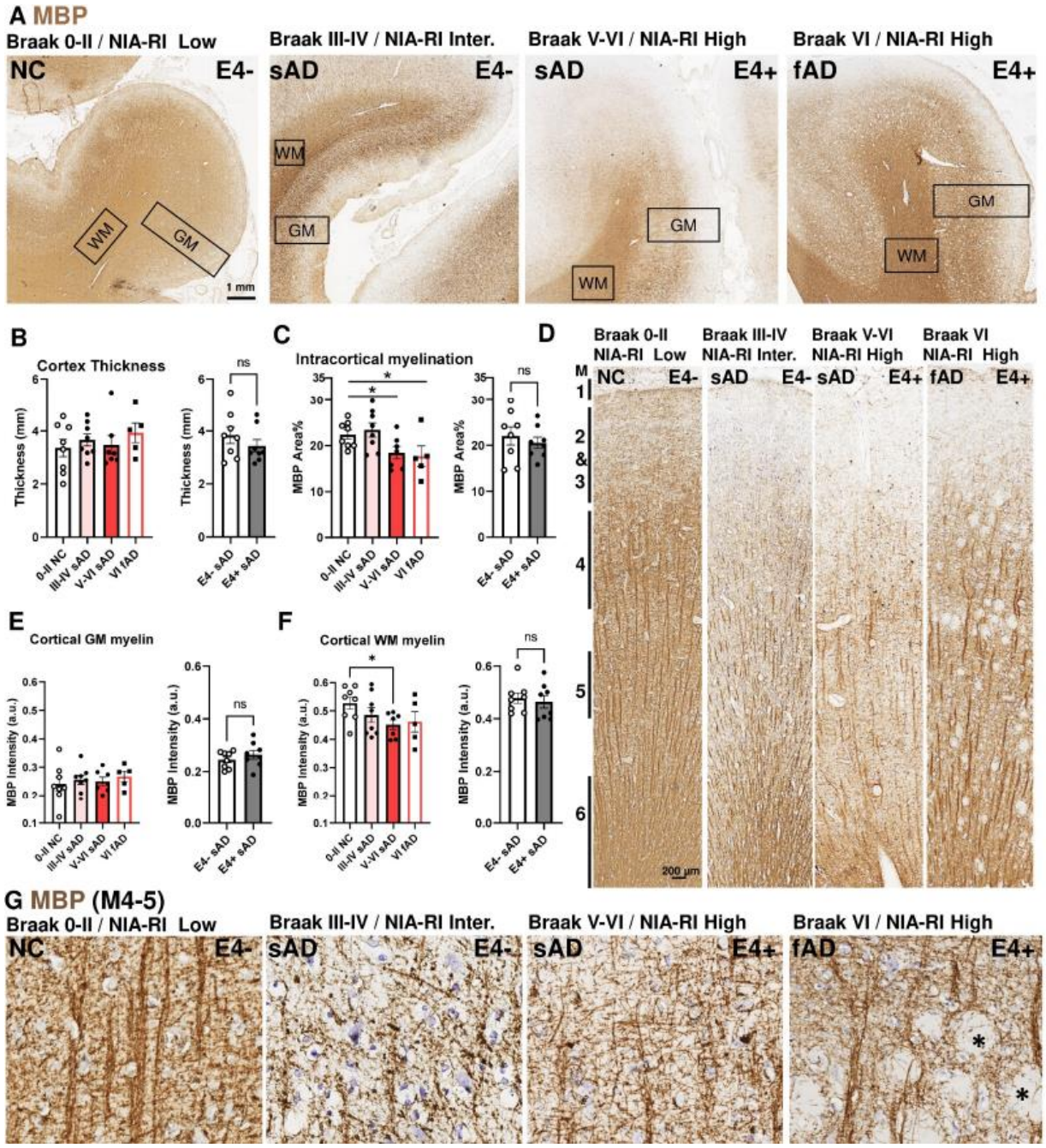

Figure 69: The frontal cortex of human brains in different Braak stages were stained for MBP and differentiated into white and grey matter (A). While cortical thickness cortical thickness among Braak staging and E4 status are consistent (B), intracortical myelination based on MBP per area is significantly reduced in late Braak stages (C). Even though grey matter myelin shows no changes among Braak and E4 status (E), there is a reduced myelination in the late Braak stages of sAD in the white matter (F). Further imaging shows more apparent myelin loss in later Braak staging of different layers of the cortex (D, G). Adapted from (1)

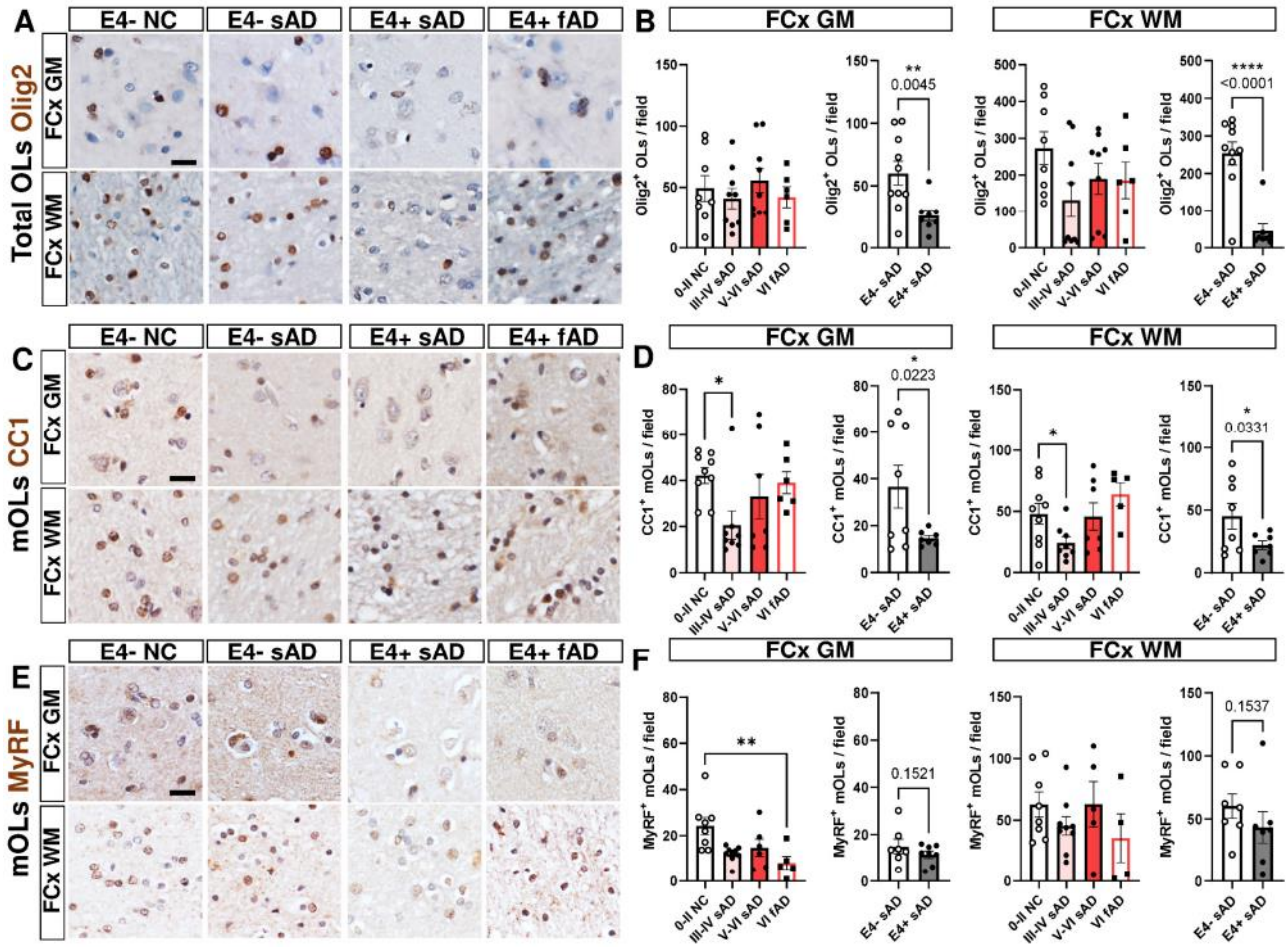

Figure 70: Quantification of gross OL populations with Olig2 show significant reductions in Olig2+ cells in E4 sAD of the grey and white matter in the frontal cortex (A, B). mOLs stained with CC1 also show significant decreases with E4 isoform (C, D). However, myelinating OL stain, MyRF, shows minimal changes in positive cells (E, F). Adapted from (1)

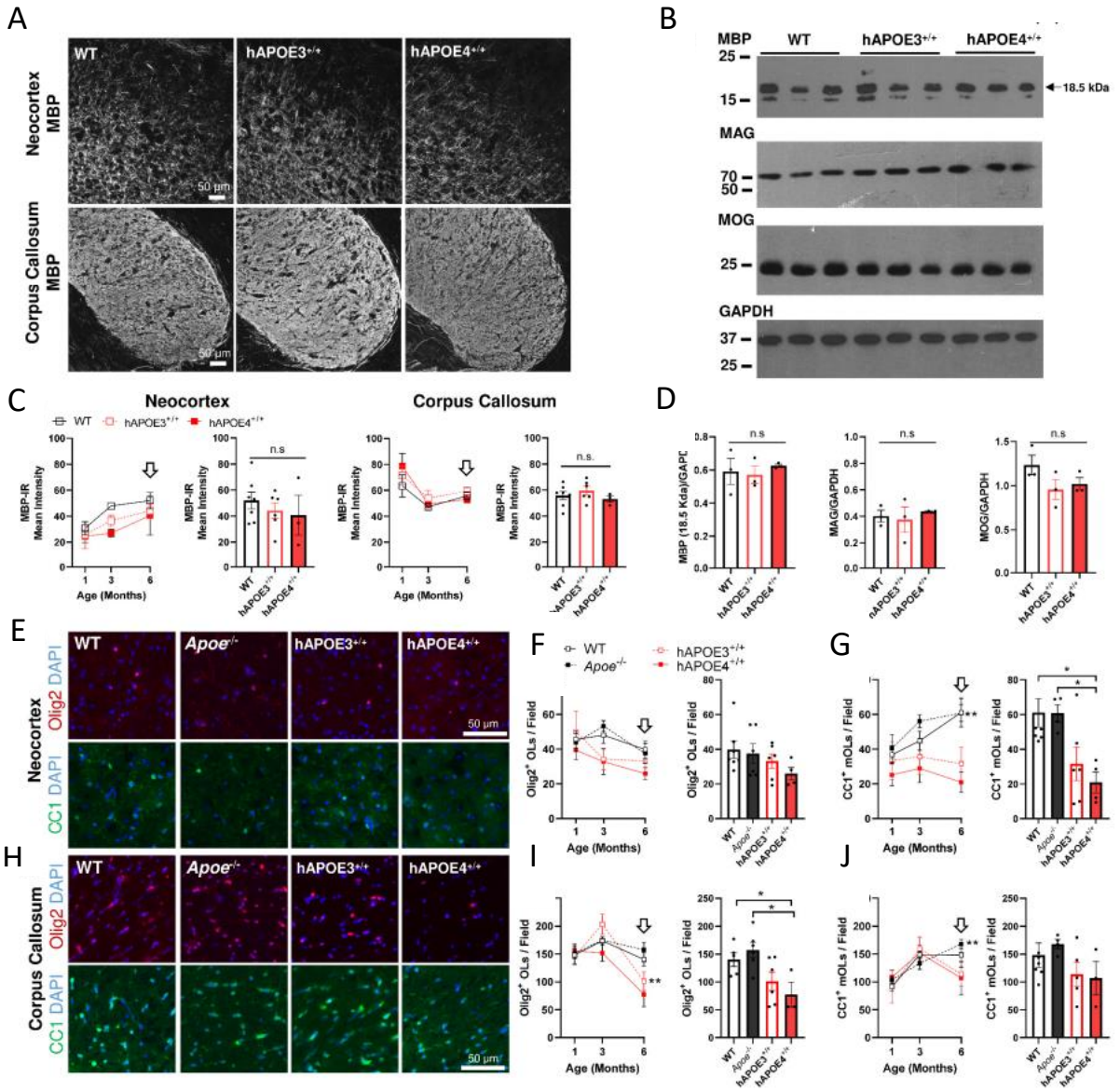

Figure 71: IHC-IF and western blot analysis show no changes in myelin protein levels among hAPOE transgenic mice (A-D). Age- and genotype-based comparisons of the neocortex (grey matter) and corpus callosum (white matter) show differing levels of OL lineage changes. While gross OL populations remain unchanged among ages and genotype in the neocortex, there is a significant reduction of Olig2+ cells in the corpus callosum by 6MO (E, F, H, I). Similarly, CC1+ mOLs show significant reductions in the neocortex (G) but not in the corpus callosum (J). Adapted from (1)

4.3 Age- and genotype-based weight differences

Age-dependent weight changes are correlated to the APOE due to its intrinsic role as a systemic lipid transport. Over 16 months, mice of four genotypes (WT, *Apoe*$^{-/-}$, hAPOE3, and hAPOE4) were allowed to mature with *ad libitum* control diets and weighed before sacrifice to see the effects of aging and APOE status on weights. Mice weights were recorded at 3, 6, 10, 13, and 16 months. No measurements of food and daily activity for APOE cohort were calculated.

A comparison of weights based on genotype shows no significant differences among different ages (Figure 72). While all mice exhibit gradual increases in weight with age, only hAPOE4 mice show significant increase between adjacent age groups of 10MO against 6MO (+35.6%, $p<0.0001$). As such, weights are then analysed within each age group to see if there are genotypic differences within identical ages. Among ages, 10MO shows significant increases of hAPOE4 weights against WT (+33.6%, $p<0.0001$), *Apoe*$^{-/-}$ (+28.0%, $p<0.0001$), and hAPOE3 (+22.1%, $p<0.0001$). However, by 13 and 16MO, mice weights fall and converge.

The trend of age and genotype dependent changes in weight shows hAPOE4's overall heavier status with WT, *Apoe*$^{-/-}$, and hAPOE3 showing similar weights throughout the mice's lives. In addition, while all mice maintained similar weights in the early stages from 3 to 6 months, by 10 months, the significant weight increase of the hAPOE4 suggests the influence of the isoform on lipid accumulation. Even though it is not shown, dissection of sacrificed mice displayed large deposits of adipose tissue.

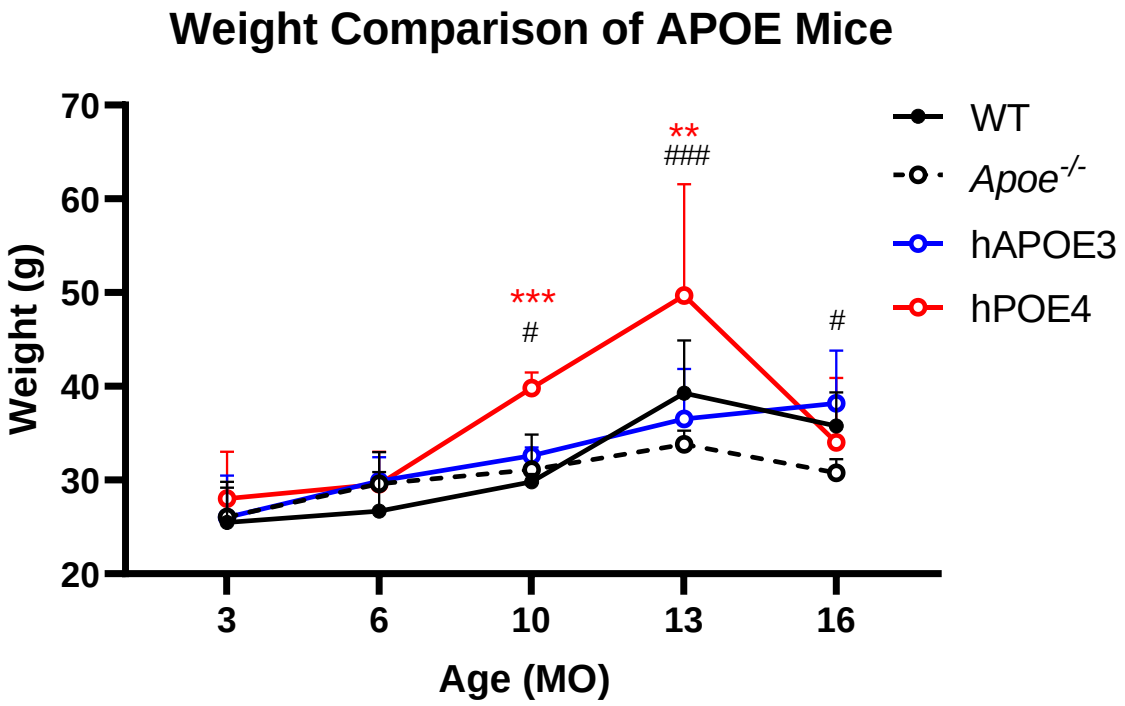

*Figure 72: Transgenic mice for apolipoprotein knock out and humanized apolipoprotein knock ins were aged between 3 to 16 months weighed before sacrifice. All mice weights were measured on the day of sacrifice. Age-dependent analysis shows an overall elevated weight of the APOE4 mice. Statistically significant stars are color-coded according to transgenic genotype against WT. **p<0.01; ***p<0.001. Statistically significant hashes are according to hAPOE4 changes against hAPOE3. #p<0.05; ###p<0.001. All values are of two-way ANOVA mean ± SEM.*

4.4 Diffusivity analysis of aged tgAPOE mice

Age is the greatest risk factor for sAD. As a result, a cross sectional study of its effects at different time points is warranted to track the changes it can have on the brain. To understand the effect of age on diffusivity of the brain independent of APOE genotypes, individual genotypes were first analysed at 6, 10, and 16 months old among three grey matter regions (neocortex, anterior cingulate, and hippocampus) and three white matter tract regions (genu, cingulum, and external capsule). The results of this analysis will propose the effects of age on independent genotypes.

4.4.1 Effect of age on WT mice

FA analysis of the grey matter shows variations among Bregma, age, and region. Overall differences based on Bregma and age are significantly observed ($p<0.0001$ and $p=0.0117$, respectively) in the neocortex. An increasing trend from the medial Bregma -1.3 to 2.7 is consistent among three age groups. While repeating longitudinal FA values of each Bregma show consistent decrease, significance is observed only between 6MO and 16MO (-28.0%, $p=0.0061$) (Figure 73). However, isolated analysis of anterior cingulate shows no changes among age groups and minimal significance in Bregma-based changes ($p=0.0393$) (Figure 74). In the hippocampus, age is a significant factor of FA ($p=0.0131$). Decreases in FA are correlated to the increase in age between 6MO and 10/16MO. Reductions of hippocampal FA are shown between Bregma -2.5 10MO (-29.4%, $p=0.021$) and 16MO (-35.3%, $p=0.0021$) against 6MO and Bregma -1.8 10MO (-26.9%, $p=0.2086$) and 16MO (-26.5%, $p=0.0129$) against 6MO (Figure 75). No changes of that magnitude are found in the frontal hippocampus at Bregma -1.3. Study of the white matter tract show contrasting FA results. While the genu shows an overall age-based significance ($p=0.0387$) (Figure 76), the cingulum shows Bregma-based significance ($p=0.02$) (Figure 77). Neither region exhibits significant changes in FA among Bregmas. Likewise, the external capsule exhibited minimal changes among positions, yet, both Bregma- and age-based factors suggested significance ($p<0.0001$ and $p=0.012$, respectively) as overall FA increased towards the anterior brain (Figure 78).

Perpendicular-based directional analysis (RD) shows preference of the anterior anatomical position. Neocortical comparisons suggest the effects of Bregma and age as significant ($p<0.0001$ and $p=0.0056$, respectively). Corresponding to FA, RD values show a decreasing trend from the posterior Bregma -1.3 to 2.7 among three age groups. Specifically, 10MO shows decrease of RD compared to 6MO in Bregma 2.0 (-11.3%, $p=0.0285$) and 2.7 (-12.4%, $p=0.0148$). Nonetheless, a small increase of RD is found of 16MO compared to 10MO in 2.0 (+6.3%, $p=0.0134$) and 2.7 (+7.1%, $p=0.0099$) (Figure 79). In the anterior cingulate, correlating Bregma 2.0 exhibit similar RD decrease of 10MO against 6MO (-12.6%, $p=0.0156$) and increase of 16MO against 10MO (+6.8%, $p=0.0489$) (Figure 80). Age-based comparison also exhibits significance ($p=0.0247$). However, hippocampal RD shows no significant changes of neither age- nor Bregma-based comparisons (Figure 81). Further RD analysis yield significance in age and Bregma of the genu ($p=0.0221$ and $p=0.0008$, respectively) (Figure 82) and external capsule ($p=0.0284$ and $p=0.0002$, respectively) (Figure 84).

AxD analysis suggests higher sensitivity in the grey matter with this modality. Investigation of the neocortex suggests age is a significant factor in the change among age groups ($p=0.0058$). Medial to anterior cortex show consistent reductions in AxD among the aged 10 and 16MO animals with 6MO. As the AxD decreases in 10MO compared to 6MO in Bregma 2.0 (-15.6%, $p=0.0151$) and 2.7 (-17.3%, $p=0.0362$) and 16MO compared to 6MO in Bregma 0.8 (-11.2%, $p=0.029$) and 2.7 (-16.9%, $p=0.0408$), values between 10MO and 16MO are unchanged (Figure 85). In Bregma 0.0, the anterior cingulate showed similar decreases of 10MO against 6MO (-13.8%, $p=0.0405$) and 16MO against 6MO (-15.1%, $p=0.0257$). This decrease is seen in Bregma 2.0 between 10MO and 6MO (-13.8%, $p=0.0365$). Overall significance is also seen in age ($p=0.0132$) and Bregma ($p=0.0134$) (Figure 86). Unchanged AxD are observed in the hippocampus. Within the white matter tract, the genu showed no age specific changes, yet, AxD is significantly affected by age ($p=0.0407$) and Bregma ($p=0.0001$) (Figure 88). Similarly, the cingulum showed the same significance of age and Bregma with age-specific decreases of 10MO (-11.0%, $p=0.0045$) and 16MO (-10.0%, $p=0.0073$) against 6MO in Bregma -1.3 (Figure 89). Interestingly, while both directional diffusivities have suggested consistent decreases with age up to 10

months, in the external capsule of Bregma 0.0, an increase of 19.8% in AxD is observed in 16MO against 10MO (p=0.0259) (Figure 90).

MD can then be taken between RD and AxD to find an overall diffusivity value. In the grey matter, the neocortex, anterior cingulate, and hippocampus seem greatly affected by age (p=0.005, p=0.0168, and p=0.0478, respectively). Of these three regions, the anterior Bregmas seem the most affected as 10MO and 16MO against 6MO show decreased diffusivities. In Bregma 2.0, both regions exhibit significantly decreased MD of 10MO against 6MO (neocortex, -13.0%, p=0.0145 and anterior cingulate, -13.1%, p=0.0183) (Figure 91 and 92). At the more anterior Bregma 2.7, a corresponding decrease of 14.6% (p=0.0227) is seen in 10MO against 6MO and increase of 4.4% (p=0.0401) in 16MO against 10MO. The hippocampus does not show age-specific MD changes. Of the white matter tract, minimal MD changes are seen in the anterior brain, but the medial Bregma -1.3 does show reductions in the genu (-12.1%, p=0.0468) and cingulum (-12.3%, p=0.0414) (Figure 94 and 95). Consistent with the relationship between 10 and 16MO, the external capsule shows an increase of MD at 16MO against 10MO (+12.6%, p=0.0316) (Figure 96).

The results of WT diffusivity show a comparable trend in decreasing FA values with age. However, directional modalities RD, AxD, and MD suggest a similar decrease in diffusivity with age. Furthermore, many changes are found in the grey matter regions compared to minimal changes in the white matter tract. These results suggest a greater degree of age-dependent white matter changes in the grey matter regions.

4.4.2 Effect of age on *Apoe*$^{-/-}$ mice

The knockout of endogenous mice Apoe is studied to understand the differential effects it has compared to WT and hAPOE. FA is compared across regions and ages of *Apoe*$^{-/-}$ mice. Neocortical comparison shows no changes among age groups and Bregma. However, overall Bregma-based variation among all age groups is significant (p<0.0001) (Figure 73). The anterior cingulate sees the most significance in the medial brain between the later stages in life at 10MO and 16MO. Comparisons of 16MO against

10MO shows Bregma -1.3 exhibiting an increase of 24.6% (p=0.0464) and Bregma 0.0 exhibiting an increase of 43.2% (p=0.0066) with an overall significance in age- and Bregma-based changes (p=0.0442 and p=0.0005, respectively) (Figure 75). In contrast, the FA of the hippocampus sees change during the earlier life between 6 and 10 months. Hippocampal FA comparisons of 10MO against 6MO show significant reductions in Bregma -2.5 (-22.4%, p=0.0343) and -1.8 (-27.7%, p=0.0199) (Figure 76). This change is further reflected in the overall significance of effect from age (p<0.0001) and Bregma (p=0.0044). White matter tract diffusivities are mainly unchanged with significance in Bregma -1.3 between 16MO against 6MO only in the genu (+19.2%, p=0.0256) (Figure 77) and cingulum (+19.5%, p=0.0435) (Figure 78). Despite similar increases of FA between these age groups, the age and Bregma factors does not yield significance in the cingulum but only in the genu (age, p=0.0363 and Bregma, p=0.0176) (Figure 77). In the external capsule, age-specific comparisons exhibited no change although the overall Bregma-based difference is significant (p<0.0001) (Figure 79).

Further RD analysis of the grey matter shows unchanged age-specific levels. Overall Bregma-based differences is observed to be significant in the neocortex (p<0.0001) (Figure 80) and anterior cingulate (p=0.0004) and age-based difference in anterior cingulate (p=0.0193) (Figure 81). Hippocampal RD shows neither factor-based nor age-specific changes (Figure 82). In the white matter tract, all three regions show significant differences of factor by Bregma (genu, p<0.0001; cingulum, p=0.004; external capsule, p<0.0001). Additionally, there are significant reductions of RD in Bregma -1.3 between 16MO against 6MO of the genu (-14.2%, p=0.0126) (Figure 83), cingulum (-14.9%, p=0.0136) (Figure 84), and external capsule (-11.2%, p=0.048) (Figure 85). AxD and MD values similarly show no age changes in all regions, yet all regional Bregma-based differences show significance.

Apoe$^{-/-}$ mice show minimal changes among age groups with unchanged directional diffusivities among regions. Interestingly, age factor does not show effect in DKI analysis. Between grey matter and white matter tract, neither of their regions show consistent changes among Bregmas and age.

4.4.3 Effect of age on hAPOE3 mice

The hAPOE3 mice represent the WT genotype of human APOE. Its effects are used as the standard to both compare with endogenous Apoe and AD risk factor hAPOE4. Bregma-based values are significantly different among all regions except genu and cingulum. Age-based differences are insignificant in all ages and regions. FA values remain unchanged among all ages and regions except external capsule. Significances are observed in external capsule comparisons of 16MO against 10MO in Bregma -1.3 (+14.6%, p=0.0345), 0.0 (+19.4%, p<0.0001), and 0.8 (+14.5%, p=0.0068) (Figure 79).

These unchanged levels among hAPOE3 ages are also present in RD with much of the significance accounted for by overall Bregma differences. AxD analysis, though, show numerous differences in the white matter tract with no significance in grey matter regions. In the genu, Bregma-based AxD differences are significant (p<0.0001) with decrease of 10MO against 6MO in Bregma 0.8 (-11.5%, p=0.0453) and increase of 16MO against 10MO in Bregma 2.0 (+9.8%, p=0.0002) (Figure 89). Even though the cingulum shows no differences, the external capsule shows parallel increases of 16MO against 10MO AxD in Bregma -1.3 (+11.1%, p=0.0021), 0.0 (+19.4%, p=0.0044), and 0.8 (+10.2%, p=0.0014), resulting in overall Bregma significance (p<0.0001) (Figure 85).

Analysis of MD shows similar trend to RD and AxD, with the grey matter mainly unaffected by age. White matter tract regional changes seem to be affected by age. In the genu, while Bregma-based difference is significant (p<0.0001), significance is only yielded in Bregma 2.0 between 16MO against 6MO (+6.2%, p=0.0047) (Figure 94). The trend of decreasing MD with age comparative to previous genotypes is continuously observed in the cingulum. In Bregma 0.8, cingulum MD shows reductions of 10MO (-13.5%, p=0.033) and 16MO (-11.5%, p=0.0309) against 6MO (Figure 95). Interestingly, consistent with previous DKI analysis, the change between 16MO against 10MO is opposite from if the comparison is against 6MO. This is seen in the genu, and in the external capsule, comparison of 16MO against 10MO in Bregma 0.0 shows an increase of MD (+13.7%, p=0.0195) (Figure 96).

Investigation of hAPOE3 mice shows generally unaffected regional grey matter diffusivities among age groups and Bregmas. Changes in the white matter tract are minimal. However, the trend of diffusivity in hAPOE3 exhibit opposite changes between comparisons of 10/6MO and 16/10MO. Despite the steady decreases in directional diffusivities with age seen when compared to 6MO, the change from 10MO to 16MO is an elevation. This consistent trend is seen among all animals.

4.4.4 Effect of age on hAPOE4 mice

The hAPOE4 mice are then evaluated for the effect the isoform protein has on diffusivity. FA analysis of grey matter regions show no age-specific differences, although, Bregma-based differences are significant in neocortex ($p<0.0001$) (Figure 73), anterior cingulate ($p<0.0001$) (Figure 74), and hippocampus ($p=0.0168$) (Figure 75). Greater changes are found in the white matter tract. In the genu, medial Bregma -1.3 shows an FA decrease of 11.3% in 10MO against 6MO ($p=0.04$) (Figure 76). However, anterior Bregma 2.0 shows an increase of 13.6% between 16MO against 6MO ($p=0.0075$). The contrasting trend between Bregma is observed to be significant ($p=0.0333$). This increase is also shown in Bregma 0.0 of the external capsule between 16MO against 6MO (+12.3%, $p=0.0248$) (Figure 78).

Interestingly, RD values show significant changes in the grey matter. All Bregma-based differences are significant, and all Bregma comparisons of 6MO and 10MO in the neocortex and anterior cingulate show significant increases of RD in 10MO. Interestingly, anterior neocortical RD in Bregma 2.0 and 2.7 show the greatest increase of RD (+10.7%, $p=0.026$ and +11.4%, $p=0.0503$, respectively) (Figure 79). Yet, in the anterior cingulate, the medial Bregma -1.3 and anterior Bregma 2.0 show the highest increase of RD (+11.5%, $p=0.0017$ and +10.0%, $p=0.0216$, respectively) (Figure 80). Even though it yields no significance, comparisons of 16MO against 10MO show decreased RD, contradicting 10MO and 16MO against 6MO. However, the hippocampus shows minimal changes, and no changes are detected in the white matter tract regions (Figure 81).

Study of AxD values in the neocortex show significance between 10MO against 6MO in medial Bregma -1.3 (+11.6%, p=0.0387) and 0.0 (+11.7%, p=0.0346) (Figure 85). Anterior cingulate and hippocampus show no age-specific differences. Among white matter tract regions, only the genu exhibits significant changes between 10MO against 6MO in anterior Bregma 2.0 (+12.5%, p=0.0297) and similar percent change between 16MO and 6MO (+9.6%, p=0.0598) (Figure 88).

MD of hAPOE4 suggests grey matter neocortex and anterior cingulate as regions of greatest diffusivity changes. Neocortical FA comparisons of 10MO against 6MO show significant increases in medial Bregma -1.3 (+9.8%, p=0.0115), 0.0 (+9.6%, p=0.0021) and anterior Bregma 2.0 (+9.2%, p=0.0379) (Figure 91). In the anterior cortex, the same significant increases are seen in the same Bregmas between 10MO and 6MO (Figure 91).

Different DKI modality-detected changes suggest their differential sensitivities in hAPOE4 mice. While FA detects most changes in the white matter tract, RD, AxD, and MD detects most changes in the grey matter. Unlike WT, *Apoe*$^{-/-}$, and hAPOE3, aging hAPOE4 mice show increases in diffusivities in the grey matter compared to other genotype's decrease with age. This contrasting trend warrants further investigation into the comparison of genotypes within each age group to understand if these changes are significant.

4.4.5 Effect of genotype at 6MO

Comparison of the four genotypes (WT, *Apoe*$^{-/-}$, hAPOE3, and hAPOE4) at 6MO could suggest the effects of apolipoprotein genotype at an early age equalling to 30 human years. FA analysis of the neocortex among genotypes at 6MO show an exponential curve of FA values from medial Bregma -1.3 to anterior 2.7 with no significance between genotypes (Figure 74). In the anterior cingulate, no changes are seen, yet graphical representation shows similar pattern of FA for WT with *Apoe*$^{-/-}$ and hAPOE3 and hAPOE4 (Figure 74). WT and *Apoe*$^{-/-}$ curves show unchanged values from Bregma -1.3 to 2.0 while hAPOE3 and hAPOE4 show an FA valley at Bregma 0.0 and peak at 0.8. Hippocampal FA in posterior Bregma -2.5 exhibits significant decrease compared to WT in hAPOE3 (-36.0%, p=0.0028) and

hAPOE4 (-26.0%, p=0.0348) (Figure 75). However, white matter tract regional comparisons show no genotypic variations. Additionally, genu and cingulum FA curves show no set pattern, yet the external capsule show an overarching linear FA increase from Bregma -1.3 to 0.8.

Using RD, the grey matter shows the greatest difference against hAPOE4. In the neocortex, overall RD values of WT show distinct high values, *Apoe*$^{-/-}$ and hAPOE3 show overlapping values, and hAPOE4 show distinct low values with significance in medial Bregma -1.3 and anterior Bregma 2.0 and 2.7. In -1.3, hAPOE4 exhibit reductions against WT (-11.5%, p=0.024) and *Apoe*$^{-/-}$ (-9.4%, p=0.0203), in 2.0 against WT (-11.9%, p=0.0352) and *Apoe*$^{-/-}$ (-7.1%, p=0.0073), and in 2.7 against WT (-12.8%, p=0.0213) (Figure 79). Similarly, in the anterior cingulate, the divergent levels of the genotypes are consistent. Likewise, significance is only found between hAPOE4 with WT and *Apoe*$^{-/-}$. Genotypic bases are observed to be significant (p=0.0103) with Bregma -1.3 (hAPOE4 against WT, -11.5%, p=0.0094), 0.8 (hAPOE4 against WT, -8.7%, p=0.0334) and 2.0 (hAPOE4 against WT, -12.8%, p=0.0223 and against *Apoe*$^{-/-}$, -6.9%, p=0.0222) (Figure 80). Interestingly, while no genotypic differences are significant, hAPOE4 hippocampal RD shows lowered values compared to overlapping WT, *Apoe*$^{-/-}$, and hAPOE3 with overall significance in both genotype (p=0.0463) and Bregma (p=0.0468) (Figure 81). White matter tract comparisons shows minimal changes with significance found only in medial Bregma -1.3 between hAPOE4 and *Apoe*$^{-/-}$ (-10.3%, p=0.0449) (Figure 84).

Similarly to RD, in the neocortex and anterior cingulate, WT and hAPOE4 have distinct highest and lowest AxD values, respectively, while *Apoe*$^{-/-}$ and hAPOE3 share similar values. Within the grey matter, AxD of Bregma -2.5 in the hippocampus show reductions of hAPOE3 (-14.8%, p=0.0489) and hAPOE4 (-16.3%, p=0.0332) against WT (Figure 87). Other grey matter and white matter tract regions show no changes. Neocortical MD values share the same distinctions in genotype compared to RD and AxD with genotypic differences only in the neocortex and anterior cingulate. Multiple Bregmas within these grey matter regions show significant MD reductions of hAPOE4 compared to WT and *Apoe*$^{-/-}$. However, white matter tract values show no changes.

In 6MO mice, there are minimal changes in diffusivity of the mice brain. Even though hAPOE4 is considered deleterious to neurological health, the effects it has is mostly against WT and *Apoe*$^{-/-}$. Furthermore, grey matter shows the largest number of alterations based on genotype. While compared to hAPOE3 there are no changes of hAPOE4 diffusivities, hAPOE4's effect on mice is shown to be different to the other genotypes.

4.4.6 Effect of genotype at 10MO

Investigation of 10MO mice show no effect of genotype on FA values in grey matter. The increasing FA pattern seen in 6MO from medial to anterior brain in neocortex is present (Figure 73). In the white matter tract, while the genu (Figure 76) and cingulum (Figure 77) exhibit no genotypic variation, the external capsule show decrease of hAPOE3 FA compared to *Apoe*$^{-/-}$ in Bregma 0.0 (-9.6%, p=0.0162) and 0.8 (-9.6%, p=0.049) while in 0.0, hAPOE4 show increase compared to hAPOE3 (+14.4%, p=0.0078).

Neocortical RD analysis show increased RD in *Apoe*$^{-/-}$ compared to WT in the anterior Bregma 2.0 (+8.1%, p=0.0035) and 2.7 (+8.1%, p=0.005) (Figure 79). In Bregma 0.8, hAPOE4 exhibits an increase of FA compared to WT (+8.0%, p=0.0298). In contrast, hAPOE3 shows decrease in RD in Bregma 0.0 of the anterior cingulate (-8.2%, p=0.0379) and both *Apoe*$^{-/-}$ and hAPOE4 show increases in RD compared to WT in Bregma 2.0 (+9.0%, p=0.0202 and +9.8%, p=0.0453, respectively) (Figure 80). No further changes are seen in the white matter tract. Furthermore, AxD results show significant increases from 10 to 14% of hAPOE4 values against WT and hAPOE3 in the neocortex (Figure 85) and 7.7% against hAPOE3 (p=0.0137) in the anterior cingulate (Figure 86). However, only in the neocortex are genotypic differences significant (p=0.0073). Within the white matter tract are many genotypic alterations of regions. In the genu, the anterior Bregma 2.0 exhibit increases of hAPOE4 AxD against WT (+17.5%, p=0.0092) and hAPOE3 (+15.1%, p=0.0097) and hAPOE3 against *Apoe*$^{-/-}$ (-7.2%, p=0.0053) with significance by Bregma (p<0.0001) (Figure 88). In the cingulum, significance is isolated in Bregma -1.3 with *Apoe*$^{-/-}$ against WT (+9.9%, p=0.0001), hAPOE3 against WT (+4.9%, p=0.0359), and hAPOE3 against *Apoe*$^{-/-}$ (-4.6%, p=0.0463) (Figure 89). Likewise, in the external

capsule, most significance is found in the medial Bregma 0.8 with hAPOE4 against WT (+13.8%, p=0.0432), hAPOE3 against *Apoe*$^{-/-}$ (-9.4%, p=0.0022), and hAPOE4 against hAPOE3 (+13.6%, p=0.0107) (Figure 90).

Analysis of MD further shows the extent of diffusivity variations mainly in grey matter regions, neocortex and anterior cingulate. hAPOE4 MD values show a global increase in these two regions compared to WT and hAPOE3. In the white matter tract regions, *Apoe*$^{-/-}$ and hAPOE4 comparisons with genotypes exhibit significant increases in MD in contrast to hAPOE3's significant decreases. Overall, 10MO *Apoe*$^{-/-}$ and hAPOE4 mice begin to show signs of neurodegeneration with increased grey matter and white matter tract diffusivities.

4.4.7 Effect of genotype at 16MO

By 16MO, mice age equals to 50 human years. FA analysis of the neocortex graphically show similar increase of values from medial to anterior brain (Figure 73). Comparatively, hAPO3 and hAPOE4 remains unchanged within 16MO and even among age groups of the same genotype. In contrast, the WT curve shows steady decrease from 6MO to 16MO, as indicated from the previous section. Statistically significant increases are observed against WT from Bregma 0.8's *Apoe*$^{-/-}$ (+35.4%, p=0.0436) and hAPOE4 (+20.8%, p=0.036) and Bregma 2.7's *Apoe*$^{-/-}$ (+21.7%, p=0.0115) with significance of genotypic and Bregma factors (p=0.0099 and p<0.0001), respectively. Despite most neocortical changes residing in the anterior brain, changes in the anterior cingulate reside in the medial brain (Figure 74). Significant is yielded in Bregma -1.3 between hAPOE4 against *Apoe*$^{-/-}$ (-22.8%, p=.0435) and Bregma 0.0 between *Apoe*$^{-/-}$ against WT (+55.1%, p=0.0054) and hAPOE3 against *Apoe*$^{-/-}$ (-26.3%, p=0.03) with significance in genotypic and Bregma factors (p=0.0028 and p<0.0001, respectively). No FA changes are found in the hippocampus (Figure 76). Of the white matter tract, most variations are found in Bregma -1.3 of the genu and cingulum. Interestingly, as significantly increased FA levels are found in *Apoe*$^{-/-}$ against WT in genu (+16.1%, p=0.0365) and cingulum (+26.4%, p=0.0419) (Figure 77), decreased levels are found in the genu against *Apoe*$^{-/-}$ in hAPOE3 (-13.7%, p=0.0494) and hAPOE4 (-13.9%, p=0.0431) (Figure 76).

Further study into RD show insignificant changes among grey matter nor white matter tract regions. However, *Apoe*$^{-/-}$ exhibits gross increases against WT of AxD in the neocortex and anterior cingulate. Significant increases of *Apoe*$^{-/-}$ AxD are found in medial Bregmas -1.3 and 0.0 of these regions (Figure 86 and 87). Because of the lack of RD and AxD changes, MD does not indicate diffusivity significance among regions of 16MO mice. By 16MO, tgAPOE mice among genotypes show minimal diffusivity changes with most variations coming from the grey matter. Based on DKI values, the white matter tract is proposed to be stable comparatively.

4.4.8 Comparative effects of age and genotype on brain diffusivity

Using WT, it is observed that neurological health, based on diffusivity, is increased with age. DKI detected diffusivity is more anisotropic and less diffusive in all WT grey matter regions with significance, and no variations are observed in white matter tract regions. Removal of Apoe does not seem to significantly alter diffusivity status as age continues to increase FA and decrease directional diffusivity modalities. However, introduction of hAPOE alters diffusivity trends by 16MO. In contrast to unchanged hAPOE3 FA values among ages, directional diffusivities show decreases up to 10MO before increasing by 16MO. Further opposition of trends is observed in hAPOE4, exhibiting reductions in anisotropy and elevations of diffusivities with age. This flip in DKI trends indicate hAPOE4's altering effects in brain diffusivity.

Comparisons among genotypes within independent age groups suggest similar deleterious effects of hAPOE4. At 6MO, the effect of hAPOE is shown as changes are mainly between hAPOE4 with endogenous Apoe. By 10MO, *Apoe*$^{-/-}$ and hAPOE4 diffusivities show apparent increases in the grey matter as compared to other genotypes. This similarity may indicate hAPOE4's comparable effect with the complete knockout of Apoe. At 16MO, diffusivity values have become less significant among genotypes. Interestingly, this convergence may demonstrate hAPOE4's earlier neurological effects as its comparison with WT, *Apoe*$^{-/-}$, and hAPOE3 show larger differences at an earlier age and smaller differences at 16MO. Further investigation into cellular structures is then done to correlate this effect with the cells responsible for white matter upkeep, OLs.

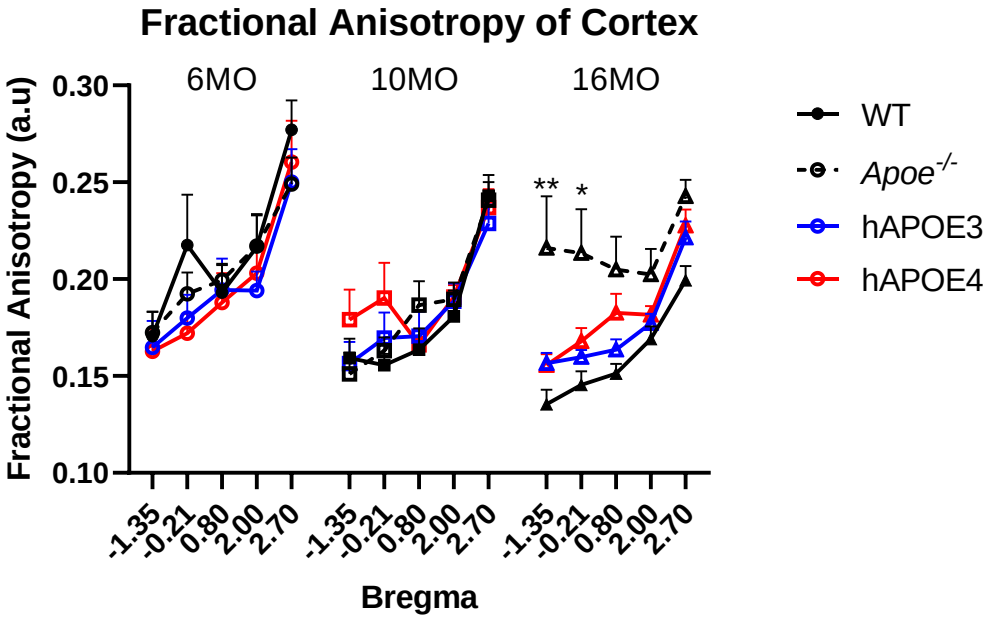

*Figure 73: The cortical FA of genotypic and age groups were analysed for changes in anisotropic diffusion of water of white matter in the mice brain. Genotypes are grouped by age and graphically compared by Bregma numbers. All values are of two-way ANOVA mean ± SEM and sex are denoted as male/female. Statistically significant stars are color-coded according to transgenic genotype against WT. *p<0.05; **p<0.01. (6MO: WT, n=3/3; Apoe$^{-/-}$, n=5/4; hAPOE3, n=3/4; hAPOE4, n=5/5. 10MO: WT, n=3/2; Apoe$^{-/-}$, n=4/6; hAPOE3, n=3/2; hAPOE4, n=4/6. 16MO: WT, n=3/2; Apoe$^{-/-}$, n=8/4; hAPOE3, n=5/10; hAPOE4, n=9/8).*

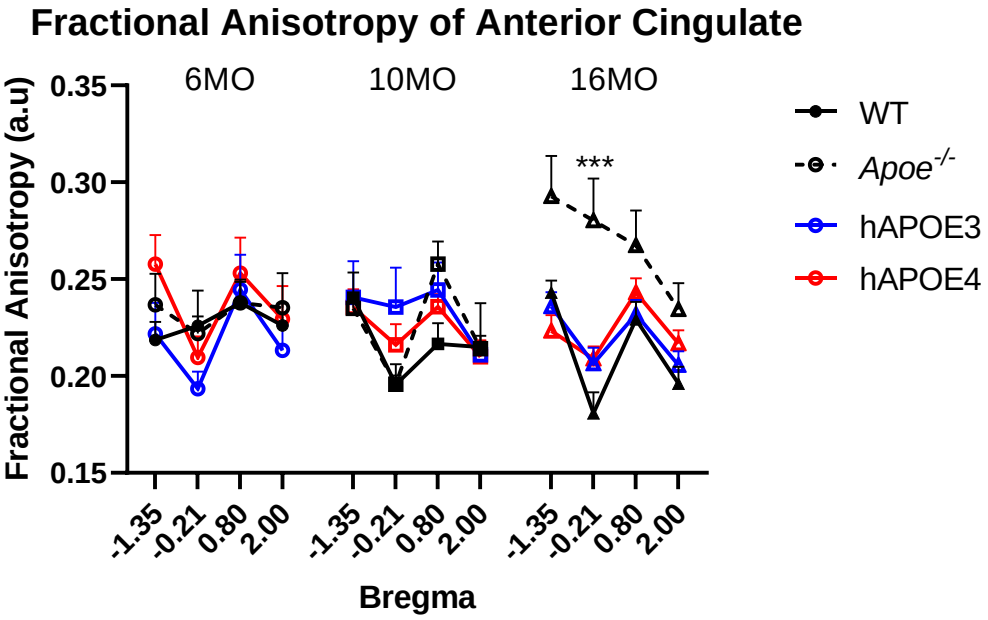

*Figure 74: The anterior cingulate FA of genotypic and age groups were analysed for changes in anisotropic diffusion of water of white matter in the mice brain. Genotypes are grouped by age and graphically compared by Bregma numbers. All values are of two-way ANOVA mean ± SEM and sex are denoted as male/female. Statistically significant stars are color-coded according to transgenic genotype against WT. ***p<0.001. (6MO: WT, n=3/3; Apoe$^{-/-}$, n=5/4; hAPOE3, n=3/4; hAPOE4, n=5/5. 10MO: WT, n=3/2; Apoe$^{-/-}$, n=4/6; hAPOE3, n=3/2; hAPOE4, n=4/6. 16MO: WT, n=3/2; Apoe$^{-/-}$, n=8/4; hAPOE3, n=5/10; hAPOE4, n=9/8).*

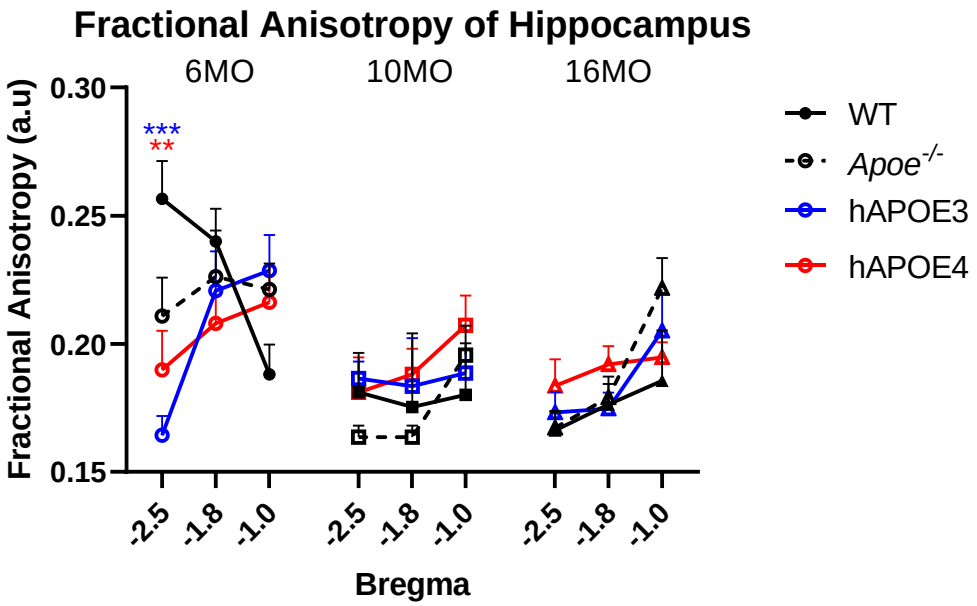

*Figure 75: The hippocampal FA of genotypic and age groups were analysed for changes in anisotropic diffusion of water of white matter in the mice brain. Genotypes are grouped by age and graphically compared by Bregma numbers. All values are of two-way ANOVA mean ± SEM and sex are denoted as male/female. Statistically significant stars are color-coded according to transgenic genotype against WT. **p<0.01; ***p<0.001. (6MO: WT, n=3/3; Apoe$^{-/-}$, n=5/4; hAPOE3, n=3/4; hAPOE4, n=5/5. 10MO: WT, n=3/2; Apoe$^{-/-}$, n=4/6; hAPOE3, n=3/2; hAPOE4, n=4/6. 16MO: WT, n=3/2; Apoe$^{-/-}$, n=8/4; hAPOE3, n=5/10; hAPOE4, n=9/8).*

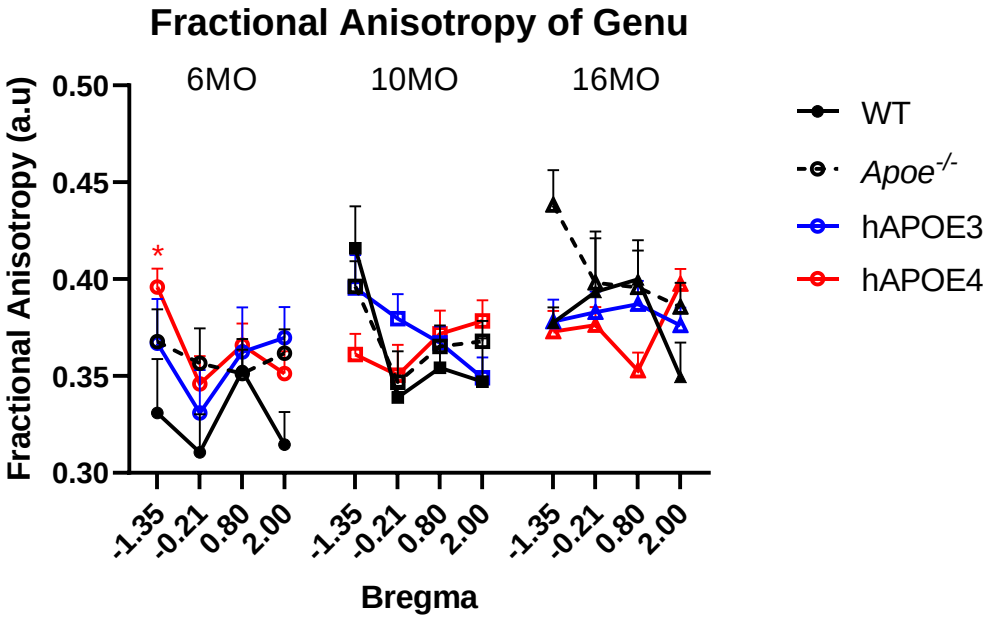

*Figure 76: The genu FA of genotypic and age groups were analysed for changes in anisotropic diffusion of water of white matter in the mice brain. Genotypes are grouped by age and graphically compared by Bregma numbers. All values are of two-way ANOVA mean ± SEM and sex are denoted as male/female. Statistically significant stars are color-coded according to transgenic genotype against WT. *p<0.05. (6MO: WT, n=3/3; Apoe$^{-/-}$, n=5/4; hAPOE3, n=3/4; hAPOE4, n=5/5. 10MO: WT, n=3/2; Apoe$^{-/-}$, n=4/6; hAPOE3, n=3/2; hAPOE4, n=4/6. 16MO: WT, n=3/2; Apoe$^{-/-}$, n=8/4; hAPOE3, n=5/10; hAPOE4, n=9/8).*

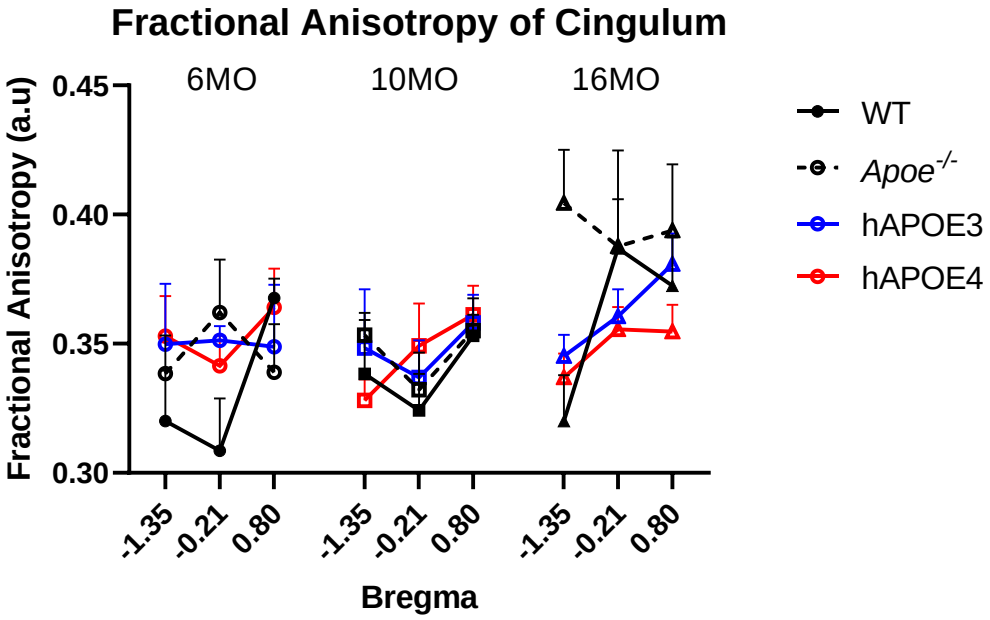

Figure 77: The cingulum FA of genotypic and age groups were analysed for changes in anisotropic diffusion of water of white matter in the mice brain. Genotypes are grouped by age and graphically compared by Bregma numbers. All values are of two-way ANOVA mean ± SEM and sex are denoted as male/female. (6MO: WT, n=3/3; Apoe$^{-/-}$, n=5/4; hAPOE3, n=3/4; hAPOE4, n=5/5. 10MO: WT, n=3/2; Apoe$^{-/-}$, n=4/6; hAPOE3, n=3/2; hAPOE4, n=4/6. 16MO: WT, n=3/2; Apoe$^{-/-}$, n=8/4; hAPOE3, n=5/10; hAPOE4, n=9/8).

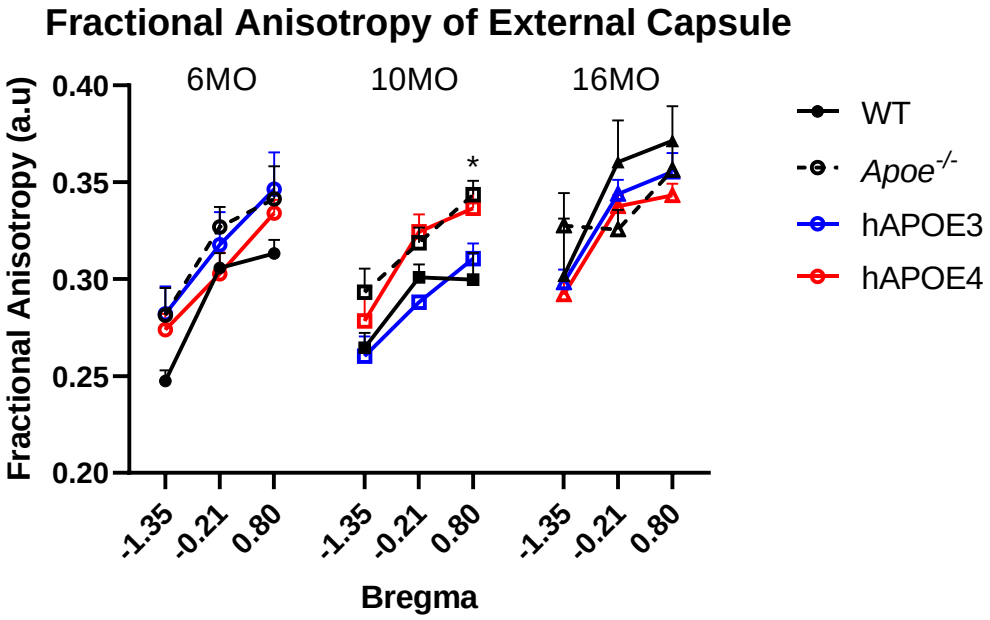

*Figure 78: The external capsule FA of genotypic and age groups were analysed for changes in anisotropic diffusion of water of white matter in the mice brain. Genotypes are grouped by age and graphically compared by Bregma numbers. All values are of two-way ANOVA mean ± SEM and sex are denoted as male/female. Statistically significant stars are color-coded according to transgenic genotype against WT. *p<0.05. (6MO: WT, n=3/3; Apoe$^{-/-}$, n=5/4; hAPOE3, n=3/4; hAPOE4, n=5/5. 10MO: WT, n=3/2; Apoe$^{-/-}$, n=4/6; hAPOE3, n=3/2; hAPOE4, n=4/6. 16MO: WT, n=3/2; Apoe$^{-/-}$, n=8/4; hAPOE3, n=5/10; hAPOE4, n=9/8).*

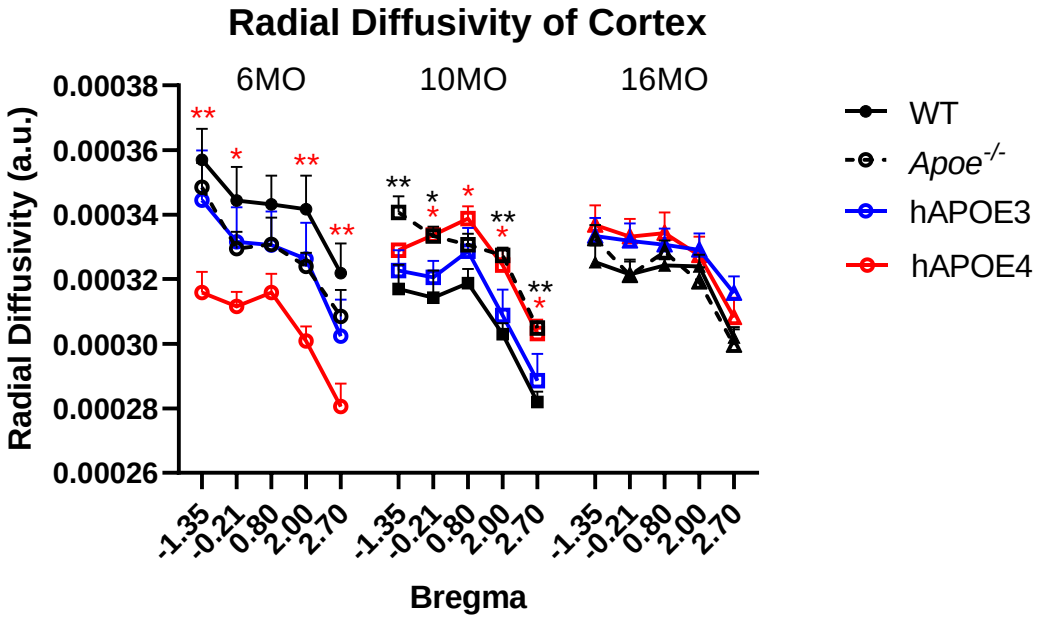

*Figure 79: The cortical RD of genotypic and age groups were analysed for changes in perpendicular diffusion of water of white matter in the mice brain. Genotypes are grouped by age and graphically compared by Bregma numbers. All values are of two-way ANOVA mean ± SEM and sex are denoted as male/female. Statistically significant stars are color-coded according to transgenic genotype against WT. *p<0.05; **p<0.01. (6MO: WT, n=3/3; Apoe$^{-/-}$, n=5/4; hAPOE3, n=3/4; hAPOE4, n=5/5. 10MO: WT, n=3/2; Apoe$^{-/-}$, n=4/6; hAPOE3, n=3/2; hAPOE4, n=4/6. 16MO: WT, n=3/2; Apoe$^{-/-}$, n=8/4; hAPOE3, n=5/10; hAPOE4, n=9/8).*

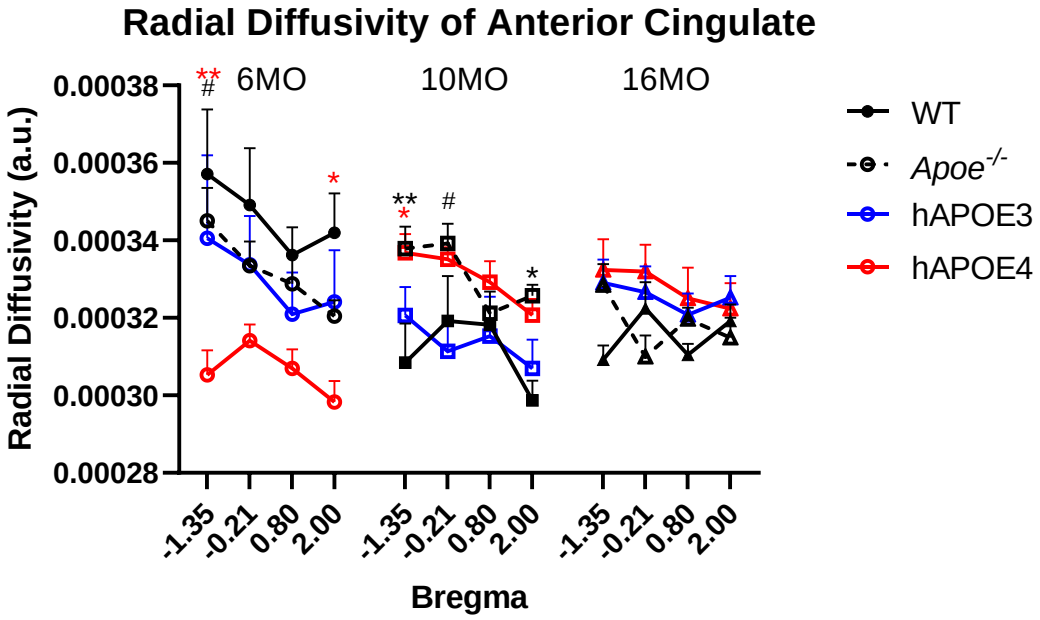

*Figure 80: The anterior cingulate RD of genotypic and age groups were analysed for changes in perpendicular diffusion of water of white matter in the mice brain. Genotypes are grouped by age and graphically compared by Bregma numbers. All values are of two-way ANOVA mean ± SEM and sex are denoted as male/female. Statistically significant stars are color-coded according to transgenic genotype against WT. *p<0.05; **p<0.01. Statistically significant hashes are according to hAPOE4 changes against hAPOE3. #p<0.05. (6MO: WT, n=3/3; Apoe$^{-/-}$, n=5/4; hAPOE3, n=3/4; hAPOE4, n=5/5. 10MO: WT, n=3/2; Apoe$^{-/-}$, n=4/6; hAPOE3, n=3/2; hAPOE4, n=4/6. 16MO: WT, n=3/2; Apoe$^{-/-}$, n=8/4; hAPOE3, n=5/10; hAPOE4, n=9/8).*

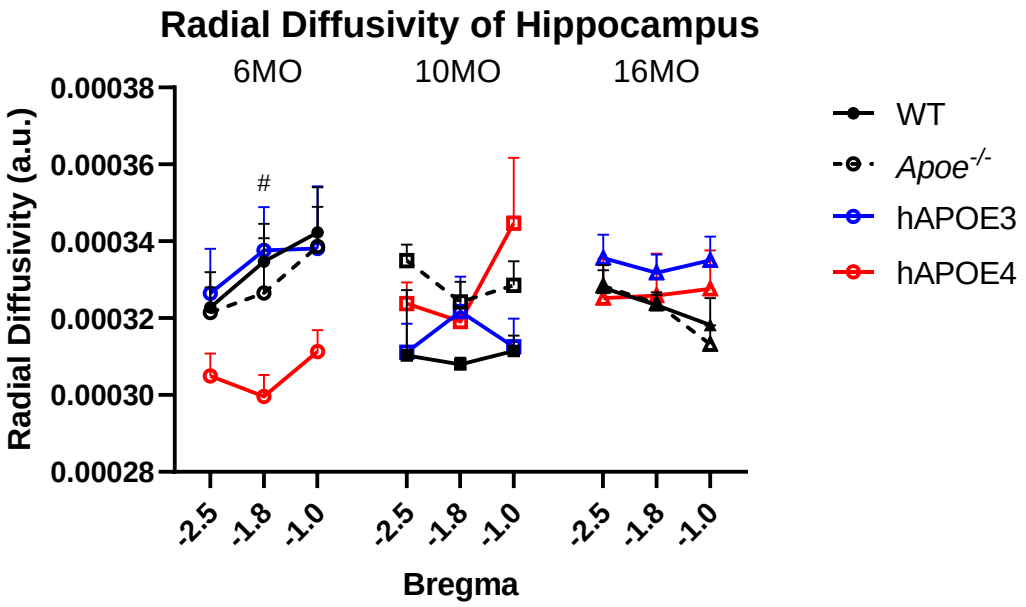

Figure 81: The hippocampal RD of genotypic and age groups were analysed for changes in perpendicular diffusion of water of white matter in the mice brain. Genotypes are grouped by age and graphically compared by Bregma numbers. All values are of two-way ANOVA mean ± SEM and sex are denoted as male/female. Statistically significant hashes are according to hAPOE4 changes against hAPOE3. #p<0.05. (6MO: WT, n=3/3; Apoe$^{-/-}$, n=5/4; hAPOE3, n=3/4; hAPOE4, n=5/5. 10MO: WT, n=3/2; Apoe$^{-/-}$, n=4/6; hAPOE3, n=3/2; hAPOE4, n=4/6. 16MO: WT, n=3/2; Apoe$^{-/-}$, n=8/4; hAPOE3, n=5/10; hAPOE4, n=9/8).

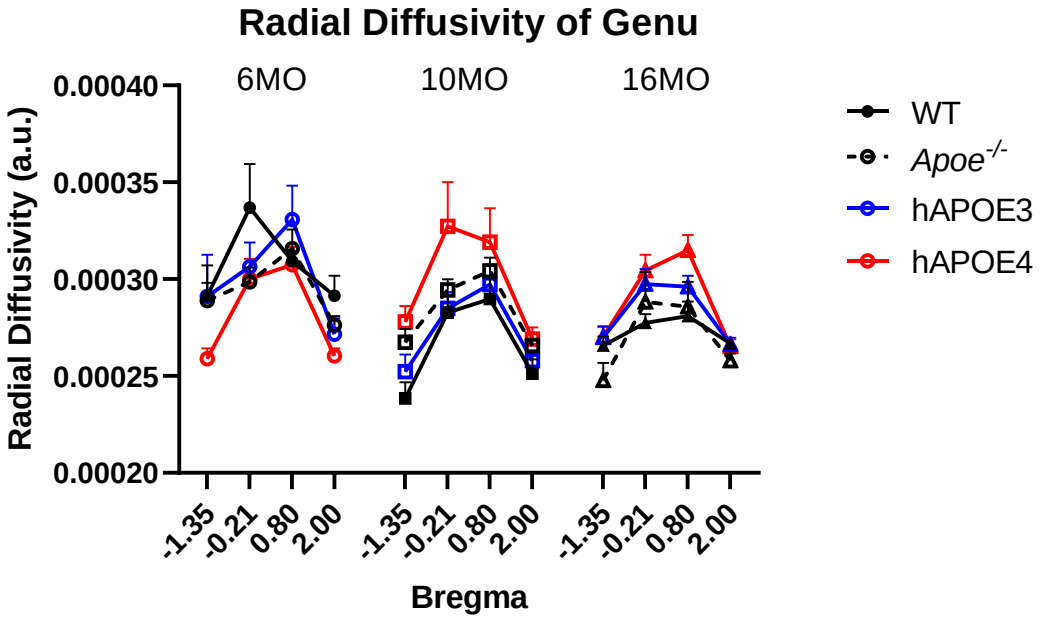

Figure 82: The genu RD of genotypic and age groups were analysed for changes in perpendicular diffusion of water of white matter in the mice brain. Genotypes are grouped by age and graphically compared by Bregma numbers. All values are of two-way ANOVA mean ± SEM and sex are denoted as male/female. (6MO: WT, n=3/3; Apoe$^{-/-}$, n=5/4; hAPOE3, n=3/4; hAPOE4, n=5/5. 10MO: WT, n=3/2; Apoe$^{-/-}$, n=4/6; hAPOE3, n=3/2; hAPOE4, n=4/6. 16MO: WT, n=3/2; Apoe$^{-/-}$, n=8/4; hAPOE3, n=5/10; hAPOE4, n=9/8).

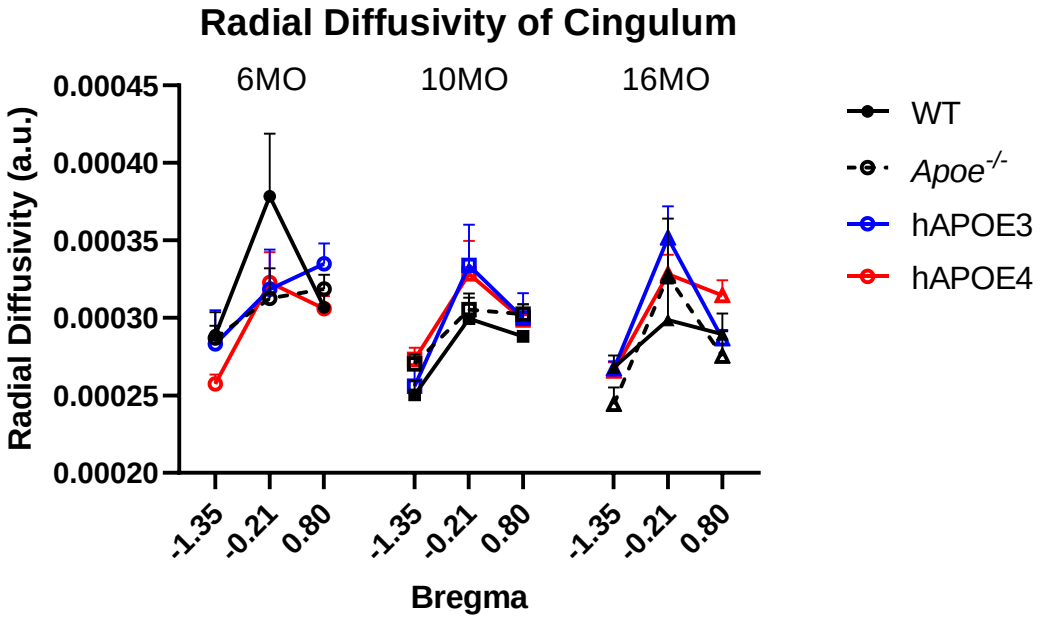

Figure 83: The cingulum RD of genotypic and age groups were analysed for changes in perpendicular diffusion of water of white matter in the mice brain. Genotypes are grouped by age and graphically compared by Bregma numbers. All values are of two-way ANOVA mean ± SEM and sex are denoted as male/female. (6MO: WT, n=3/3; Apoe$^{-/-}$, n=5/4; hAPOE3, n=3/4; hAPOE4, n=5/5. 10MO: WT, n=3/2; Apoe$^{-/-}$, n=4/6; hAPOE3, n=3/2; hAPOE4, n=4/6. 16MO: WT, n=3/2; Apoe$^{-/-}$, n=8/4; hAPOE3, n=5/10; hAPOE4, n=9/8).

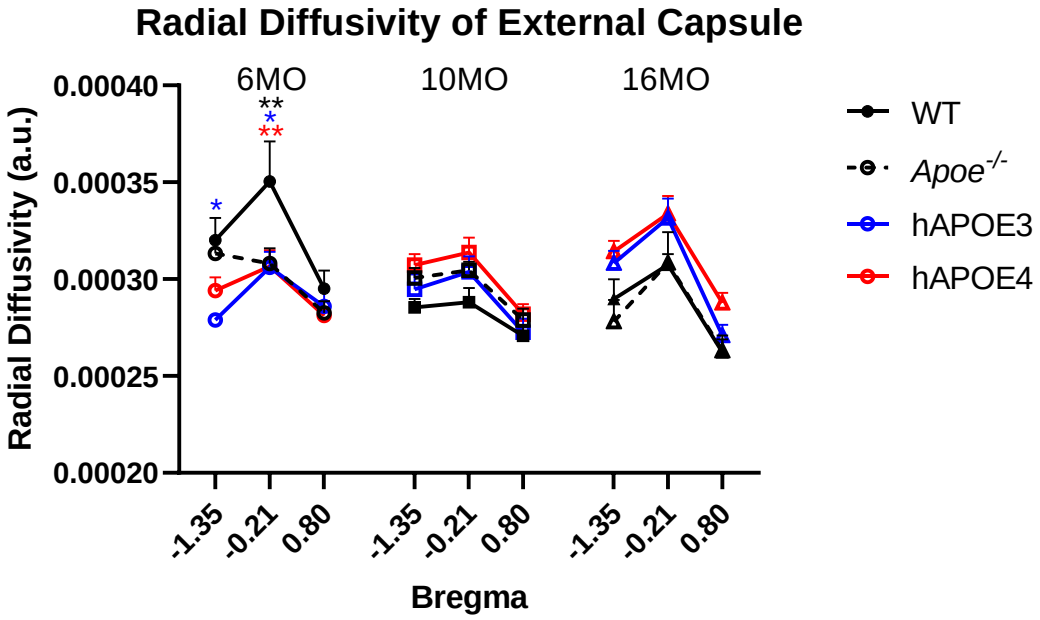

*Figure 84: The external capsule RD of genotypic and age groups were analysed for changes in perpendicular diffusion of water of white matter in the mice brain. Genotypes are grouped by age and graphically compared by Bregma numbers. All values are of two-way ANOVA mean ± SEM and sex are denoted as male/female. Statistically significant stars are color-coded according to transgenic genotype against WT. *p<0.05; **p<0.01. (6MO: WT, n=3/3; Apoe$^{-/-}$, n=5/4; hAPOE3, n=3/4; hAPOE4, n=5/5. 10MO: WT, n=3/2; Apoe$^{-/-}$, n=4/6; hAPOE3, n=3/2; hAPOE4, n=4/6. 16MO: WT, n=3/2; Apoe$^{-/-}$, n=8/4; hAPOE3, n=5/10; hAPOE4, n=9/8).*

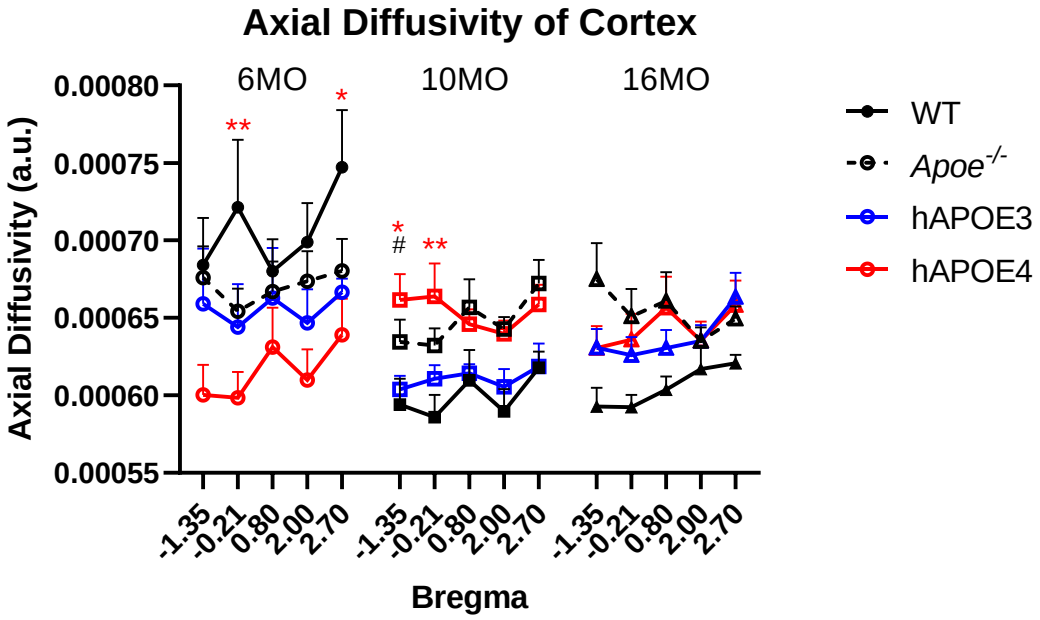

*Figure 85: The cortical AxD of genotypic and age groups were analysed for changes in axial diffusion of water of white matter in the mice brain. Genotypes are grouped by age and graphically compared by Bregma numbers. All values are of two-way ANOVA mean ± SEM and sex are denoted as male/female. Statistically significant stars are color-coded according to transgenic genotype against WT. *p<0.05; **p<0.01. Statistically significant hashes are according to hAPOE4 changes against hAPOE3. #p<0.05. (6MO: WT, n=3/3; Apoe$^{-/-}$, n=5/4; hAPOE3, n=3/4; hAPOE4, n=5/5. 10MO: WT, n=3/2; Apoe$^{-/-}$, n=4/6; hAPOE3, n=3/2; hAPOE4, n=4/6. 16MO: WT, n=3/2; Apoe$^{-/-}$, n=8/4; hAPOE3, n=5/10; hAPOE4, n=9/8).*

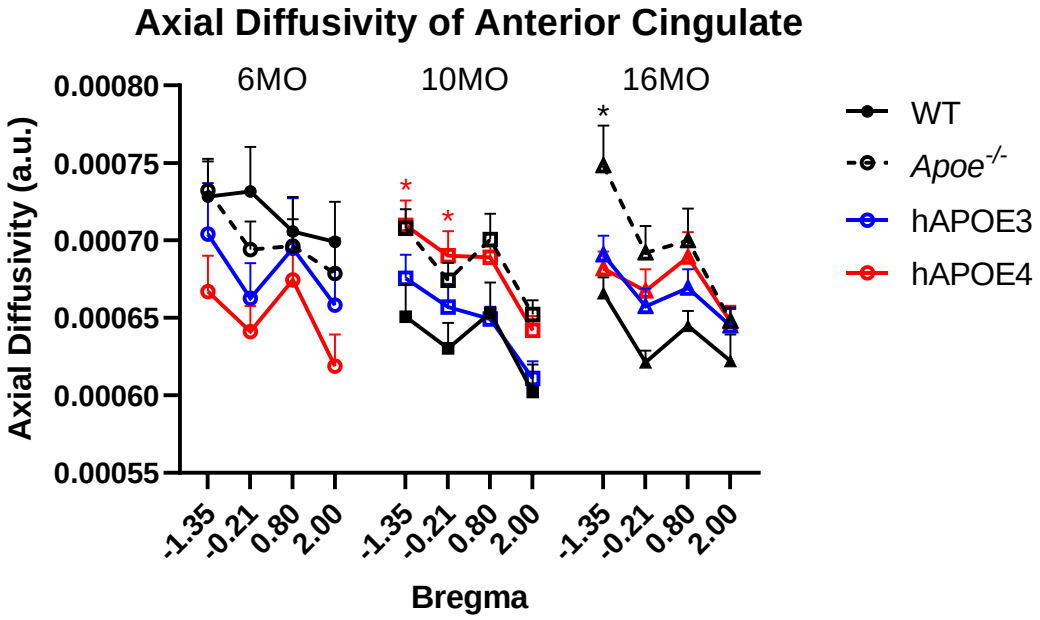

*Figure 86: The anterior cingulate AxD of genotypic and age groups were analysed for changes in axial diffusion of water of white matter in the mice brain. Genotypes are grouped by age and graphically compared by Bregma numbers. All values are of two-way ANOVA mean ± SEM and sex are denoted as male/female. Statistically significant stars are color-coded according to transgenic genotype against WT. *p<0.05. (6MO: WT, n=3/3; Apoe$^{-/-}$, n=5/4; hAPOE3, n=3/4; hAPOE4, n=5/5. 10MO: WT, n=3/2; Apoe$^{-/-}$, n=4/6; hAPOE3, n=3/2; hAPOE4, n=4/6. 16MO: WT, n=3/2; Apoe$^{-/-}$, n=8/4; hAPOE3, n=5/10; hAPOE4, n=9/8).*

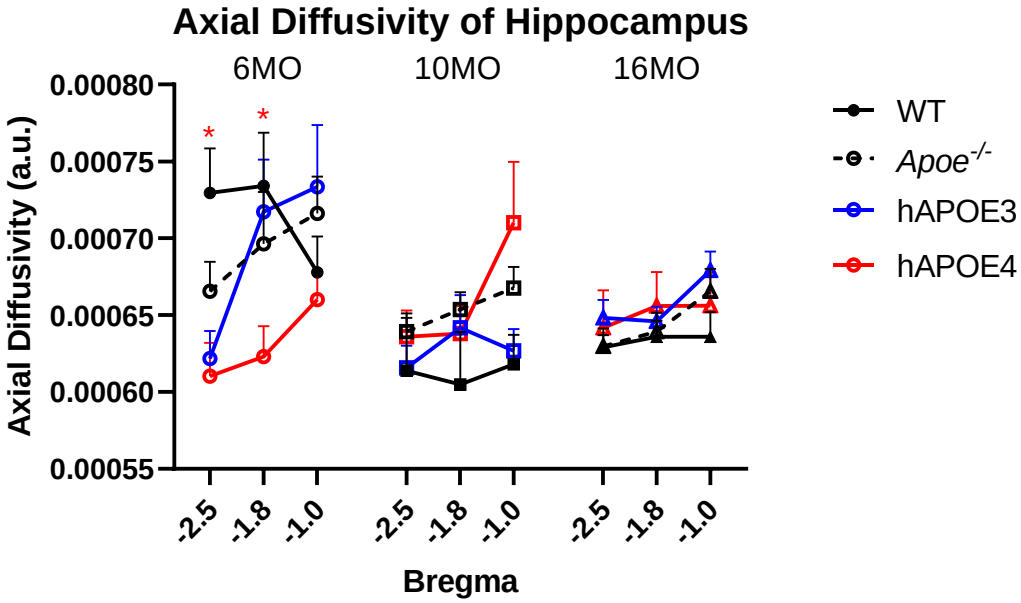

*Figure 87: The hippocampal AxD of genotypic and age groups were analysed for changes in axial diffusion of water of white matter in the mice brain. Genotypes are grouped by age and graphically compared by Bregma numbers. All values are of two-way ANOVA mean ± SEM and sex are denoted as male/female. Statistically significant stars are color-coded according to transgenic genotype against WT. *p<0.05. (6MO: WT, n=3/3; Apoe$^{-/-}$, n=5/4; hAPOE3, n=3/4; hAPOE4, n=5/5. 10MO: WT, n=3/2; Apoe$^{-/-}$, n=4/6; hAPOE3, n=3/2; hAPOE4, n=4/6. 16MO: WT, n=3/2; Apoe$^{-/-}$, n=8/4; hAPOE3, n=5/10; hAPOE4, n=9/8).*

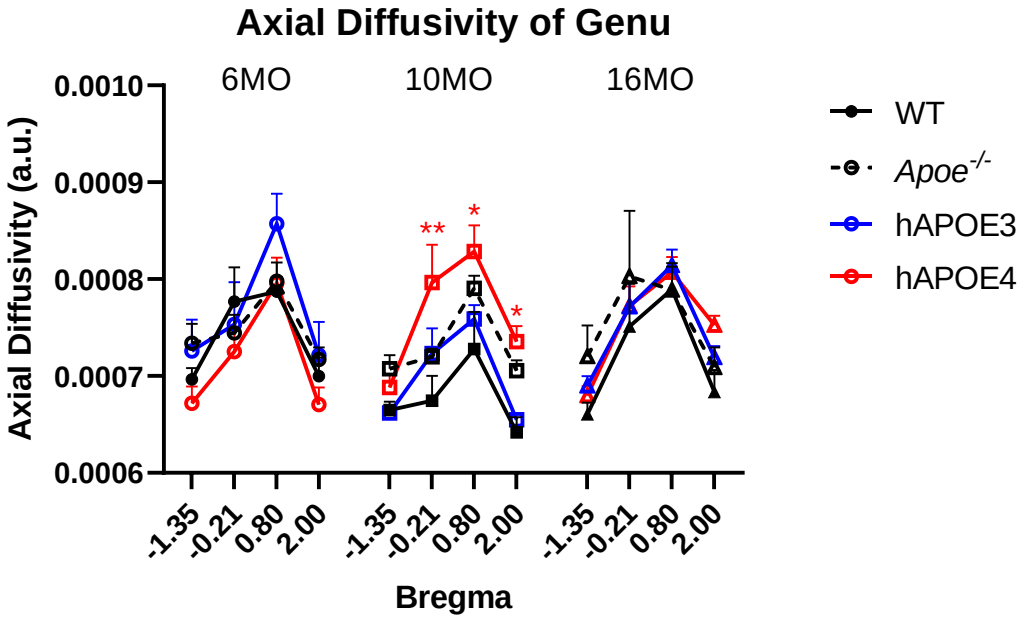

*Figure 88: The genu AxD of genotypic and age groups were analysed for changes in axial diffusion of water of white matter in the mice brain. Genotypes are grouped by age and graphically compared by Bregma numbers. All values are of two-way ANOVA mean ± SEM and sex are denoted as male/female. Statistically significant stars are color-coded according to transgenic genotype against WT. *p<0.05; **p<0.01. (6MO: WT, n=3/3; Apoe$^{-/-}$, n=5/4; hAPOE3, n=3/4; hAPOE4, n=5/5. 10MO: WT, n=3/2; Apoe$^{-/-}$, n=4/6; hAPOE3, n=3/2; hAPOE4, n=4/6. 16MO: WT, n=3/2; Apoe$^{-/-}$, n=8/4; hAPOE3, n=5/10; hAPOE4, n=9/8).*

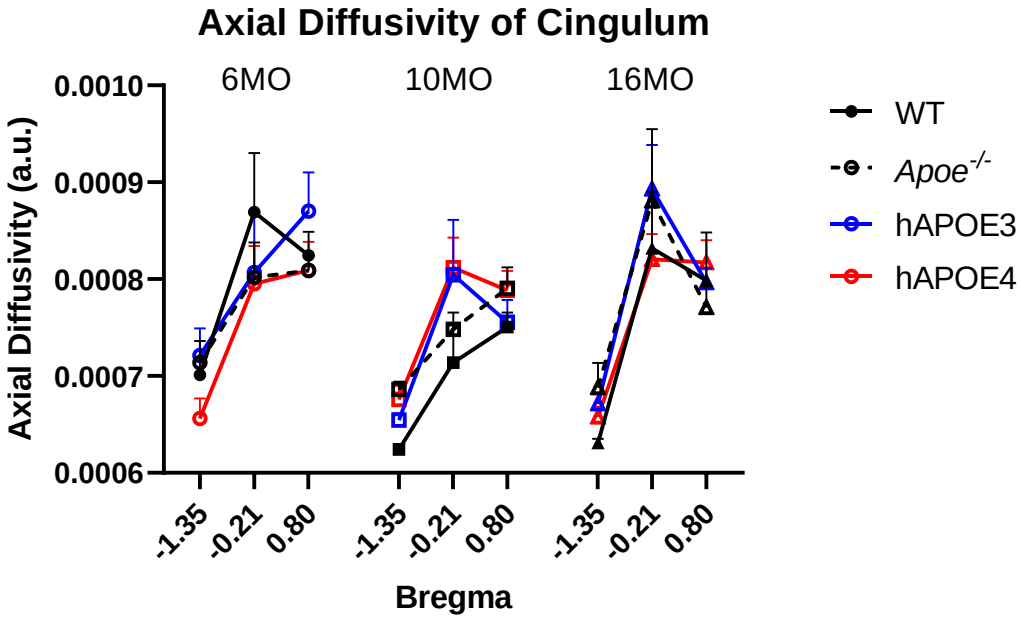

Figure 89: The cingulum AxD of genotypic and age groups were analysed for changes in axial diffusion of water of white matter in the mice brain. Genotypes are grouped by age and graphically compared by Bregma numbers. All values are of two-way ANOVA mean ± SEM and sex are denoted as male/female. (6MO: WT, n=3/3; Apoe$^{-/-}$, n=5/4; hAPOE3, n=3/4; hAPOE4, n=5/5. 10MO: WT, n=3/2; Apoe$^{-/-}$, n=4/6; hAPOE3, n=3/2; hAPOE4, n=4/6. 16MO: WT, n=3/2; Apoe$^{-/-}$, n=8/4; hAPOE3, n=5/10; hAPOE4, n=9/8).

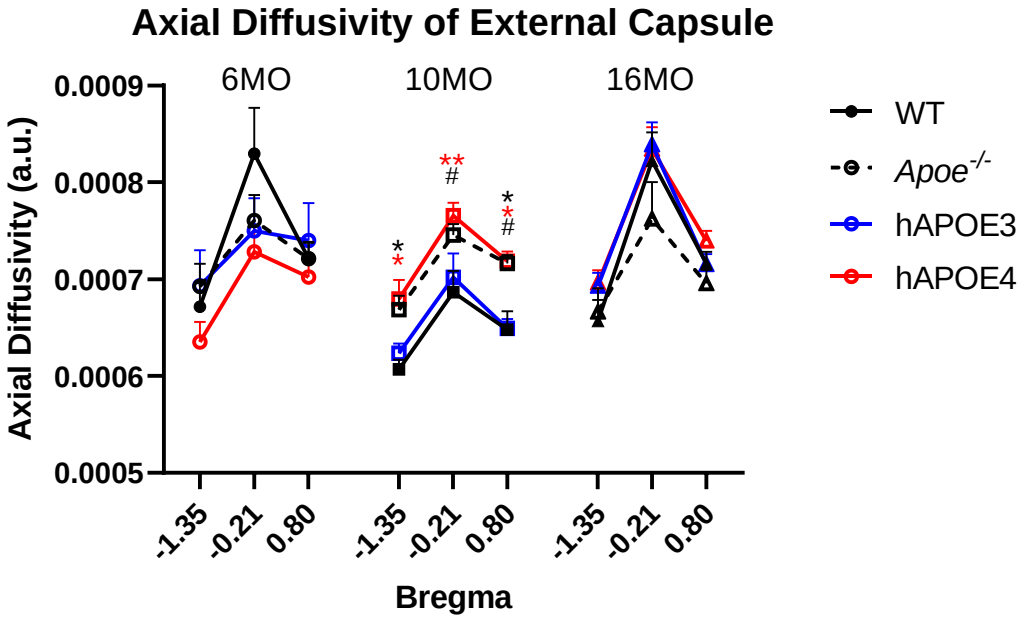

*Figure 90: The external capsule AxD of genotypic and age groups were analysed for changes in axial diffusion of water of white matter in the mice brain. Genotypes are grouped by age and graphically compared by Bregma numbers. All values are of two-way ANOVA mean ± SEM and sex are denoted as male/female. Statistically significant stars are color-coded according to transgenic genotype against WT. *p<0.05; **p<0.01. Statistically significant hashes are according to hAPOE4 changes against hAPOE3. #p<0.05. (6MO: WT, n=3/3; Apoe$^{-/-}$, n=5/4; hAPOE3, n=3/4; hAPOE4, n=5/5. 10MO: WT, n=3/2; Apoe$^{-/-}$, n=4/6; hAPOE3, n=3/2; hAPOE4, n=4/6. 16MO: WT, n=3/2; Apoe$^{-/-}$, n=8/4; hAPOE3, n=5/10; hAPOE4, n=9/8).*

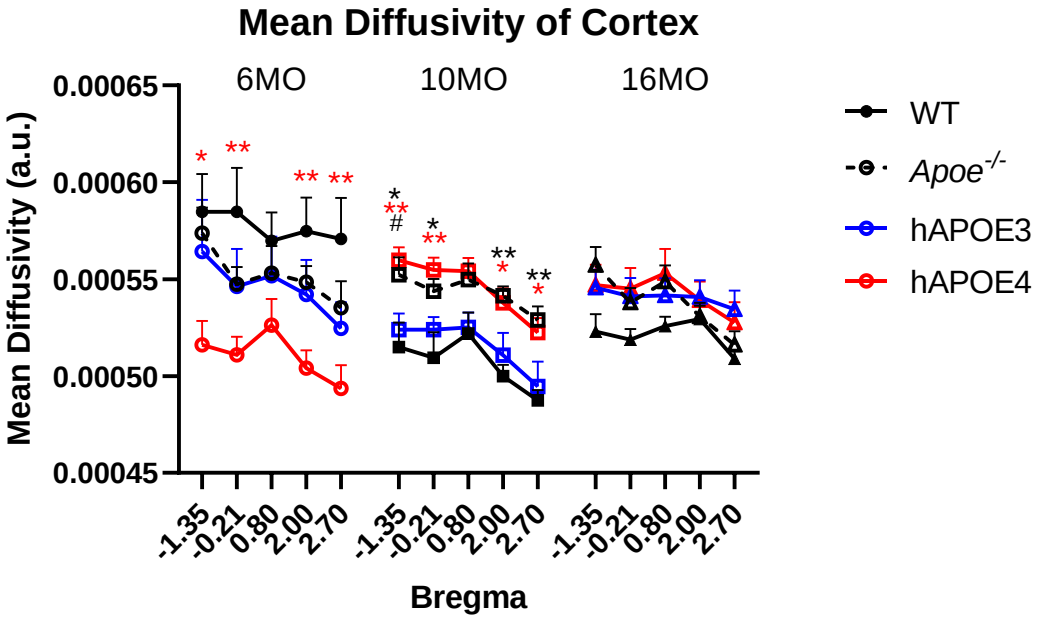

*Figure 91: The cortical MD of genotypic and age groups were analysed for changes in mean diffusion of water of white matter in the mice brain. Genotypes are grouped by age and graphically compared by Bregma numbers. All values are of two-way ANOVA mean ± SEM and sex are denoted as male/female. Statistically significant stars are color-coded according to transgenic genotype against WT. *p<0.05; **p<0.01. Statistically significant hashes are according to hAPOE4 changes against hAPOE3. #p<0.05. (6MO: WT, n=3/3; Apoe$^{-/-}$, n=5/4; hAPOE3, n=3/4; hAPOE4, n=5/5. 10MO: WT, n=3/2; Apoe$^{-/-}$, n=4/6; hAPOE3, n=3/2; hAPOE4, n=4/6. 16MO: WT, n=3/2; Apoe$^{-/-}$, n=8/4; hAPOE3, n=5/10; hAPOE4, n=9/8).*

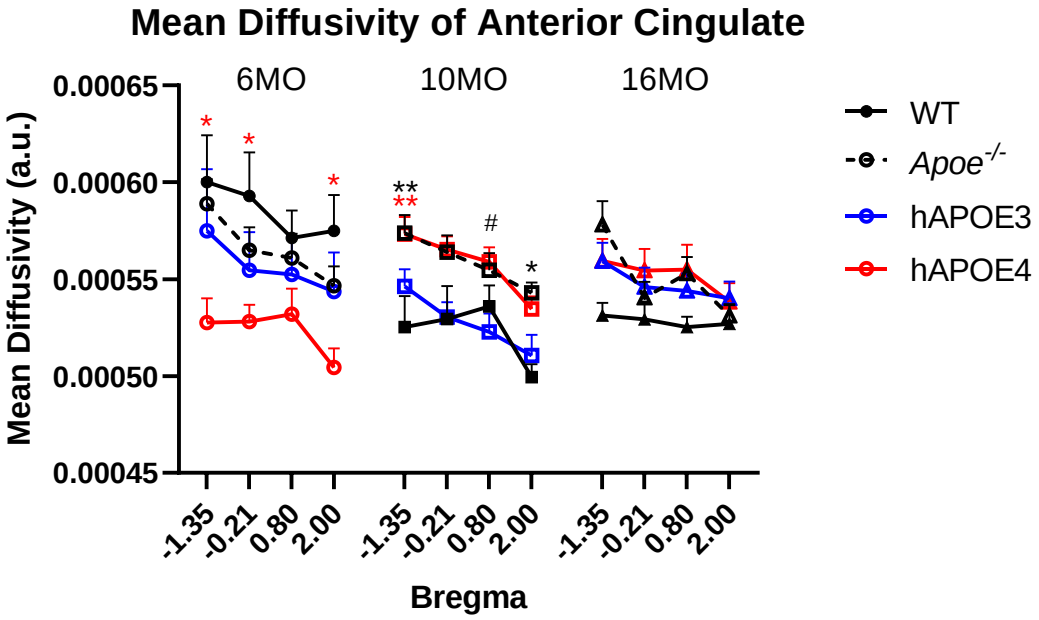

*Figure 92: The anterior cingulate MD of genotypic and age groups were analysed for changes in mean diffusion of water of white matter in the mice brain. Genotypes are grouped by age and graphically compared by Bregma numbers. All values are of two-way ANOVA mean ± SEM and sex are denoted as male/female. Statistically significant stars are color-coded according to transgenic genotype against WT. *p<0.05; **p<0.01. Statistically significant hashes are according to hAPOE4 changes against hAPOE3. #p<0.05. (6MO: WT, n=3/3; Apoe$^{-/-}$, n=5/4; hAPOE3, n=3/4; hAPOE4, n=5/5. 10MO: WT, n=3/2; Apoe$^{-/-}$, n=4/6; hAPOE3, n=3/2; hAPOE4, n=4/6. 16MO: WT, n=3/2; Apoe$^{-/-}$, n=8/4; hAPOE3, n=5/10; hAPOE4, n=9/8).*

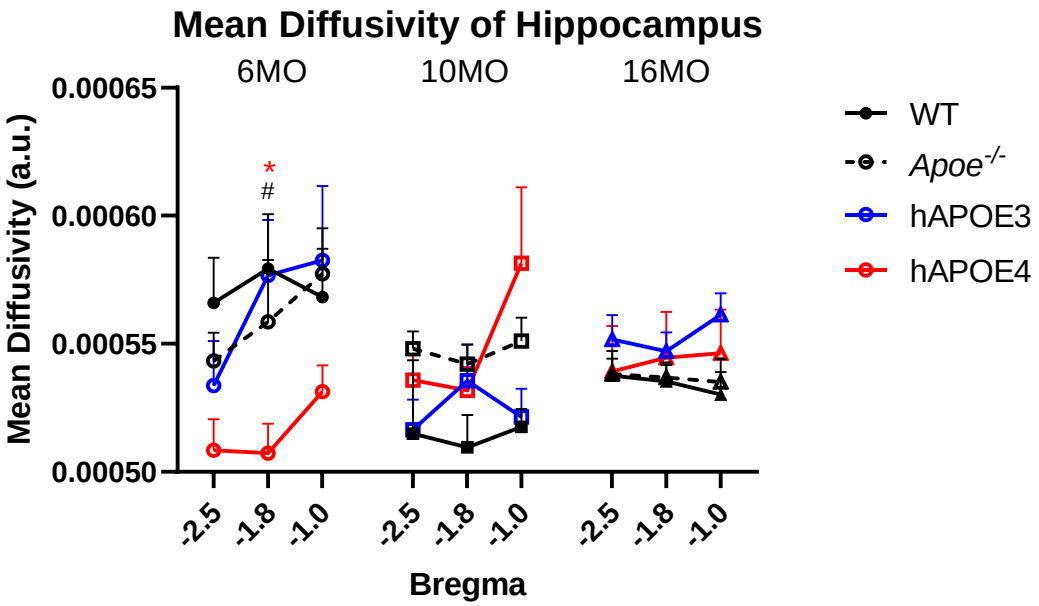

*Figure 93: The hippocampal MD of genotypic and age groups were analysed for changes in mean diffusion of water of white matter in the mice brain. Genotypes are grouped by age and graphically compared by Bregma numbers. All values are of two-way ANOVA mean ± SEM and sex are denoted as male/female. Statistically significant stars are color-coded according to transgenic genotype against WT. *p<0.05. Statistically significant hashes are according to hAPOE4 changes against hAPOE3. #p<0.05. (6MO: WT, n=3/3; Apoe$^{-/-}$, n=5/4; hAPOE3, n=3/4; hAPOE4, n=5/5. 10MO: WT, n=3/2; Apoe$^{-/-}$, n=4/6; hAPOE3, n=3/2; hAPOE4, n=4/6. 16MO: WT, n=3/2; Apoe$^{-/-}$, n=8/4; hAPOE3, n=5/10; hAPOE4, n=9/8).*

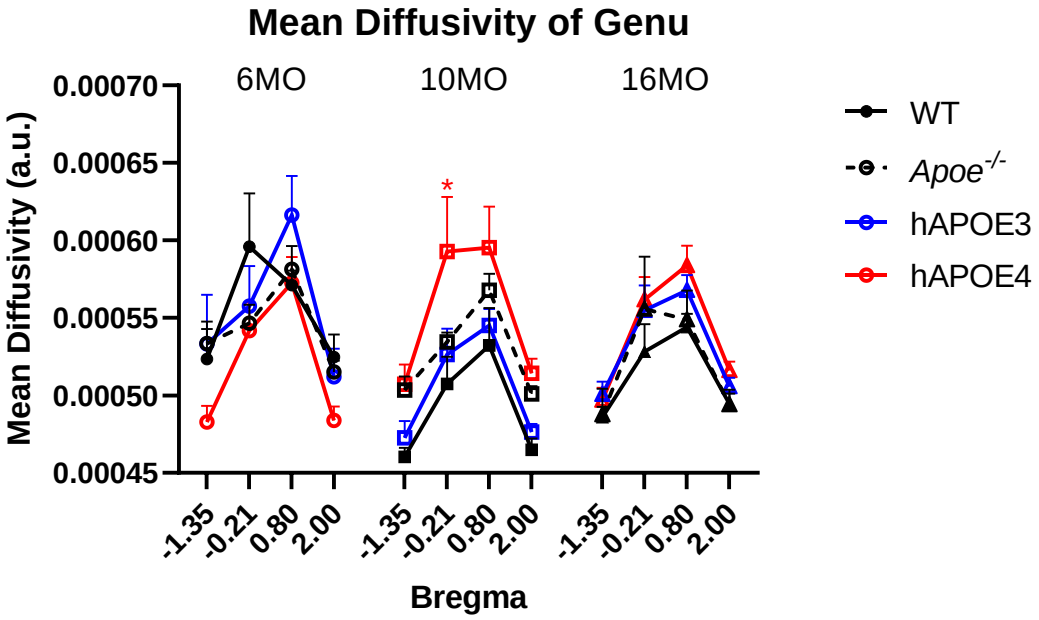

*Figure 94: The genu MD of genotypic and age groups were analysed for changes in mean diffusion of water of white matter in the mice brain. Genotypes are grouped by age and graphically compared by Bregma numbers. All values are of two-way ANOVA mean ± SEM and sex are denoted as male/female. Statistically significant stars are color-coded according to transgenic genotype against WT. *p<0.05. (6MO: WT, n=3/3; Apoe$^{-/-}$, n=5/4; hAPOE3, n=3/4; hAPOE4, n=5/5. 10MO: WT, n=3/2; Apoe$^{-/-}$, n=4/6; hAPOE3, n=3/2; hAPOE4, n=4/6. 16MO: WT, n=3/2; Apoe$^{-/-}$, n=8/4; hAPOE3, n=5/10; hAPOE4, n=9/8).*

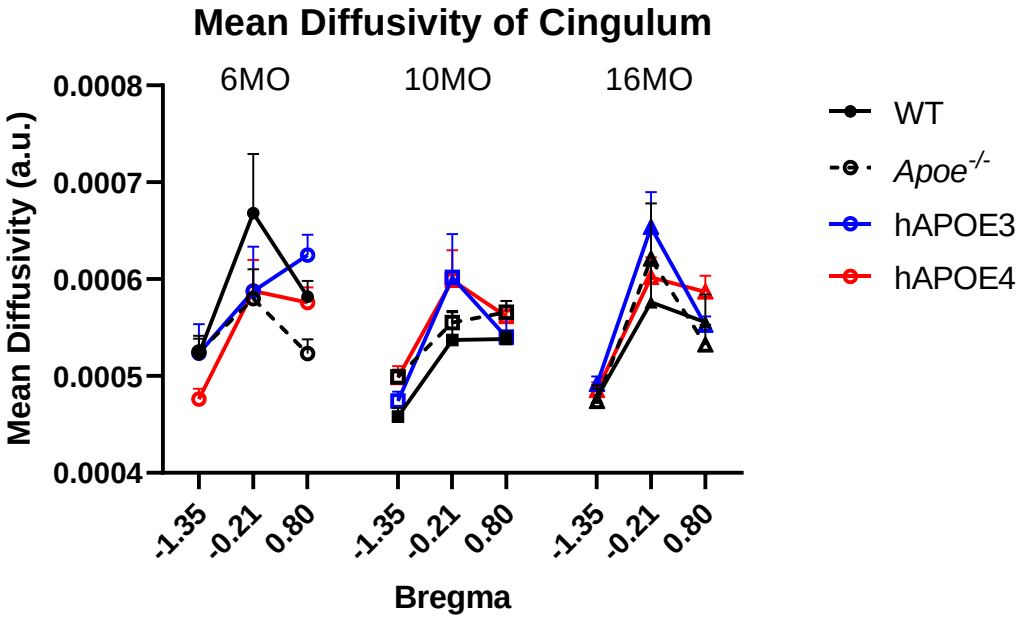

Figure 95: The cingulum MD of genotypic and age groups were analysed for changes in mean diffusion of water of white matter in the mice brain. Genotypes are grouped by age and graphically compared by Bregma numbers. All values are of two-way ANOVA mean ± SEM and sex are denoted as male/female. (6MO: WT, n=3/3; Apoe$^{-/-}$, n=5/4; hAPOE3, n=3/4; hAPOE4, n=5/5. 10MO: WT, n=3/2; Apoe$^{-/-}$, n=4/6; hAPOE3, n=3/2; hAPOE4, n=4/6. 16MO: WT, n=3/2; Apoe$^{-/-}$, n=8/4; hAPOE3, n=5/10; hAPOE4, n=9/8).

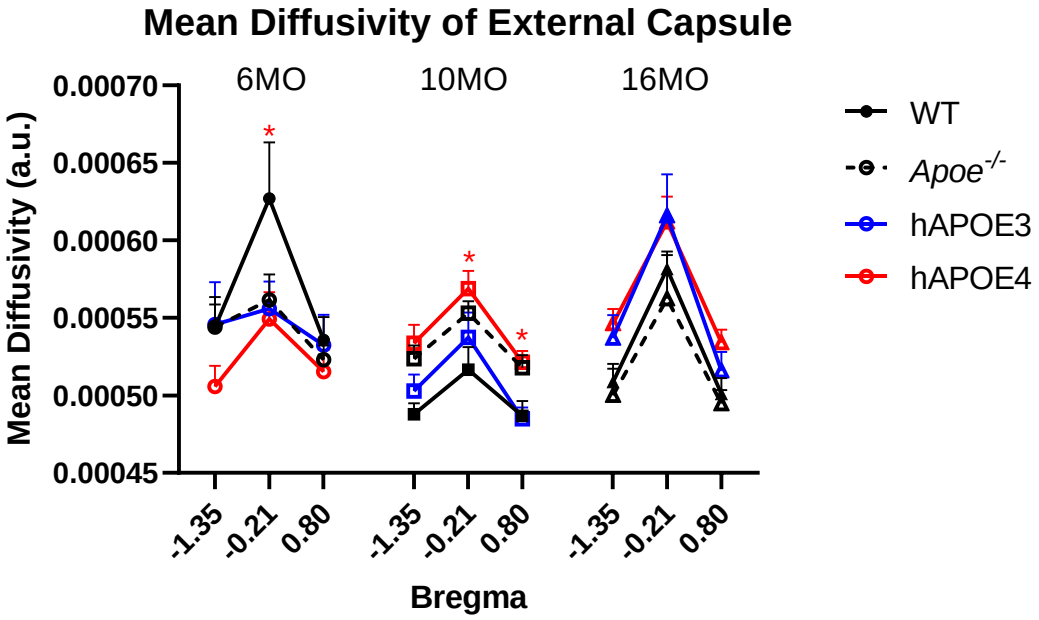

*Figure 96: The external capsule MD of genotypic and age groups were analysed for changes in mean diffusion of water of white matter in the mice brain. Genotypes are grouped by age and graphically compared by Bregma numbers. All values are of two-way ANOVA mean ± SEM and sex are denoted as male/female. Statistically significant stars are color-coded according to transgenic genotype against WT. *p<0.05. (6MO: WT, n=3/3; Apoe$^{-/-}$, n=5/4; hAPOE3, n=3/4; hAPOE4, n=5/5. 10MO: WT, n=3/2; Apoe$^{-/-}$, n=4/6; hAPOE3, n=3/2; hAPOE4, n=4/6. 16MO: WT, n=3/2; Apoe$^{-/-}$, n=8/4; hAPOE3, n=5/10; hAPOE4, n=9/8).*

4.5 Metabolite detection with magnetic resonance spectroscopy of aged tgAPOE mice

Neurotransmitters and metabolite content is vital in the functions of the brain. By utilising MRS, the levels of specific compounds could be studied. In this investigation, a 3mm x 3mm x 3mm voxel, spanning Bregmas -2.5, -1.8, and -0.8, within the medial brain is used to evaluate the levels of five metabolites: myo-inositol, choline, glutamate/glutamine, NAA, and lipid/lactate. Peaks of each chemical shift is normalised with the peak of creatine (Figure 97). Additionally, DKI calculations are done on each investigated Bregma voxel. The region analysed includes both grey matter and white matter tract regions without differentiation. Levels of (MRS) detected metabolite changes against creatine were established in Alzheimer's evaluations. Two considerations were made for the use of ratio quantification and creatine levels for normalization. First, MRS acquisitions were performed over a period of three years, with two instances of re-calibration of the 3T Bruker functional MRI. Absolute quantification over this time would introduce errors due to calibrations of the machine. Thus, ratio analysis was preferred. Second, the choice of creatine as the normalization method is due to its supported literature using ratios of myo-inositol, choline, n-acetylaspartate, and lipids against creatine in Alzheimer's patients (337, 338, 339, 340, 341).

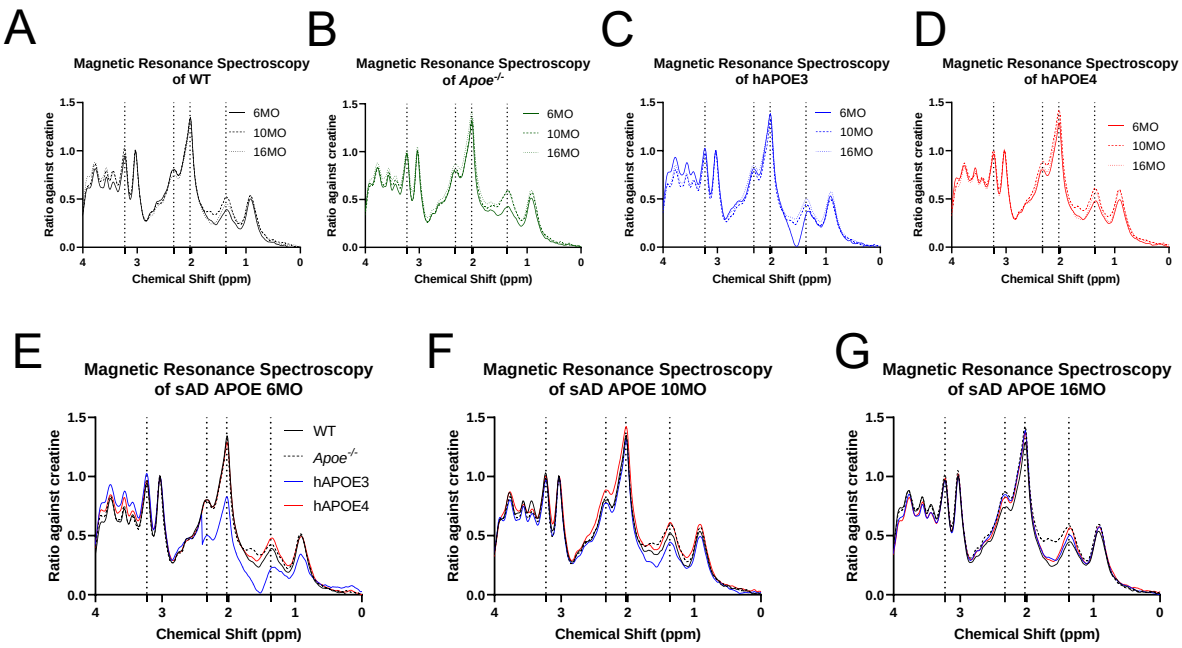

Figure 97: The mean curves of MRS value are presented as age-dependent per genotype (A-D) or genotype-dependent per age (E-G). Vertical dotted lines represent the peaks of interested metabolites: myo-inositol (3.5ppm), choline (3.2ppm), glutamate/glutamine (2.3ppm), NAA (2.0ppm), and lipid/lactate (1.3ppm). Sex are denoted as male/female. (6MO: WT, n=3/3; Apoe$^{-/-}$, n=5/4; hAPOE3, n=3/4; hAPOE4, n=5/5. 10MO: WT, n=3,2; Apoe$^{-/-}$, n=4/6; hAPOE3, n=3/2; hAPOE4, n=4/6. 16MO: WT, n=1,3; Apoe$^{-/-}$, n=8/4; hAPOE3, n=5/10; hAPOE4, n=9/8).

4.5.1 Metabolite and DKI changes based on age in individual genotypes

WT mice exhibit no changes among 6, 10, and 16MO of all five metabolites (Figure 98). Percent changes among metabolites are minimal. Anisotropic analysis shows significant reductions of Bregma -1.8 between 10MO against 6MO (-13.2%, p=0.0287) (Figure 99). RD shows no changes among Bregmas and ages (Figure 99), but AxD shows comparable reductions of 10MO against 6MO in Bregma -1.8 (-14.6%, p=0.0383) and -0.8 (-11.9%, p=0.0476) with age representing a significant factor in the difference (p=0.0313) (Figure 99). This age-based significance is also observed in MD (p=0.0357) with no age-specific changes (Figure 99).

With the knockout of Apoe, significance is yielded in the comparison of 16MO against 6MO lipid/lactate levels (+32.5%, p=0.04) (Figure 98). Likewise, comparisons of 6MO and 10MO generates similar increases with age, albeit without significance. Diffusivity analysis shows no differences among age groups. Comparatively, hAPOE3 produces the same significant increase of lipid/lactate levels in 16MO against 6MO (+23.4%, p=0.04) with substantial insignificant increases with age (Figure 99). Aging is associated with increased lactate levels. Previous studies have shown that by using a normally aging and prematurely aging mice model, there is a two-fold increase in lactate levels between the two mice using H-MR (342). This was correlated to an increase in lactate dehydrogenase activity in the mitochondria, converting pyruvate to lactate for respiration. Thus, this result could be caused by aging. Diffusivity analysis of hAPOE3 also shows no differences among age groups.

However, in hAPOE4, lipid/lactate levels no longer show difference. However, glutamate/glutamine and NAA exhibit significant changes. Glutamate/glutamine levels show significant increase between 10MO against 6MO (+12.9%, p=0.04) and decrease between 16MO against 10MO (-11.8%, p=0.01). Comparison of 10MO against 6MO NAA also shows significance (+12.1%, p=0.02) (Figure 98). DKI analysis of this voxel shows no changes of FA and AxD of these mice, but identical significance is observed in RD and MD. Significant increase of 10MO against 6MO RD is found at posterior Bregma -2.5 (+8.5%, p=0.0043) and -1.8 (+11.4%, p=0.0007) and of MD at -2.5 (+7.9%, p=0.0169) and -1.8 (+10.5%, p=0.0059) (Figure 99).

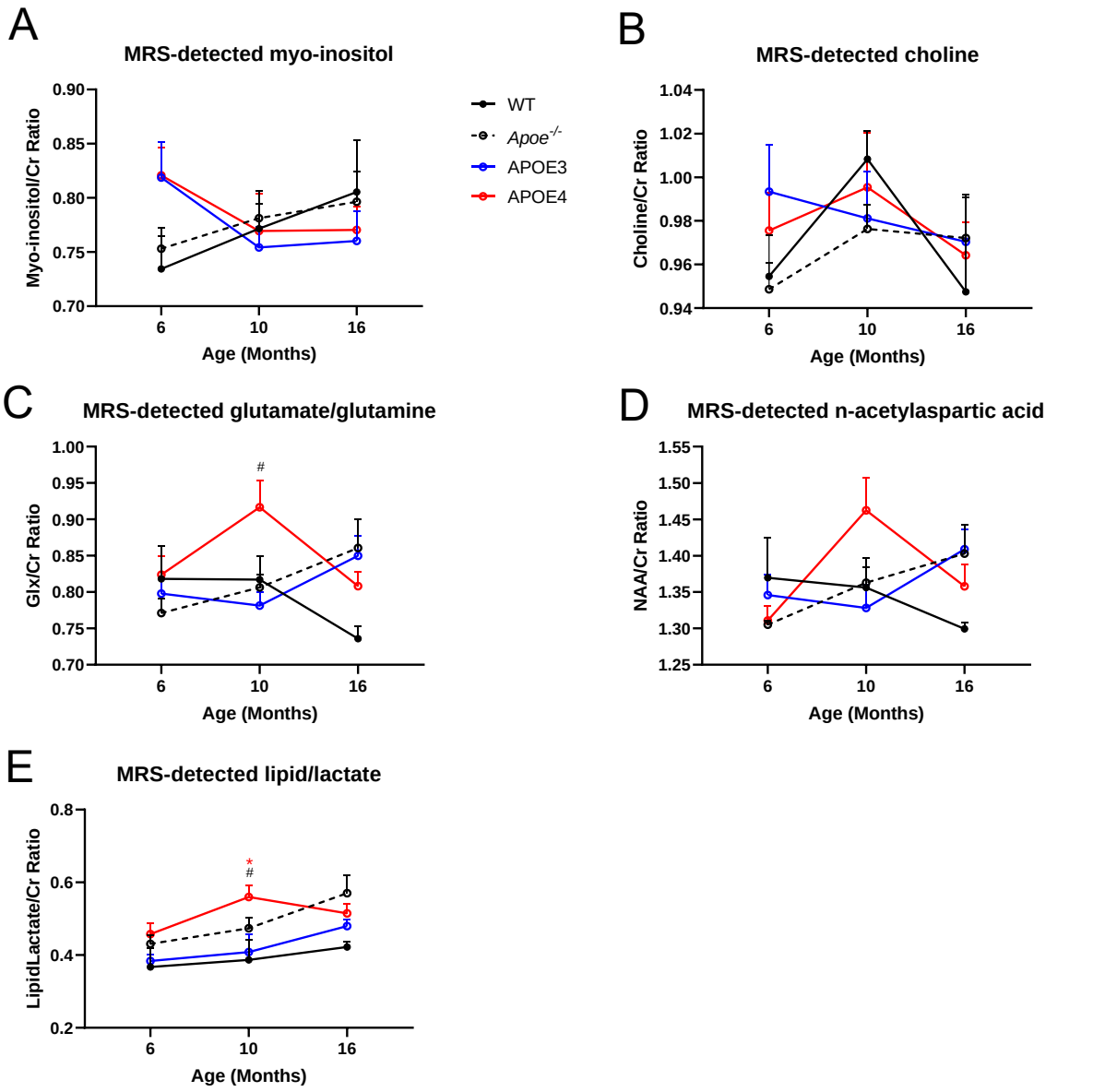

*Figure 98: Area under curve for metabolites of interest are independently compared at their respective peaks and standardized with creatine (A-E). Analysis suggests no significant changes of myo-inositol (A), choline (B), glutamate/glutamine (F), and NAA (D). However, significant increase of glutamate/glutamine in 10MO APOE4 against APOE3 (C) and lipid/lactate levels in 10MO APOE4 against WT was observed (E). All values are of two-way ANOVA mean ± SEM and sex are denoted as male/female. Statistically significant stars are color-coded according to transgenic genotype against WT. *p<0.05. Statistically significant hashes are according to hAPOE4 changes against hAPOE3. #p<0.05. (6MO: WT, n=3/3; Apoe$^{-/-}$, n=5/4; hAPOE3, n=3/4; hAPOE4, n=5/5. 10MO: WT, n=3/2; Apoe$^{-/-}$, n=4/6; hAPOE3, n=3/2; hAPOE4, n=4/6. 16MO: WT, n=3/2; Apoe$^{-/-}$, n=8/4; hAPOE3, n=5/10; hAPOE4, n=9*

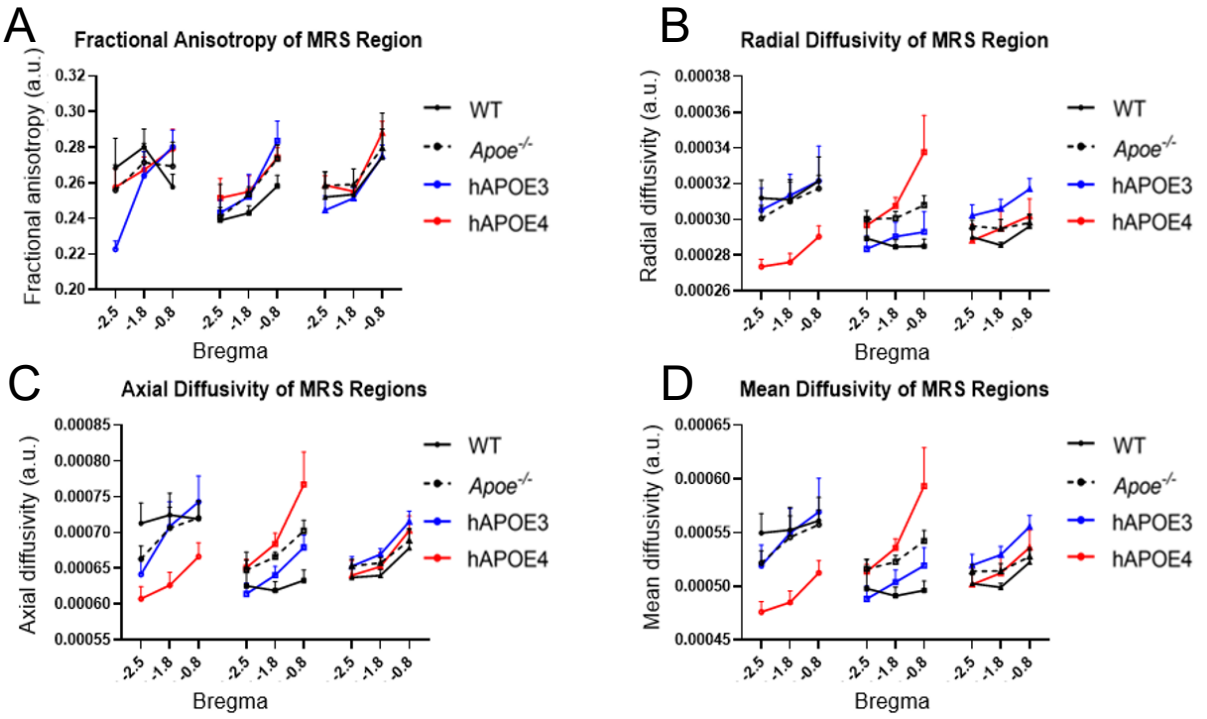

Figure 99: The MRS voxels for FA (A), RD (B), AxD (C), and MD (D) of genotypic and age groups were analysed for changes in diffusion of water of white matter in the mice brain. Genotypes are grouped by age and graphically compared by Bregma numbers. All values are of two-way ANOVA mean ± SEM and sex are denoted as male/female. (6MO: WT, n=3/3; Apoe$^{-/-}$, n=5/4; hAPOE3, n=3/4; hAPOE4, n=5/5. 10MO: WT, n=3/2; Apoe$^{-/-}$, n=4/6; hAPOE3, n=3/2; hAPOE4, n=4/6. 16MO: WT, n=3/2; Apoe$^{-/-}$, n=8/4; hAPOE3, n=5/10; hAPOE4, n=9/8).

4.5.2 Metabolite and DKI changes based on genotype in individual age groups

Age-based analysis shows the effects of aging in different genotypes. While WT MRS and DKI in the associated 3mm x 3mm x 3mm region remains consistent with age, tgAPOE mice show greater variation in their metabolite levels and diffusivities. Here, the genotypes are compared at matching ages to show at which age are the differences in MRS and DKI levels the greatest.

At 6MO, metabolite differences are not observed, with all genotypes showing comparable levels. Diffusivity changes, though, are seen in comparisons of hAPOE4 to other genotypes. Significant FA increase is found in Bregma -2.5 against hAPOE3 (+15.7%, p=0.0427) (Figure 99). Directional diffusivity of RD shows correlational decrease in Bregma -2.5 against WT (-12.3%, p=0.0399) and *Apoe*$^{-/-}$ (-9.0%, p=0.0306) with no such change in AxD (Figure 99). However, age-based changes are significant in RD (p=0.0123) and AxD (p=0.0464). Correspondingly, MD shows significance in the same Bregma against WT (-14.4%, p=0.0307) and *Apoe*$^{-/-}$ (-8/8%, p=0.0355) (Figure 99). These results suggest hAPOE4's effect on diffusivity before alterations in metabolite levels.

By 10MO, hAPOE4 exhibits greater effects on metabolite values. Glutamate/glutamine levels are significantly increased in hAPOE4 against *Apoe*$^{-/-}$ (+13.7%, p=0.0243) and hAPOE3 (+17.3%, p=0.0229). Likewise, lipid/lactate levels are also greatly increased in hAPOE4 against WT (+44.8%, p=0.0347) and hAPOE3 (+37.0%, p=0.0505). Other metabolites remain at consistent levels. Further DKI investigation shows unchanged FA values with significant increases of hAPOE4 against WT and *Apoe*$^{-/-}$ against WT directional diffusivities. RD analysis of Bregma -1.8 shows significant increase of hAPOE4 against WT (+8.0%, p=0.0171) and Bregma -0.8 *Apoe*$^{-/-}$ against WT (+8.0%, p=0.0239) (Figure 99). Correspondingly, AxD analysis shows comparative significance in Bregma -1.8 of hAPOE4 against WT (+10.5%, p=0.0297) and -0.8 of *Apoe*$^{-/-}$ against WT (+11.0%, p=0.0336) (Figure 99). As a result, MD shows identical regions and genotype significance. However, by 16MO, no changes are observed in neither metabolite nor DKI levels.

4.6 Immunohistochemistry analysis for oligodendrocyte and myelin changes

Radiological study of the tgAPOE mice suggests variations of diffusivity and metabolite levels at different ages. To further identify the effects of the APOE genotype, immunohistology using markers for gross, immature, and mature OLs and myelin is performed at Bregma 0.8 due to the increased variations at this Bregma from DKI. Gross OLs are stained with Olig2, immature OLs are stained with Nkx2.2., mature OLs are stained with ASPA and CC1, and myelin is stained with PLP. Six regions representing three grey matter (anterior cingulate, motor cortex, and somatosensory cortex) and white matter tract (genu, cingulum, and external capsule) are used for analysis.

4.6.1 Oligodendrocyte and myelin changes based on age in individual genotypes

First, gross OL populations among individual regions are quantified with Olig2 OL marker in each genotype. The Olig2+ cells are seen to be consistent for each genotype with no significant changes among ages. Within the anterior cingulate, there is a consistent number of Olig2+ gross OL population among all three age groups in all genotypes with hAPOE4 showing consistent lower numbers. By 16MO, hAPOE4 shows significant decrease of Olig2+ populations compared to WT (-71.0%, p=0.0035) (Figure 100A). In the motor cortex and somatosensory cortex, age-related significances are observed only in individual hAPOE3 6MO compared to 10 and 16MO. Specifically, 6MO hAPOE shows significantly increased OL populations against WT in motor cortex (+237%, p=0.0009) (Figure 100B) and somatosensory cortex (+149.1%, p=0.0152)(Figure 100C). Comparisons of hAPOE3 and hAPOE4 shows significant decrease similarly in 6MO in motor cortex (-72.4%, p<0.0001) and somatosensory cortex (-62.2%, p=0.0027). In the genu, no observable trend nor significance is found. In contrast, the cingulum and external capsule show no changes in Olig2+ populations among ages with significantly reduced hAPOE4 against WT in only the 16MO of cingulum (-69.9%, p=0.0216) (Figure 100E) and external capsule (-67.3%, p=0.0194) (Figure 100F). Overall Olig2+ changes indicate a common reduced gross OL population in hAPOE4 among age groups.

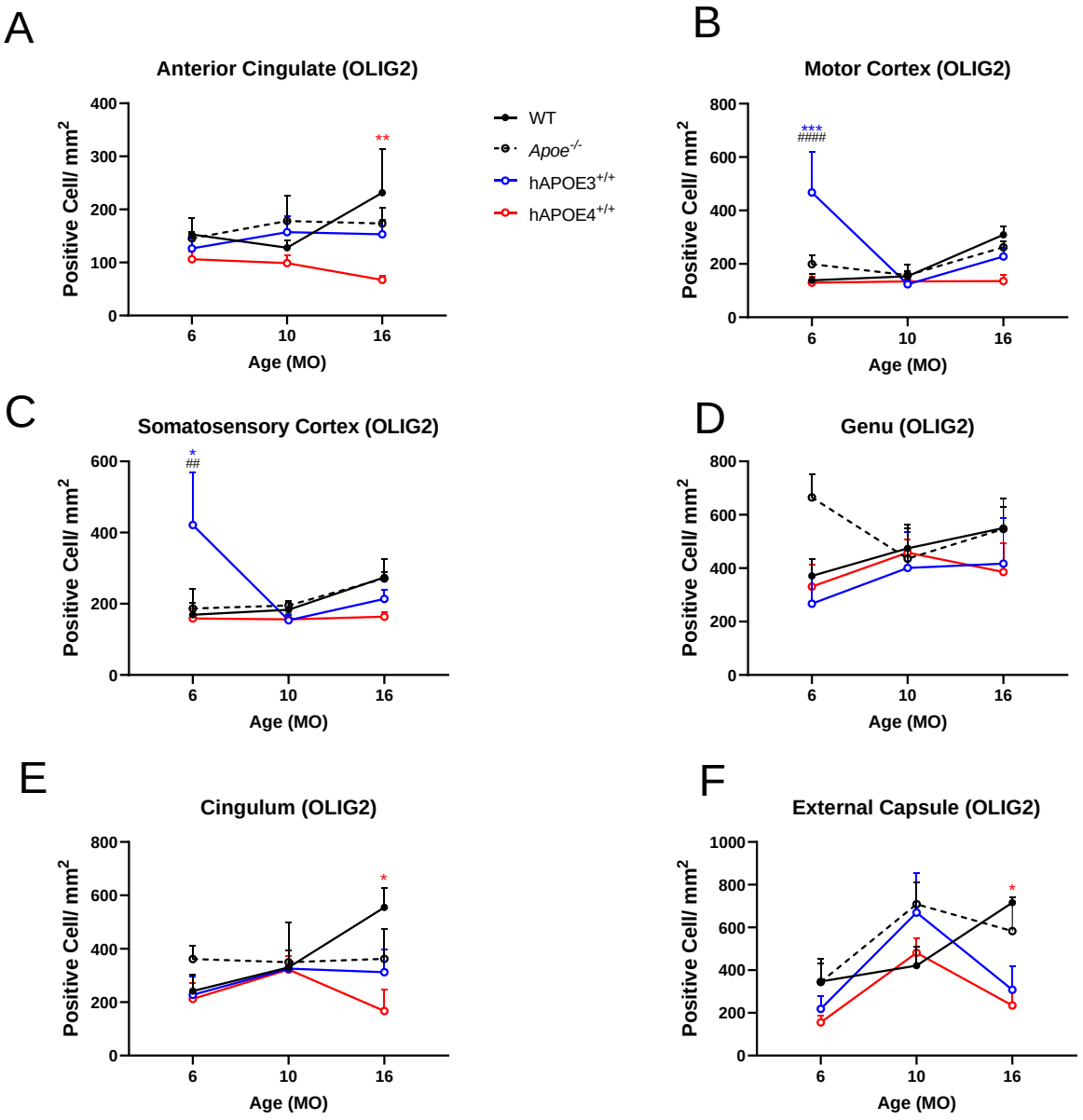

*Figure 100: Olig2+ populations in three grey matter regions (anterior cingulate (A), motor cortex (B), somatosensory cortex (C)) and white matter regions (genu (D), cingulum (E), external capsule(F)). All values are of two-way ANOVA mean ± SEM and sex are denoted as male/female. Statistically significant stars are color-coded according to transgenic genotype against WT. *p<0.05; **p<0.01. Statistically significant hashes are according to hAPOE4 changes against hAPOE3. ##p<0.01; ####p<0.0001. (6MO: WT, n=3/3; Apoe$^{-/-}$, n=3/3; hAPOE3, n=3/3; hAPOE4, n=4/5. 10MO: WT, n=3/2; Apoe$^{-/-}$, n=4/6; hAPOE3, n=3/2; hAPOE4, n=4/6. 16MO: WT, n=3/2; Apoe$^{-/-}$, n=2/2; hAPOE3, n=1/3; hAPOE4, n=2/2).*

Immature OLs are then quantified with Nkx2.2 (Figure 101). Analysis of anterior cingulate shows no significant changes of Nkx2.2+ cells in all genotypes. In the motor cortex and somatosensory cortex, significant increase is found in 6MO hAPOE3 against WT (+166.3%, p=0.0019; +233.7%, p=0.0004) and hAPOE4 (+39.8%, p=0.045; +55.4%, p=0.0025) (Figure 101B and C). Overall age- and genotype-based alterations are significant in the motor cortex ($p<0.0001$ and p=0.0496, respectively) and somatosensory cortex (p=0.0107 and p=0.0062, respectively). In the white matter tract, both genu and external capsule show valleys of Nkx2.2+ cells at 10MO among ages of all four genotypes. Significance is found between the genu of 6MO hAPOE4 against hAPOE3 (+124.6%, p=0.0023) (Figure 101D) and external capsule of 6MO hAPOE3 against WT (+49.3%, p=0.0467) (Figure 101F). More Nkx2.2 variations are observed in the white matter tract as these regions contain the most OLs and their lineages.

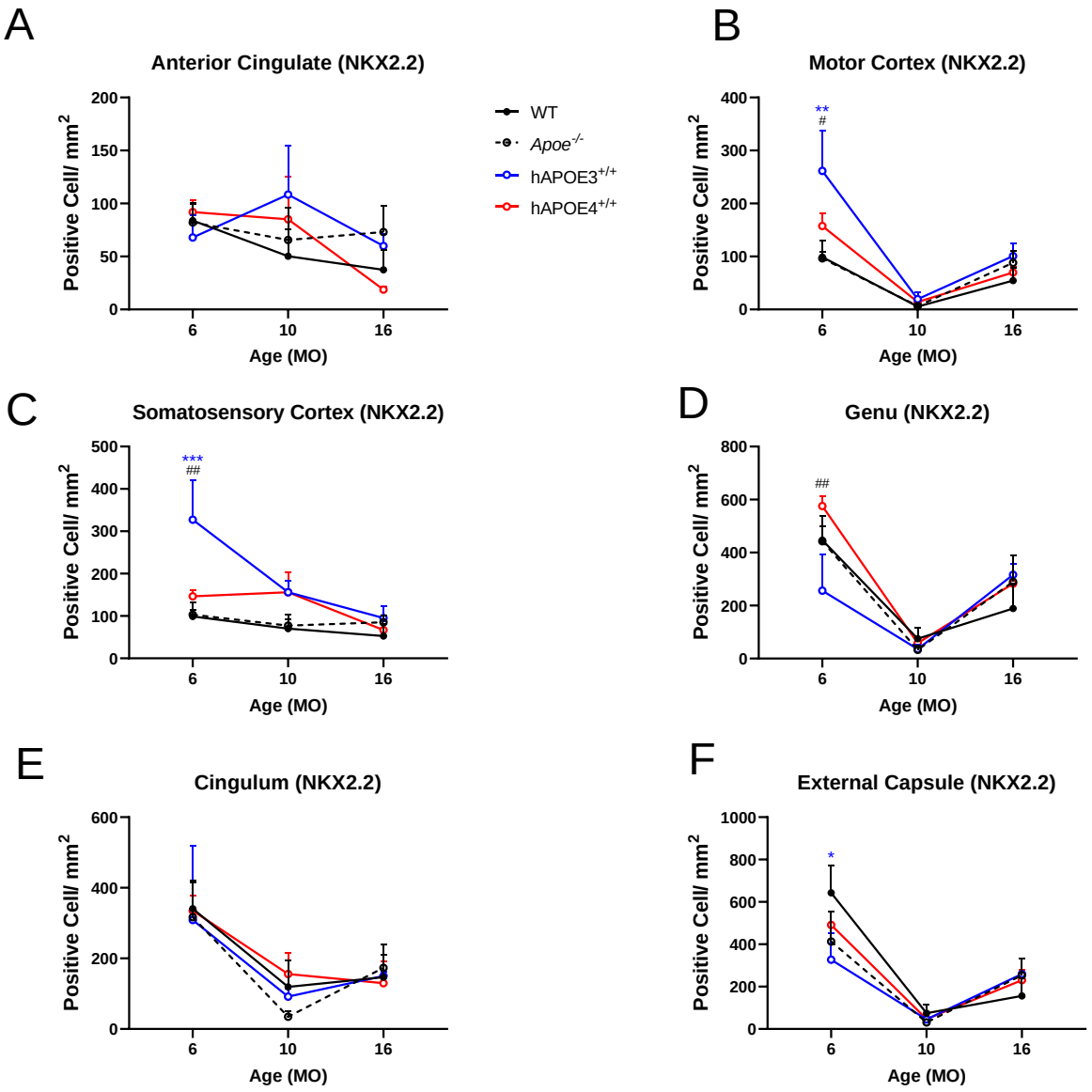

*Figure 101: Nkx2.2+ populations in three grey matter regions (anterior cingulate (A), motor cortex (B), somatosensory cortex (C)) and white matter regions (genu (D), cingulum (E), external capsule(F)). All values are of two-way ANOVA mean ± SEM and sex are denoted as male/female. Statistically significant stars are color-coded according to transgenic genotype against WT. *p<0.05; **p<0.01; ***p<0.001. Statistically significant hashes are according to hAPOE4 changes against hAPOE3. #p<0.05; ##p<0.01. (6MO: WT, n=3/3; Apoe$^{-/-}$, n=3/3; hAPOE3, n=3/3; hAPOE4, n=4/5. 10MO: WT, n=3/2; Apoe$^{-/-}$, n=4/6; hAPOE3, n=3/2; hAPOE4, n=4/6. 16MO: WT, n=3/2; Apoe$^{-/-}$, n=2/2; hAPOE3, n=1/3; hAPOE4, n=2/2).*

Mature OLs, stained with ASPA and CC1, show differing patterns in cell numbers. ASPA+ populations have consistent significant reductions with age in all regions of grey matter and white matter tract (Figure 102). While all genotypes show decrease from 6MO to 16MO, hAPOE3 ASPA+ cells show significant increase at 10MO against WT in motor cortex (+128.4%, p=0.0025) (Figure 102B), somatosensory cortex (+173.9%, p=0.0296) (Figure 103C), and genu (+248.9%, p=0.0088) (Figure 102D). Differently, 6MO hAPOE3 ASPA shows significant reductions against WT in all three white matter regions of genu (-68.5%, p=0.0046) (Figure 102D), cingulum (-62.4%, p=0.0321) (Figure 102E), and external capsule (-61.6%, p=0.0093) (Figure 102F).

Mature OLs stained with CC1, though, do not show observable trend among age groups. In the anterior cingulate, CC1+ populations show levelled numbers among ages with 6MO hAPOE3 showing significant reductions against WT (-59.6%, p=0.0003) (Figure 103A). Like ASPA, hAPOE3 CC1+ populations show significant increases at 10MO against WT in the motor cortex (+165.3%, p=0.0011) (Figure 103B) and somatosensory cortex (+157.5%, p=0.0033) (Figure 103C). In the white matter regions, only at 6MO are there significant increases of hAPOE3 against WT in genu (+33.2%, p=0.0445) (Figure 103D), cingulum (+52.4%, p=0.0172) (Figure 103E), and external capsule (+56.4%, p=0.0002) (Figure 103F).

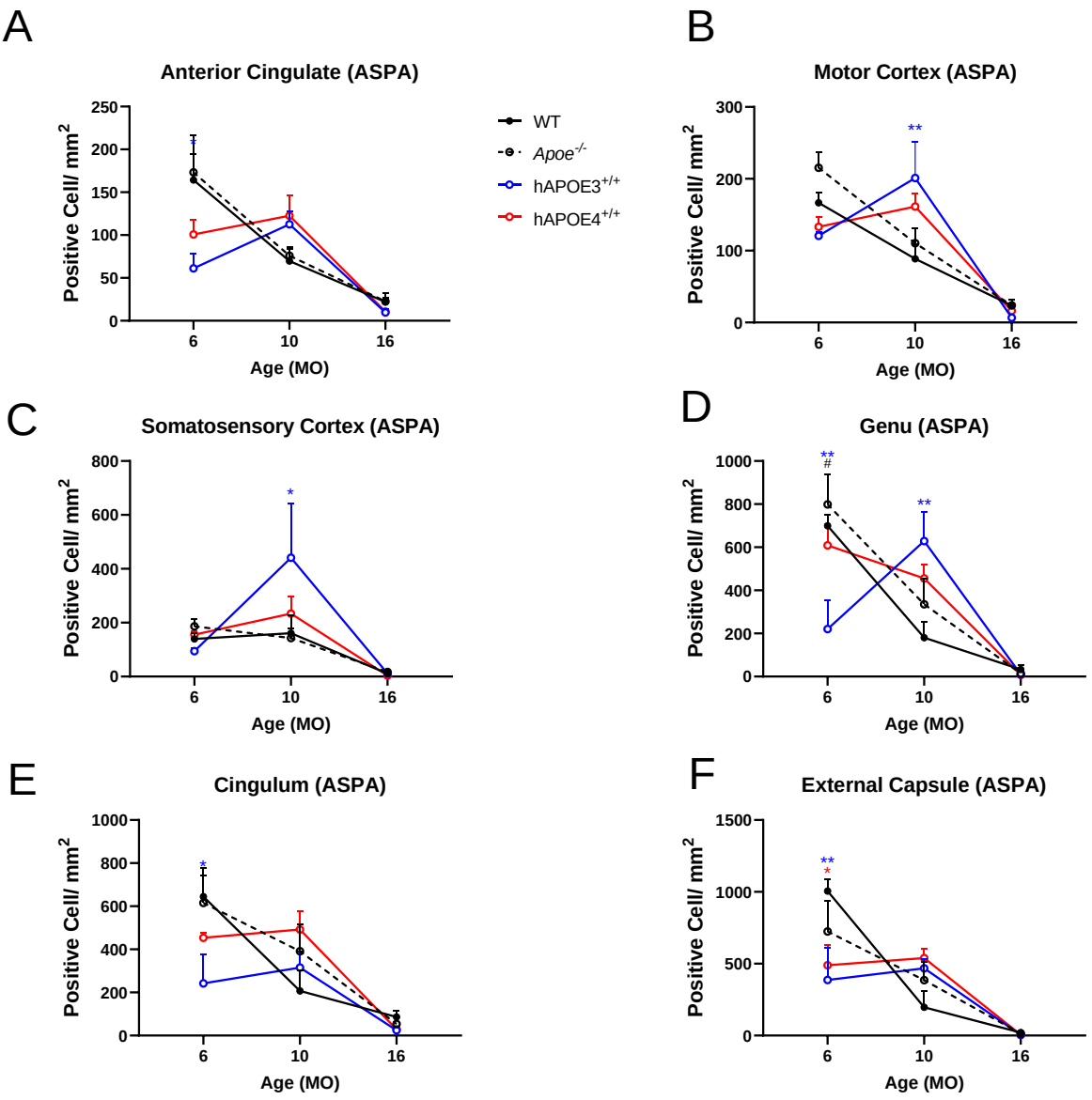

*Figure 102: ASPA+ populations in three grey matter regions (anterior cingulate (A), motor cortex (B), somatosensory cortex (C)) and white matter regions (genu (D), cingulum (E), external capsule(F)). All values are of two-way ANOVA mean ± SEM and sex are denoted as male/female. Statistically significant stars are color-coded according to transgenic genotype against WT. *p<0.05; **p<0.01. Statistically significant hashes are according to hAPOE4 changes against hAPOE3. #p<0.05. (6MO: WT, n=3/3; Apoe$^{-/-}$, n=3/3; hAPOE3, n=3/3; hAPOE4, n=4/5. 10MO: WT, n=3/2; Apoe$^{-/-}$, n=4/6; hAPOE3, n=3/2; hAPOE4, n=4/6. 16MO: WT, n=3/2; Apoe$^{-/-}$, n=2/2; hAPOE3, n=1/3; hAPOE4, n=2/2).*

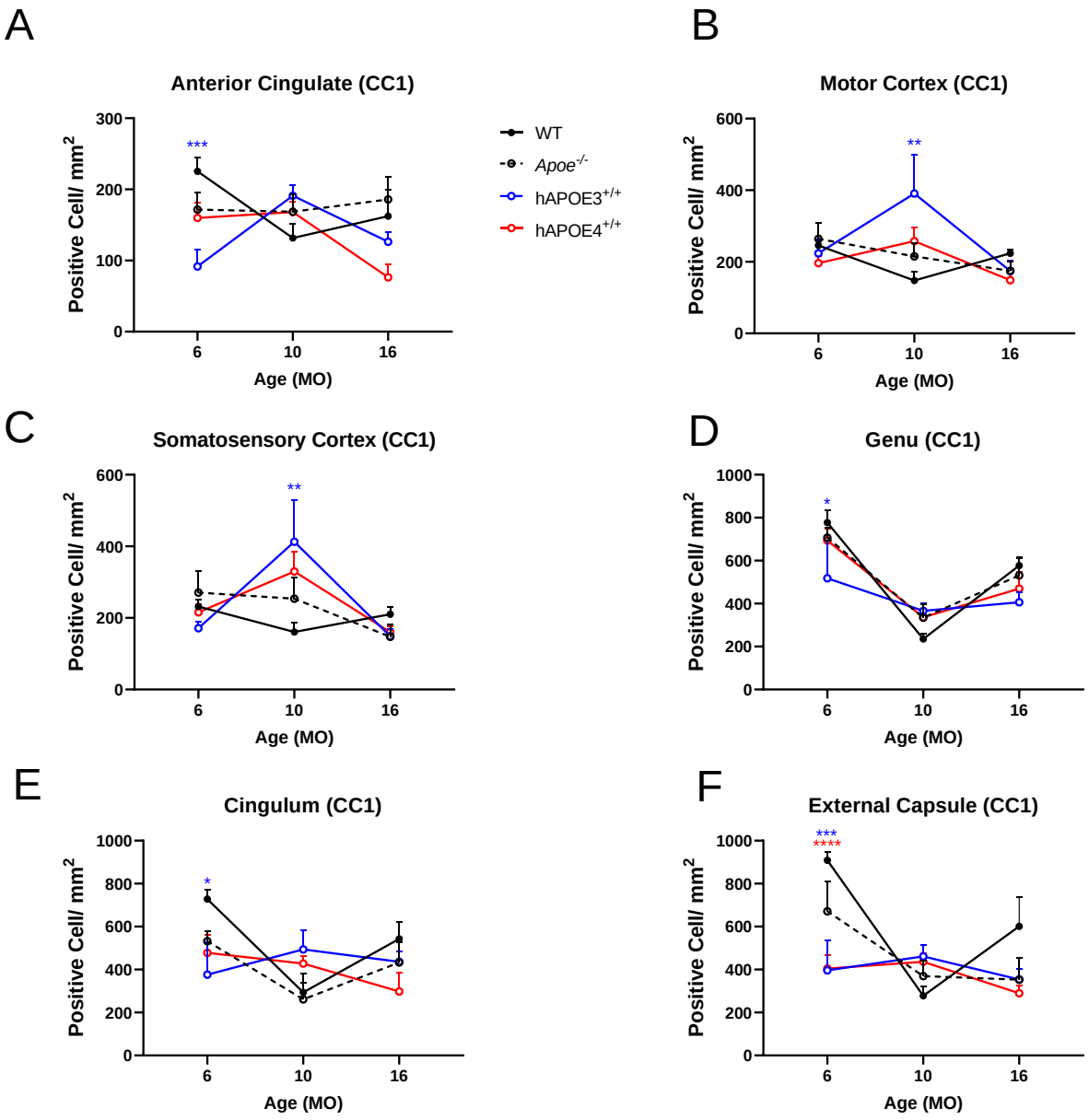

*Figure 103: CC1+ populations in three grey matter regions (anterior cingulate (A), motor cortex (B), somatosensory cortex (C)) and white matter regions (genu (D), cingulum (E), external capsule(F)). All values are of two-way ANOVA mean ± SEM and sex are denoted as male/female. Statistically significant stars are color-coded according to transgenic genotype against WT. *p<0.05; **p<0.01; ***p<0.001; ****p<0.0001. (6MO: WT, n=3/3; Apoe-/-, n=3/3; hAPOE3, n=3/3; hAPOE4, n=4/5. 10MO: WT, n=3/2; Apoe-/-, n=4/6; hAPOE3, n=3/2; hAPOE4, n=4/6. 16MO: WT, n=3/2; Apoe-/-, n=2/2; hAPOE3, n=1/3; hAPOE4, n=2/2).*

These OL changes warrant further investigation into densities of myelin fibres stained with PLP (Figure 104). Grey matter PLP+ fibres are unchanged among ages of genotypes. However, significance is observed in both age-based factors ($p=0.0018$) (Figure 104A). White matter tract similarly shows minimal significance with only cingulum showing significant reduction in PLP percentage in 16MO in hAPOE4 against WT (-42.1%, $p=0.0488$) (Figure 104E). Further analysis of trend shows hAPOE4 PLP percentages in all regions to be consistently the lowest among genotypes, especially by 16MO. This may indicate an aging effect that makes APOE4 more susceptible to myelin loss, yet, because no significance could be drawn, further studies are warranted for the representation of myelin content.

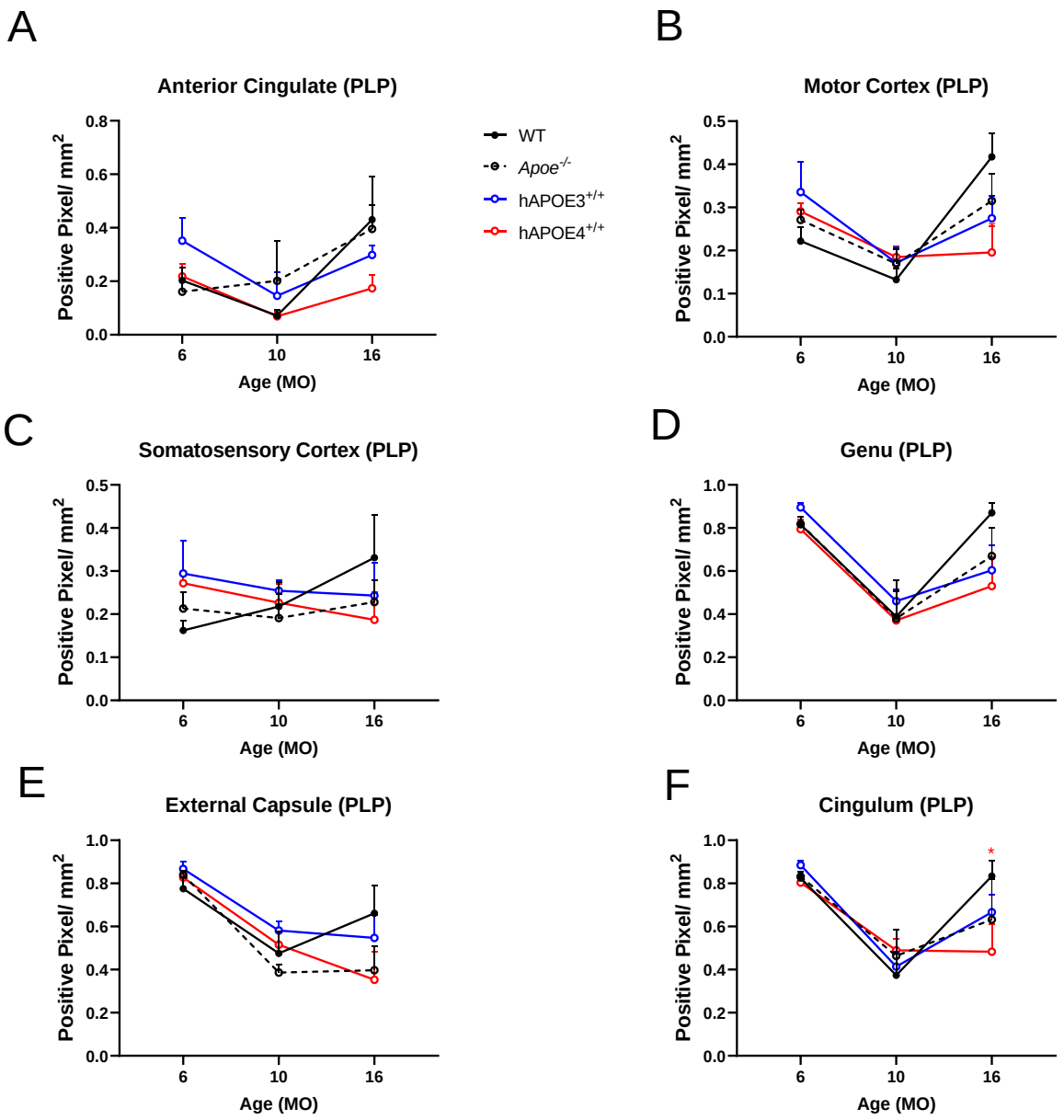

*Figure 104: PLP densities in three grey matter regions (anterior cingulate (A), motor cortex (B), somatosensory cortex (C)) and white matter regions (genu (D), cingulum (E), external capsule(F)). All values are of two-way ANOVA mean ± SEM and sex are denoted as male/female. Statistically significant stars are color-coded according to transgenic genotype against WT. *p<0.05. (6MO: WT, n=3/3; Apoe-/-, n=3/3; hAPOE3, n=3/3; hAPOE4, n=4/5. 10MO: WT, n=3/2; Apoe-/-, n=4/6; hAPOE3, n=3/2; hAPOE4, n=4/6. 16MO: WT, n=3/2; Apoe-/-, n=2/2; hAPOE3, n=1/3; hAPOE4, n=2/2).*

4.7 Cognitive abilities and behavioural test using Y-maze

Working memory test was separated into reference memory and episodic memory and done with three-pronged y-maze. The spontaneous alternation, distance travelled, movement speed, time of immobility, and total entries were measured for reference memory as all three arms of the maze were opened during this eight-minute trial. Comparatively, the total entries, total correct entries, and percentage of time in the correct entry were measured for episodic memory as this trial is separated into a four-minute trial period where one arm was closed and a consecutive four-minute trial after one hour where all arms were opened. 16MO WT are not included in the two-way ANOVA analysis due to a lack of 6MO and 10MO WT.

Investigation of the reference memory among *Apoe*$^{-/-}$, hAPOE3, and hAPOE4 shows overlapping spontaneous alternation percentages at all three timepoints. WT mice were not compared due to lack of apparatus while performing the 6MO and 10MO cohorts. However, comparison between 10MO and 16MO shows significant decreases by 16MO in *Apoe*$^{-/-}$ (-50.1%, $p<0.0001$), hAPOE3 (-59.9%, $p<0.0001$), and hAPOE4 (-57.0%, $p<0.0001$) (Figure 105A). Independent analysis of 16MO with WT, though, shows significant decrease between WT with *Apoe*$^{-/-}$ (-25.7%, $p=0.0469$), hAPOE3 (-33.0%, $p=0.0078$) and hAPOE4 (-29.3%, $p=0.0324$) (Figure 107A). The movements and total number of arm entries among *Apoe*$^{-/-}$, hAPOE3, and hAPOE4 against age show no change in their distance travelled, movement speeds, nor arm entries. Yet, 16MO analysis show significant decreases of these three parameters of the transgenic mice against WT (Figure 107B-D). Differences in APOE status seem to induce an age-dependent effect with transgenic mice showing more severe reductions in spatial references in addition to lower physical activity. The APOE4 mice has been shown to exhibit poor spatial learning and memory when compared to APOE3 in the Barnes maze in mice as young as 3 months up to 18 months (343). While this study did not look at aspects of cell quantities, they found significantly shortened dendrites and lower spine densities in the layers II and III of the medial entorhinal cortex pyramidal cells. Due to the close association of the medial entorhinal cortex network with the hippocampus, it is proposed that shorter dendrites inhibited efficient projections into the

hippocampal perforant pathway (344). Among the transgenic mice, no specific mutation seems to influence the mice's cognitive abilities more, suggesting an intrinsic effect of a non-murine APOE.

Episodic memory test shows minimal changes among genotypes with age. Total entries of all mice show no changes (Figure 106A). Regarding the percent of entries into the correct arm, statistically, all values are insignificant. However, the plotted curve suggests that at 10 months, hAPOE3 against *Apoe*$^{-/-}$ and hAPOE4 exhibit an apparent decrease of 22.1% and 21.7%, respectively, without significance (Figure 106B). By 16 months, both *Apoe*$^{-/-}$ and hAPOE4 rises back up to the hAPOE3 percentage. Furthermore, the percentage of time spent in the correct arm remains similar among genotypes and ages (Figure 109). Analysis of episodic memory suggests minimal changes with differing APOE status.

Through the behaviour test, it is shown that cognitive changes could be affected by lack of the murine APOE as significant changes in reference memory are from transgenic mice against the WT. The synchronous decrease of spontaneous alternation from 10 to 16 months shows an age-dependent change, inherent to aging mice. Moreover, overall decreased movement of the transgenic mice suggests APOE's effect on the mice's motor skills. With the increased weights shown previously, both these factors could impact mice activity.

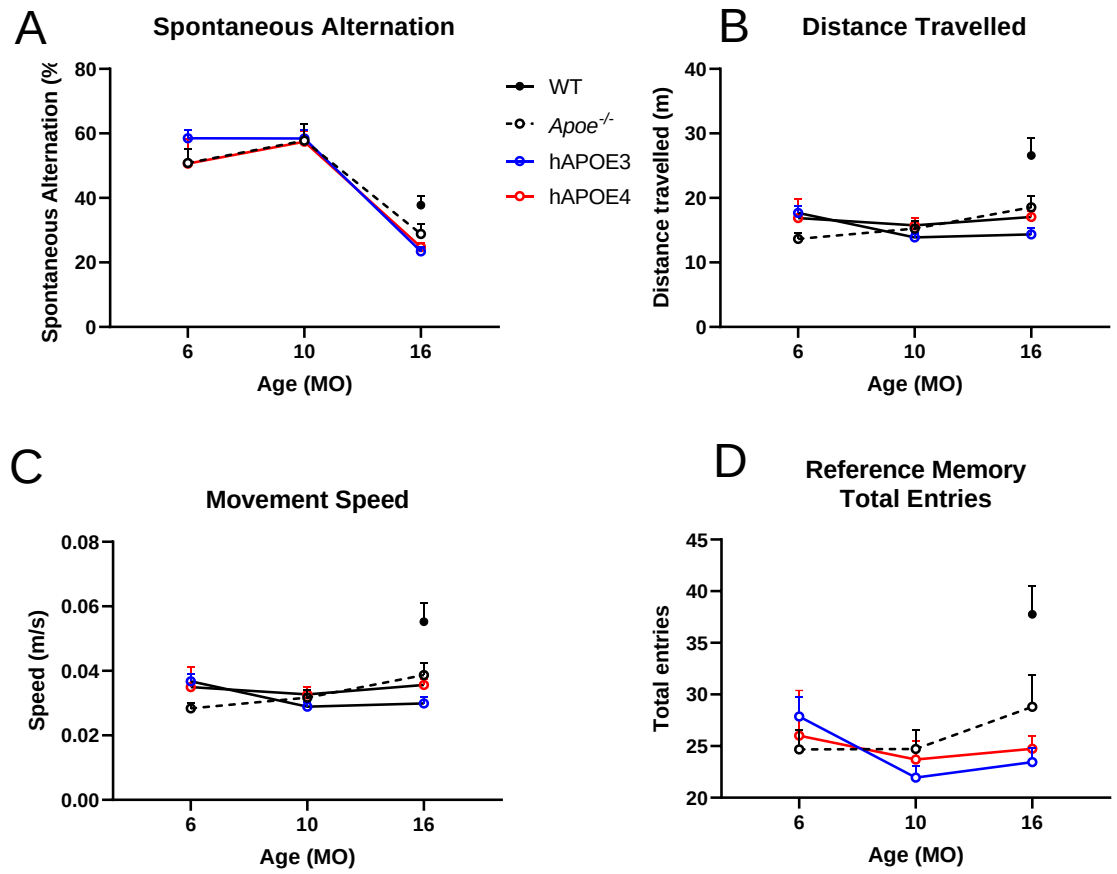

*Figure 106: Working memory was investigated with Y-maze behaviour test and separated into reference memory and episodic memory. Analysis of the spontaneous alternation (A), distance travelled (B), movement speed (C), and total arm entries (D) from this trial suggest significant age-dependent changes in spontaneous alternation. Significant differences of two-way ANOVA in behaviour between genotype and diet are indicated by asterisks: **p < 0.01. All values are of two-way ANOVA mean ± SEM.*

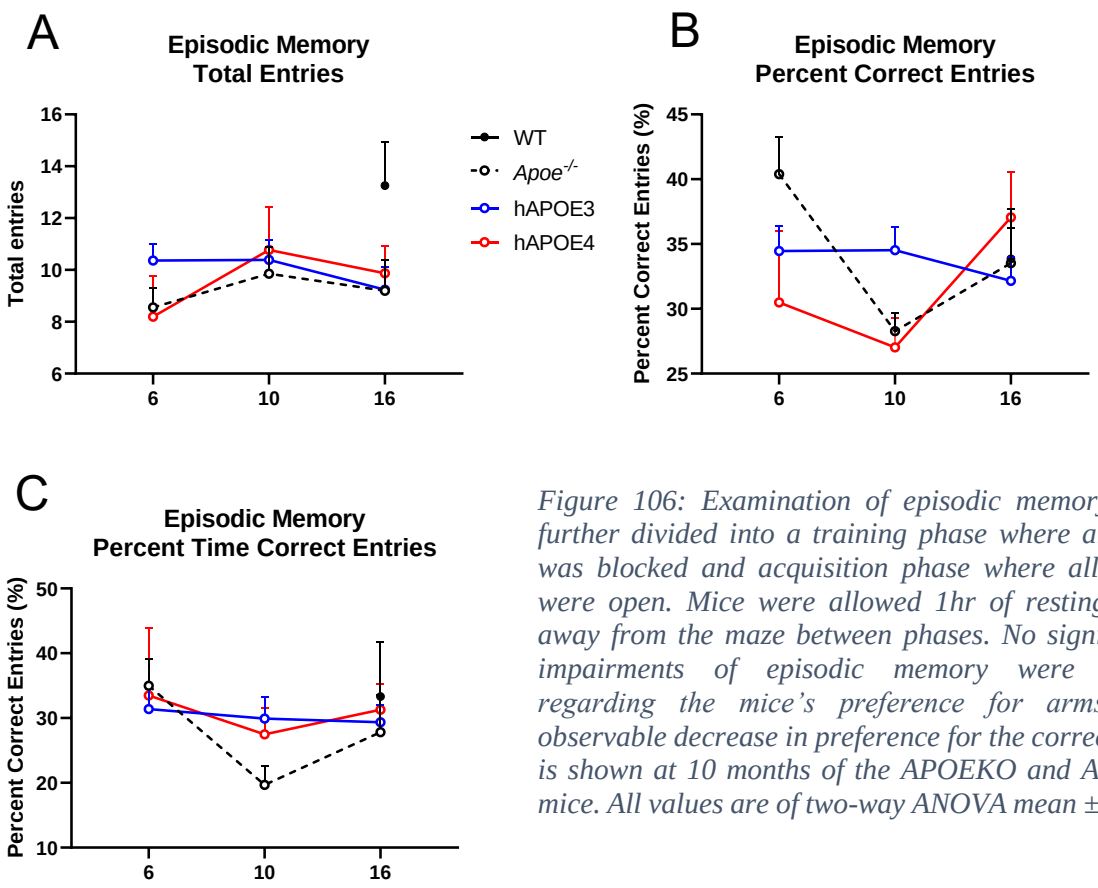

Figure 106: Examination of episodic memory was further divided into a training phase where an arm was blocked and acquisition phase where all arms were open. Mice were allowed 1hr of resting time away from the maze between phases. No significant impairments of episodic memory were found regarding the mice's preference for arms, yet observable decrease in preference for the correct arm is shown at 10 months of the APOEKO and APOE4 mice. All values are of two-way ANOVA mean ± SEM.

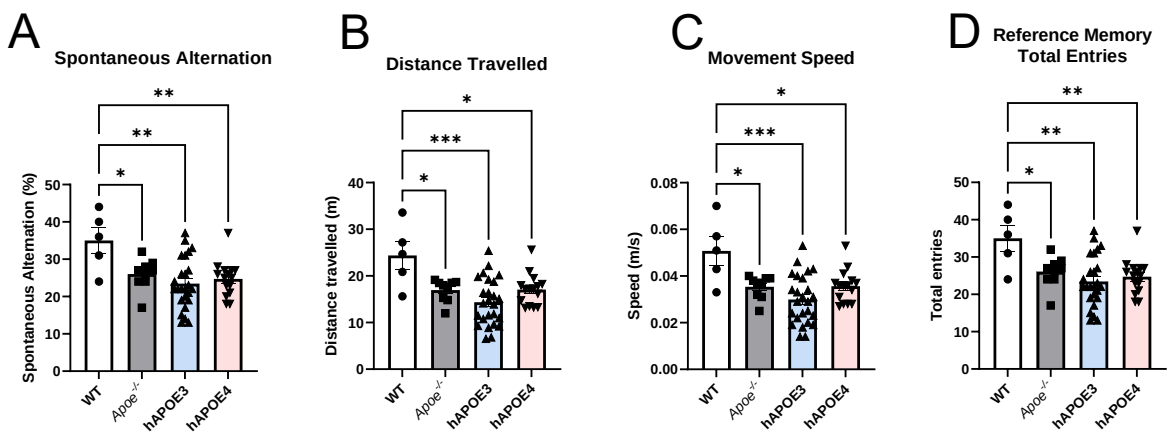

*Figure 107: Individual analysis on 16MO samples was done independently due to the lack of the WT in 6 and 10MO. Working memory was investigated with Y-maze behaviour test and separated into reference memory and episodic memory. Analysis of the spontaneous alternation (A), distance travelled (B), movement speed (C), and total arm entries (D) from this trial shows WT's continual increased movement around the maze. Transgenic mice show no change among parameters and genotype. *p < 0.05, **p < 0.01, ***p < 0.001. All values are of one-way ANOVA mean ± SEM.*

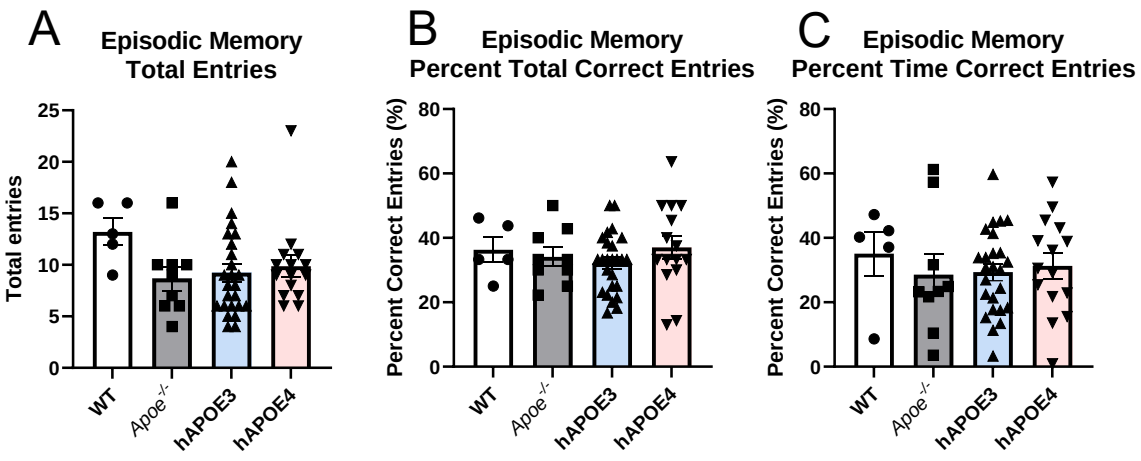

Figure 108: Examination of 16MO episodic memory was further divided into a training phase where an arm was blocked and acquisition phase where all arms were open. Mice were allowed 1hr of resting time away from the maze between phases. No significant impairments of episodic memory were found regarding the mice's preference for arms. All values are of one-way ANOVA mean ± SEM.

4.8 Astrocytes, not OLs, express hAPOE

To confirm the presence of hAPOE in transgenic hAPOE mice, 6 and 12MO hAPOE transgenic mice were stained for hAPOE, astrocytes (GFAP), and gross OL populations (Olig2) (Figure 109). It has been previously proposed that hAPOE is proposed systemically in the liver, but in the brain, due to the strict integrity of the blood-brain barrier, astrocytes are the main producers of APOE (345, 346). Thus, to confirm the parallel production of humanized APOE in transgenic mice in astrocytes similar to humans, GFAP and hAPOE were co-stained with fluorescence in sagittal brains (Figure 109A-E).

The expression of hAPOE is seen in the whole brain of the hAPOE3 and hAPOE4 mice, with the grey matter regions, cortex and hippocampus, showing higher expression than the white matter tract, corpus callosum (Figure 109G). Accordingly, WT mice show no expression of hAPOE in the brain (Figure 109C and 109G). Co-staining with Olig2 and GFAP show independent expression of hAPOE with Olig2 but co-localisation of hAPOE and GFAP. Of course, not all hAPOE signals co-localised with GFAP, but the multi-polar morphology of hAPOE suggest expression in microglia (346).

Astrocytes undergo abnormal proliferation, or astrogliosis when the neuro-environment is damaged, causing an immune response. As such, astrogliosis is an integral defence mechanism in patients with AD (347, 348, 349). However, comparison of hAPOE3 and hAPOE4 show no difference in GFAP+ astrocytes numbers in the cortex, hippocampus, and corpus callosum (Figure 109H-J). Altogether, this set of data proposes that while the effects of reduced OLs are seen in the aging hAPOE4 mice, this result is not an inherent toxicity within OLs. Instead, the reasoning for this decreasing effect may be contributed by the lipids packaged by astrocytes with APOE. Further investigation is warranted for the relationship among OL, hAPOE, and astrocytes to reveal the mechanism that connects these three factors.

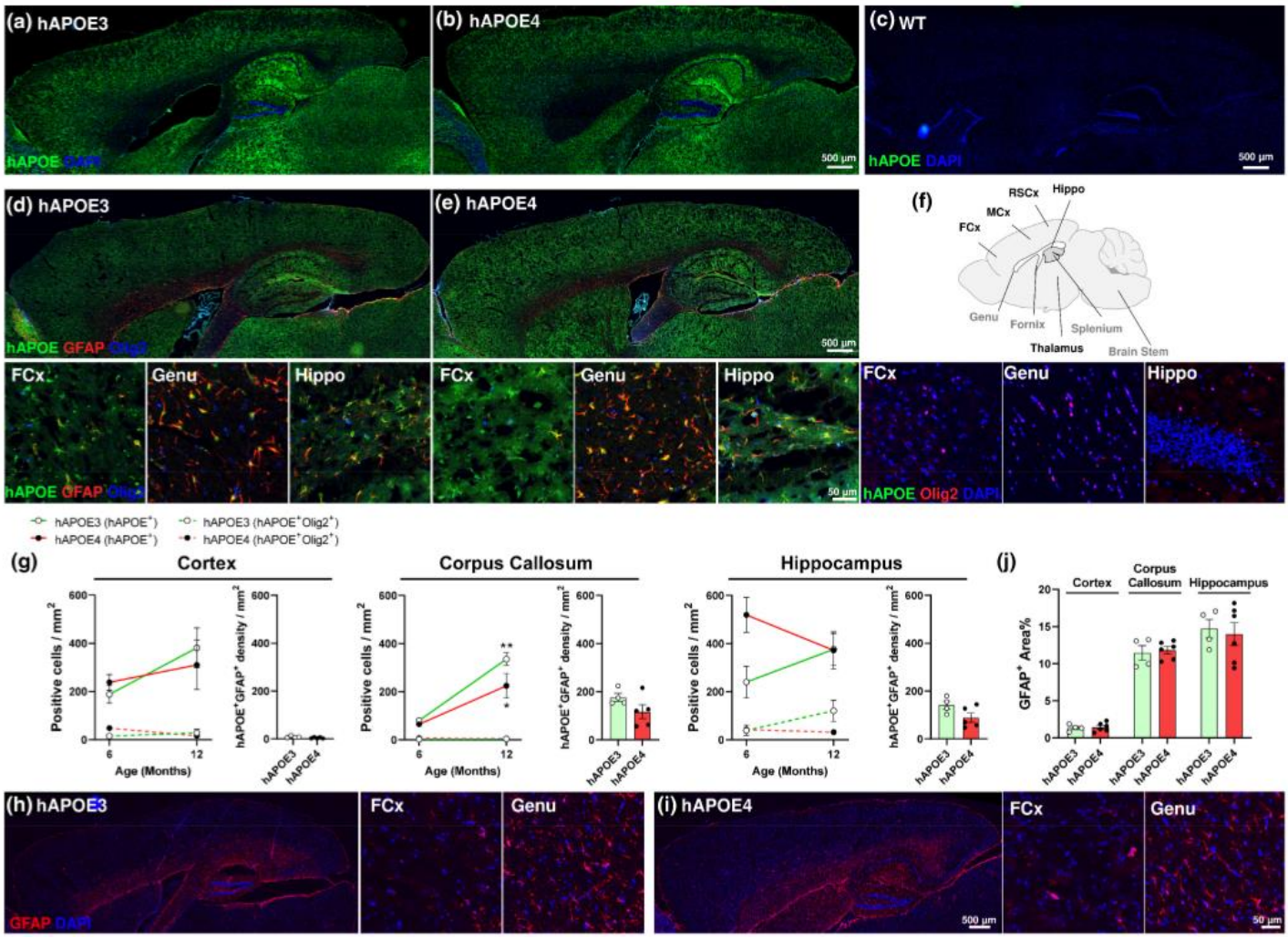

Figure 109: Co-staining for hAPOE, astrocytes (GFAP), and gross OL populations (Olig2) were done for WT and transgenic hAPOE3 and hAPOE4 mice at 6 and 12MO. Overall hAPOE expression are shown in hAPOE3 (a), hAPOE4 (b), and WT (c) mice. No expression is observed in WT while hAPOE3 and hAPOE4 show no difference in hAPOE expression. Co-stain with Olig2 shows independently localised hAPOE and Olig2 expression in frontal cortex, genu, and hippocampus (d, e) as shown in the diagram (f). Quantification of hAPOE and hAPOE/Olig2 double positive show similar hAPOE expression levels of hAPOE3 and hAPOE4 across 6MO and 12MO (g). Quantification of astrocyte populations show no sign of astrogliosis in hAPOE3 (h) and hAPOE4 (i) brain with consistent GFAP levels between genotypes (j). Figure is adapted from (2).

4.9 Discussion: APOE4 is detrimental to myelination and oligodendrocyte in the aging brain

APOE4 is the greatest genetic risk factor for sAD. As a lipid carrier, APOE may have its responsibilities altered due to isoform differences. This has been shown with each isoform having increased or decreased risks of vascular and lipid-based disorders. In our study, we employed WT, Apoe knockout, and transgenic humanised APOE3 and APOE4 mice aged to 6, 10 and 16 months to understand the effects of aging and APOE genotype on white matter integrity and OL status. Behaviour tests are done to further show cognitive manifestations if they exist in these ages and genotypes. We report that cellular events due to age and genotypic differences are independent of cognitive functions up to 16MO. While cognitive assessment by reference memory testing in y-maze show no differences, white matter diffusivity and OL lineage populations show significant alterations based on age with minimal changes based on genotype.

Our human study found a differing relationship between myelin densities and OL populations in AD patients of varying Braak stages and APOE status. The gradient of Braak staging indicates the severity of amyloid plaque deposition. We found that within the frontal cortex, later Braak stages significantly decreased myelin densities while gross OL populations were unaffected. However, APOE4 carriers showed significant OL reductions with both Olig2+ and CC1+ stained cells compared to non-carriers consistent to a previous report (309). To solidify this finding, a preliminary cross-sectional study of mice from 1 to 6 months was done with similar parameters investigating on OL status with age and APOE status. Indeed, OLs stained for Olig2 and CC1 both showed reductions in hAPOE4 mice grey and white matter with significance by 6 months with no genotype-based myelin changes through immunohistochemistry and western blot of MBP, MAG, and MOG, consistent with human studies. It is widely accepted that even though white matter loss is correlated to age (83), OL populations continually proliferate in the adult cortex (350). Here, we show that while this may be true across genotypes, hAPOE4 mice maintain consistent lower levels of OLs among ages. Interestingly, there is no differences in neuronal populations. Our lack of a comprehensive study of neuronal effects such as synaptic loss or effects on neurotransmitters prevents us from making conclusions of the effect of

APOE4, but this finding may suggest that OL alterations may precede neuronal changes associated with neurodegenerative diseases. Moreover, an interpretation of the conflicting relationship between OL and myelin is that each OL with hAPOE4 may be responsible for the myelination of more than the accepted 20 to 60 axons. The additional stress of excessive myelination may ultimately lead to OL death through post-mitotic cell cycle re-entry due to DNA damage accumulations (309). This is supported by the previous study using cuprizone treatment where increased DNA damage (53BP1) is correlated to severe reductions in OLs. Of course, the mechanism of how APOE4 may induce OL reductions is unknown, and further investigation is warranted to understand if APOE4 is related to DNA damage or if its mechanism is lipid based.

To further implicate these findings for future prospectives, we wanted to see if these cellular changes complement neurological behaviour or detectable in a live organism. Diagnosis of AD is difficult in living patients as brain tissue sample is unobtainable. In addition, PET scans with PiB are effective only with the deposition of amyloid plaques, predisposing the assumption that cognitive impairments are already noticeable. However, APOE4 carriers would never know their AD status as plaques do not accumulate until late life. Thus, diagnosing for neurological health is compulsory to further the understanding of APOE4 on AD. By implementing radiological, cellular, and behavioural investigations on aged transgenic APOE mice, a larger spectrum of data could be collected to help in future diagnosis of neurodegeneration. Transgenic APOE mice at 6, 10, and 16 months were employed to correlate radiological data with cellular and behavioural subsets.

MRI analysis shows variating diffusivity patterns within the brain of different genotypes. WT brain regions show an increasingly integral brain as diffusivity is decreased with age. While its FA remains levelled across ages, directional diffusivities decrease with age. This trend is consistent with human findings where white matter volume peaks at almost 40 years old (83), correlating to 16 months mice age. However, further aging in humans is shown to decrease FA and increase directional diffusivity modalities (351, 352). Additionally, greater grey matter changes are found, possibly due to less dense myelin fibres comparatively to the white matter tract. As a result, changes of these regions may be more

significant due to fewer myelinating OLs and generally lower myelin densities. In contrast, *Apoe*$^{-/-}$ mice show unchanged white matter diffusivities among ages. While this may suggest APOE's independent relationship with myelin, our previous work has shown that APOE does affect OL differentiation (2). *Apoe*$^{-/-}$ primary culture of OPCs show significantly reduced MBP+ OL populations after addition of VLDL with rhAPOE4 compared to only VLDL and VLDL with rhAPOE3. However, even without neither VLDL nor rhAPOE, *Apoe*$^{-/-}$ culture can express MBP in OLs. This indicates that an alternate pathway of myelination is possible that is intrinsic in OLs independent from the lipid carrier nor other cell types. Comparatively, the diffusivities of *Apoe*$^{-/-}$ reflect this compensatory effect from the lack of APOE. hAPOE3, though, show peak white matter status at 10MO with an increase of diffusivity by 16MO. While this is considered early in contrast to WT's continuous decrease of diffusivity up to 16MO, it must be reminded that the APOE within the mice are human APOE, and it is possible that mice have their own response to foreign APOE. As such, hAPOE3's effects are best only compared to hAPOE4. Interestingly, hAPOE has been compared to *Apoe*$^{-/-}$, suggesting their transgenic effects on neuroinflammation to be similar (353). In contrast to hAPOE3 though, hAPOE4 shows constant increases in diffusivity among ages, suggesting compromised myelin structures leading to leaky axons.

Comparisons of genotypes within individual ages show minimal difference among genotypes in each age group. At 6MO, hAPOE4 mice show overall healthier brain as suggested with lower RD, AxD, and MD. This contrasting result is consistent to previous reports showing larger hippocampi and frontal cortical regions (354). In addition, human studies of APOE4 carrier children between the ages of 7 and 15 have shown similar IQ and cognitive performances (355, 356). Using y-maze, we also showed these similar cognitive abilities of the varying mice, where their spontaneous alternations were unchanged at 6MO. However, it is only at 16MO did transgenic mice showed significant decreases of spontaneous alternation against WT, suggesting the effects of APOE genotype manifests more severely in the aged. The investigation into the comparison of age and genotype suggests age as a prominent factor in brain diffusivity. While genotypic changes do not account for diffusivity variations as seen in same age groups, the effect of age for each genotype is more significant. Even though by 16MO, equalling to 50 human years, the effects are minimal, the difference of diffusivities of hAPOE4 and hAPOE3 have

shown the higher vulnerability of hAPOE4 white matter integrity. Furthermore, these diffusivity differences have occurred before noticeable cognitive dysfunctions.

Metabolite changes in the brain can constitute a variety of neurological symptoms seen in neurodegenerative diseases. For example, the reduction of dopamine is highly correlated to the severity of Parkinson's and the depletion of serotonin and norepinephrine underlie the symptoms of depression (357). Here, we are able to show the differences in levels of common metabolites responsible for myelination and neurological disorders. We find that based on age, *Apoe*$^{-/-}$ and hAPOE3 sees increased levels of lipid/lactate at 16MO when compared to 6MO. This accumulation may be due to both the lack of a lipid transporter to cells such as OLs to process the lipids or even the animal's inability to process humanised APOE. Further investigation will need to be done to understand if non-murine APOE could induce a reaction that is not inherent to the animal. Interestingly, in hAPOE4 mice, there is a significant increase in glutamate/glutamine and NAA levels at 10MO. With glutamate/glutamine, both elevated and reduced levels have been implicated in AD (190, 358). Glutamate is the major excitatory neurotransmitter responsible for synaptic plasticity and repair of the CNS. At high concentrations, glutamate/glutamine becomes cytotoxic and may induce neuronal death (359). One proposed mechanism of how APOE is related to glutamate levels is APOE's relevance to Reelin, a glycoprotein responsible for cortical equilibrium and glutamate receptor activity. It has been previously shown that APOE4 reduces the expression of Apoer2, a receptor for both APOE and Reelin, and thereby, prevent binding of glutamate (360). This may account for the higher levels of glutamate/glutamine. In addition, increased NAA levels may indicate the inhibitory effects of APOE4 on OL differentiation. NAA is the second most abundant molecule in the brain after glutamate. While it is multifunctional, the deacylation of NAA by ASPA into acetate is necessary for the myelination of the brain. Here, we show consistent NAA levels in WT, *Apoe*$^{-/-}$, and hAPOE3 while significantly elevated levels in 10MO hAPOE4. Correspondingly, the ASPA levels in IHC show insignificant differences among genotypes. While the myelin density of 10MO hAPOE4 is similar to other genotypes, the accumulation of NAA in addition to a stable level of ASPA may suggest the inefficiency of ASPA to deacylate NAA to produce acetate

for myelination. While we do not see myelin differences, an accumulation of this defect may influence the mice at an older age.

5.0 General discussion

AD is a complex neurodegenerative disease with no cure. Even though researchers and doctors are continuously making progress in treating the multifaceted nature of AD's aetiology, there is still no direct answer to the severe cognitive complications hallmark of this disease. In our study, we propose a connection between amyloid deposition and APOE4. Findings have shown that mutations of the APP and PS1 gene cause an abnormal accumulation of insoluble amyloid-β protein due to an unknown preference towards the amyloidogenic pathway (120). Here, we showed that by using cuprizone, a demyelinating treatment, the amount of APP stained with amyloid plaque marker, 6E10, is expressed in higher levels in mice with this treatment. Even at an early age of 4 months, cuprizone treated mice brains exhibited increased 6E10 expression compared to mice with normal diet. Concurrently, the cuprizone treatment severely reduced OL populations and myelin densities. This reduction of OLs was also seen in the APOE4 cohort specifically at 10 months while the older 16 months showed minimal differences in OL populations or myelin densities. Additional investigation into the radiological aspects of white matter diffusivity in both APP and APOE cohorts suggest a correlating increase in diffusivity with decrease in OLs. Interestingly, these alterations did not result in cognitive impairments shown in reference memory analysis from Y-maze. Therefore, we propose that the increased risk of AD due to APOE4 is caused by the protein's deleterious effect on OLs, resulting in an increase of APP deposition.

Mutations of *APP* and *PS1* are known to predispose patients to an early form of AD. These mutations directly influence the processing of APP, and thereby, increase the production of the insoluble amyloid-β fragment. Likewise, increased blood pressure and hypertension have also been associated with increased amyloid burden (361). In our study, we showed that demyelination can also be an initiator of amyloid deposition. By employing young mice at 3 to 4MO, we showed that while AD is an age-related disease, amyloid pathology is not fully dependent on age. Neither R1.40 nor APP/PS1 mice are aging models for Alzheimer's. Instead, their ages between 3 and 4 months are considered early due to this

time frame preceding documented appearance of amyloid plaques. As the earliest detected amyloid aggregations begin at 16 months and 6 months for R1.40 and APP/PS1, respectively, any differences seen at 3 to 4 months would be considered early. Additionally, the effect of cuprizone on intraneuronal amyloid deposition could be observed before aggregations.

Instead, myelin and OL loss is seen to accelerate the deposition. One interpretation of this relationship is APP's location and the axonopathy associated with demyelination. The APP protein is in the plasma membranes of cells and some in the post-synaptic regions of axons and dendrites (141). Previous studies have shown that axonal injury could be induced by demyelination (228, 362, 363). Mutations of APP and PS1 may result in overproduction of APP fragments within the neuronal cell body before being transported to their associated regions. Normally, at a younger age, this extra transport may still be manageable due to the integrity and compactness of the myelin sheath, preventing axonal defects. However, myelination is peaked at around 40 years old, and myelin loss occurs. At this age, as myelin integrity decreases, axonal transport exacerbates, unable to support the elevated amounts of APP transport. As a result, axonal damage may induce neuronal apoptosis (364), releasing the excessive amounts of APP fragments into the environment. Of course, this theory would reverse the order of events of the accepted amyloid cascade hypothesis; instead of amyloid plaques being the causative agent of neuronal death, amyloid plaques are the result of neuronal death caused by myelin loss. However, our study did not fully investigate into neuronal properties, hence this theory is not fully supported. Further research into the role of myelin in AD has shown that enhancing OL proliferation and myelination have rescued dementia-like symptoms (365, 366).

With the previous cohort, we propose demyelination and myelin loss as an initiator of amyloid pathology and neuronal loss. As APOE is a lipid transporter within the brain, we further propose that the alteration of APOE4 is connected to OL survival and myelin integrity, affecting AD pathology. Even though APOE4 severely increases the risk of having AD by up to 14.9 times, this does not indicate this allelic variation as a causative agent of AD. Our study suggests that APOE4 affects OL survivability at a specific time window. Coincidentally, this window of 10 months mice age correlates to Bartzokis's

(83) proposed age of peak myelination at 40 years human age. At 10 months, we found that hAPOE4 mice showed significantly elevated weights, reduced OL populations, and increased white matter diffusivity. This suggests that while APOE4 is a functional lipid carrier, intrinsic myelin loss may be exacerbated by the isoform. Indeed, APOE4 carriers showed significant difference in correlation between late-myelinating white matter with cognitive processing speed (367), suggesting delineating pathways in myelin maintenance of different APOE isoforms. Multiple reports have indicated APOE's significance role in myelin upkeep from clearing accumulated myelin debris from demyelinating lesions to associations with myelination reductions (368, 369, 370). Additionally, our previous report had shown that rescue of Lovastatin treated *Apoe*$^{-/-}$ OPCs with rhAPOE showed attenuated the rescue effects specifically in rhAPOE4 (2). One interpretation is the binding ability of the APOE4 compared to APOE3. Lipid accumulations in APOE4 OLs, astrocytes, and microglia have been proposed by various reports (45, 371, 372), proposing an inefficient release of lipids into these cells for processing. While the mechanism for this inefficiency is unknown, it was proposed that the separation of the N- and C-terminals of the protein causes a disordered separation of these two domains, leading to different binding affinities of the APOE isomers (373). This resulting lipid deficiency may lead to increased myelin loss as OLs can no longer support and maintain the myelination process. This would further indicate that the OL population have a myelin density threshold, unable to myelinate any more than its status. The APOE4 may lower this threshold compared to APOE3, only able to myelinate a limited number of axons. This is exemplified by APOE4's significant decline in relaxation rates measuring white matter structural integrity (374). We also propose that APOE4 causes OL death, leading to accelerated myelin loss. We had shown both in human AD patients and tgAPOE mice that myelin densities are relatively unaffected. However, hAPOE4 OL populations of both gross OLs stained with Olig2 and mOLs stained with CC1 show significant reductions at 10MO with no change in Nkx2.2 OPCs. While the mechanism of OL death by APOE4 is unknown, our findings suggest that DNA damage could induce OL death. Specifically, DNA damage may initiate cell cycle re-entry of the post-mitotic OL, leading to apoptosis (375). Overall, these results emphasise the deleterious effects of APOE4 and propose how APOE4 can drive amyloid deposition.

These findings could help further understand the mechanisms of which AD risk factors could play. More importantly, radiological findings would help correlate with white matter status, a contributing factor to many neurodegenerative diseases. Our investigation showed increased diffusivities in correlation with decreases in OL populations in the APP predisposed mice. Of course, the acute OL reductions caused acute demyelination, which were radiologically observed. Interestingly, in the tgAPOE cohort, the increased diffusivities of 10MO hAPOE4 mice was observed with correlating decreased OL populations preceding myelin loss. In addition, both these findings preceded cognitive impairments. Diagnostic tools for AD are few, as many depend on subjective self-assessing cognitive tests or post-mortem tissue analysis. Here, we showed that MRI detections of white matter diffusivity could give us the look at the beginning of AD pathology. Because of the relationship of demyelination with amyloid deposition, future AD diagnosis may utilise MRI as a risk-assessment tool for the aging person. Early signs of white matter diffusivity may indicate an increased risk of AD especially if the patient incurs one of the many risk factors of AD. Additionally, increased diffusivity may indicate OL injuries that may factor into other neurological disorders. Altogether, these findings could help set a new baseline in AD research and understanding. Neurons are important in cognition, but they require the support of OLs and myelin to maintain themselves.

6.0 Limitations

Limitations of this study include the age of endpoint and limiting immunohistochemistry targets. Age is the greatest risk factor for AD, but in both of our fAD and sAD cohorts, neither of their age groups could represent their common age of onset, 50 years old for fAD and 65 years old for sAD. These ages correlate to 20 and 25MO, respectively. In addition, in the R1.40 and APP/PS1 mice, neither strain was allowed to mature to an appropriate age of amyloid deposition. By allowing mice to reach these ages with or without cuprizone, a more apparent effect of demyelination on amyloid plaques could be observed. Regarding the hAPOE mice, because it is well-established that APOE is a lipid carrier and responsible for lipid metabolism, it may be helpful to treat these mice with high fat diets. For example, Janssen et al proposed that hAPOE4 mice treated with high fat diet may inhibit the compensatory effects

of neuroinflammation in *Apoe*$^{-/-}$ (376). Polarizing the effect of regular and high fat diet may further deepen the understanding of APOE in the brain. Throughout the IHC results, we focused on OLs without analysis of other cell types such as neurons, astrocytes, and microglia. Previous research has shown that both APP and APOE genotypes have induced deleterious effects of neurons in addition to impaired mitochondrial functions of astrocytes and proliferation of microglia (377, 378). Further radiological analysis using magnetization transfer and chemical exchange saturation transfer could be implemented to find more detailed changes in diffusivity and neurological compound concentrations.

7.0 Conclusion

In this investigation, we showed that demyelination due to OL death from cuprizone treatment accelerates intraneuronal amyloid deposition even at an early age, which proposes that amyloid plaques may be age independent, yet affected by myelin status. Elevated myelin loss resulted in an increase in diffuse amyloid depositions. Concurrently, hAPOE4 mice showed significant reductions of OL by 10MO. While the study of the mechanism in which this occurs is still in progress, we have showed that between 6MO and 10MO, the effects of hAPOE4 is most apparent with significant reductions of OL populations and observable increase in cerebral diffusivity without detectable myelin protein loss. Altogether with our previous study on the inability of the hAPOE4 to efficiently rescue the depletion of cholesterol in OLs, the influence of APOE4 is shown to have substantial effect on myelination. Thus, these cohorts suggest that the age-dependent effects of APOE4 on OL reductions, which could increase myelin loss, may drive increased amyloid deposition and AD pathologies.

7.0 References

1. Cheng GW, Mok KK, Yeung SH, Kofler J, Herrup K, Tse KH. Apolipoprotein E epsilon4 Mediates Myelin Breakdown by Targeting Oligodendrocytes in Sporadic Alzheimer Disease. J Neuropathol Exp Neurol. 2022;81(9):717-30.
2. Mok KK, Yeung SH, Cheng GW, Ma IW, Lee RH, Herrup K, et al. Apolipoprotein E epsilon4 disrupts oligodendrocyte differentiation by interfering with astrocyte-derived lipid transport. J Neurochem. 2022.
3. Purves D AG, Fitzpatrick D, et al. Increased Conduction Velocity as a Result of Myelination. Neuroscience. Sunderland: Sinauer Associates; 2001.
4. Bourbon-Teles J, Bells S, Jones DK, Coulthard E, Rosser A, Metzler-Baddeley C. Myelin Breakdown in Human Huntington's Disease: Multi-Modal Evidence from Diffusion MRI and Quantitative Magnetization Transfer. Neuroscience. 2019;403:79-92.
5. Jalal FY, Yang Y, Thompson J, Lopez AC, Rosenberg GA. Myelin loss associated with neuroinflammation in hypertensive rats. Stroke. 2012;43(4):1115-22.
6. Kato D, Wake H, Lee PR, Tachibana Y, Ono R, Sugio S, et al. Motor learning requires myelination to reduce asynchrony and spontaneity in neural activity. Glia. 2020;68(1):193-210.
7. Park M, Moon Y, Han SH, Kim HK, Moon WJ. Myelin loss in white matter hyperintensities and normal-appearing white matter of cognitively impaired patients: a quantitative synthetic magnetic resonance imaging study. Eur Radiol. 2019;29(9):4914-21.
8. Simic G, Stanic G, Mladinov M, Jovanov-Milosevic N, Kostovic I, Hof PR. Does Alzheimer's disease begin in the brainstem? Neuropathol Appl Neurobiol. 2009;35(6):532-54.
9. Toyama BH, Savas JN, Park SK, Harris MS, Ingolia NT, Yates JR, 3rd, et al. Identification of long-lived proteins reveals exceptional stability of essential cellular structures. Cell. 2013;154(5):971-82.
10. Quarles RH. Myelin sheaths: glycoproteins involved in their formation, maintenance and degeneration. Cell Mol Life Sci. 2002;59(11):1851-71.
11. Quarles RH. Glycoproteins of myelin sheaths. J Mol Neurosci. 1997;8(1):1-12.
12. Trapp BD. Myelin-associated glycoprotein. Location and potential functions. Ann N Y Acad Sci. 1990;605:29-43.
13. Lassmann H, Bartsch U, Montag D, Schachner M. Dying-back oligodendrogliopathy: a late sequel of myelin-associated glycoprotein deficiency. Glia. 1997;19(2):104-10.
14. Schachner M, Bartsch U. Multiple functions of the myelin-associated glycoprotein MAG (siglec-4a) in formation and maintenance of myelin. Glia. 2000;29(2):154-65.
15. Li C, Tropak MB, Gerlai R, Clapoff S, Abramow-Newerly W, Trapp B, et al. Myelination in the absence of myelin-associated glycoprotein. Nature. 1994;369(6483):747-50.
16. Weil MT, Mobius W, Winkler A, Ruhwedel T, Wrzos C, Romanelli E, et al. Loss of Myelin Basic Protein Function Triggers Myelin Breakdown in Models of Demyelinating Diseases. Cell Rep. 2016;16(2):314-22.
17. Gendelman HE, Pezeshkpour GH, Pressman NJ, Wolinsky JS, Quarles RH, Dobersen MJ, et al. A quantitation of myelin-associated glycoprotein and myelin basic protein loss in different demyelinating diseases. Ann Neurol. 1985;18(3):324-8.
18. Wang ML, Yu MM, Yang DX, Liu YL, Wei XE, Li WB. Diffusion Kurtosis Imaging Characterizes Brain Microstructural Changes Associated with Cognitive Impairment in a Rat Model of Chronic Traumatic Brain Injury. Neuroscience. 2018;392:180-9.
19. Johnson VE, Stewart JE, Begbie FD, Trojanowski JQ, Smith DH, Stewart W. Inflammation and white matter degeneration persist for years after a single traumatic brain injury. Brain. 2013;136(Pt 1):28-42.
20. Liu MC, Akle V, Zheng W, Kitlen J, O'Steen B, Larner SF, et al. Extensive degradation of myelin basic protein isoforms by calpain following traumatic brain injury. J Neurochem. 2006;98(3):700-12.
21. Roth MP, Malfroy L, Offer C, Sevin J, Enault G, Borot N, et al. The human myelin oligodendrocyte glycoprotein (MOG) gene: complete nucleotide sequence and structural characterization. Genomics. 1995;28(2):241-50.

22. Hrdina PD. Basic neurochemistry: Molecular, cellular and medical aspects - Siegel,GJ. J Psychiatr Neurosci. 1996;21(5):352-3.
23. Coetzee T, Fujita N, Dupree J, Shi R, Blight A, Suzuki K, et al. Myelination in the absence of galactocerebroside and sulfatide: normal structure with abnormal function and regional instability. Cell. 1996;86(2):209-19.
24. Matthews MA, Duncan D. A quantitative study of morphological changes accompanying the initiation and progress of myelin production in the dorsal funiculus of the rat spinal cord. J Comp Neurol. 1971;142(1):1-22.
25. Spassky N, Goujet-Zalc C, Parmantier E, Martinez S, Ivanova A, Ikenaka K, et al. Multiple restricted origin of oligodendrocytes. Neural Development-Book. 1999;2:337-.
26. Woodruff RH, Tekki-Kessaris N, Stiles CD, Rowitch DH, Richardson WD. Oligodendrocyte development in the spinal cord and telencephalon: common themes and new perspectives. International Journal of Developmental Neuroscience. 2001;19(4):379-85.
27. Kessaris N, Fogarty M, Iannarelli P, Grist M, Wegner M, Richardson WD. Competing waves of oligodendrocytes in the forebrain and postnatal elimination of an embryonic lineage. Nature Neuroscience. 2006;9(2):173-9.
28. Jakovcevski I, Filipovic R, Mo Z, Rakic S, Zecevic N. Oligodendrocyte development and the onset of myelination in the human fetal brain. Front Neuroanat. 2009;3:5.
29. Yang Y, Lewis R, Miller RH. Interactions between oligodendrocyte precursors control the onset of CNS myelination. Dev Biol. 2011;350(1):127-38.
30. Cui QL, D'Abate L, Fang J, Leong SY, Ludwin S, Kennedy TE, et al. Human fetal oligodendrocyte progenitor cells from different gestational stages exhibit substantially different potential to myelinate. Stem Cells Dev. 2012;21(11):1831-7.
31. Zhu X, Bergles DE, Nishiyama A. NG2 cells generate both oligodendrocytes and gray matter astrocytes. Development. 2008;135(1):145-57.
32. Zhu X, Hill RA, Dietrich D, Komitova M, Suzuki R, Nishiyama A. Age-dependent fate and lineage restriction of single NG2 cells. Development. 2011;138(4):745-53.
33. Butts BD, Houde C, Mehmet H. Maturation-dependent sensitivity of oligodendrocyte lineage cells to apoptosis: implications for normal development and disease. Cell Death Differ. 2008;15(7):1178-86.
34. Windrem MS, Schanz SJ, Guo M, Tian GF, Washco V, Stanwood N, et al. Neonatal chimerization with human glial progenitor cells can both remyelinate and rescue the otherwise lethally hypomyelinated shiverer mouse. Cell Stem Cell. 2008;2(6):553-65.
35. Nishiyama A, Komitova M, Suzuki R, Zhu X. Polydendrocytes (NG2 cells): multifunctional cells with lineage plasticity. Nat Rev Neurosci. 2009;10(1):9-22.
36. Sawamura S, Sawada M, Ito M, Nagatsu T, Nagatsu I, Suzumura A, et al. The bipotential glial progenitor cell line can develop into both oligodendrocytes and astrocytes in the mouse forebrain. Neurosci Lett. 1995;188(1):1-4.
37. Sim FJ, Zhao C, Penderis J, Franklin RJM. The age-related decrease in CNS remyelination efficiency is attributable to an impairment of both oligodendrocyte progenitor recruitment and differentiation. Journal of Neuroscience. 2002;22(7):2451-9.
38. Chari DM, Crang AJ, Blakemore WF. Decline in rate of colonization of oligodendrocyte progenitor cell (OPC)-depleted tissue by adult OPCs with age. J Neuropath Exp Neur. 2003;62(9):908-16.
39. Neumann B, Segel M, Ghosh T, Zhao C, Tourlomousis P, Young A, et al. Myc determines the functional age state of oligodendrocyte progenitor cells. Nat Aging. 2021;1(9):826-37.
40. Magri L, Gacias M, Wu M, Swiss VA, Janssen WG, Casaccia P. c-Myc-dependent transcriptional regulation of cell cycle and nucleosomal histones during oligodendrocyte differentiation. Neuroscience. 2014;276:72-86.
41. Li N, Yao M, Liu J, Zhu Z, Lam TL, Zhang P, et al. Vitamin D Promotes Remyelination by Suppressing c-Myc and Inducing Oligodendrocyte Precursor Cell Differentiation after Traumatic Spinal Cord Injury. Int J Biol Sci. 2022;18(14):5391-404.
42. Camargo N, Goudriaan A, van Deijk AF, Otte WM, Brouwers JF, Lodder H, et al. Oligodendroglial myelination requires astrocyte-derived lipids. PLoS Biol. 2017;15(5):e1002605.

43. Hofmann K, Rodriguez-Rodriguez R, Gaebler A, Casals N, Scheller A, Kuerschner L. Astrocytes and oligodendrocytes in grey and white matter regions of the brain metabolize fatty acids. Sci Rep. 2017;7(1):10779.
44. Liang Y, Lin S, Beyer TP, Zhang Y, Wu X, Bales KR, et al. A liver X receptor and retinoid X receptor heterodimer mediates apolipoprotein E expression, secretion and cholesterol homeostasis in astrocytes. J Neurochem. 2004;88(3):623-34.
45. Blanchard JW, Akay LA, Davila-Velderrain J, von Maydell D, Mathys H, Davidson SM, et al. APOE4 impairs myelination via cholesterol dysregulation in oligodendrocytes. Nature. 2022;611(7937):769-79.
46. Gyllensten L, Malmfors T. Myelinization of the optic nerve and its dependence on visual function--a quantitative investigation in mice. J Embryol Exp Morphol. 1963;11:255-66.
47. Omlin FX. Optic disc and optic nerve of the blind cape mole-rat (Georychus capensis): a proposed model for naturally occurring reactive gliosis. Brain Res Bull. 1997;44(5):627-32.
48. Demerens C, Stankoff B, Logak M, Anglade P, Allinquant B, Couraud F, et al. Induction of myelination in the central nervous system by electrical activity. Proc Natl Acad Sci U S A. 1996;93(18):9887-92.
49. Simons M, Trajkovic K. Neuron-glia communication in the control of oligodendrocyte function and myelin biogenesis. J Cell Sci. 2006;119(Pt 21):4381-9.
50. Lee S, Leach MK, Redmond SA, Chong SY, Mellon SH, Tuck SJ, et al. A culture system to study oligodendrocyte myelination processes using engineered nanofibers. Nat Methods. 2012;9(9):917-22.
51. Paik JS, Ha M, Jung YH, Kim GH, Han KD, Kim HS, et al. Low vision and the risk of dementia: a nationwide population-based cohort study. Sci Rep. 2020;10(1):9109.
52. Clemons TE, Rankin MW, McBee WL, Age-Related Eye Disease Study Research G. Cognitive impairment in the Age-Related Eye Disease Study: AREDS report no. 16. Arch Ophthalmol. 2006;124(4):537-43.
53. Pye A, Charalambous AP, Leroi I, Thodi C, Dawes P. Screening tools for the identification of dementia for adults with age-related acquired hearing or vision impairment: a scoping review. Int Psychogeriatr. 2017;29(11):1771-84.
54. Wang L, Klingeborn M, Travis AM, Hao Y, Arshavsky VY, Gospe SM, 3rd. Progressive optic atrophy in a retinal ganglion cell-specific mouse model of complex I deficiency. Sci Rep. 2020;10(1):16326.
55. Hsiao YH, Chang CH, Gean PW. Impact of social relationships on Alzheimer's memory impairment: mechanistic studies. J Biomed Sci. 2018;25(1):3.
56. Shen LX, Yang YX, Kuo K, Li HQ, Chen SD, Chen KL, et al. Social Isolation, Social Interaction, and Alzheimer's Disease: A Mendelian Randomization Study. J Alzheimers Dis. 2021;80(2):665-72.
57. Gutierrez R, Boison D, Heinemann U, Stoffel W. Decompaction of CNS myelin leads to a reduction of the conduction velocity of action potentials in optic nerve. Neurosci Lett. 1995;195(2):93-6.
58. Pinckers A, Cruysberg JRM, Renier WO. Delayed Myelination of the Optic-Nerve and Pseudooptic Atrophy of Beauvieux. Neuro-Ophthalmology. 1993;13(3):165-70.
59. Lam AK, Pang PC. The effect of myelination on perimetry and retinal nerve fibre analysis. Clin Exp Optom. 2000;83(1):4-11.
60. Tran EM, Stefanick ML, Henderson VW, Rapp SR, Chen JC, Armstrong NM, et al. Association of Visual Impairment With Risk of Incident Dementia in a Women's Health Initiative Population. JAMA Ophthalmol. 2020;138(6):624-33.
61. Farias TL, Marinho V, Carvalho V, Rocha K, da Silva PRA, Silva F, et al. Methylphenidate modifies activity in the prefrontal and parietal cortex accelerating the time judgment. Neurol Sci. 2019;40(4):829-37.
62. Tauber H, Waehneldt TV, Neuhoff V. Myelination in rabbit optic nerves is accelerated by artificial eye opening. Neurosci Lett. 1980;16(3):235-8.
63. Fukui Y, Hayasaka S, Bedi KS, Ozaki HS, Takeuchi Y. Quantitative study of the development of the optic nerve in rats reared in the dark during early postnatal life. J Anat. 1991;174:37-47.

64. Rojo D, Badner A, Gibson EM. Circadian Control of Glial Cell Homeodynamics. J Biol Rhythms. 2022;37(6):593-608.
65. Pedraza L, Huang JK, Colman D. Disposition of axonal caspr with respect to glial cell membranes: Implications for the process of myelination. J Neurosci Res. 2009;87(15):3480-91.
66. Snaidero N, Mobius W, Czopka T, Hekking LH, Mathisen C, Verkleij D, et al. Myelin membrane wrapping of CNS axons by PI(3,4,5)P3-dependent polarized growth at the inner tongue. Cell. 2014;156(1-2):277-90.
67. Knobler RL, Stempak JG, Laurencin M. Nonuniformity of the oligodendroglial ensheathment of axons during myelination in the developing rat central nervous system. A serial section electron microscopical study. J Ultrastruct Res. 1976;55(3):417-32.
68. Nawaz S, Sanchez P, Schmitt S, Snaidero N, Mitkovski M, Velte C, et al. Actin Filament Turnover Drives Leading Edge Growth during Myelin Sheath Formation in the Central Nervous System. Developmental Cell. 2015;34(2):139-51.
69. Shine HD, Readhead C, Popko B, Hood L, Sidman RL. Morphometric analysis of normal, mutant, and transgenic CNS: correlation of myelin basic protein expression to myelinogenesis. J Neurochem. 1992;58(1):342-9.
70. Deber CM, Reynolds SJ. Central nervous system myelin: structure, function, and pathology. Clin Biochem. 1991;24(2):113-34.
71. Stadelmann C, Timmler S, Barrantes-Freer A, Simons M. Myelin in the Central Nervous System: Structure, Function, and Pathology. Physiol Rev. 2019;99(3):1381-431.
72. Dietrich RB, Bradley WG, Zaragoza EJt, Otto RJ, Taira RK, Wilson GH, et al. MR evaluation of early myelination patterns in normal and developmentally delayed infants. AJR Am J Roentgenol. 1988;150(4):889-96.
73. Osborn AG, Hedlund GL, Salzman KL. Osborn's brain : imaging, pathology, and anatomy. Second edition. ed. Philadelphia, PA: Elsevier; 2018. xiii, 1372 pages p.
74. Barkovich AJ, Raybaud C. Pediatric neuroimaging. Philadelphia: Wolters Kluwer Health/Lippincott Williams & Wilkins; 2012. Available from: http://ovidsp.ovid.com/ovidweb.cgi?T=JS&NEWS=N&PAGE=booktext&DF=bookdb&AN=01438880/5th_Edition&XPATH=/PG(0).
75. Raz N, Gunning FM, Head D, Dupuis JH, McQuain J, Briggs SD, et al. Selective aging of the human cerebral cortex observed in vivo: differential vulnerability of the prefrontal gray matter. Cereb Cortex. 1997;7(3):268-82.
76. Bender AR, Volkle MC, Raz N. Differential aging of cerebral white matter in middle-aged and older adults: A seven-year follow-up. Neuroimage. 2016;125:74-83.
77. Douaud G, Groves AR, Tamnes CK, Westlye LT, Duff EP, Engvig A, et al. A common brain network links development, aging, and vulnerability to disease. Proc Natl Acad Sci U S A. 2014;111(49):17648-53.
78. Boyd A, Zhang H, Williams A. Insufficient OPC migration into demyelinated lesions is a cause of poor remyelination in MS and mouse models. Acta Neuropathol. 2013;125(6):841-59.
79. Chang A, Nishiyama A, Peterson J, Prineas J, Trapp BD. NG2-positive oligodendrocyte progenitor cells in adult human brain and multiple sclerosis lesions. J Neurosci. 2000;20(17):6404-12.
80. Lucchinetti C, Bruck W, Parisi J, Scheithauer B, Rodriguez M, Lassmann H. A quantitative analysis of oligodendrocytes in multiple sclerosis lesions. A study of 113 cases. Brain. 1999;122 (Pt 12):2279-95.
81. Jakel S, Agirre E, Mendanha Falcao A, van Bruggen D, Lee KW, Knuesel I, et al. Altered human oligodendrocyte heterogeneity in multiple sclerosis. Nature. 2019;566(7745):543-7.
82. Yeung MSY, Djelloul M, Steiner E, Bernard S, Salehpour M, Possnert G, et al. Dynamics of oligodendrocyte generation in multiple sclerosis. Nature. 2019;566(7745):538-42.
83. Bartzokis G, Beckson M, Lu PH, Nuechterlein KH, Edwards N, Mintz J. Age-related changes in frontal and temporal lobe volumes in men: a magnetic resonance imaging study. Arch Gen Psychiatry. 2001;58(5):461-5.
84. Gard AL, Burrell MR, Pfeiffer SE, Rudge JS, Williams WC, 2nd. Astroglial control of oligodendrocyte survival mediated by PDGF and leukemia inhibitory factor-like protein. Development. 1995;121(7):2187-97.

85. Taveggia C, Thaker P, Petrylak A, Caporaso GL, Toews A, Falls DL, et al. Type III neuregulin-1 promotes oligodendrocyte myelination. Glia. 2008;56(3):284-93.
86. Watkins TA, Emery B, Mulinyawe S, Barres BA. Distinct stages of myelination regulated by gamma-secretase and astrocytes in a rapidly myelinating CNS coculture system. Neuron. 2008;60(4):555-69.
87. Kumar S, Biancotti JC, Yamaguchi M, de Vellis J. Combination of growth factors enhances remyelination in a cuprizone-induced demyelination mouse model. Neurochem Res. 2007;32(4-5):783-97.
88. Ishibashi T, Dakin KA, Stevens B, Lee PR, Kozlov SV, Stewart CL, et al. Astrocytes promote myelination in response to electrical impulses. Neuron. 2006;49(6):823-32.
89. Pajevic S, Basser PJ, Fields RD. Role of myelin plasticity in oscillations and synchrony of neuronal activity. Neuroscience. 2014;276:135-47.
90. Ponath G, Ramanan S, Mubarak M, Housley W, Lee S, Sahinkaya FR, et al. Myelin phagocytosis by astrocytes after myelin damage promotes lesion pathology. Brain. 2017;140(2):399-413.
91. Hirata K, Kawabuchi M. Myelin phagocytosis by macrophages and nonmacrophages during Wallerian degeneration. Microsc Res Tech. 2002;57(6):541-7.
92. Neumann H, Kotter MR, Franklin RJ. Debris clearance by microglia: an essential link between degeneration and regeneration. Brain. 2009;132(Pt 2):288-95.
93. Rotshenker S. Microglia and macrophage activation and the regulation of complement-receptor-3 (CR3/MAC-1)-mediated myelin phagocytosis in injury and disease. J Mol Neurosci. 2003;21(1):65-72.
94. Gensel JC, Kopper TJ, Zhang B, Orr MB, Bailey WM. Predictive screening of M1 and M2 macrophages reveals the immunomodulatory effectiveness of post spinal cord injury azithromycin treatment. Sci Rep. 2017;7:40144.
95. Orr MB, Simkin J, Bailey WM, Kadambi NS, McVicar AL, Veldhorst AK, et al. Compression Decreases Anatomical and Functional Recovery and Alters Inflammation after Contusive Spinal Cord Injury. J Neurotrauma. 2017;34(15):2342-52.
96. D'Aversa TG, Eugenin EA, Lopez L, Berman JW. Myelin basic protein induces inflammatory mediators from primary human endothelial cells and blood-brain barrier disruption: implications for the pathogenesis of multiple sclerosis. Neuropathol Appl Neurobiol. 2013;39(3):270-83.
97. Linington C, Bradl M, Lassmann H, Brunner C, Vass K. Augmentation of demyelination in rat acute allergic encephalomyelitis by circulating mouse monoclonal antibodies directed against a myelin/oligodendrocyte glycoprotein. Am J Pathol. 1988;130(3):443-54.
98. Westland KW, Pollard JD, Sander S, Bonner JG, Linington C, McLeod JG. Activated non-neural specific T cells open the blood-brain barrier to circulating antibodies. Brain. 1999;122 (Pt 7):1283-91.
99. Buschmann JP, Berger K, Awad H, Clarner T, Beyer C, Kipp M. Inflammatory response and chemokine expression in the white matter corpus callosum and gray matter cortex region during cuprizone-induced demyelination. J Mol Neurosci. 2012;48(1):66-76.
100. Krauspe BM, Dreher W, Beyer C, Baumgartner W, Denecke B, Janssen K, et al. Short-term cuprizone feeding verifies N-acetylaspartate quantification as a marker of neurodegeneration. J Mol Neurosci. 2015;55(3):733-48.
101. Acs P, Kipp M, Norkute A, Johann S, Clarner T, Braun A, et al. 17beta-estradiol and progesterone prevent cuprizone provoked demyelination of corpus callosum in male mice. Glia. 2009;57(8):807-14.
102. Gudi V, Moharregh-Khiabani D, Skripuletz T, Koutsoudaki PN, Kotsiari A, Skuljec J, et al. Regional differences between grey and white matter in cuprizone induced demyelination. Brain Res. 2009;1283:127-38.
103. Skripuletz T, Hackstette D, Bauer K, Gudi V, Pul R, Voss E, et al. Astrocytes regulate myelin clearance through recruitment of microglia during cuprizone-induced demyelination. Brain. 2013;136(Pt 1):147-67.
104. Taylor LC, Gilmore W, Matsushima GK. SJL mice exposed to cuprizone intoxication reveal strain and gender pattern differences in demyelination. Brain Pathol. 2009;19(3):467-79.

105. Sen MK, Almuslehi MSM, Gyengesi E, Myers SJ, Shortland PJ, Mahns DA, et al. Suppression of the Peripheral Immune System Limits the Central Immune Response Following Cuprizone-Feeding: Relevance to Modelling Multiple Sclerosis. Cells. 2019;8(11).
106. Zirngibl M, Assinck P, Sizov A, Caprariello AV, Plemel JR. Oligodendrocyte death and myelin loss in the cuprizone model: an updated overview of the intrinsic and extrinsic causes of cuprizone demyelination. Mol Neurodegener. 2022;17(1):34.
107. Matsushima GK, Morell P. The neurotoxicant, cuprizone, as a model to study demyelination and remyelination in the central nervous system. Brain Pathol. 2001;11(1):107-16.
108. Carassiti D, Altmann DR, Petrova N, Pakkenberg B, Scaravilli F, Schmierer K. Neuronal loss, demyelination and volume change in the multiple sclerosis neocortex. Neuropath Appl Neuro. 2018;44(4):377-90.
109. Zhan J, Mann T, Joost S, Behrangi N, Frank M, Kipp M. The Cuprizone Model: Dos and Do Nots. Cells. 2020;9(4).
110. Graeber MB, Kosel S, Egensperger R, Banati RB, Muller U, Bise K, et al. Rediscovery of the case described by Alois Alzheimer in 1911: historical, histological and molecular genetic analysis. Neurogenetics. 1997;1(1):73-80.
111. Klunemann HH, Fronhofer W, Wurster H, Fischer W, Ibach B, Klein HE. Alzheimer's second patient: Johann F. and his family. Ann Neurol. 2002;52(4):520-3.
112. Hardy JA, Higgins GA. Alzheimer's disease: the amyloid cascade hypothesis. Science. 1992;256(5054):184-5.
113. Knopman DS, Jones DT, Greicius MD. Failure to demonstrate efficacy of aducanumab: An analysis of the EMERGE and ENGAGE trials as reported by Biogen, December 2019. Alzheimers Dement. 2021;17(4):696-701.
114. Bohrmann B, Baumann K, Benz J, Gerber F, Huber W, Knoflach F, et al. Gantenerumab: a novel human anti-Abeta antibody demonstrates sustained cerebral amyloid-beta binding and elicits cell-mediated removal of human amyloid-beta. J Alzheimers Dis. 2012;28(1):49-69.
115. Salloway S, Sperling R, Fox NC, Blennow K, Klunk W, Raskind M, et al. Two Phase 3 Trials of Bapineuzumab in Mild-to-Moderate Alzheimer's Disease. New Engl J Med. 2014;370(4):322-33.
116. Doody RS, Thomas RG, Farlow M, Iwatsubo T, Vellas B, Joffe S, et al. Phase 3 Trials of Solanezumab for Mild-to-Moderate Alzheimer's Disease. New Engl J Med. 2014;370(4):311-21.
117. Janssen JC, Beck JA, Campbell TA, Dickinson A, Fox NC, Harvey RJ, et al. Early onset familial Alzheimer's disease: Mutation frequency in 31 families. Neurology. 2003;60(2):235-9.
118. Esch FS, Keim PS, Beattie EC, Blacher RW, Culwell AR, Oltersdorf T, et al. Cleavage of amyloid beta peptide during constitutive processing of its precursor. Science. 1990;248(4959):1122-4.
119. Garcia-Ayllon MS, Lopez-Font I, Boix CP, Fortea J, Sanchez-Valle R, Lleo A, et al. C-terminal fragments of the amyloid precursor protein in cerebrospinal fluid as potential biomarkers for Alzheimer disease. Sci Rep. 2017;7(1):2477.
120. Tyler SJ, Dawbarn D, Wilcock GK, Allen SJ. alpha- and beta-secretase: profound changes in Alzheimer's disease. Biochem Biophys Res Commun. 2002;299(3):373-6.
121. Mullan M, Crawford F, Axelman K, Houlden H, Lilius L, Winblad B, et al. A pathogenic mutation for probable Alzheimer's disease in the APP gene at the N-terminus of beta-amyloid. Nat Genet. 1992;1(5):345-7.
122. Nilsberth C, Westlind-Danielsson A, Eckman CB, Condron MM, Axelman K, Forsell C, et al. The 'Arctic' APP mutation (E693G) causes Alzheimer's disease by enhanced Abeta protofibril formation. Nat Neurosci. 2001;4(9):887-93.
123. de Graaf G, Buckley F, Skotko BG. Estimation of the number of people with Down syndrome in the United States. Genet Med. 2017;19(4):439-47.
124. Tanzi RE, Gusella JF, Watkins PC, Bruns GA, St George-Hyslop P, Van Keuren ML, et al. Amyloid beta protein gene: cDNA, mRNA distribution, and genetic linkage near the Alzheimer locus. Science. 1987;235(4791):880-4.
125. Neve RL, Finch EA, Dawes LR. Expression of the Alzheimer amyloid precursor gene transcripts in the human brain. Neuron. 1988;1(8):669-77.
126. Tanaka S, Shiojiri S, Takahashi Y, Kitaguchi N, Ito H, Kameyama M, et al. Tissue-specific expression of three types of beta-protein precursor mRNA: enhancement of protease inhibitor-harboring types in Alzheimer's disease brain. Biochem Biophys Res Commun. 1989;165(3):1406-14.

127. Koistinaho J, Pyykonen I, Keinanen R, Hokfelt T. Expression of beta-amyloid precursor protein mRNAs following transient focal ischaemia. Neuroreport. 1996;7(15-17):2727-31.
128. Schmaier AH, Dahl LD, Rozemuller AJ, Roos RA, Wagner SL, Chung R, et al. Protease nexin-2/amyloid beta protein precursor. A tight-binding inhibitor of coagulation factor IXa. J Clin Invest. 1993;92(5):2540-5.
129. Van Nostrand WE, Schmaier AH, Wagner SL. Potential role of protease nexin-2/amyloid beta-protein precursor as a cerebral anticoagulant. Ann N Y Acad Sci. 1992;674:243-52.
130. Kang DE, Pietrzik CU, Baum L, Chevallier N, Merriam DE, Kounnas MZ, et al. Modulation of amyloid beta-protein clearance and Alzheimer's disease susceptibility by the LDL receptor-related protein pathway. J Clin Invest. 2000;106(9):1159-66.
131. Kang DE, Saitoh T, Chen X, Xia Y, Masliah E, Hansen LA, et al. Genetic association of the low-density lipoprotein receptor-related protein gene (LRP), an apolipoprotein E receptor, with late-onset Alzheimer's disease. Neurology. 1997;49(1):56-61.
132. Zhou Z, Liang Y, Zhang X, Xu J, Lin J, Zhang R, et al. Low-Density Lipoprotein Cholesterol and Alzheimer's Disease: A Systematic Review and Meta-Analysis. Front Aging Neurosci. 2020;12:5.
133. Clark MJ, Gagnon J, Williams AF, Barclay AN. MRC OX-2 antigen: a lymphoid/neuronal membrane glycoprotein with a structure like a single immunoglobulin light chain. EMBO J. 1985;4(1):113-8.
134. Hung AY, Koo EH, Haass C, Selkoe DJ. Increased expression of beta-amyloid precursor protein during neuronal differentiation is not accompanied by secretory cleavage. Proc Natl Acad Sci U S A. 1992;89(20):9439-43.
135. Rohan de Silva HA, Jen A, Wickenden C, Jen LS, Wilkinson SL, Patel AJ. Cell-specific expression of beta-amyloid precursor protein isoform mRNAs and proteins in neurons and astrocytes. Brain Res Mol Brain Res. 1997;47(1-2):147-56.
136. Selkoe DJ, Podlisny MB, Joachim CL, Vickers EA, Lee G, Fritz LC, et al. Beta-amyloid precursor protein of Alzheimer disease occurs as 110- to 135-kilodalton membrane-associated proteins in neural and nonneural tissues. Proc Natl Acad Sci U S A. 1988;85(19):7341-5.
137. Zheng H, Jiang M, Trumbauer ME, Sirinathsinghji DJ, Hopkins R, Smith DW, et al. beta-Amyloid precursor protein-deficient mice show reactive gliosis and decreased locomotor activity. Cell. 1995;81(4):525-31.
138. Heber S, Herms J, Gajic V, Hainfellner J, Aguzzi A, Rulicke T, et al. Mice with combined gene knock-outs reveal essential and partially redundant functions of amyloid precursor protein family members. J Neurosci. 2000;20(21):7951-63.
139. von Koch CS, Zheng H, Chen H, Trumbauer M, Thinakaran G, van der Ploeg LH, et al. Generation of APLP2 KO mice and early postnatal lethality in APLP2/APP double KO mice. Neurobiol Aging. 1997;18(6):661-9.
140. Herms J, Anliker B, Heber S, Ring S, Fuhrmann M, Kretzschmar H, et al. Cortical dysplasia resembling human type 2 lissencephaly in mice lacking all three APP family members. EMBO J. 2004;23(20):4106-15.
141. Schubert W, Prior R, Weidemann A, Dircksen H, Multhaup G, Masters CL, et al. Localization of Alzheimer beta A4 amyloid precursor protein at central and peripheral synaptic sites. Brain Res. 1991;563(1-2):184-94.
142. Shigematsu K, McGeer PL, McGeer EG. Localization of amyloid precursor protein in selective postsynaptic densities of rat cortical neurons. Brain Res. 1992;592(1-2):353-7.
143. DeBoer SR, Dolios G, Wang R, Sisodia SS. Differential release of beta-amyloid from dendrite- versus axon-targeted APP. J Neurosci. 2014;34(37):12313-27.
144. Tomita T, Wong PC. Selectivity to amyloid-beta precursor protein cleavage provides hope against Alzheimer's. Alzheimers Res Ther. 2011;3(2):7.
145. Sannerud R, Declerck I, Peric A, Raemaekers T, Menendez G, Zhou L, et al. ADP ribosylation factor 6 (ARF6) controls amyloid precursor protein (APP) processing by mediating the endosomal sorting of BACE1. Proc Natl Acad Sci U S A. 2011;108(34):E559-68.
146. Das U, Scott DA, Ganguly A, Koo EH, Tang Y, Roy S. Activity-induced convergence of APP and BACE-1 in acidic microdomains via an endocytosis-dependent pathway. Neuron. 2013;79(3):447-60.

147. Das U, Wang L, Ganguly A, Saikia JM, Wagner SL, Koo EH, et al. Visualizing APP and BACE-1 approximation in neurons yields insight into the amyloidogenic pathway. Nat Neurosci. 2016;19(1):55-64.
148. Lacor PN, Buniel MC, Chang L, Fernandez SJ, Gong Y, Viola KL, et al. Synaptic targeting by Alzheimer's-related amyloid beta oligomers. J Neurosci. 2004;24(45):10191-200.
149. LaFerla FM. Calcium dyshomeostasis and intracellular signalling in Alzheimer's disease. Nat Rev Neurosci. 2002;3(11):862-72.
150. Demuro A, Mina E, Kayed R, Milton SC, Parker I, Glabe CG. Calcium dysregulation and membrane disruption as a ubiquitous neurotoxic mechanism of soluble amyloid oligomers. J Biol Chem. 2005;280(17):17294-300.
151. Li S, Hong S, Shepardson NE, Walsh DM, Shankar GM, Selkoe D. Soluble oligomers of amyloid Beta protein facilitate hippocampal long-term depression by disrupting neuronal glutamate uptake. Neuron. 2009;62(6):788-801.
152. Shankar GM, Bloodgood BL, Townsend M, Walsh DM, Selkoe DJ, Sabatini BL. Natural oligomers of the Alzheimer amyloid-beta protein induce reversible synapse loss by modulating an NMDA-type glutamate receptor-dependent signaling pathway. J Neurosci. 2007;27(11):2866-75.
153. Grothe MJ, Barthel H, Sepulcre J, Dyrba M, Sabri O, Teipel SJ, et al. In vivo staging of regional amyloid deposition. Neurology. 2017;89(20):2031-8.
154. Teipel SJ, Dyrba M, Chiesa PA, Sakr F, Jelistratova I, Lista S, et al. In vivo staging of regional amyloid deposition predicts functional conversion in the preclinical and prodromal phases of Alzheimer's disease. Neurobiol Aging. 2020;93:98-108.
155. Hartmann T. Intracellular biology of Alzheimer's disease amyloid beta peptide. Eur Arch Psychiatry Clin Neurosci. 1999;249(6):291-8.
156. Gouras GK, Tsai J, Naslund J, Vincent B, Edgar M, Checler F, et al. Intraneuronal Abeta42 accumulation in human brain. Am J Pathol. 2000;156(1):15-20.
157. Cuello AC. Intracellular and extracellular Abeta, a tale of two neuropathologies. Brain Pathol. 2005;15(1):66-71.
158. Umeda T, Tomiyama T, Sakama N, Tanaka S, Lambert MP, Klein WL, et al. Intraneuronal amyloid beta oligomers cause cell death via endoplasmic reticulum stress, endosomal/lysosomal leakage, and mitochondrial dysfunction in vivo. J Neurosci Res. 2011;89(7):1031-42.
159. Zhao L, Longo-Guess C, Harris BS, Lee JW, Ackerman SL. Protein accumulation and neurodegeneration in the woozy mutant mouse is caused by disruption of SIL1, a cochaperone of BiP. Nat Genet. 2005;37(9):974-9.
160. Oakley H, Cole SL, Logan S, Maus E, Shao P, Craft J, et al. Intraneuronal beta-amyloid aggregates, neurodegeneration, and neuron loss in transgenic mice with five familial Alzheimer's disease mutations: potential factors in amyloid plaque formation. J Neurosci. 2006;26(40):10129-40.
161. Hamdane M, Bretteville A, Sambo AV, Schindowski K, Begard S, Delacourte A, et al. p25/Cdk5-mediated retinoblastoma phosphorylation is an early event in neuronal cell death. J Cell Sci. 2005;118(Pt 6):1291-8.
162. Patrick GN, Zukerberg L, Nikolic M, de La Monte S, Dikkes P, Tsai LH. reply: Neurobiologyp25 protein in neurodegeneration. Nature. 2001;411(6839):764-5.
163. Braak H, Alafuzoff I, Arzberger T, Kretzschmar H, Del Tredici K. Staging of Alzheimer disease-associated neurofibrillary pathology using paraffin sections and immunocytochemistry. Acta Neuropathol. 2006;112(4):389-404.
164. Braak H, Braak E. Neuropathological stageing of Alzheimer-related changes. Acta Neuropathol. 1991;82(4):239-59.
165. Tsao A, Sugar J, Lu L, Wang C, Knierim JJ, Moser MB, et al. Integrating time from experience in the lateral entorhinal cortex. Nature. 2018;561(7721):57-62.
166. Roberts RO, Knopman DS, Przybelski SA, Mielke MM, Kantarci K, Preboske GM, et al. Association of type 2 diabetes with brain atrophy and cognitive impairment. Neurology. 2014;82(13):1132-41.
167. Killin LO, Starr JM, Shiue IJ, Russ TC. Environmental risk factors for dementia: a systematic review. BMC Geriatr. 2016;16(1):175.
168. Arevalo-Rodriguez I, Smailagic N, Roque IFM, Ciapponi A, Sanchez-Perez E, Giannakou A, et al. Mini-Mental State Examination (MMSE) for the detection of Alzheimer's disease and other

dementias in people with mild cognitive impairment (MCI). Cochrane Database Syst Rev. 2015;2015(3):CD010783.
169. Ferrarini L, Palm WM, Olofsen H, van der Landen R, Jan Blauw G, Westendorp RG, et al. MMSE scores correlate with local ventricular enlargement in the spectrum from cognitively normal to Alzheimer disease. Neuroimage. 2008;39(4):1832-8.
170. Chu LW, Chiu KC, Hui SL, Yu GK, Tsui WJ, Lee PW. The reliability and validity of the Alzheimer's Disease Assessment Scale Cognitive Subscale (ADAS-Cog) among the elderly Chinese in Hong Kong. Ann Acad Med Singap. 2000;29(4):474-85.
171. Cano SJ, Posner HB, Moline ML, Hurt SW, Swartz J, Hsu T, et al. The ADAS-cog in Alzheimer's disease clinical trials: psychometric evaluation of the sum and its parts. J Neurol Neurosurg Psychiatry. 2010;81(12):1363-8.
172. Statement from The Memory and Aging Program at Butler Hospital on CMS National Coverage Determination for Monoclonal Antibodies Directed Against Amyloid for the Treatment of Alzheimer's Disease. R I Med J (2013). 2022;105(4):75.
173. Rao RV, Kumar S, Gregory J, Coward C, Okada S, Lipa W, et al. ReCODE: A Personalized, Targeted, Multi-Factorial Therapeutic Program for Reversal of Cognitive Decline. Biomedicines. 2021;9(10).
174. Liu CC, Liu CC, Kanekiyo T, Xu H, Bu G. Apolipoprotein E and Alzheimer disease: risk, mechanisms and therapy. Nat Rev Neurol. 2013;9(2):106-18.
175. Liu M, Kuhel DG, Shen L, Hui DY, Woods SC. Apolipoprotein E does not cross the blood-cerebrospinal fluid barrier, as revealed by an improved technique for sampling CSF from mice. Am J Physiol Regul Integr Comp Physiol. 2012;303(9):R903-8.
176. Nagy Z, Esiri MM, Jobst KA, Johnston C, Litchfield S, Sim E, et al. Influence of the apolipoprotein E genotype on amyloid deposition and neurofibrillary tangle formation in Alzheimer's disease. Neuroscience. 1995;69(3):757-61.
177. Serrano-Pozo A, Qian J, Monsell SE, Betensky RA, Hyman BT. APOEepsilon2 is associated with milder clinical and pathological Alzheimer disease. Ann Neurol. 2015;77(6):917-29.
178. Reiman EM, Arboleda-Velasquez JF, Quiroz YT, Huentelman MJ, Beach TG, Caselli RJ, et al. Exceptionally low likelihood of Alzheimer's dementia in APOE2 homozygotes from a 5,000-person neuropathological study. Nat Commun. 2020;11(1):667.
179. Berlau DJ, Corrada MM, Head E, Kawas CH. APOE epsilon2 is associated with intact cognition but increased Alzheimer pathology in the oldest old. Neurology. 2009;72(9):829-34.
180. Berlau DJ, Kahle-Wrobleski K, Head E, Goodus M, Kim R, Kawas C. Dissociation of neuropathologic findings and cognition: case report of an apolipoprotein E epsilon2/epsilon2 genotype. Arch Neurol. 2007;64(8):1193-6.
181. Shinohara M, Kanekiyo T, Yang L, Linthicum D, Shinohara M, Fu Y, et al. APOE2 eases cognitive decline during Aging: Clinical and preclinical evaluations. Ann Neurol. 2016;79(5):758-74.
182. Deelen J, Beekman M, Uh HW, Helmer Q, Kuningas M, Christiansen L, et al. Genome-wide association study identifies a single major locus contributing to survival into old age; the APOE locus revisited. Aging Cell. 2011;10(4):686-98.
183. Nebel A, Kleindorp R, Caliebe A, Nothnagel M, Blanche H, Junge O, et al. A genome-wide association study confirms APOE as the major gene influencing survival in long-lived individuals. Mech Ageing Dev. 2011;132(6-7):324-30.
184. Zeng Y, Nie C, Min J, Liu X, Li M, Chen H, et al. Novel loci and pathways significantly associated with longevity. Sci Rep. 2016;6:21243.
185. Nelson PT, Pious NM, Jicha GA, Wilcock DM, Fardo DW, Estus S, et al. APOE-epsilon2 and APOE-epsilon4 correlate with increased amyloid accumulation in cerebral vasculature. J Neuropathol Exp Neurol. 2013;72(7):708-15.
186. Kim TY, Chung HG, Shin HS, Kim SJ, Choi JH, Chung MY, et al. Apolipoprotein E gene polymorphism, alcohol use, and their interactions in combat-related posttraumatic stress disorder. Depress Anxiety. 2013;30(12):1194-201.
187. McKay GJ, Patterson CC, Chakravarthy U, Dasari S, Klaver CC, Vingerling JR, et al. Evidence of association of APOE with age-related macular degeneration: a pooled analysis of 15 studies. Hum Mutat. 2011;32(12):1407-16.

188. Tachibana M, Holm ML, Liu CC, Shinohara M, Aikawa T, Oue H, et al. APOE4-mediated amyloid-beta pathology depends on its neuronal receptor LRP1. J Clin Invest. 2019;129(3):1272-7.
189. Liu CC, Zhao N, Fu Y, Wang N, Linares C, Tsai CW, et al. ApoE4 Accelerates Early Seeding of Amyloid Pathology. Neuron. 2017;96(5):1024-32 e3.
190. Mahley RW. Development of accelerated atherosclerosis. Concepts derived from cell biology and animal model studies. Arch Pathol Lab Med. 1983;107(8):393-9.
191. Mok KK, Yeung SH, Cheng GW, Ma IW, Lee RH, Herrup K, et al. Apolipoprotein E epsilon4 disrupts oligodendrocyte differentiation by interfering with astrocyte-derived lipid transport. J Neurochem. 2023;165(1):55-75.
192. Dong LM, Wilson C, Wardell MR, Simmons T, Mahley RW, Weisgraber KH, et al. Human apolipoprotein E. Role of arginine 61 in mediating the lipoprotein preferences of the E3 and E4 isoforms. J Biol Chem. 1994;269(35):22358-65.
193. Garai K, Frieden C. The association-dissociation behavior of the ApoE proteins: kinetic and equilibrium studies. Biochemistry. 2010;49(44):9533-41.
194. Perugini MA, Schuck P, Howlett GJ. Self-association of human apolipoprotein E3 and E4 in the presence and absence of phospholipid. J Biol Chem. 2000;275(47):36758-65.
195. Vila-Rodriguez F, Honer WG, Innis SM, Wellington CL, Beasley CL. ApoE and cholesterol in schizophrenia and bipolar disorder: comparison of grey and white matter and relation with APOE genotype. J Psychiatry Neurosci. 2011;36(1):47-55.
196. Rebeck GW, Reiter JS, Strickland DK, Hyman BT. Apolipoprotein E in sporadic Alzheimer's disease: allelic variation and receptor interactions. Neuron. 1993;11(4):575-80.
197. Sabbagh MN, Malek-Ahmadi M, Dugger BN, Lee K, Sue LI, Serrano G, et al. The influence of Apolipoprotein E genotype on regional pathology in Alzheimer's disease. BMC Neurol. 2013;13:44.
198. Rowe CC, Ellis KA, Rimajova M, Bourgeat P, Pike KE, Jones G, et al. Amyloid imaging results from the Australian Imaging, Biomarkers and Lifestyle (AIBL) study of aging. Neurobiol Aging. 2010;31(8):1275-83.
199. Tiraboschi P, Hansen LA, Masliah E, Alford M, Thal LJ, Corey-Bloom J. Impact of APOE genotype on neuropathologic and neurochemical markers of Alzheimer disease. Neurology. 2004;62(11):1977-83.
200. Farfel JM, Yu L, De Jager PL, Schneider JA, Bennett DA. Association of APOE with tau-tangle pathology with and without beta-amyloid. Neurobiol Aging. 2016;37:19-25.
201. Rojas S, Brugulat-Serrat A, Bargallo N, Minguillon C, Tucholka A, Falcon C, et al. Higher prevalence of cerebral white matter hyperintensities in homozygous APOE-varepsilon4 allele carriers aged 45-75: Results from the ALFA study. J Cereb Blood Flow Metab. 2018;38(2):250-61.
202. Saher G, Stumpf SK. Cholesterol in myelin biogenesis and hypomyelinating disorders. Biochim Biophys Acta. 2015;1851(8):1083-94.
203. Weintraub H, Abramovici A, Sandbank U, Booth AD, Pentchev PG, Sela B. Dysmyelination in NCTR-Balb/C mouse mutant with a lysosomal storage disorder. Morphological survey. Acta Neuropathol. 1987;74(4):374-81.
204. German DC, Liang CL, Song T, Yazdani U, Xie C, Dietschy JM. Neurodegeneration in the Niemann-Pick C mouse: glial involvement. Neuroscience. 2002;109(3):437-50.
205. Yan X, Lukas J, Witt M, Wree A, Hubner R, Frech M, et al. Decreased expression of myelin gene regulatory factor in Niemann-Pick type C 1 mouse. Metab Brain Dis. 2011;26(4):299-306.
206. Lombardi M, Parolisi R, Scaroni F, Bonfanti E, Gualerzi A, Gabrielli M, et al. Detrimental and protective action of microglial extracellular vesicles on myelin lesions: astrocyte involvement in remyelination failure. Acta Neuropathol. 2019;138(6):987-1012.
207. Nieweg K, Schaller H, Pfrieger FW. Marked differences in cholesterol synthesis between neurons and glial cells from postnatal rats. J Neurochem. 2009;109(1):125-34.
208. Makoukji J, Shackleford G, Meffre D, Grenier J, Liere P, Lobaccaro JM, et al. Interplay between LXR and Wnt/beta-catenin signaling in the negative regulation of peripheral myelin genes by oxysterols. J Neurosci. 2011;31(26):9620-9.
209. Meffre D, Shackleford G, Hichor M, Gorgievski V, Tzavara ET, Trousson A, et al. Liver X receptors alpha and beta promote myelination and remyelination in the cerebellum. Proc Natl Acad Sci U S A. 2015;112(24):7587-92.

210. Bezine M, Namsi A, Sghaier R, Ben Khalifa R, Hamdouni H, Brahmi F, et al. The effect of oxysterols on nerve impulses. Biochimie. 2018;153:46-51.
211. Boublay N, Bouet R, Dorey JM, Padovan C, Makaroff Z, Federico D, et al. Brain Volume Predicts Behavioral and Psychological Symptoms in Alzheimer's Disease. J Alzheimers Dis. 2020;73(4):1343-53.
212. Reiter K, Nielson KA, Durgerian S, Woodard JL, Smith JC, Seidenberg M, et al. Five-Year Longitudinal Brain Volume Change in Healthy Elders at Genetic Risk for Alzheimer's Disease. Journal of Alzheimers Disease. 2017;55(4):1363-77.
213. Mofrad SA, Lundervold A, Lundervold AS, Alzheimer's Disease Neuroimaging I, Australian Imaging B, Lifestyle Flagship Study of A. A predictive framework based on brain volume trajectories enabling early detection of Alzheimer's disease. Comput Med Imaging Graph. 2021;90:101910.
214. Henneman WJ, Sluimer JD, Barnes J, van der Flier WM, Sluimer IC, Fox NC, et al. Hippocampal atrophy rates in Alzheimer disease: added value over whole brain volume measures. Neurology. 2009;72(11):999-1007.
215. Sluimer JD, Vrenken H, Blankenstein MA, Fox NC, Scheltens P, Barkhof F, et al. Whole-brain atrophy rate in Alzheimer disease: identifying fast progressors. Neurology. 2008;70(19 Pt 2):1836-41.
216. Spulber G, Niskanen E, MacDonald S, Smilovici O, Chen K, Reiman EM, et al. Whole brain atrophy rate predicts progression from MCI to Alzheimer's disease. Neurobiol Aging. 2010;31(9):1601-5.
217. Fotenos AF, Mintun MA, Snyder AZ, Morris JC, Buckner RL. Brain volume decline in aging: evidence for a relation between socioeconomic status, preclinical Alzheimer disease, and reserve. Arch Neurol. 2008;65(1):113-20.
218. Sykova E. Diffusion properties of the brain in health and disease. Neurochem Int. 2004;45(4):453-66.
219. Kochunov P, Williamson DE, Lancaster J, Fox P, Cornell J, Blangero J, et al. Fractional anisotropy of water diffusion in cerebral white matter across the lifespan. Neurobiol Aging. 2012;33(1):9-20.
220. Liu Y, Spulber G, Lehtimaki KK, Kononen M, Hallikainen I, Grohn H, et al. Diffusion tensor imaging and tract-based spatial statistics in Alzheimer's disease and mild cognitive impairment. Neurobiol Aging. 2011;32(9):1558-71.
221. Clark KA, Nuechterlein KH, Asarnow RF, Hamilton LS, Phillips OR, Hageman NS, et al. Mean diffusivity and fractional anisotropy as indicators of disease and genetic liability to schizophrenia. J Psychiatr Res. 2011;45(7):980-8.
222. Cercignani M, Inglese M, Pagani E, Comi G, Filippi M. Mean diffusivity and fractional anisotropy histograms of patients with multiple sclerosis. AJNR Am J Neuroradiol. 2001;22(5):952-8.
223. Ibrahim I, Tintera J, Skoch A, Jiru F, Hlustik P, Martinkova P, et al. Fractional anisotropy and mean diffusivity in the corpus callosum of patients with multiple sclerosis: the effect of physiotherapy. Neuroradiology. 2011;53(11):917-26.
224. Jonkman LE, Klaver R, Fleysher L, Inglese M, Geurts JJ. The substrate of increased cortical FA in MS: A 7T post-mortem MRI and histopathology study. Mult Scler. 2016;22(14):1804-11.
225. Song SK, Sun SW, Ramsbottom MJ, Chang C, Russell J, Cross AH. Dysmyelination revealed through MRI as increased radial (but unchanged axial) diffusion of water. Neuroimage. 2002;17(3):1429-36.
226. Song SK, Yoshino J, Le TQ, Lin SJ, Sun SW, Cross AH, et al. Demyelination increases radial diffusivity in corpus callosum of mouse brain. Neuroimage. 2005;26(1):132-40.
227. Stidworthy MF, Genoud S, Suter U, Mantei N, Franklin RJ. Quantifying the early stages of remyelination following cuprizone-induced demyelination. Brain Pathol. 2003;13(3):329-39.
228. Sun SW, Liang HF, Trinkaus K, Cross AH, Armstrong RC, Song SK. Noninvasive detection of cuprizone induced axonal damage and demyelination in the mouse corpus callosum. Magn Reson Med. 2006;55(2):302-8.
229. Basser PJ, Pierpaoli C. Microstructural and physiological features of tissues elucidated by quantitative-diffusion-tensor MRI. J Magn Reson B. 1996;111(3):209-19.
230. Xie M, Tobin JE, Budde MD, Chen CI, Trinkaus K, Cross AH, et al. Rostrocaudal analysis of corpus callosum demyelination and axon damage across disease stages refines diffusion tensor imaging correlations with pathological features. J Neuropathol Exp Neurol. 2010;69(7):704-16.

231. Takeuchi H, Kawashima R. Mean Diffusivity in the Dopaminergic System and Neural Differences Related to Dopaminergic System. Curr Neuropharmacol. 2018;16(4):460-74.
232. Beaulieu C. The basis of anisotropic water diffusion in the nervous system - a technical review. NMR Biomed. 2002;15(7-8):435-55.
233. Sagi Y, Tavor I, Hofstetter S, Tzur-Moryosef S, Blumenfeld-Katzir T, Assaf Y. Learning in the fast lane: new insights into neuroplasticity. Neuron. 2012;73(6):1195-203.
234. Nordengen K, Heuser C, Rinholm JE, Matalon R, Gundersen V. Localisation of N-acetylaspartate in oligodendrocytes/myelin. Brain Struct Funct. 2015;220(2):899-917.
235. Skripuletz T, Manzel A, Gropengiesser K, Schafer N, Gudi V, Singh V, et al. Pivotal role of choline metabolites in remyelination. Brain. 2015;138(Pt 2):398-413.
236. Montani L. Lipids in regulating oligodendrocyte structure and function. Semin Cell Dev Biol. 2021;112:114-22.
237. MacDonald SC, Simcoff R, Jordan LM, Dodd JG, Cheng KW, Hochman S. A population of oligodendrocytes derived from multipotent neural precursor cells expresses a cholinergic phenotype in culture and responds to ciliary neurotrophic factor. J Neurosci Res. 2002;68(3):255-64.
238. Skripuletz T, Linker RA, Stangel M. The choline pathway as a strategy to promote central nervous system (CNS) remyelination. Neural Regen Res. 2015;10(9):1369-70.
239. Ogawa S, Lee TM, Kay AR, Tank DW. Brain magnetic resonance imaging with contrast dependent on blood oxygenation. Proc Natl Acad Sci U S A. 1990;87(24):9868-72.
240. Ogawa S, Tank DW, Menon R, Ellermann JM, Kim SG, Merkle H, et al. Intrinsic signal changes accompanying sensory stimulation: functional brain mapping with magnetic resonance imaging. Proc Natl Acad Sci U S A. 1992;89(13):5951-5.
241. Bandettini PA, Wong EC, Hinks RS, Tikofsky RS, Hyde JS. Time course EPI of human brain function during task activation. Magn Reson Med. 1992;25(2):390-7.
242. Campion T, Smith RJP, Altmann DR, Brito GC, Turner BP, Evanson J, et al. FLAIR* to visualize veins in white matter lesions: A new tool for the diagnosis of multiple sclerosis? Eur Radiol. 2017;27(10):4257-63.
243. Kilsdonk ID, Wattjes MP, Lopez-Soriano A, Kuijer JP, de Jong MC, de Graaf WL, et al. Improved differentiation between MS and vascular brain lesions using FLAIR* at 7 Tesla. Eur Radiol. 2014;24(4):841-9.
244. Sinnecker T, Dorr J, Pfueller CF, Harms L, Ruprecht K, Jarius S, et al. Distinct lesion morphology at 7-T MRI differentiates neuromyelitis optica from multiple sclerosis. Neurology. 2012;79(7):708-14.
245. Fleisher AS, Sun S, Taylor C, Ward CP, Gamst AC, Petersen RC, et al. Volumetric MRI vs clinical predictors of Alzheimer disease in mild cognitive impairment. Neurology. 2008;70(3):191-9.
246. Ridha BH, Anderson VM, Barnes J, Boyes RG, Price SL, Rossor MN, et al. Volumetric MRI and cognitive measures in Alzheimer disease : comparison of markers of progression. J Neurol. 2008;255(4):567-74.
247. Long X, Chen L, Jiang C, Zhang L, Alzheimer's Disease Neuroimaging I. Prediction and classification of Alzheimer disease based on quantification of MRI deformation. PLoS One. 2017;12(3):e0173372.
248. Huang J, van Zijl PCM, Han X, Dong CM, Cheng GWY, Tse KH, et al. Altered d-glucose in brain parenchyma and cerebrospinal fluid of early Alzheimer's disease detected by dynamic glucose-enhanced MRI. Sci Adv. 2020;6(20):eaba3884.
249. Maillard P, Fletcher E, Lockhart SN, Roach AE, Reed B, Mungas D, et al. White matter hyperintensities and their penumbra lie along a continuum of injury in the aging brain. Stroke. 2014;45(6):1721-6.
250. Fu J, Tang J, Han J, Hong Z. The reduction of regional cerebral blood flow in normal-appearing white matter is associated with the severity of white matter lesions in elderly: a Xeon-CT study. PLoS One. 2014;9(11):e112832.
251. Zhong G, Lou M. Multimodal imaging findings in normal-appearing white matter of leucoaraiosis: a review. Stroke Vasc Neurol. 2016;1(2):59-63.
252. Consensus recommendations for the postmortem diagnosis of Alzheimer's disease. The National Institute on Aging, and Reagan Institute Working Group on Diagnostic Criteria for the Neuropathological Assessment of Alzheimer's Disease. Neurobiol Aging. 1997;18(4 Suppl):S1-2.

253. Cerghet M, Skoff RP, Swamydas M, Bessert D. Sexual dimorphism in the white matter of rodents. J Neurol Sci. 2009;286(1-2):76-80.
254. Massella A, D'Intino G, Fernandez M, Sivilia S, Lorenzini L, Giatti S, et al. Gender effect on neurodegeneration and myelin markers in an animal model for multiple sclerosis. BMC Neurosci. 2012;13:12.
255. Zahaf A, Kassoussi A, Hutteau-Hamel T, Mellouk A, Marie C, Zoupi L, et al. Androgens show sex-dependent differences in myelination in immune and non-immune murine models of CNS demyelination. Nat Commun. 2023;14(1):1592.
256. Zhou CN, Chao FL, Zhang Y, Jiang L, Zhang L, Luo YM, et al. Sex Differences in the White Matter and Myelinated Fibers of APP/PS1 Mice and the Effects of Running Exercise on the Sex Differences of AD Mice. Front Aging Neurosci. 2018;10:243.
257. Paton KF, Hong S, Biggerstaff A, Kivell BM. Sex Differences in the Behavioural Aspects of the Cuprizone-Induced Demyelination Model in Mice. Brain Sci. 2022;12(12).
258. Taylor LC, Gilmore W, Ting JP, Matsushima GK. Cuprizone induces similar demyelination in male and female C57BL/6 mice and results in disruption of the estrous cycle. J Neurosci Res. 2010;88(2):391-402.
259. Ajayi AF, Akhigbe RE. Staging of the estrous cycle and induction of estrus in experimental rodents: an update. Fertil Res Pract. 2020;6:5.
260. Long KLP, Breton JM, Barraza MK, Perloff OS, Kaufer D. Hormonal Regulation of Oligodendrogenesis I: Effects across the Lifespan. Biomolecules. 2021;11(2).
261. Gonzalez-Orozco JC, Moral-Morales AD, Camacho-Arroyo I. Progesterone through Progesterone Receptor B Isoform Promotes Rodent Embryonic Oligodendrogenesis. Cells. 2020;9(4).
262. Ibanez C, Shields SA, El-Etr M, Baulieu EE, Schumacher M, Franklin RJ. Systemic progesterone administration results in a partial reversal of the age-associated decline in CNS remyelination following toxin-induced demyelination in male rats. Neuropathol Appl Neurobiol. 2004;30(1):80-9.
263. Lamb BT, Call LM, Slunt HH, Bardel KA, Lawler AM, Eckman CB, et al. Altered metabolism of familial Alzheimer's disease-linked amyloid precursor protein variants in yeast artificial chromosome transgenic mice. Hum Mol Genet. 1997;6(9):1535-41.
264. Ketner G, Spencer F, Tugendreich S, Connelly C, Hieter P. Efficient manipulation of the human adenovirus genome as an infectious yeast artificial chromosome clone. Proc Natl Acad Sci U S A. 1994;91(13):6186-90.
265. Radde R, Bolmont T, Kaeser SA, Coomaraswamy J, Lindau D, Stoltze L, et al. Abeta42-driven cerebral amyloidosis in transgenic mice reveals early and robust pathology. EMBO Rep. 2006;7(9):940-6.
266. Piedrahita JA, Zhang SH, Hagaman JR, Oliver PM, Maeda N. Generation of mice carrying a mutant apolipoprotein E gene inactivated by gene targeting in embryonic stem cells. Proc Natl Acad Sci U S A. 1992;89(10):4471-5.
267. Hamanaka H, Katoh-Fukui Y, Suzuki K, Kobayashi M, Suzuki R, Motegi Y, et al. Altered cholesterol metabolism in human apolipoprotein E4 knock-in mice. Hum Mol Genet. 2000;9(3):353-61.
268. d'Isa R, Comi G, Leocani L. Apparatus design and behavioural testing protocol for the evaluation of spatial working memory in mice through the spontaneous alternation T-maze. Sci Rep. 2021;11(1):21177.
269. Prieur EAK, Jadavji NM. Assessing Spatial Working Memory Using the Spontaneous Alternation Y-maze Test in Aged Male Mice. Bio Protoc. 2019;9(3):e3162.
270. Yoshizaki K, Asai M, Hara T. High-Fat Diet Enhances Working Memory in the Y-Maze Test in Male C57BL/6J Mice with Less Anxiety in the Elevated Plus Maze Test. Nutrients. 2020;12(7).
271. Fitzgerald RE, Rosenberg E, Oettinger R, Isler R, Buzzi R, Battig K. Maze Patrolling by Rats with and without Food Reward. Experientia. 1985;41(9):1219-.
272. Habedank A, Kahnau P, Lewejohann L. Alternate without alternative: neither preference nor learning explains behaviour of C57BL/6J mice in the T-maze. Behaviour. 2021;158(7):625-62.
273. Hussain H, Ahmad S, Shah SWA, Ullah A, Ali N, Almehmadi M, et al. Attenuation of Scopolamine-Induced Amnesia via Cholinergic Modulation in Mice by Synthetic Curcumin Analogs. Molecules. 2022;27(8).

274. Maurice T, Hiramatsu M, Kameyama T, Hasegawa T, Nabeshima T. Behavioral evidence for a modulating role of sigma ligands in memory processes. II. Reversion of carbon monoxide-induced amnesia. Brain Res. 1994;647(1):57-64.
275. Holcomb L, Gordon MN, McGowan E, Yu X, Benkovic S, Jantzen P, et al. Accelerated Alzheimer-type phenotype in transgenic mice carrying both mutant amyloid precursor protein and presenilin 1 transgenes. Nat Med. 1998;4(1):97-100.
276. Li B, Arime Y, Hall FS, Uhl GR, Sora I. Impaired spatial working memory and decreased frontal cortex BDNF protein level in dopamine transporter knockout mice. Eur J Pharmacol. 2010;628(1-3):104-7.
277. Lee GY, Lee C, Park GH, Jang JH. Amelioration of Scopolamine-Induced Learning and Memory Impairment by alpha-Pinene in C57BL/6 Mice. Evid Based Complement Alternat Med. 2017;2017:4926815.
278. de Sousa LP, de Almeida RF, Ribeiro-Gomes FL, de Moura Carvalho LJ, TM ES, de Souza DOG, et al. Long-term effect of uncomplicated Plasmodium berghei ANKA malaria on memory and anxiety-like behaviour in C57BL/6 mice. Parasit Vectors. 2018;11(1):191.
279. Kraeuter AK, Guest PC, Sarnyai Z. The Y-Maze for Assessment of Spatial Working and Reference Memory in Mice. Methods Mol Biol. 2019;1916:105-11.
280. Jones MV, Brooks PA, Harrison NL. Enhancement of gamma-aminobutyric acid-activated Cl- currents in cultured rat hippocampal neurones by three volatile anaesthetics. J Physiol. 1992;449:279-93.
281. Bieda MC, Su H, Maciver MB. Anesthetics discriminate between tonic and phasic gamma-aminobutyric acid receptors on hippocampal CA1 neurons. Anesth Analg. 2009;108(2):484-90.
282. Ramirez-Jarquin UN, Lazo-Gomez R, Tovar YRLB, Tapia R. Spinal inhibitory circuits and their role in motor neuron degeneration. Neuropharmacology. 2014;82:101-7.
283. Jie F, Yin G, Yang W, Yang M, Gao S, Lv J, et al. Stress in Regulation of GABA Amygdala System and Relevance to Neuropsychiatric Diseases. Front Neurosci. 2018;12:562.
284. Dhaya I, Griton M, Konsman JP. Magnetic resonance imaging under isoflurane anesthesia alters cortical cyclooxygenase-2 expression and glial cell morphology during sepsis-associated neurological dysfunction in rats. Animal Model Exp Med. 2021;4(3):249-60.
285. Chamberlain KA, Chapey KS, Nanescu SE, Huang JK. Creatine Enhances Mitochondrial-Mediated Oligodendrocyte Survival After Demyelinating Injury. J Neurosci. 2017;37(6):1479-92.
286. Rosko LM, Gentile T, Smith VN, Manavi Z, Melchor GS, Hu J, et al. Cerebral Creatine Deficiency Affects the Timing of Oligodendrocyte Myelination. J Neurosci. 2023;43(7):1143-53.
287. Parnetti L, Tarducci R, Presciutti O, Lowenthal DT, Pippi M, Palumbo B, et al. Proton magnetic resonance spectroscopy can differentiate Alzheimer's disease from normal aging. Mech Ageing Dev. 1997;97(1):9-14.
288. Kantarci K. 1H magnetic resonance spectroscopy in dementia. Br J Radiol. 2007;80 Spec No 2:S146-52.
289. Ross BD, Bluml S, Cowan R, Danielsen E, Farrow N, Tan J. In vivo MR spectroscopy of human dementia. Neuroimaging Clin N Am. 1998;8(4):809-22.
290. Valenzuela MJ, Sachdev P. Magnetic resonance spectroscopy in AD. Neurology. 2001;56(5):592-8.
291. Bankhead P, Loughrey MB, Fernandez JA, Dombrowski Y, McArt DG, Dunne PD, et al. QuPath: Open source software for digital pathology image analysis. Sci Rep. 2017;7(1):16878.
292. Zhang H, Chiu PW, Ip I, Liu TY, Wong GHY, Song YQ, et al. Small-World Networks and Their Relationship With Hippocampal Glutamine/Glutamate Concentration in Healthy Adults With Varying Genetic Risk for Alzheimer's Disease. J Magn Reson Imaging. 2021;54(3):952-61.
293. Jung F, Kazemifar S, Bartha R, Rajakumar N. Semiautomated Assessment of the Anterior Cingulate Cortex in Alzheimer's Disease. J Neuroimaging. 2019;29(3):376-82.
294. Ferreri F, Pauri F, Pasqualetti P, Fini R, Dal Forno G, Rossini PM. Motor cortex excitability in Alzheimer's disease: a transcranial magnetic stimulation study. Ann Neurol. 2003;53(1):102-8.
295. Wiesman AI, Mundorf VM, Casagrande CC, Wolfson SL, Johnson CM, May PE, et al. Somatosensory dysfunction is masked by variable cognitive deficits across patients on the Alzheimer's disease spectrum. Ebiomedicine. 2021;73.

296. Stephen JM, Montano R, Donahue CH, Adair JC, Knoefel J, Qualls C, et al. Somatosensory responses in normal aging, mild cognitive impairment, and Alzheimer's disease. J Neural Transm. 2010;117(2):217-25.
297. Teipel SJ, Bayer W, Alexander GE, Zebuhr Y, Teichberg D, Kulic L, et al. Progression of corpus callosum atrophy in Alzheimer disease. Arch Neurol. 2002;59(2):243-8.
298. Zhu M, Gao W, Wang X, Shi C, Lin Z. Progression of corpus callosum atrophy in early stage of Alzheimer's disease: MRI based study. Acad Radiol. 2012;19(5):512-7.
299. Adler DH, Wisse LEM, Ittyerah R, Pluta JB, Ding SL, Xie L, et al. Characterizing the human hippocampus in aging and Alzheimer's disease using a computational atlas derived from ex vivo MRI and histology. Proc Natl Acad Sci U S A. 2018;115(16):4252-7.
300. Schuff N, Woerner N, Boreta L, Kornfield T, Shaw LM, Trojanowski JQ, et al. MRI of hippocampal volume loss in early Alzheimer's disease in relation to ApoE genotype and biomarkers. Brain. 2009;132(Pt 4):1067-77.
301. Katabathula S, Wang Q, Xu R. Predict Alzheimer's disease using hippocampus MRI data: a lightweight 3D deep convolutional network model with visual and global shape representations. Alzheimers Res Ther. 2021;13(1):104.
302. Schneider CA, Rasband WS, Eliceiri KW. NIH Image to ImageJ: 25 years of image analysis. Nat Methods. 2012;9(7):671-5.
303. Kim HY. Statistical notes for clinical researchers: Two-way analysis of variance (ANOVA)-exploring possible interaction between factors. Restor Dent Endod. 2014;39(2):143-7.
304. Hashimoto T. [Sample size determination given data of preliminary experiment for student's t-test, ANOVA and Tukey's multiple comparison]. Shinrigaku Kenkyu. 2004;75(3):213-9.
305. Ruxton GD, Beauchamp G. Time for some a priori thinking about post hoc testing. Behavioral Ecology. 2008;19(3):690-3.
306. Rogan JC, Keselman HJ, Breen LJ. Assumption Violations and Rates of Type-I Error for Tukey Multiple Comparison Test - Review and Empirical-Investigation Via a Coefficient of Variance Variation. Journal of Experimental Education. 1977;46(1):20-5.
307. Keselman HJ. Power Investigation of Tukey Multiple Comparison Statistic. Educational and Psychological Measurement. 1976;36(1):97-104.
308. Keselman HJ, Rogan JC. Tukey Multiple Comparison Test - 1953-1976. Psychological Bulletin. 1977;84(5):1050-6.
309. Tse KH, Cheng A, Ma F, Herrup K. DNA damage-associated oligodendrocyte degeneration precedes amyloid pathology and contributes to Alzheimer's disease and dementia. Alzheimers Dement. 2018;14(5):664-79.
310. Kulnane LS, Lamb BT. Neuropathological characterization of mutant amyloid precursor protein yeast artificial chromosome transgenic mice. Neurobiol Dis. 2001;8(6):982-92.
311. Bentahir M, Nyabi O, Verhamme J, Tolia A, Horre K, Wiltfang J, et al. Presenilin clinical mutations can affect gamma-secretase activity by different mechanisms. Journal of Neurochemistry. 2006;96(3):732-42.
312. Steiner H, Romig H, Grim MG, Philipp U, Pesold B, Citron M, et al. The biological and pathological function of the presenilin-1 Delta exon 9 mutation is independent of its defect to undergo proteolytic processing. Journal of Biological Chemistry. 1999;274(12):7615-8.
313. De Strooper B. Loss-of-function presenilin mutations in Alzheimer disease. Talking Point on the role of presenilin mutations in Alzheimer disease. EMBO Rep. 2007;8(2):141-6.
314. Edwards SR, Hamlin AS, Marks N, Coulson EJ, Smith MT. Comparative studies using the Morris water maze to assess spatial memory deficits in two transgenic mouse models of Alzheimer's disease. Clin Exp Pharmacol Physiol. 2014;41(10):798-806.
315. Depp C, Sun T, Sasmita AO, Spieth L, Berghoff SA, Nazarenko T, et al. Myelin dysfunction drives amyloid-beta deposition in models of Alzheimer's disease. Nature. 2023;618(7964):349-57.
316. Webster SJ, Bachstetter AD, Van Eldik LJ. Comprehensive behavioral characterization of an APP/PS-1 double knock-in mouse model of Alzheimer's disease. Alzheimers Res Ther. 2013;5(3):28.
317. Carrera I, Etcheverria I, Fernandez-Novoa L, Lombardi V, Cacabelos R, Vigo C. Vaccine Development to Treat Alzheimer's Disease Neuropathology in APP/PS1 Transgenic Mice. Int J Alzheimers Dis. 2012;2012:376138.

318. Chen X, Guo C, Kong J. Oxidative stress in neurodegenerative diseases. Neural Regen Res. 2012;7(5):376-85.
319. McKinnon PJ. Maintaining genome stability in the nervous system. Nat Neurosci. 2013;16(11):1523-9.
320. Caldecott KW, Ward ME, Nussenzweig A. The threat of programmed DNA damage to neuronal genome integrity and plasticity. Nat Genet. 2022;54(2):115-20.
321. Konopka A, Atkin JD. The Role of DNA Damage in Neural Plasticity in Physiology and Neurodegeneration. Front Cell Neurosci. 2022;16:836885.
322. Kondo MA, Fukudome D, Smith DR, Gallagher M, Kamiya A, Sawa A. Dimensional assessment of behavioral changes in the cuprizone short-term exposure model for psychosis. Neurosci Res. 2016;107:70-4.
323. Makinodan M, Yamauchi T, Tatsumi K, Okuda H, Takeda T, Kiuchi K, et al. Demyelination in the juvenile period, but not in adulthood, leads to long-lasting cognitive impairment and deficient social interaction in mice. Prog Neuropsychopharmacol Biol Psychiatry. 2009;33(6):978-85.
324. Chang HX, Liu JH, Zhang YF, Wang F, Wu YC, Zhang L, et al. Increased central dopaminergic activity might be involved in the behavioral abnormality of cuprizone exposure mice. Behav Brain Res. 2017;331:143-50.
325. Shao Y, Peng H, Huang QJ, Kong JM, Xu HY. Quetiapine mitigates the neuroinflammation and oligodendrocyte loss in the brain of C57BL/6 mouse following cuprizone exposure for one week. Eur J Pharmacol. 2015;765:249-57.
326. Koutsoudaki PN, Skripuletz T, Gudi V, Moharregh-Khiabani D, Hildebrandt H, Trebst C, et al. Demyelination of the hippocampus is prominent in the cuprizone model. Neuroscience Letters. 2009;451(1):83-8.
327. Norkute A, Hieble A, Braun A, Johann S, Clarner T, Baumgartner W, et al. Cuprizone Treatment Induces Demyelination and Astrocytosis in the Mouse Hippocampus. Journal of Neuroscience Research. 2009;87(6):1343-55.
328. Stokin GB, Almenar-Queralt A, Gunawardena S, Rodrigues EM, Falzone T, Kim J, et al. Amyloid precursor protein-induced axonopathies are independent of amyloid-beta peptides. Hum Mol Genet. 2008;17(22):3474-86.
329. Stokin GB, Lillo C, Falzone TL, Brusch RG, Rockenstein E, Mount SL, et al. Axonopathy and transport deficits early in the pathogenesis of Alzheimer's disease. Science. 2005;307(5713):1282-8.
330. Zhang J, Jones MV, McMahon MT, Mori S, Calabresi PA. In vivo and ex vivo diffusion tensor imaging of cuprizone-induced demyelination in the mouse corpus callosum. Magn Reson Med. 2012;67(3):750-9.
331. Brady ST, Witt AS, Kirkpatrick LL, de Waegh SM, Readhead C, Tu PH, et al. Formation of compact myelin is required for maturation of the axonal cytoskeleton. J Neurosci. 1999;19(17):7278-88.
332. Edgar JM, McLaughlin M, Yool D, Zhang SC, Fowler JH, Montague P, et al. Oligodendroglial modulation of fast axonal transport in a mouse model of hereditary spastic paraplegia. J Cell Biol. 2004;166(1):121-31.
333. Zeisel SH, Blusztajn JK. Choline and human nutrition. Annu Rev Nutr. 1994;14:269-96.
334. Wang Y, Guan X, Chen X, Cai Y, Ma Y, Ma J, et al. Choline Supplementation Ameliorates Behavioral Deficits and Alzheimer's Disease-Like Pathology in Transgenic APP/PS1 Mice. Mol Nutr Food Res. 2019;63(18):e1801407.
335. Ehrenstein G, Galdzicki Z, Lange GD. The choline-leakage hypothesis for the loss of acetylcholine in Alzheimer's disease. Biophys J. 1997;73(3):1276-80.
336. Mustafa IH, Elkamel A, Chen P, Ibrahim G, Elnashaie SSEH. Effect of cholineacetyltransferase activity and choline recycle ratio on diffusion-reaction modeling, bifurcation and chaotic behavior of acetylcholine neurocycle and their relation to Alzheimer's and Parkinson's diseases. Chem Eng Sci. 2012;68(1):19-35.
337. Waragai M, Moriya M, Nojo T. Decreased N-Acetyl Aspartate/Myo-Inositol Ratio in the Posterior Cingulate Cortex Shown by Magnetic Resonance Spectroscopy May Be One of the Risk Markers of Preclinical Alzheimer's Disease: A 7-Year Follow-Up Study. J Alzheimers Dis. 2017;60(4):1411-27.

338. Voevodskaya O, Sundgren PC, Strandberg O, Zetterberg H, Minthon L, Blennow K, et al. Myo-inositol changes precede amyloid pathology and relate to APOE genotype in Alzheimer disease. Neurology. 2016;86(19):1754-61.
339. Graff-Radford J, Kantarci K. Magnetic resonance spectroscopy in Alzheimer's disease. Neuropsychiatr Dis Treat. 2013;9:687-96.
340. Shirbandi K, Rikhtegar R, Khalafi M, Mirza Aghazadeh Attari M, Rahmani F, Javanmardi P, et al. Functional Magnetic Resonance Spectroscopy of Lactate in Alzheimer Disease: A Comprehensive Review of Alzheimer Disease Pathology and the Role of Lactate. Top Magn Reson Imaging. 2023;32(2):15-26.
341. Murray ME, Przybelski SA, Lesnick TG, Liesinger AM, Spychalla A, Zhang B, et al. Early Alzheimer's disease neuropathology detected by proton MR spectroscopy. J Neurosci. 2014;34(49):16247-55.
342. Ross JM, Oberg J, Brene S, Coppotelli G, Terzioglu M, Pernold K, et al. High brain lactate is a hallmark of aging and caused by a shift in the lactate dehydrogenase A/B ratio. P Natl Acad Sci USA. 2010;107(46):20087-92.
343. Rodriguez GA, Burns MP, Weeber EJ, Rebeck GW. Young APOE4 targeted replacement mice exhibit poor spatial learning and memory, with reduced dendritic spine density in the medial entorhinal cortex. Learn Mem. 2013;20(5):256-66.
344. Van Hoesen GW. Ventromedial temporal lobe anatomy, with comments on Alzheimer's disease and temporal injury. J Neuropsychiatry Clin Neurosci. 1997;9(3):331-41.
345. Sun Y, Wu S, Bu G, Onifade MK, Patel SN, LaDu MJ, et al. Glial fibrillary acidic protein-apolipoprotein E (apoE) transgenic mice: astrocyte-specific expression and differing biological effects of astrocyte-secreted apoE3 and apoE4 lipoproteins. J Neurosci. 1998;18(9):3261-72.
346. Lanfranco MF, Sepulveda J, Kopetsky G, Rebeck GW. Expression and secretion of apoE isoforms in astrocytes and microglia during inflammation. Glia. 2021;69(6):1478-93.
347. Harada R, Ishiki A, Kai H, Sato N, Furukawa K, Furumoto S, et al. Correlations of (18)F-THK5351 PET with Postmortem Burden of Tau and Astrogliosis in Alzheimer Disease. J Nucl Med. 2018;59(4):671-4.
348. Kamphuis W, Mamber C, Moeton M, Kooijman L, Sluijs JA, Jansen AH, et al. GFAP isoforms in adult mouse brain with a focus on neurogenic astrocytes and reactive astrogliosis in mouse models of Alzheimer disease. PLoS One. 2012;7(8):e42823.
349. Osborn LM, Kamphuis W, Wadman WJ, Hol EM. Astrogliosis: An integral player in the pathogenesis of Alzheimer's disease. Prog Neurobiol. 2016;144:121-41.
350. Peters A, Sethares C. Oligodendrocytes, their progenitors and other neuroglial cells in the aging primate cerebral cortex. Cereb Cortex. 2004;14(9):995-1007.
351. Boban J, Thurnher MM, Boban N, Law M, Jahanshad N, Nir TM, et al. Gradient Patterns of Age-Related Diffusivity Changes in Cerebral White Matter. Front Neurol. 2022;13:870909.
352. Behler A, Kassubek J, Muller HP. Age-Related Alterations in DTI Metrics in the Human Brain-Consequences for Age Correction. Front Aging Neurosci. 2021;13:682109.
353. Tai LM, Balu D, Avila-Munoz E, Abdullah L, Thomas R, Collins N, et al. EFAD transgenic mice as a human APOE relevant preclinical model of Alzheimer's disease. J Lipid Res. 2017;58(9):1733-55.
354. Chang L, Douet V, Bloss C, Lee K, Pritchett A, Jernigan TL, et al. Gray matter maturation and cognition in children with different APOE epsilon genotypes. Neurology. 2016;87(6):585-94.
355. Shaw P, Lerch JP, Pruessner JC, Taylor KN, Rose AB, Greenstein D, et al. Cortical morphology in children and adolescents with different apolipoprotein E gene polymorphisms: an observational study. Lancet Neurol. 2007;6(6):494-500.
356. Taylor AE, Guthrie PA, Smith GD, Golding J, Sattar N, Hingorani AD, et al. IQ, educational attainment, memory and plasma lipids: associations with apolipoprotein E genotype in 5995 children. Biol Psychiatry. 2011;70(2):152-8.
357. Hasler G. Pathophysiology of depression: do we have any solid evidence of interest to clinicians? World Psychiatry. 2010;9(3):155-61.
358. Antuono PG, Jones JL, Wang Y, Li SJ. Decreased glutamate + glutamine in Alzheimer's disease detected in vivo with (1)H-MRS at 0.5 T. Neurology. 2001;56(6):737-42.

359. Greene JG, Greenamyre JT. Bioenergetics and glutamate excitotoxicity. Prog Neurobiol. 1996;48(6):613-34.
360. Chen Y, Durakoglugil MS, Xian X, Herz J. ApoE4 reduces glutamate receptor function and synaptic plasticity by selectively impairing ApoE receptor recycling. Proc Natl Acad Sci U S A. 2010;107(26):12011-6.
361. Rodrigue KM, Rieck JR, Kennedy KM, Devous MD, Sr., Diaz-Arrastia R, Park DC. Risk factors for beta-amyloid deposition in healthy aging: vascular and genetic effects. JAMA Neurol. 2013;70(5):600-6.
362. Irvine KA, Blakemore WF. Age increases axon loss associated with primary demyelination in cuprizone-induced demyelination in C57BL/6 mice. J Neuroimmunol. 2006;175(1-2):69-76.
363. Tsunoda I, Fujinami RS. Inside-Out versus Outside-In models for virus induced demyelination: axonal damage triggering demyelination. Springer Semin Immunopathol. 2002;24(2):105-25.
364. Adle-Biassette H, Chretien F, Wingertsmann L, Hery C, Ereau T, Scaravilli F, et al. Neuronal apoptosis does not correlate with dementia in HIV infection but is related to microglial activation and axonal damage. Neuropathol Appl Neurobiol. 1999;25(2):123-33.
365. Chen JF, Liu K, Hu B, Li RR, Xin W, Chen H, et al. Enhancing myelin renewal reverses cognitive dysfunction in a murine model of Alzheimer's disease. Neuron. 2021;109(14):2292-307 e5.
366. Chen Y, Sheng J, Tang X, Zhao Y, Zhu S, Liu Q. Clemastine Rescues Chemotherapy-Induced Cognitive Impairment by Improving White Matter Integrity. Neuroscience. 2022;484:66-79.
367. Bartzokis G, Lu PH, Geschwind DH, Tingus K, Huang D, Mendez MF, et al. Apolipoprotein E affects both myelin breakdown and cognition: implications for age-related trajectories of decline into dementia. Biol Psychiatry. 2007;62(12):1380-7.
368. Cantuti-Castelvetri L, Fitzner D, Bosch-Queralt M, Weil MT, Su M, Sen P, et al. Defective cholesterol clearance limits remyelination in the aged central nervous system. Science. 2018;359(6376):684-8.
369. Dean DC, 3rd, Hurley SA, Kecskemeti SR, O'Grady JP, Canda C, Davenport-Sis NJ, et al. Association of Amyloid Pathology With Myelin Alteration in Preclinical Alzheimer Disease. JAMA Neurol. 2017;74(1):41-9.
370. Wu Y, Ma Y, Liu Z, Geng Q, Chen Z, Zhang Y. Alterations of myelin morphology and oligodendrocyte development in early stage of Alzheimer's disease mouse model. Neurosci Lett. 2017;642:102-6.
371. Sienski G, Narayan P, Bonner JM, Kory N, Boland S, Arczewska AA, et al. APOE4 disrupts intracellular lipid homeostasis in human iPSC-derived glia. Sci Transl Med. 2021;13(583).
372. Victor MB, Leary N, Luna X, Meharena HS, Scannail AN, Bozzelli PL, et al. Lipid accumulation induced by APOE4 impairs microglial surveillance of neuronal-network activity. Cell Stem Cell. 2022;29(8):1197-212 e8.
373. Frieden C, Wang H, Ho CMW. A mechanism for lipid binding to apoE and the role of intrinsically disordered regions coupled to domain-domain interactions. Proc Natl Acad Sci U S A. 2017;114(24):6292-7.
374. Bartzokis G, Lu PH, Geschwind DH, Edwards N, Mintz J, Cummings JL. Apolipoprotein E genotype and age-related myelin breakdown in healthy individuals: implications for cognitive decline and dementia. Arch Gen Psychiatry. 2006;63(1):63-72.
375. Tse KH, Herrup K. DNA damage in the oligodendrocyte lineage and its role in brain aging. Mech Ageing Dev. 2017;161(Pt A):37-50.
376. Janssen CI, Jansen D, Mutsaers MP, Dederen PJ, Geenen B, Mulder MT, et al. The Effect of a High-Fat Diet on Brain Plasticity, Inflammation and Cognition in Female ApoE4-Knockin and ApoE-Knockout Mice. PLoS One. 2016;11(5):e0155307.
377. Fernandez CG, Hamby ME, McReynolds ML, Ray WJ. The Role of APOE4 in Disrupting the Homeostatic Functions of Astrocytes and Microglia in Aging and Alzheimer's Disease. Front Aging Neurosci. 2019;11:14.
378. Rodriguez GA, Tai LM, LaDu MJ, Rebeck GW. Human APOE4 increases microglia reactivity at Abeta plaques in a mouse model of Abeta deposition. J Neuroinflammation. 2014;11:111.